

Electron Spins in Single and Double Quantum Dots: Transport, Correlations and Decoherence

Inauguraldissertation

zur

Erlangung der Würde eines Doktors der Philosophie

vorgelegt der

Philosophisch-Naturwissenschaftlichen Fakultät
der Universität Basel

von

Vitaly N. Golovach
aus Czernowitz (Ukraine)

Basel, 2005

Genehmigt von der Philosophisch-Naturwissenschaftlichen Fakultät
auf Antrag von

Prof. Dr. Daniel Loss

Prof. Dr. Leonid Glazman

Prof. Dr. Christoph Bruder

Basel, den 5. Juli 2005

Prof. Dr. Jakob Wirz
Dekan

Acknowledgments

I would like to thank Prof. Dr. Daniel Loss for giving me the opportunity to work on this interesting topic in physics, which I believe will keep fascinating everyone for quite some time. I started as a graduate student at the Department of Physics and Astronomy of the University of Basel about four years ago and at that time I knew very little about quantum computing and about spins of electrons in quantum dots. I learned a lot from Prof. Loss and from the research group here in Basel, and I find it great that I have now this occasion to thank everyone for their help.

I thank Prof. Dr. D. Loss for guiding my research work and supporting me in writing this thesis. It has been a useful experience for me to work with Prof. Loss. The topics we chose to work on were timely and realistic to observe in experiment. I thank Prof. Loss for countless discussions on physics and for always being available to talk to and give advice. I thank Prof. Dr. C. Bruder and Prof. Dr. L. Glazman for kindly agreeing to co-referee this thesis.

Next, I would like to thank the people I worked with during my time as a graduate student in Basel. I thank M. Borhani for collaborating with me on QPC-induced spin decay in quantum dots, Prof. Dr. G. Burkard and B. Coish for collaborating on Pauli-blockaded double dots, Prof. Dr. M.-S. Choi for collaborating on Kondo effect, Dr. J. Elzerman, Dr. H.-A. Engel, Dr. R. Hanson, Prof. Dr. L. Kouwenhoven, and Prof. Dr. L. Vandersypen for collaborating on n -shot read-out and QPC-based charge measurements in double dots, Dr. A. Khaetskii for collaborating on phonon-induced spin decay in quantum dots. I would also like to thank Prof. Dr. E. Sukhorukov for supporting me in the beginning of my graduate study in Basel, and for many scientific discussions on transport in quantum dots. I would also like to acknowledge my colleagues A. Alkauskas, Prof. Dr. W. Belzig, Dr. D. Bulaev, Dr. V. Cerletti, Dr. O. Chalaev, B. Coish, Dr. A. Cottet, C. Doiron, M. Duckheim, Prof. Dr. J. Egues, Dr. S. Erlingsson, Dr. H. Gassmann, Dr. O. Gywat, Dr. T. Heikkilä, D. Klauser, Dr. M. Lee, Dr. J. Lehmann, Dr. M. Leuenberger, A. Lyakhov, Dr. F. Marquardt, Dr. F. Meier, Dr. P. Recher, Dr. D. Saraga, Dr. J. Schliemann, C. Schroll, Dr. P. Simon, M. Vanevic, for creating a lively and stimulating atmosphere in the research group. Special thanks go to my office mates Prof. Dr. G. Burkard, Dr. V. Cerletti, Dr. F. Brachwitz, and D. Salem for interesting discussions.

Finally, I would like to thank my wife, Sophia Bloch, for her love, support, and encouragement to write this thesis.

Abstract

This thesis is devoted to the study of electron spins in quantum dots. In recent years, the quantum dots have evolved towards smaller sizes and a better control over the number of electrons on a dot. Comparing to a decade ago, when the quantum dots were containing hundreds of electrons and behaving unpredictably under small changes of their electrostatic or magnetic environment, today, the state-of-the-art quantum dots resemble rather atoms (with well-organized electronic shells and energy gaps of several meV) than chaotic systems (with randomly distributed energy levels). These man-made atoms display lucent quantum-mechanical properties, suitable for use as a resource to extend the *classical* information processing to the ultimate *quantum* one. The electron spin, being solely quantum by its nature, enriches the physics of quantum dots and opens a new (quantum) dimension, which can be used as a degree of freedom to store and process information. The need to coexist at the same scale of both quantum degrees of freedom (to encode qubits) and classical degrees of freedom (to use as local gates to control qubits) renders the scale of quantum information processing to the *meso*-scale — the borderline between the worlds of *classical* and *quantum*. The quantum dots are examples of refined mesoscopic systems, where the quantum degrees of freedom can be deterministically controlled by classical gates to implement the quantum Turing machine.

While this is the long-term goal and requires progressive development of appropriate technologies, the present interest to quantum dots is focused on characterizing the quantum dots (finding ways to learn their parameters), identifying the dominant mechanisms of decoherence, and engineering *interactions on demand*, which are needed for quantum computing. The flexibility of quantum dots to design and their dynamical tunability promises an easy integration of quantum dots into (quantum) circuits. Once a single building block with required physical properties is constructed, it can be replicated to a large number of such blocks. Interestingly, this fundamental building block has to consist of at least two quantum dots (two qubits), owing to entanglement as a new resource in quantum information processing. This thesis considers, thus, single and double quantum dots and studies their spin-related phenomena in a variety of contexts.

Electron transport is a common method of studying quantum dots. A quantum dot or a small quantum-dot circuit can be probed by leads at finite source-drain bias. Based on transport measurements, specific regimes of interest can be identified, to

which the quantum dots can then be tuned by gates at any time. For quantum computing, it is necessary to have access to specific coupling constants and to know their dependence on gates. In this thesis, we study in detail two coupled quantum dots and show that a number of parameters can be extracted from transport measurements. In particular, the Heisenberg exchange interaction between spins of tunnel-coupled quantum dots can be accessed in transport in the regimes of sequential tunneling, cotunneling, and Kondo effect. The electron-electron correlations, such as entanglement, are also of great interest in the physics of quantum dots and for applications to quantum information processing. In Chaps. 2 and 3, we show that correlations between electrons can be accessed in transport as well. Most vividly they show up in the cotunneling conductance at the singlet-triplet transition and in some specific *strong* heating regimes away from the singlet-triplet transition. Our results have recently been used in experiment to access these correlations in a two-electron quantum dot of elongated shape.

The Kondo effect is a correlated many-body phenomenon, distinct by peculiar features in transport, such as unitary limit of conductance. It arises under specific conditions that allow the many-body correlations to build up. In tunnel-coupled quantum dots, the Kondo effect is sensitive to the exchange interaction between spins. The competition between Kondo effect and exchange interaction brings the system close to a quantum critical point (first studied for the two-impurity Kondo model in context of magnetic impurities in metals). This quantum critical point can be studied experimentally in the asymptotic limit of weakly coupled quantum dots. It gives rise to a narrow peak in the linear conductance as function of the inter-dot tunnel coupling, provided the latter is much smaller than the dot-lead coupling ($t \ll \Gamma$). The competition between Kondo effect and exchange interaction is far more fragile than the Kondo effect itself, and is thus characterized by a much smaller energy scale than the Kondo temperature. Observation of the sharp peak in transport will therefore signify that extremely fragile many-body correlations build up in the system, which alone is fascinating. The long range nature of the Coulomb interaction between electrons also reflects on the transport properties of coupled quantum dots. A wide peak emerges in the linear conductance as function of inter-dot tunnel-coupling due to singlet-triplet Kondo correlations. With applying an orbital magnetic field this peak turns into a singlet-triplet Kondo effect, distinct by an enhanced Kondo temperature. Finally, the Kondo correlations also enhance the signatures of Heisenberg exchange interaction in the temperature dependence of linear conductance and further access to this important for quantum computing parameter.

Coherence of electron spin is a fundamental question in solid state. In semiconductor quantum dots, the spin coherence is limited by the dot *intrinsic* degrees of freedom, such as phonons, spins of nuclei, particle-hole excitations in metallic gates, switching impurities nearby the dot ($1/f$ noise), electromagnetic fields, etc. The electron spin interacts weakly with matter, which makes it a promising candidate for use in quantum information processing. One important interaction in semiconductors is the spin-orbit interaction. The spin-orbit interaction mediates coupling of the electron

spin to any degree of freedom that couples to the electron charge. In this thesis, we study spin decoherence due to the spin-orbit interaction.

The spin decoherence time T_2 — the lifetime of a coherent superposition of spin-up and spin-down states — must be sufficiently long for quantum computing algorithms and quantum error correction schemes to be implemented. The decoherence time T_2 is limited by spin-flip processes occurring over the spin relaxation time T_1 . This gives an upper bound for T_2 , $T_2 \leq 2T_1$. The spin relaxation time T_1 is extremely long in quantum dots (measured values range from $100 \mu\text{s}$ to 20ms). Additional reduction of T_2 can occur only due to dephasing, *i.e.* loss of phase of coherent Larmor precession, which requires a (quantum) fluctuating magnetic field along the spin quantization axis. Most solid state implementations of qubits suffer strongly from dephasing, which makes $T_2 \ll T_1$. In Chap. 4, we show that the spin-orbit interaction in quantum dots is not responsible for a strong reduction of T_2 . We consider the Rashba and Dresselhaus spin-orbit interactions in quantum dots and find that only spin relaxation (*i.e.* no dephasing) is possible in the leading order in these interactions. We obtain an effective spin Hamiltonian which contains only purely transverse fluctuations of magnetic field in the leading order of the spin-orbit interaction. Our finding means that the decoherence time T_2 is close to its upper bound $T_2 = 2T_1$ for spin-decay mechanisms based on the spin-orbit interaction (additional decoherence can occur due to the hyperfine interaction in a quantum dot). We also calculate the relaxation time T_1 due to phonon emission and find an excellent agreement with experiment if we use an independently measured spin-orbit length of $(8 - 10) \mu\text{m}$. Our results indicate that phonon emission is a dominant mechanism of spin relaxation in GaAs quantum dots.

For a two-electron quantum dot, we study spin relaxation between singlet and triplet levels in Chap. 5. Since the orbital wave functions of singlet and triplet differ significantly from each other, decoherence is expected to set in at a short time scale ($\sim 1 \text{ns}$) due to charge noise. In contrast, the spin-flip transitions require spin-orbit interaction, similarly to spin relaxation in a single-electron quantum dot, and therefore, they have a much longer time scale ($\sim 100 \mu\text{s}$). The spin relaxation in a two-electron quantum dot can thus be used as an additional test to verify the dominant mechanism of spin relaxation in quantum dots and to obtain an estimate for spin relaxation between Zeeman sub-levels in single-electron quantum dots. In experiment, the triplet-to-singlet spin relaxation is easier to study than the relaxation between Zeeman sub-levels, since the latter requires application of a large magnetic field to resolve in energy the spin-up and spin-down levels. The singlet and triplet levels are well separated from each other already at zero magnetic field and makes it possible to study experimentally spin relaxation in the low B -field limit. With applying an orbital magnetic field the two-electron quantum dot undergoes a singlet-triplet transition, which allows one to probe the low energy part of the spectral function of the environment at a finite magnetic field. Due to the spin-orbit interaction we find avoided crossings of singlet and triplet levels at the singlet-triplet transition. We calculate the relaxation rates due to phonon-emission and find a rich behavior of rates

as functions of magnetic field around the singlet-triplet transition. We also analyze the effect of Coulomb interaction and show that it enhances the role of spin-orbit interaction in the quantum dot, however it suppresses the interaction with phonons for the singlet-triplet relaxation.

Motivated by recent spin read-out experiments, we study the effect of a QPC, functioning close to a quantum dot, on the spin relaxation in the quantum dot. We derive a microscopic model for the spin-charge interaction and calculate the spin relaxation time T_1 in Chap. 6. The interaction of spin with charge occurs due to the spin-orbit interaction in the quantum dot at a finite magnetic field. We find a strong dependence ($1/r^6$) of the relaxation rate on the distance to the QPC.

In Chap. 7, we consider several spin read-out schemes based on spin-to-charge conversion and subsequent charge detection by a QPC. We introduce the notion of n -shot read-out, as opposite to the single-shot read-out, for the case when the “measuring apparatus” has an systematic measurement inefficiency. This measurement inefficiency is *intrinsic* to the measurement setup, *i.e.* it is not related to the signal-to-noise ratio in a measurement output. In this case, for a qubit which is in either “spin-up” or “spin-down” state, one has to repeat the preparation and measurement of qubit some number of times n until the qubit state is known with a given infidelity α . We characterize the spin read-out using the formalism of positive-operator-valued (POV) measurements, and calculate n as a function of α and the POV probabilities (specific to measurement setup). We introduce a measurement efficiency e ($0 \leq e \leq 1$) which characterizes the measurement apparatus, and analyze examples for which $e \approx 0.5$ and $e \approx 1$. We show that $e < 1$ results in a reduced visibility in measurements of coherent oscillations.

The shot noise of a double quantum dot is studied in Chap. 8 using a phenomenological approach. We formulate a stochastic model for shot noise in a multilevel system. We relate the parameters entering our model to the transmission/reflection amplitudes of the scattering matrix. We study shot-noise close to the Kondo regime in the double quantum dot. We find super-poissonian noise in the limit of weakly coupled quantum dots.

Contents

Acknowledgments	iii
Abstract	v
1 Introduction	1
1.1 Spintronics and quantum computing	1
1.2 Electron spins in quantum dots	8
1.3 Quantum entanglement	9
1.4 Decoherence	13
1.5 Transport and Kondo effect in quantum dots	17
2 Kondo effect and singlet-triplet splitting in coupled quantum dots in a magnetic field	23
2.1 Introduction	23
2.2 Model Hamiltonian	24
2.3 Kondo effect in the double dot	28
2.4 Signatures of the Kondo effect in transport	28
3 Transport through a double quantum dot in the sequential tunneling and cotunneling regimes	33
3.1 Introduction	33
3.2 Energy spectrum of a double quantum dot	36
3.3 Sequential tunneling through the double dot	38
3.3.1 Master equation	41
3.3.2 Sequential tunneling current	47
3.3.3 Charge detection via a QPC	49

3.4	Cotunneling in the $N = 1$ Coulomb blockade valley	51
3.5	Cotunneling in the $N = 2$ Coulomb blockade valley	53
3.6	Cotunneling-assisted sequential tunneling	55
3.7	Conclusions	59
4	Phonon-induced decay of the electron spin in quantum dots	61
4.1	Introduction	61
4.2	Model Hamiltonian	63
4.3	Bloch equation	64
4.4	Phonon-induced spin decay	65
4.5	Other spin-orbit mechanisms	68
4.6	Conclusions	68
5	Spin relaxation at the singlet-triplet transition in a quantum dot	69
5.1	Introduction	69
5.2	Model Hamiltonian	71
5.3	Energy spectrum and wave functions	72
5.4	Matrix elements of H_{SO}	77
5.5	Electron states with spin-orbit interaction	80
5.5.1	Case of zero Zeeman interaction ($g = 0$)	80
5.5.2	Case of finite Zeeman interaction ($g \neq 0$)	85
5.6	Phonon-induced spin relaxation	96
5.6.1	Secular approximation	99
5.6.2	Relaxation rates	103
6	Spin decay in a quantum dot coupled to a quantum point contact	111
6.1	Introduction	111
6.2	Quantum dot coupled to a QPC	112
6.3	Effective Hamiltonian	113
6.4	Relaxation time T_1	117
6.5	Conclusions	119

7	Measurement efficiency and n-shot read out of spin qubits	121
7.1	Introduction	121
7.1.1	n -shot read out and measurement efficiency e	121
7.1.2	Visibility v	123
7.2	Single spin read out	124
7.2.1	Read out with different Zeeman splittings	124
7.2.2	Spin-dependent tunneling	124
7.2.3	Read out with Pauli principle	125
7.3	Read-out model	126
7.3.1	Incoherent tunneling	128
7.3.2	Read out with time-dependent currents	128
7.4	Conclusions	128
8	Shot noise in transport through a double quantum dot close to the Kondo regime	129
8.1	Introduction	129
8.2	From scattering matrix to a stochastic model	130
8.3	Results	131
A	Double dot states in the L-R basis	133
B	Sequential tunneling rates	135
C	Cotunneling rates	137
D	Variational parameters $\tilde{\omega}$ and γ	139
E	Matrix elements of V	143
F	Exact relations at the singlet-triplet transition	145
	Bibliography	147
	Curriculum Vitae	159

Chapter 1

Introduction

1.1 Spintronics and quantum computing

In the last decade, there has been much interest in the electron spin as a degree of freedom in semiconductor devices. This interest comes from the solid-state electronics industry, which has enjoyed several decades of constant downscaling of on-chip integrated circuits, governed by Moore's law.¹ As this progressive miniaturization is approaching the borderline between the worlds of *classical* and *quantum*, further advances can be made either with the help of purely quantum systems or by utilizing new physical phenomena, capable of improving the functionality of still-classical devices. An example of the latter is the spin-polarized electronic transport, where carriers of opposite spins rather than carriers of opposite charges are utilized to build transistors [1]. This new approach to electronics is called magnetoelectronics [1], and it started soon after the discovery of the giant magnetoresistance effect (GMR) [2] in 1988. Since then, almost every today's computer hard drive has magnetic read-out heads based on the GMR, a non-volatile type of random access memory (memory that holds its content without power) has successfully been developed using magnetic materials, and reprogrammable logic microprocessors are going to be developed in the future. The success of the GMR and the use of magnetic materials in electronics has initiated a wave of investigation of the spin-related effects in semiconductor materials, with the focus on spin-coherent effects. This field of research became known as spintronics² [3, 4]. Semiconductors are generally easier to integrate into complex circuits than metals, and they provide a richer and almost continuous variety of materials, due to their strong sensitivity to doping. The spin-polarized electronic transport

¹This is an empirical observation, made by Gordon Moore in 1965, stating that the complexity of the integrated circuits grows exponentially with time (the number of transistors per unit area of integrated circuit doubles, roughly, every 18 months).

²Spintronics stands for "spin-based electronics" and considers both magnetic metals (ferromagnets) and magnetic semiconductors (such as dilute magnetic semiconductors). The term magnetoelectronics is often used to refer specifically to electronics that is based on ferromagnets, *e.g.* electronics utilizing GMR.

is finding more and more potential applications [3–6] as the electronic devices are getting smaller and the spin-polarized carriers have to travel over shorter distances. Ultimately, the quantum-mechanical coherence of the electron spin becomes of great practical relevance, since it offers the prospect of a better and fundamentally new spin-based electronics. Both the creation of spin-polarized carriers and their spin coherence effects have been addressed in a number of experiments [7–9] performed on electrons in two-dimensional (2D) semiconductor structures. The results show, *e.g.*, that the electron spin in semiconductor materials has a very long coherence time (~ 100 ns) and that the electron can travel over distances of $100 \mu\text{m}$ without loss of spin coherence. This makes the spin of the band electron in semiconductors attractive for applications in spintronics and motivates further experimental and theoretical studies of spin-related phenomena in these materials.

The interest in electron spin is motivated also by nanotechnology [10–12], which is a new and rapidly developing field. Nanotechnology benefits from the support of different scientific communities, such as biologists, chemists, physicists and computational scientists, who all contribute to the development of a new interdisciplinary subject, called nanoscience. Although, it is still unsettled which areas of research ought to be included into nanoscience, the objective of nanoscience is clear: to explore the world at the nanometer scale, often expressed as “there’s plenty of room at the bottom” (due to R. Feynman). With the techniques available at present one can manipulate single molecules and have them act as nano-machines [13], image single atoms residing on a substrate and arrange to see their “quantum mirages” [14], contact and pass current through single molecules (such as DNA’s) [15], manufacture and study “artificial atoms” (quantum dots) [16] and many other interesting nanostructures. The electron spin has a large potential for application at the nanometer scale. Many of the spin-related effects can be observed only in confined systems, where the spin and charge degrees of freedom can be correlated with each other via the Pauli exclusion principle and Coulomb interaction. This takes place to an equal extent in atoms, molecules, and quantum dots. The interest in quantum dots is, however, higher because in these structures it is easier to control the electron confinement, to contact the structures to leads, and to integrate them into circuits. The quantum dot devices made with the help of modern nanofabrication techniques are good enough to serve as building blocks for spintronics, as well as to study the spin coherence and spin-related phenomena of localized electrons in a variety of materials.

The fast development of nanotechnology promises to reach an ultimate limit, where purely quantum systems are controlled by classical gates in a deterministic fashion, inducing only a negligible amount of decoherence (from both gates and environment). If this is to be achieved, then a new way of computing — quantum computing — becomes feasible. In quantum computing [17,18], one assumes the existence of a quantum bit (qubit) — a piece of hardware that stores and processes a “bit”³ of quantum information. A qubit, thus, is a coherent two level system, which can be prepared in any superposition of its component states and can be coupled to other systems of its

³In general, quantum information is not divisible, because of quantum entanglement.

like to form coherent superpositions of two- or many-qubit states. In addition, the qubit should have a property that allows one to read out its content, *i.e.* collapse the qubit into one of its component states. All these requirements are explained in detail in Ref. [19]. Having a number of such qubits and being able to scale it up to any desired quantity is a dream in the field of quantum information. A scalable quantum computer would allow one to efficiently simulate quantum-mechanical systems and solve a number of classical tasks with a better efficiency than classical computers can do. At present, there are only several quantum computing algorithms that are known to solve classical tasks more efficiently than their classical counterparts. The most popular are the number factoring algorithm by Shor [20] and the database search algorithm by Grover [21]. I will review only the former.

The algorithm developed by Shor [20] allows one to factor numbers into primes with an efficiency that outperforms all known classical algorithms. The Shor algorithm utilizes the parallelism of quantum-mechanical superpositions of states to find the period r of the following function

$$f(k) = x^k \pmod{N}, \quad (1.1)$$

where N is the number to be factored and x is an arbitrarily chosen positive integer. It is known from number theory that the function $f(k)$ is a periodic function of k when the integers x and N are relatively prime,⁴ *i.e.* when the greatest common divisor $(x, N) = 1$. Finding the period of $f(k)$ for different x allows one to guess the factors of N . By definition, the period r satisfies the equality $f(r) = f(0)$. Using this equality and Eq. (1.1), one can derive the following:

$$(x^{r/2} - 1)(x^{r/2} + 1) = 0 \pmod{N}. \quad (1.2)$$

The two factors on the left-hand-side of Eq. (1.2) are likely to have a non-trivial common divisor with N and, by trying out different x , one can eventually find a factor of N . The Shor algorithm finds r in a very efficient way on a quantum computer. In contrast to classical computers, quantum computers have a fully coherent register (consisting of a number of qubits) and can combine states with different content of their register into quantum-mechanical superpositions. The first step in Shor's algorithm is to prepare the following superposition of states

$$\frac{1}{\sqrt{N}} \sum_{k=0}^{N-1} |k\rangle |f(k)\rangle, \quad (1.3)$$

where the first register, $|k\rangle$, records the value of k and the second register, $|f\rangle$, records the value of $f(k)$. In the second step, one reads out the register $|f\rangle$ and obtains some random value $f = f_0$. If the function $f(k)$ is periodic, with the period $r < N$, then there are several values of k that satisfy $f(k) = f_0$. After the projection on $|f_0\rangle$, the state in Eq. (1.3) takes the form

$$\frac{1}{\sqrt{N/r}} \sum_j |k_0 + jr\rangle |f_0\rangle, \quad (1.4)$$

⁴The probability that two integers picked at random are relatively prime equals $6/\pi^2 \approx 0.6$.

where $k_0 < r$ and $0 \leq j \leq N/r - 1$. In the next step, a quantum discrete Fourier transform is applied to the first register,

$$|k\rangle \longrightarrow \frac{1}{\sqrt{N}} \sum_{k'=0}^{N-1} e^{\frac{2\pi i}{N}kk'} |k'\rangle. \quad (1.5)$$

Application of the quantum discrete Fourier transform to the number factoring problem is Shor's major contribution to this algorithm (both the factoring property (1.2) and the quantum discrete Fourier transform (1.5) have been known before). The discrete Fourier transform is implemented in a purely quantum-mechanical fashion, using unitary operations as quantum gates. The final state of the two registers then reads,

$$\sum_{k=0}^{N-1} c_k |k\rangle |f_0\rangle, \quad \text{where} \quad c_k = \frac{\sqrt{r}}{N} \sum_j e^{\frac{2\pi i}{N}k(k_0+jr)}. \quad (1.6)$$

As seen from Eq. (1.6), an interference effect has enhanced the amplitude of the states $|k\rangle = |mN/r\rangle$, where m is an integer, and has reduced the amplitude of the others. Reading out the content of the first register, thus, yields a multiple of N/r , which can be used to find the period r (after a number of repetitions). It is important to note that the coherence of the states in Eqs. (1.3) and (1.4) is crucial for the Shor algorithm. The discrete Fourier transform used in the algorithm can be interpreted as a quantum mechanical interference between different parallel outputs/paths of computation. This parallelism is characteristic also to other quantum computing algorithms and is, perhaps, the main feature that distinguishes quantum computers from classical. In the case of Shor's algorithm, the number of computational steps, needed to factor a large number N , scales with N as $\sim n^2 \ln n \ln \ln n$, where $n = \log_2 N$. If, instead, classical algorithms are used, the number of computational steps scales, at best, as $\sim \exp(cn^{1/3} \ln^{2/3} n)$, where c is a numerical constant of order 1. For large N the Shor algorithm, thus, needs a much shorter computational time than the classical algorithms, owing to the parallelism of quantum mechanics.

The physical implementation of a quantum computer is a new paradigm in physics, and it is a big theoretical and experimental challenge. The ability to prepare (on demand) coherent superpositions of significantly different states of a system of many qubits brings up questions about the interpretation of quantum mechanics, best known as ‘‘Schrödinger’s cat’’ paradox (for a recent point of view see Ref. [22]). Of course, the coherence of a system of many qubits is far more fragile than the coherence of a single qubit, and states like ‘‘Schrödinger’s cat’’ would last very short. However, there are quantum error correction schemes [23, 24], which allow one to substantially increase the qubit coherence time and, at least in principle, build qubits with arbitrarily long coherence times. In these schemes, the qubit is encoded into a block of several physical qubits. Once in a while, the physical qubits are accessed by a read-out procedure that traces out errors occurring at the level of the physical qubits, while leaving the encoded qubit unaffected. Correcting these errors then reduces the probability of an error to occur at the level of the encoded qubit, and

thus, the encoded qubit is maintained coherent for a longer time. The quantum error correction schemes use a constant supply of ancilla qubits (qubits in a known state) in order to compensate for the entropy growth in the system due to coupling to the environment. This encoding of qubits can further be scaled up to higher levels, *i.e.* qubits are encoded into blocks of already encoded qubits and so on. In this way, the qubit coherence time can be prolonged indefinitely, at the cost of a larger amount of physical qubits and sustaining operations. However, the physical qubit should operate with an error rate that is below a certain threshold value ($\sim 10^{-4}$ per gate operation) for the quantum error correction to scale towards a better qubit. It is therefore desirable to find physical implementations of qubits with the least coupling to the environment and the largest (most precise) control over the quantum state.

There is a large number of proposals for implementing qubits (for a review see *e.g.* Ref. [25,26]). They differ by the physical system used to define the qubit and by the interactions used to implement the quantum logic gates. Several examples of such proposals are:

- Electron spins in quantum dots are promising candidates for a scalable quantum computer [27]. The qubits are the lowest in energy spin doublets of single-electron quantum dots. The spin state of each quantum dot is controlled by “pushing” the electron wave function into a layer with a different g -factor or effective magnetic field. Neighboring qubits are coupled with each other using the Heisenberg exchange interaction between the spins of tunnel-coupled quantum dots.
- Cold ions confined in a linear trap and interacting with laser beams can be used to perform small-scale quantum computing [28]. The qubit is defined on the internal states of the ion and is controlled by laser beams. The coupling between qubits is mediated by quantized collective motion of ions in the chain (*i.e.* by phonons). Quantum logic gates [29] and quantum error correction [30] have been demonstrated for this system.
- Atoms in a cavity can also be used for a small-scale quantum computer [31], similar to trapped ions. The cavity mode couples strongly to the atomic states and makes it possible to access the atoms on a shorter time scale than in ion traps. The atoms are usually accessed while they are moving through the cavity in a beam. The cavity mode is also used to couple different qubits with each other. Quantum logic gates can be implemented experimentally in this system [32].
- Nuclear spins in certain molecules can be accessed individually, using nuclear magnetic resonance (NMR) pulses. A small-scale quantum computer can be implemented within one molecule using the states of the nuclear spins to define qubits [33–38]. The experiments are usually performed on a macroscopic amount of molecules in liquid state at room temperature. Both Grover’s algorithm [35,36] and Shor’s [38] algorithm have been implemented in these systems,

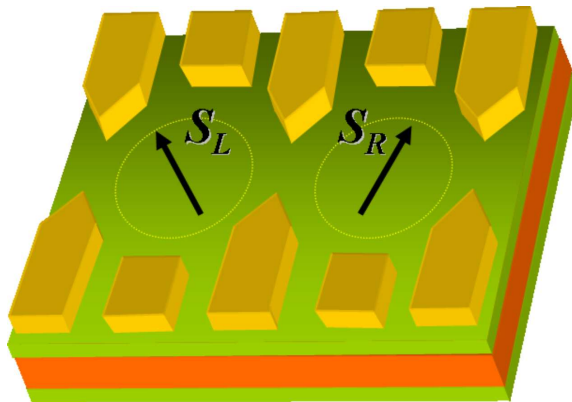


Figure 1.1: Electrons in quantum dots as spin qubits. Each quantum dot contains a single electron in the Coulomb blockade regime. The Coulomb repulsion “forbids” two electrons to occupy one and the same quantum dot. The spin $1/2$ ground state of each dot is used to define a qubit. The tunneling between quantum dots mediates a spin-spin exchange interaction, with the help of which one can implement a universal two-qubit quantum gate.

using the concept of quasi-pure states [34]. With the Shor algorithm, the number 15 has been factored into primes ($15 = 3 \times 5$), using a quantum computer with 7 qubits [38].

- In a Josephson junction, the phase difference φ between superconductors is a continuous variable mod 2π . And the number N of Cooper pairs transferred through the junction is conjugated with φ , *i.e.* $[\varphi, N] = i$. Using Josephson junctions, superconductor islands, and capacitances one can build devices that display quantum-mechanical behavior and can be used as qubits. The simplest examples are: (i) the Cooper pair box [39–41], where the qubit is defined on two charge states of a superconductor island, and (ii) the superconducting flux qubit [42–44], where two persistent currents in a loop with several Josephson junctions are used to define the qubit. More complicated structures can be built, such as *e.g.* quntronium [45], where the qubit is defined using intermediate states between charge and flux. Utilizing d-wave superconductors to construct π -junctions has also been suggested [46].

Among other proposals, charge degrees of freedom in quantum dots [47–51], quantum dot spins in cavity QED [52], electrons trapped by surface acoustic waves [53], atoms in optical lattices [54], nuclear spins of phosphorus donors in silicon [55], electrons on surface of liquid helium [56], nuclei and electrons in quantum-Hall systems [57], electron-spin-resonance (ESR) transistors in silicon-germanium heterostructures [58] have been proposed as candidates for qubits.

This thesis is inspired by the work of Loss and DiVincenzo [27], which proposes to use the spins of electrons confined to quantum dots as qubits. The electron spin is a natural candidate for the qubit. The whole Hilbert space of spin consists of only two

states, $|\uparrow\rangle$ and $|\downarrow\rangle$, which can form any superposition of the form

$$|\psi\rangle = \alpha|\uparrow\rangle + \beta|\downarrow\rangle, \quad (1.7)$$

with $|\alpha|^2 + |\beta|^2 = 1$. Such a superposition of states is expected to be long lived in solid state devices. The reason for this is that the spin interacts weakly with the environment and the spin states are not composite states, and thus, need not be protected by a gap. Placing two electrons in two quantum dots, as shown in Fig. 1.1, defines two qubits, which can then be coupled to each other via the Heisenberg exchange interaction,

$$H_s(t) = J(t)\mathbf{S}_L \cdot \mathbf{S}_R. \quad (1.8)$$

This effective Hamiltonian describes the low-energy part of the Hilbert space of two electrons in a double dot potential [59]. The exchange interaction between spins originates from the inter-dot tunnel-coupling, while the Coulomb repulsion forbids two electrons to occupy one and the same quantum dot. By lowering/rising the tunnel-barrier between quantum dots, one can turn on/off the coupling constant $J(t)$ in Eq. (1.8) as a function of time. Devising a $\pi/2$ -pulse of this interaction creates a universal two-qubit quantum gate [27]. Such a universal quantum gate, if complimented with arbitrary single-qubit rotations, suffices to carry out any quantum computing algorithm. This follows from the quantum-gate decomposition theorem [60]. The single-qubit rotations can be achieved by locally changing the electron g -factor [19, 61]. Such a g -factor modulation has been experimentally demonstrated for extended electrons in two dimensions [62] and should also be feasible for localized electrons in quantum dots. A different possibility to implement single-qubit rotations is to have local control over the effective magnetic field seen by the electron. This can be achieved by combining quantum dots with magnetic materials [4, 27]. Having, *e.g.*, a magnetic layer with a definite magnetization close to the quantum dots would allow one to change the effective magnetic field by changing the tunnel coupling between the quantum dot and magnetic layer. The initialization of the electron spins can also be easily performed in quantum dots. For this, one applies a magnetic field which induces a Zeeman splitting much larger than the temperature. The electron spins relax to the ground state over a time characterized by the spin relaxation time T_1 . At the end of the computation the electron spin can be read out using a spin-to-charge conversion [27] and measuring the charge state of the quantum dot with the help of a sensitive charge detector. This has recently been implemented in experiment [64].

Spin-based quantum computing [27] belongs to the class of *scalable* quantum computing proposals. Scalable means here that the number of qubits in a quantum computer can be increased indefinitely, once a small number of qubits is realized. This feature is common to most of the solid state quantum computing proposals. And it is also common to the classical solid state electronics.

1.2 Electron spins in quantum dots

In semiconductor quantum dots [16], the conduction band electron is confined to a small region of space ($\lambda_d \lesssim 100$ nm) in all three spatial dimensions. The electron energy is quantized to a set of discrete values due to the wave nature of the electron. In few electron quantum dots [16], the electrons form shells of electronic density, like in atoms. On this reason the quantum dots are often called “artificial atoms”. In contrast to atoms, the quantum dots are extremely tunable, owing to a set of gates that define the electrostatic confining potential for the electrons.⁵ For example, the average number of electrons on the quantum dot can be controlled with a sub-electron precision by changing the gate voltage that shifts the dot electrostatic potential [16]. As a function of this gate voltage, the linear conductance through the dot shows a set of (sequential tunneling) peaks, corresponding to the zeroes of the dot addition/extraction energy $E_+(N) = E_-(N+1) = 0$, where $E_{\pm}(N) = E(N \pm 1) - E(N) \mp \mu$ is the addition/extraction energy with respect to the lead, with $E(N)$ being the energy of the dot with N electrons, and μ the chemical potential in the lead. The Coulomb blockade (CB) effect [65] is pronounced in the presence of a Coulomb correlation energy U , which does not allow more than one electron to enter or exit the quantum dot. Thus, the sum of the addition and extraction energies obeys the following inequality

$$E_+(N) + E_-(N) \geq U(N), \quad \text{with } U(N) > 0, \quad (1.9)$$

which results in the electrons occupying/emptying the quantum dot one by one with shifting the dot electrostatic potential. In the last decade, control over the dot occupation number down to one electron per dot has been achieved in both vertical [67] and lateral [68] GaAs quantum dots, as well as in self-assembled InGaAs quantum dots [66] and rings [69]. Recently, charge control down to one electron per dot has also been realized in double quantum dots [70–73]. In Ref. [70], a quantum point contact was used as a sensitive charge detector [74, 75] to monitor change of dot occupation. This method has a number of advantages compared to the traditional, transport-based method of charge control. In particular, it can be used in quantum circuits with a too low conductance to be measured.

The simplest signatures of spin in quantum dots are seen in the CB regime [65, 76] ($T \ll U$). When adding electrons one by one onto the dot, one finds alternating small and large Coulomb blockade valleys [67, 76, 77], indicating the presence of spin doublets. In symmetric quantum dots [16, 67, 78], the filling of dot orbitals is governed by Hund’s rule,⁶ observation of which indicates that the Coulomb exchange interaction within the quantum dot is relevant and spins larger than $S = 1/2$ can build

⁵There exist also self-assembled quantum dots, which are not defined by electrostatic gates, and hence, cannot be controlled locally in the same fashion. However, these quantum dots can be manipulated optically, by lasers. The resolution of a local control is usually limited by laser’s spot size, but an improvement can be achieved using near-field optics.

⁶When filling a set of (almost) degenerate orbital levels, the states with one and the same spin component are filled first.

up. Signatures of such spin-transitions have been observed in experiments [78–83]. Relaxation between quantum dot states with different spin have also been addressed in experiment [84] and excited states with different spins have been studied using pulse excitation measurements [85].

Single-electron quantum dots have attracted much interest in recent years in the context of the spin-based quantum computing proposal [27]. For the first time, the Zeeman energy has been directly observed in transport spectroscopy [86, 87], which allowed the authors of Ref. [86] to apply the pulse excitation technique [84, 85] to a single-electron GaAs quantum dot and establish a lower bound on the spin-relaxation time, $T_1 \geq 50 \mu\text{s}$, in a magnetic field of $B = 7.5 \text{ T}$. In a subsequent experiment [64], a sensitive charge detector was incorporated in the scheme, and the true spin-relaxation time was found to be $T_1 \simeq 1 \text{ ms}$. The spin relaxation time was also measured in an array of self-assembled InGaAs quantum dots using optical methods [88]. Spin lifetimes of up to $T_1 = 20 \text{ ms}$ [88] have been found in these smaller quantum dots, with a strong dependence of T_1 on the magnetic field B . The measurements of the spin T_1 time suggest that the mechanism considered in Refs. [89, 90] is responsible for spin relaxation in quantum dots. This mechanism is based on the spin-orbit interaction and phonon emission and it is considered in detail in Chap. 4 of this thesis.

Two tunnel-coupled quantum dots, each with one electron, have also been realized recently [70–72]. The exchange interaction J between the spins of such coupled quantum dots is of central interest for spin-based quantum computing [27]. In transport spectroscopy, the exchange energy J can be seen in a number of ways [91], however a direct access to J , similar to how the Zeeman energy was accessed [86, 87], remains a challenging task. The difficulties to access J are primarily due to extremely small values of J achieved in double dots, and also due to not sufficiently stable double-dot structures. In recent years, a new approach has been taken by Zumbühl *et al.* [120], in which the double dot is replaced by a single dot of elongated shape. In the two-electron regime, this quantum dot has electronic orbitals which are similar to those of a double quantum dot [121]. The typical values of J are here much larger than in the state-of-the-art double dots, and can be accessed in transport. This allowed Zumbühl *et al.* [120] to measure J as a function of an applied orbital magnetic field B . The results agree well with the Hund-Mulliken model for the double dot [59], in particular what concerns the singlet-to-triplet transition occurring with increasing B . The next step in this approach is to add a side gate to control J down to small values.

1.3 Quantum entanglement

Quantum entanglement is an important resource, which is provided by the world of *quantum* and can be used in a number of ways in communication and cryptography. Entangled quantum states of two *parties* (systems) are states that cannot be presented as a product of states of the two parties. Physically, one can imagine this as a situation

when each party separately has no definite state, while both parties together have a definite state. The simplest example (due to Bohm, 1951) is two spin 1/2 particles in a singlet state and separated from each other at a distance where they no longer interact. The state of these two particles has the following form

$$|\psi\rangle = \frac{1}{\sqrt{2}} (|\uparrow\rangle_L |\downarrow\rangle_R - |\downarrow\rangle_L |\uparrow\rangle_R), \quad (1.10)$$

where $|\uparrow\rangle_L$ denotes the particle on the *left* in *spin up* state, etc. Now, if one performs a measurement on the left particle and finds it in the spin up state, then a subsequent measurement on the right particle yields spin down with certainty. This type of (anti-)correlation is at the heart of the Einstein-Podolsky-Rosen (EPR) paradox⁷ [92]. Of course, it is rather counterintuitive to assume that, by measuring the state of one particle, one can change (instantaneously!) the state of the other particle; the latter might even be at the other end of the universe. The EPR paradox occurs because we are used to thinking that the physical reality exists on its own, independent of the knowledge that is available about it. It is however not so in the example above. An experimentalist that measures the state of the right particle can by no local means deduce whether or not any measurement has been performed on the left particle. In this sense, the local physical reality of the right particle is independent of measurements carried out on the left particle. This is natural because the particles do not interact with each other. It is only when the outcome of a measurement performed on the left particle is available to the experimentalist who measures the right particle, that he can conclude that measuring the left particle has affected the state of the right particle.

Pairs of entangled particles became known as EPR pairs. They cannot be used alone for communication. However, if combined with a classical communication channel, they can be used for superdense coding [93], quantum cryptography [94], and quantum teleportation [95]. In addition, entangled states can be used to experimentally verify whether any local hidden-variable theory might be responsible for the quantum behavior that we observe in this world [96]. To test this one performs a set of measurements (called the Bell inequality test) that measure all different non-local correlations produced by the EPR pairs. According to quantum mechanics, the wave function in (1.10) is the complete knowledge about the EPR pair, and no local hidden-variable theory is capable of reproducing as many different correlations as follow from Eq. (1.10). Thus, the Bell inequality test can rule out the possibility of any local hidden-variable theory, without even considering the details of such a theory. While such a test aims at proving the completeness of quantum mechanics, it can also be used to measure the decoherence of the EPR pairs.

⁷In this context, the EPR paradox occurs if one considers two possible choices for the spin measurement axis: (i) z and (ii) x . After measuring the left particle, the right particle ends up in a definite state of: \mathbf{S}_z in case (i) and \mathbf{S}_x in case (ii). Since the operators \mathbf{S}_z and \mathbf{S}_x do not commute, the physical reality of the right particle depends on the type of measurement carried out on the left particle, in spite of the fact that the particles are non-interacting. This constitutes the EPR paradox.

Creation and detection of EPR pairs is the state-of-the-art in quantum optics, where photons with entangled polarizations are used to perform Bell inequality tests [97]. In the solid state, however, this task is rather challenging and has not been put to practice so far. Both the coherence times and the length scales at which entangled particles can be separated from one another are much shorter in the solid state. Thus, a Bell inequality test will rather be a test of the quantum-mechanical coherence of the quasi-particles than of the fundamentals of quantum mechanics. Nevertheless, entanglement is a very interesting and actual topic in condensed matter physics. A large number of proposals for creating EPR pairs has been put forward in recent years [98–107]. Schemes for detection of spin entanglement have also been suggested [108–114].

In the solid state, it is often difficult to separate two particles away from one another and still preserve their two-particle state coherent. One might ask the question of whether the notion of entanglement is meaningful also when the two parties overlap. This becomes particularly controversial when indistinguishable particles are involved. A simple example is the double dot shown in Fig. 1.1 at a finite inter-dot tunnel coupling. The singlet state of the two electrons in the double dot reads [115],

$$|\psi\rangle = \frac{1}{\sqrt{1+\phi^2}}(d_{+\uparrow}^\dagger d_{+\downarrow}^\dagger - \phi d_{-\uparrow}^\dagger d_{-\downarrow}^\dagger)|0\rangle, \quad (1.11)$$

where $|0\rangle$ is the vacuum state and d_{ns}^\dagger creates an electron in the orbital state $\Phi_n(\mathbf{r})$ and spin state $\chi_s(\sigma)$. $\Phi_+(\mathbf{r})$ is the symmetric and $\Phi_-(\mathbf{r})$ the antisymmetric orbital wave function of a single electron in the double dot potential. In Eq. (1.11), we neglected the contribution of highly excited double dot orbitals, assuming that the tunnel coupling is small compared to the single-dot level spacing. The parameter ϕ in Eq. (1.11) describes the correlation between the electrons in the singlet state induced by the Coulomb interaction. In the Hund-Mulliken approach, it is given by [115]

$$\phi = \sqrt{1 + \left(\frac{4t_H}{U_H}\right)^2} - \frac{4t_H}{U_H}, \quad (1.12)$$

where t_H and U_H stand for the Hubbard tunneling amplitude and on-site Coulomb repulsion [59]. Using the measure of entanglement η , introduced by Schliemann *et al.* [116,117], we obtain that the singlet state in Eq. (1.11) is entangled, with [91,118]

$$\eta = \frac{2\phi}{1+\phi^2} \equiv \underbrace{\frac{(1+\phi)^2}{2(1+\phi^2)}}_{\text{single \& double occupancies}} - \underbrace{\frac{(1-\phi)^2}{2(1+\phi^2)}}. \quad (1.13)$$

The measure η [116,117] characterizes the amount of electron-electron correlations contained in a given state. According to this measure the singlet state in Eq. (1.11) is not entangled at $\phi = 0$, because it represents a state of the Hartree-Fock type, which has no quantum correlations beyond the anti-symmetrization of the wave function.

Note that this state occurs in the double dot if the Coulomb interaction is absent (see Eq. (1.12)). In the presence of Coulomb interaction, however, detaching the dots from each other results in creating entanglement. For decoupled quantum dots ($\phi = 1$), the singlet state (1.11) is maximally entangled, and can be written in the form of Eq. (1.10).

The interaction-induced correlations are not the only correlations that give rise to entanglement. A finite amount of entanglement is contained in the state (1.11) even at $\phi = 0$, due to the fermionic nature of the electrons. Using a different measure of entanglement, as introduced by Wiseman and Vaccaro [119], we obtain that the entanglement between the left and right dots in the singlet state (1.11) is given by⁸

$$E_P = \frac{(1 + \phi)^2}{2(1 + \phi^2)}. \quad (1.14)$$

Note the difference between the measures E_P and η for our double dot example. E_P gives the probability to distill an EPR pair from a given quantum state, using local operations and classical communications (LOCC). Whereas η gives the difference between the probabilities to distill an EPR and a non-EPR pair, see Eq. (1.13). The EPR pair is the singlet state with one electron per quantum dot (single occupancy), and the non-EPR pairs are the singlets with both electrons occupying one and the same quantum dot (double occupancy).

The *interaction* parameter ϕ has recently been accessed experimentally in transport spectroscopy by Zumbühl *et al.* [120]. The singlet state (1.11) was realized in an elongated quantum dot with two electrons. Owing to the Coulomb interaction, the two electrons repel each other to opposite corners of the quantum dot and form a charge distribution that is similar to the double dot case. This picture is confirmed by numerical studies of electronic structure in elliptic quantum dots [121]. The cotunneling conductance through the elongated quantum dot allowed the authors of Ref. [120] to measure the singlet-triplet energy J as a function of the magnetic field B . Due to the orbital effect of the magnetic field, $J(B)$ changes sign at a particular value of B . The cotunneling conductance shows a rich behavior in the neighborhood of $J = 0$ [120], as expected from the theory [115]. This has been exploited in Ref. [120] to extract ϕ .

Note that the measurement of ϕ is a measurement of the correlations between the electrons, and it goes beyond traditional measurements of the dot energy spectrum. Zumbühl *et al.* [120] have thus demonstrated for the first time that one can access the state of correlated electrons in transport spectroscopy, and determine the degree of its entanglement.

⁸For this, we write the singlet state in the following form

$$|\psi\rangle = \frac{1}{2\sqrt{1 + \phi^2}} \left[(1 + \phi)(d_{L\uparrow}^\dagger d_{R\downarrow}^\dagger - d_{L\downarrow}^\dagger d_{R\uparrow}^\dagger) + (1 - \phi)(d_{L\uparrow}^\dagger d_{L\downarrow}^\dagger + d_{R\uparrow}^\dagger d_{R\downarrow}^\dagger) \right] |0\rangle.$$

1.4 Decoherence

Decoherence is a phenomenon that transforms the *quantum* world into the *classical* one, as one goes from simple systems to more complex ones. The systems that interact with a bath of many degrees of freedom lose their quantum coherence due to the system-bath interaction and the complexity of the bath. These systems appear to us as *classical*, which is a word for saying that they are being continuously measured and reside in states that exhibit no uncertainty for a macroscopic observer⁹. We can be sure of such systems that if their state changes over time then all physical quantities (those that we have introduced to describe the classical world) have existed at all times during this change. This appears of course natural to anyone used to the classical world, whereas in fact it is a fascinating phenomenon of systems with many degrees of freedom.

The most illustrative example of decoherence is, perhaps, the motion of a pendulum in the air. The air molecules scatter off the suspended object, and by doing so they induce a measurement of the coordinate. The quantum mechanical motion of the pendulum, which would be that of a harmonic oscillator, is perturbed by a continuous measurement from the environment and, as a result, obeys Newton's laws of mechanics with a high precision.

The electron spin is also subjected to decoherence. A superposition of states, as given in Eq. (1.7), lasts only for a finite amount of time in a realistic system. The coupling to the environment “entangles” the spin with the environmental degrees of freedom. Depending on whether the spin state is $|\uparrow\rangle$ or $|\downarrow\rangle$, the environment undergoes slightly different evolutions. The spin state becomes “known”, in some sense, to the environment, although, this knowledge might be completely inaccessible to us, due to the complexity of the environment. The superposition of states in Eq. (1.7) will decohere to a mixture of states described by the density matrix [122]. For example, the following state can be realized

$$\rho = \frac{1}{2} (|\uparrow\rangle\langle\uparrow| + |\downarrow\rangle\langle\downarrow|). \quad (1.15)$$

This mixed state is identical to the state of a coin tossed in the air and falling onto the floor with equal chances for “heads” or “tails”. The state of the electron spin has therefore been transformed from a quantum state in Eq. (1.7) to a classical one in Eq. (1.15), due to the interaction with the environment.

The decay of a quantum-mechanical state, due to the interaction with the environment, is a complex process and is fully described by the density matrix $\rho(t)$. The

⁹To be precise here, we must say that decoherence is responsible only for the absence of quantum-mechanical superpositions of states in the classical world. The simultaneous reality of observables, such as momentum and coordinate, comes about in the classical world due to the fact that the quantum-mechanical uncertainty of a macroscopic observable is usually small compared to its mean value. The decoherence ensures only that large uncertainties (*e.g.* “squeezed” states) are not formed on the scale of the measured macroscopic observable.

time evolution of the density matrix depends on the details of both system and environment, their (mutual) initial state, and their coupling to each other. In most cases, however, the environment consists of a large number of degrees of freedom, which interact with each other in a complicated way. As a consequence, the environment loses the “memory” about its state over some correlation time τ_c . [This is to say that no coherent evolution is expected between the system and any environmental degree of freedom over a time scale larger than τ_c .] If the system couples weakly enough to the environment, then it will take a large number of time intervals τ_c in order for the density matrix $\rho(t)$ to change by a sizable amount. Under this condition, the environment is said to be Markovian with respect to the system. In this case, one can make the following (Markov) approximation. Instead of describing the system by its microscopic density matrix $\rho(t)$, one introduces a “coarse graining” of the time variable t with a time scale τ_g and describes the system with an effective density matrix [123],

$$\tilde{\rho}(t) = \frac{1}{\tau_g} \int_t^{t+\tau_g} \rho(t') dt', \quad (1.16)$$

where both $\rho(t)$ and $\tilde{\rho}(t)$ are in the interaction representation. The time scale τ_g is chosen such that $\tau_c \ll \tau_g \ll \tau$, where τ stands here for system’s decoherence time. The averaging in Eq. (1.16) smoothes out the rapid changes in $\rho(t)$ that occur on the time scale τ_c due to the coherent coupling of the system with the environmental degrees of freedom. Furthermore, for this approximation to be meaningful in experiment, both the initialization and the measurement of system’s state should be carried out adiabatically with respect to this coherent coupling, *i.e.* on the time scale $\tau_g \gg \tau_c$. The Markov approximation implies that the time evolution of $\tilde{\rho}(t)$, to a future moment in time, is independent of the way the system arrived at the density matrix $\tilde{\rho}(t)$. This is so, because the environment is virtually the same at all moments in time on the “coarse grain” axis, whereas in reality the environment relaxes to its stationary state on the time scale $\tau_c \ll \tau_g$.

The interaction of the spin $S = 1/2$ with the environment can be generally written in the following form

$$H = \hbar\omega_Z S_z + \mathbf{S} \cdot \mathbf{h}(t), \quad (1.17)$$

where $\hbar\omega_Z = g\mu_B B$ is the Zeeman energy, $\mathbf{S} = \boldsymbol{\sigma}/2$ is the electron spin operator, with $\boldsymbol{\sigma} = (\sigma_x, \sigma_y, \sigma_z)$ being the Pauli matrices. The environmental fluctuations are represented by $\mathbf{h}(t)$ in the interaction representation with the Hamiltonian of the environment. $\mathbf{h}(t)$ can contain both classical and quantum fluctuations. We assume that averaging over the environment gives $\overline{\mathbf{h}(t)} = 0$; otherwise, the mean value of $\mathbf{h}(t)$ can be absorbed into the first term in Eq. (1.17), resulting, in general, in a renormalized ω_Z and a different direction of the z -axis. The correlation time τ_c can be inferred from the decay of the correlator $c_{ij}(t) = \overline{h_i(t)h_j(0)}$ as a function of time. For a sufficiency weak coupling $\mathbf{h}(t)$, the environment is Markovian, and $\tilde{\rho}(t)$ decays exponentially to the equilibrium density matrix ρ^T . In general, this decay is governed by three decoherence times. For the sake of simplicity, we consider here only the case when the Zeeman energy $\hbar\omega_Z$ is much larger than the decoherence rates (secular

approximation [123]). Then, the spin precession around the z -axis averages out the inhomogeneity of the fluctuating field $\mathbf{h}(t)$ in the (x, y) -plane and the decay of $\tilde{\rho}(t)$ is governed only by two times ($\tau = T_1, T_2$). In the Schrödinger representation, the time evolution of the density matrix then reads,

$$\begin{aligned}\tilde{\rho}_{\uparrow\uparrow}(t) &= \tilde{\rho}_{\uparrow\uparrow}(0)e^{-t/T_1} + \rho_{\uparrow}^T(1 - e^{-t/T_1}), \\ \tilde{\rho}_{\downarrow\downarrow}(t) &= \tilde{\rho}_{\downarrow\downarrow}(0)e^{-t/T_1} + \rho_{\downarrow}^T(1 - e^{-t/T_1}), \\ \tilde{\rho}_{\uparrow\downarrow}(t) &= \tilde{\rho}_{\uparrow\downarrow}(0)e^{-t/T_2 - i\omega_Z t} = \tilde{\rho}_{\downarrow\uparrow}^*(t),\end{aligned}\tag{1.18}$$

where $\rho_{\uparrow}^T = 1 - \rho_{\downarrow}^T = [1 + \exp(\hbar\omega_Z/T)]^{-1}$, with the temperature T measured in energy units. The decay times are given by the following expressions:

$$\frac{1}{T_1} = \frac{1}{2\hbar^2} \int_{-\infty}^{+\infty} dt e^{-i\omega_Z t} \text{Re} \left(\overline{h_x(0)h_x(t)} + \overline{h_y(0)h_y(t)} \right),\tag{1.19}$$

$$\frac{1}{T_2} = \frac{1}{2T_1} + \frac{1}{2\hbar^2} \int_{-\infty}^{+\infty} dt \overline{h_z(0)h_z(t)}.\tag{1.20}$$

The electron spin relaxes to thermal equilibrium on the time scale T_1 . The processes that contribute to $1/T_1$, see Eq. (1.19), involve energy exchange with the environment. In contrast, the last term in Eq. (1.20) is due to purely elastic processes, and is called the *dephasing* contribution. The decoherence time T_2 is determined, thus, by both inelastic and elastic processes, and as a result T_2 has the upper bound $T_2 \leq 2T_1$, see Eq. (1.20). In some cases, the environment cannot efficiently exchange energy with the electron spin. Then, the elastic processes dominate the decoherence, resulting in $T_2 \ll T_1$. However, the contribution of the elastic processes can be suppressed by reducing the correlation time τ_c , *i.e.* making the environment more Markovian. [Note that the last term in Eq. (1.20) decreases with decreasing τ_c , because the integrand contributes only in the time interval $|t| \lesssim \tau_c$.] This effect is known as “motional narrowing” [123], and it occurs usually when the spin is moving in the sample, thus “seeing” a rapidly changing environment.

A long decoherence time T_2 is of great importance for spin-based quantum computing [27]. In quantum dots, the electron spin interacts with the environment via a number of interactions:

- The Zeeman interaction $H_Z = g\mu_B \mathbf{S} \cdot \mathbf{B}$ allows coupling of external fluctuating magnetic fields to the electron spin. In addition, if the g -factor is coordinate dependent in the sample, such as in Ref. [62], then the electron spin becomes vulnerable towards charge noise.
- In bulk semiconductors, the spin-orbit interaction leads to a strong spin decoherence, caused by the electron being scattered off static impurities. In quantum dots, however, this effect is absent, because the electron is localized. The spin-orbit interaction is typically a small perturbation on top of a large size-quantization energy of the dot. The dot ground state is a Kramers doublet

and can be considered as an effective spin 1/2. At zero magnetic field, the time-reversal symmetry protects the electron spin from decoherence. In a magnetic field, however, the electron spin couples via the spin-orbit interaction to all degrees of freedom that interact with the electron charge. In particular, the electron spin can be efficiently relaxed to thermal equilibrium by the electron-phonon interaction [90,124]. Measurements of the spin relaxation time T_1 [64,88] reveal features specific to this mechanism. In quantum dots defined on a 2DEG, the spin orbit-interaction is linear in momentum. Then, the decoherence time T_2 , due to the spin-orbit interaction and any orbital bath, reaches its upper bound $T_2 = 2T_1$ [90].

- The hyperfine interaction couples the electron spin to a large number N ($\sim 10^5$) of nuclear spins inside the quantum dot. The spin decoherence takes place due to the uncertainty of the Overhauser field,¹⁰ $\mathbf{H}_{\text{Ov}} = \langle \mathbf{H}_{\text{Ov}} \rangle + \delta \mathbf{H}_{\text{Ov}}$. Typically, the nuclear spins are at thermal equilibrium and the temperature is much larger than their Zeeman energy. Then, $\langle H_{\text{Ov}} \rangle = 0$ and $\delta H_{\text{Ov}} \simeq A/\sqrt{N}$, where A is the atomic hyperfine interaction constant; A/\sqrt{N} corresponds to a magnetic field of 100 Gauss in GaAs. The correlation time τ_c of the nuclear bath is rather large ($\tau_c \sim 10^{-4}$ s), being determined by the dipolar interaction between the nuclear spins. The decoherence of the electron spin occurs in this case on the time scale $\tau = \hbar\sqrt{N}/A$, as given by the strength of δH_{Ov} . Applying a strong magnetic field ($E_Z \gg A/\sqrt{N}$) suppresses the electron spin relaxation, since the electron Zeeman energy (E_Z) is too large to be dissipated by the hyperfine interaction. The decoherence of the electron spin occurs then only due to the uncertainty of $\delta \mathbf{H}_{\text{Ov}}$ along the direction of the external magnetic field. The decoherence time can thus be increased by reducing this uncertainty. The decay of the electron spin due to the hyperfine interaction has been studied in Refs. [125–130].
- The exchange interaction of the electron spin with magnetic impurities can also lead to decoherence. At zero magnetic field, this is similar to the decoherence due to the nuclear spins. However, with applying a magnetic field, the magnetic impurities “freeze out” and do not give rise to decoherence. In some materials, like GaAs, the concentration of magnetic impurities can be negligibly small ($n_M \simeq 10^{13}$ cm⁻³). There, this mechanism is expected to show up only if a large number of quantum dots ($\sim 10^3$) is fabricated.

The decoherence time of the electron spin in quantum dots can be accessed easily, if spin manipulation and read-out are combined. The Larmor precession can be monitored as a function of time in a measurement of Ramsey fringes. For this, the spin is first initialized in a given state, say $|\uparrow\rangle$, in the presence of a magnetic field. Then, one applies a $\pi/2$ -pulse that prepares the spin, at $t = 0$, in the state (1.7) with

¹⁰As a quantum object, the Overhauser field is capable of mixing the electron spin with the nuclear spins, giving rise to a quantum-mechanical uncertainty. In addition, however, the state of the nuclear spins is not certain, as it is described by the density matrix at thermal equilibrium. This adds another source of uncertainty — statistical uncertainty — to the Overhauser field.

$\alpha = \beta = 1/\sqrt{2}$. This state is left to evolve freely with time according to Eq. (1.18), and after some time t another $\pi/2$ -pulse is applied in the same way. Finally, the spin is measured, yielding $|\uparrow\rangle$ or $|\downarrow\rangle$ with probabilities $p_\uparrow = (1 - e^{-t/T_2} \cos \omega_z t)/2$ and $p_\downarrow = (1 + e^{-t/T_2} \cos \omega_z t)/2$. If the environment is not Markovian, then T_2 can be viewed as a time-dependent quantity. An example is the decoherence due to the hyperfine interaction, which gives $T_2(t) = \tau^2/t$.

The decoherence time T_2 can also be accessed in transport and optical measurements as proposed in Refs. [131] and [132], *resp.* For this, a monochromatic ESR source is required, which should efficiently couple only to the electron spin on the quantum dot and induce Rabi oscillations. The Rabi oscillations act as a *heating* mechanism on the quantum dot and induce non-equilibrium occupation of the excited spin state. This can be utilized in transport to allow ESR-assisted sequential tunneling through the quantum dot, or in optics to change the photoluminescence intensity of quantum dots. The decoherence rate $1/T_2$ is seen in the current, or in the photoluminescence intensity, as a function of the ESR frequency ω_{ESR} , because the heating efficiency depends on how well ω_{ESR} matches ω_z . The decoherence “smears” the Zeeman energy over an interval $\sim \hbar/T_2$, thus the current (or the photoluminescence intensity) has a peak of width $\sim 1/T_2$ around $\omega_{\text{ESR}} = \langle \omega_z \rangle$. It is crucial for this method that the ESR source has a narrow frequency width $\delta\omega_{\text{ESR}} \ll 1/T_2$.

Finally, a third method to assess the decoherence time of spin has recently been demonstrated in experiment [133]. It exploits the physics of the Pauli blockade regime in an asymmetric double quantum dot with two electrons [134]. Instead of leads, however, a sensitive charge detector is used in Ref. [133] to monitor instances of Pauli blocking of the double dot. The decay of the inter-dot singlet state as a function of time can be studied by applying a sequence of pulses to the double dot [133], which allows one to access the decoherence time of a single spin. A decoherence time of 10 ns was found in Ref. [133], which is attributed to the decoherence due to the hyperfine interaction.

1.5 Transport and Kondo effect in quantum dots

Electron transport is a common method of studying quantum dots. The differential conductance $G = dI/dV$ as a function of the source-drain bias V reveals the internal energy structure of the dot [16]. More recently, also the electron-electron correlations (entanglement) have been accessed in a two-electron quantum dot using transport measurements [120]. The simplest transport setup is shown in Fig. 1.2 (a). The quantum dot is probed by two leads at chemical potentials μ_L and μ_R . The dot Hamiltonian H_d contains the interaction between the electrons in the quantum dot. Assuming that H_d is not significantly changed by applying a source-drain bias, $\Delta\mu = \mu_L - \mu_R = -eV$, one can access the energy spectrum of H_d by measuring G as a function of V and V_g . A typical gray-scale plot of $G(V, V_g)$ will look as shown in Fig. 1.2 (b), where Δ_N denotes the excitation energy of the quantum dot with N

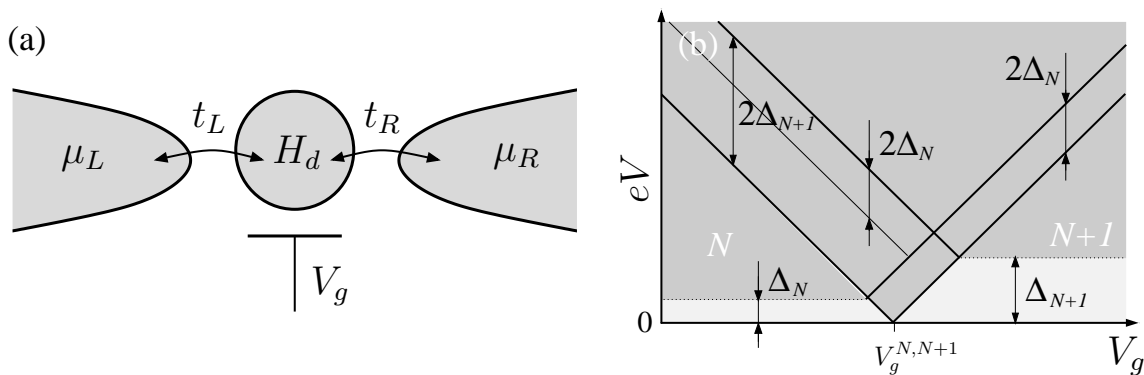


Figure 1.2: (a) A quantum dot with Hamiltonian H_d is tunnel-coupled to two Fermi-liquid leads at chemical potentials μ_L and μ_R . The number of electrons on the dot is controlled by the gate voltage V_g and the coupling to the leads by the tunneling amplitudes t_L and t_R . (b) The differential conductance $G = dI/dV$ as a function of eV and V_g reveals the energy spectrum of the quantum dot. The quantum dot is biased symmetrically, *i.e.* $\partial(\mu_L + \mu_R)/\partial V = 0$. The excitation energies Δ_N and Δ_{N+1} ($\Delta_{N+1} > \Delta_N$) can be seen both in the sequential tunneling (solid line) and in the cotunneling (dotted line) regimes.

electrons ($\Delta_{N+1} > \Delta_N$). For simplicity, we consider only one lowest excitation energy per dot occupation number. The transport through the quantum dot is governed by either sequential-tunneling [16] or cotunneling [135] processes.

Sequential tunneling is the lowest (first) order process in the dot-lead tunnel coupling. It involves either tunneling of a quantum dot electron into the leads or tunneling of a lead electron onto the quantum dot. The dot occupation number N , thus, changes by $\Delta N = \pm 1$ as a result of this process. The transport through the dot takes place in the following sequence (assuming $\mu_L > \mu_R$): an electron from the left lead hops onto the dot and changes its occupation number from N to $N + 1$, then, at a later time, an electron from the dot hops out into the right lead and restores the quantum dot to its initial occupation number N . As a result of this sequence, one net electron is transferred from the left to the right lead. The energy conservation restricts the sequential-tunneling transport to a regime of *large* source-drain voltages:

$$\begin{cases} e|V|/2 \geq \min\{E_+(N), E_-(N)\}, \\ E_{\pm}(N) \geq 0, \end{cases} \quad (1.21)$$

where $E_{\pm}(N) = E(N \pm 1) - E(N) \mp \mu$, with $\mu = (\mu_L + \mu_R)/2$, and we have assumed that the source-drain voltage is applied symmetrically, $\partial\mu/\partial V = 0$. The dot occupation number N used in the first line of Eq. (1.21) is defined in the second line by the inequalities therein. Note that $E_{\pm}(N)$ depends linearly on V_g . By an appropriate choice of scale for V_g , one can achieve $E_+(N) = -E_-(N + 1) = V_g^{N,N+1} - V_g$, where $V_g^{N,N+1}$ is the position of the sequential-tunneling peak at $V \rightarrow 0$ (linear regime). The bias region not covered by Eq. (1.21) represents a set of Coulomb blockade (CB) diamonds aligned along the axis $V = 0$. Inside these diamonds, the transport is

governed by higher order processes in the dot-lead tunnel coupling.

Cotunneling is the second order process in the dot-lead tunnel coupling. It involves tunneling of an electron from one lead to the other (or same lead) via the quantum dot. In contrast to the sequential tunneling, cotunneling does not change the dot occupation number N . One can distinguish between two kinds of cotunneling processes: (i) *elastic cotunneling*, where the dot state does not change after the electron tunnels through, and (ii) *inelastic cotunneling*, where the dot state changes after the electron tunnels through. Note that, for the elastic cotunneling, the quantum dot is analogous to a tunnel barrier. For the inelastic cotunneling, however, the same analogy would imply that the quantum dot is similar to a tunnel barrier which switches its transmission after an electron tunnels through. The elastic and inelastic cotunneling can be separated from each other in transport, provided the quantum dot has a finite excitation energy. For example, the region of elastic cotunneling is represented by a light-gray scale in Fig. 1.2 (b). The inelastic cotunneling is activated when the source-drain bias $e|V|$ is larger than the dot excitation energy (Δ_N or Δ_{N+1}).

Besides sequential tunneling and cotunneling, the electron transport in quantum dots can be governed also by the Kondo effect [136]. The Kondo effect is a textbook example of correlated many-body physics. It was discovered nearly a century ago [137] in transport through metals which contained magnetic impurities. Since then, the Kondo effect has been extensively studied in a variety of contexts [136, 138–140]. A “revival” of the Kondo effect [141] occurred with its observation in semiconductor quantum dots [142]. Because the quantum dots are extremely tunable, they allow one to study experimentally a variety of models, which before could be studied only theoretically. Particularly interesting are instances of non-Fermi-liquid behavior, which display peculiar features in transport or other properties of the quantum dots. One such quantum critical point is addressed in Chap. 2.

The simplest Hamiltonian displaying Kondo effect is that of the Kondo model [138],

$$H = \sum_s \int \int dx dx' \psi_s^\dagger(x) \varepsilon(x - x') \psi_s(x') + J \mathbf{S} \cdot \sum_{ss'} \frac{\boldsymbol{\sigma}_{ss'}}{2} \psi_s^\dagger(0) \psi_{s'}(0), \quad (1.22)$$

$$\text{where } \varepsilon(x - x') = \frac{1}{2\pi} \int_{-K}^K dk \varepsilon_k e^{ik(x-x')}, \quad \text{with } \varepsilon_k = \hbar v_F k, \quad (1.23)$$

Here, $\psi_s(x)$ annihilates a lead electron with spin s at position x , ε_k is the kinetic energy of an electron with wave-vector k , \mathbf{S} is the dot spin ($S = 1/2$), which couples to the lead electrons at position $x = 0$ with the coupling constant J . The lead band ranges in the interval $k \in (-K, K)$ and is half-filled with electrons, so that the Fermi level corresponds to $k_F = 0$. An electron at the Fermi level has the kinetic energy $E_F = \hbar v_F K$ with respect to the lowest band edge $\varepsilon_{-K} = -\hbar v_F K$. The interaction of a single electron in the lead with the dot spin \mathbf{S} can at most have the strength $E_{\text{int}} \simeq JK$. Note that both energy scales are proportional to K . Typically, $J \ll \hbar v_F$ and one obtains $E_{\text{int}} \ll E_F$. In spite of its smallness, the second term in Eq. (1.22)

builds up a many-body correlation between the dot spin and the lead electrons at low temperatures.

The Kondo effect is exhibited in localizing a lead electron to the neighborhood of the quantum dot at low temperatures. The dot spin \mathbf{S} forms a singlet state with the lead electron and binds it under the Fermi level with some characteristic energy T_K . The spatial extension of the localized electron (Kondo cloud) is given by $\xi_K = \hbar v_F / T_K$. Two distinct phenomena are at the heart of the Kondo effect:

1. *Localization.* If the first term in Eq. (1.22) was not present, then the quantum dot would favor localization of a lead electron to a region of space of size $\xi = 1/K$ around the dot (at $x = 0$) and with a binding energy $T_K \equiv E_{\text{int}} \simeq JK$. Note that this limit corresponds to a very flat band of lead electrons ($v_F \ll J/\hbar$). At $v_F \sim J/\hbar$, the first and second terms in Eq. (1.22) compete with each other and, at the single-particle level, the localization disappears as v_F reached some critical value $\sim J/\hbar$. A similar localization effect also occurs in a much simpler model, which describes a spin-less particle moving freely along the x -axis and interacting in one point with a harmonic oscillator in its ground state. The corresponding Hamiltonian has the following form [143]

$$H = -\frac{\partial^2}{\partial x^2} + \frac{1}{2} \left(-\frac{\partial^2}{\partial q^2} + q^2 \right) + \Lambda q \delta(x), \quad (1.24)$$

where q is the harmonic oscillator coordinate and Λ is the coupling constant. The role of the spin-spin interaction in Eq. (1.22) is played here by the linear in q interaction, and the role of the energy penalty E_F for localizing an electron from the Fermi surface is played here by the potential energy of the harmonic oscillator. The interaction term in Eq. (1.24) favors a shift of the equilibrium position of the harmonic oscillator, provided $\Lambda \geq \sqrt{2}$, and a localized state of the particle emerges. Similarly to this, a spontaneous formation of a singlet state occurs in Eq. (1.22), provided J exceeds its critical value $J \simeq \hbar v_F$.

2. *Scaling.* At low temperatures, the lead electrons below the Fermi level are “frozen” due to the Pauli blockade. The “active” electrons are those at the Fermi level within an energy band $\sim T$. In this case, one can reduce the bandwidth from $\hbar v_F K$ to $\sim T$, introducing an effective Hamiltonian in which the frozen electrons from the lead are excluded. This significantly simplifies the problem, since then we have to deal with fewer electrons in the lead. It also introduces additional coherent effects, which before were hidden behind the numerosness of electrons. Thus, when scaling K down to $\sim T/\hbar v_F$, one has to take into account the virtual excitations of the frozen electrons/holes to the active band at the Fermi level. For example, an electron at the Fermi surface can scatter from state k to k' either directly, *i.e.* in the first order of J , or indirectly, via an intermediate state k'' of a frozen electron/hole, *i.e.* a process of order J^2 . In the Kondo model (1.22), such virtual excitations add up coherently to the coupling constant J . This renormalization of J is a many-body effect and it would not occur if the lead contained a single electron at the energy $\varepsilon_{k_F} = 0$. The physical reason behind this renormalization is that the quantum dot acts as a memory unit

(qubit) and correlates the virtual processes of many electrons/holes with each other. Mathematically, it is expressed in a non-vanishing commutator,

$$\sum_{s''} [\mathbf{S} \cdot \boldsymbol{\sigma}_{ss''}, \mathbf{S} \cdot \boldsymbol{\sigma}_{s''s'}] = -2\mathbf{S} \cdot \boldsymbol{\sigma}_{ss'} \neq 0. \quad (1.25)$$

The coupling constant J is enhanced by the scaling procedure (for $J > 0$), and, for a sufficiently low temperature, J reaches its critical value $J_c \simeq \hbar v_F$. Since the band edge is not sharp, this results in a crossover from the weak to strong coupling, with a width $\sim T$. In the Kondo model, the scaling of J has an “infrared divergence”, which means that for an arbitrarily small bare J there will be always a finite temperature $T = T_K$ at which the effective J reaches J_c . Then, the spin \mathbf{S} and a lead electron form a bound state, with a binding energy that exceeds the scaled-down bandwidth. The characteristic T of the Kondo effect is the Kondo temperature $T_K = \hbar v_F K \exp(-2\pi\hbar v_F/J)$.

Chapter 2

Kondo effect and singlet-triplet splitting in coupled quantum dots in a magnetic field

The interplay between the Kondo effect and the exchange interaction K of two electron spins in a double quantum dot are studied in this chapter. We calculate [115] the cotunneling current with elastic and inelastic contributions and its renormalization due to Kondo correlations, away and at the degeneracy point $K = 0$. We show that these Kondo correlations induce pronounced peaks in the conductance G as function of magnetic field B , inter-dot coupling t_H , and temperature. The long-range part of the Coulomb interaction becomes visible due to Kondo correlations resulting in an additional peak in G vs t_H with a strong B -field dependence. These conductance peaks thus provide direct experimental access to K , and thus to a crucial control parameter for spin-based qubits and entanglement.

2.1 Introduction

Semiconductor quantum dots have attracted much interest over the years due to their rich and reproducible transport properties in the Coulomb blockade (CB) regime, where the number of electrons on the dot is quantized due to charging effects [76]. More recently, attention has focused on the spin of the electron in such nanostructures, with the spin introducing new correlation effects such as Kondo effect [139, 140, 142, 144–147], and an interplay of the spin exchange interaction and Kondo effect in single [148–157] and double dots [158–161]. On the other hand, it has been pointed out that the spin, confined to a quantum dot or atom, is a suitable candidate for quantum information processing [27], due to unusually long decoherence time of spin [7]. A crucial element in such spin-based quantum computing schemes is the Heisenberg exchange interaction K between spins of adjacent dots, being controlled via the interdot tunneling [27]. Thus, the primary goal is to achieve control over

K which then allows one to generate deterministic entanglement of spins. Using a Hund-Mulliken (HM) approach to describe a realistic double dot (DD) it has been shown [59] that K is very sensitive to long range Coulomb interaction as well as to magnetic fields by which a singlet-triplet (ST) crossing can be tuned. Also, recent experiments [149] and calculations [153–155] on single dots show an enhancement of the Kondo temperature T_K at the ST transition. Motivated by this we study here transport and the Kondo effect in such a realistic DD system within the HM approach, thereby going beyond short-range on-site models used so far to describe the Kondo effect in double dots [158, 160]. In particular, we calculate the current through the DD via a Schrieffer-Wolff transformation and via a systematic cotunneling calculation including elastic and inelastic contributions. Using a perturbative renormalization group (RG) approach we find an exponentially increasing T_K with increasing the inter-dot coupling t_H at the ST degeneracy $K = 0$. We show that the conductance in the cotunneling regime shows pronounced peaks induced by Kondo correlations and long range Coulomb interactions as function of t_H , magnetic field, and temperature. Such Kondo enhanced peaks in the conductance thus provide direct experimental access to singlet/triplet states and their exchange splitting K —the quantities of crucial importance for spin-based qubit schemes.

2.2 Model Hamiltonian

We consider a DD system consisting of two lateral quantum dots tunnel-coupled to metallic leads (Fig. 1a) in the presence of a perpendicular B -field. At low temperatures T , the conductance G of the DD versus the common gate voltage V_g shows sharp doublets of sequential tunneling peaks [162] separated by CB valleys. We consider a CB valley, where the occupation number of each dot is odd. The low energy sector of the DD consists of a singlet and a triplet,

$$\begin{aligned}
 |00\rangle &= \frac{1}{\sqrt{1+\phi^2}}(d_{+\uparrow}^\dagger d_{+\downarrow}^\dagger - \phi d_{-\uparrow}^\dagger d_{-\downarrow}^\dagger)|0\rangle, \\
 |11\rangle &= d_{-\uparrow}^\dagger d_{+\uparrow}^\dagger|0\rangle, \quad |1-1\rangle = d_{-\downarrow}^\dagger d_{+\downarrow}^\dagger|0\rangle, \\
 |10\rangle &= \frac{1}{\sqrt{2}}(d_{-\uparrow}^\dagger d_{+\downarrow}^\dagger + d_{-\downarrow}^\dagger d_{+\uparrow}^\dagger)|0\rangle.
 \end{aligned} \tag{2.1}$$

Here, we assumed a symmetric DD, which has two electrons on its outermost symmetric ($d_{+\sigma}^\dagger$) and anti-symmetric ($d_{-\sigma}^\dagger$) orbitals; $|0\rangle$ is the state of the inner-shell electrons. A detailed analysis of the DD spectrum has been performed for $N = 2$ [59] and $N = 6$ [167] electrons. The competition between the kinetic energy gain and Coulomb repulsion is described by the *interaction* parameter $\phi = \sqrt{1+r_H^2} - r_H$, with the Hubbard ratio $r_H = 4t_H/U_H$ determined by the extended inter-dot tunneling amplitude t_H and the on-site Coulomb repulsion U_H [59]. The Heisenberg exchange interaction between the DD spins is given by

$$K = \frac{1}{2}\sqrt{U_H^2 + 16t_H^2} - \frac{U_H}{2} + V_C = K_H + V_C, \tag{2.2}$$

2.2. MODEL HAMILTONIAN

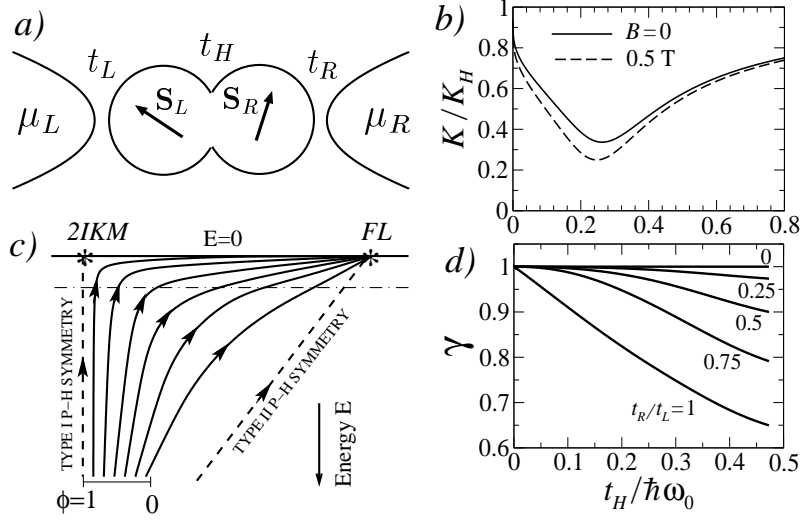


Figure 2.1: (a) Double-dot setup: two spin-1/2 quantum dots tunnel-coupled to two metallic leads at chemical potentials μ_L and $\mu_R = \mu_L - \Delta\mu$. (b) The ratio $K/K_H = 1 - |V_C|/K_H$, showing the significance of long range Coulomb interaction; we apply our model to GaAs dots with $\hbar\omega_0 = 3\text{meV}$ and $N = 2$. (c) A schematic RG flow diagram, showing the crossover region between two types of particle-hole (P-H) symmetry at $t_L = t_R$. The fixed point of the two-impurity Kondo model (2IKM) is approached for $\phi \rightarrow 1$; whereas for $\phi \approx 0$ the RG flow evolves efficiently toward the universal Fermi-liquid fixed point (FL). The dot-dashed line shows the termination point ($D \sim T_K^{(1)}$) in a realistic system with finite coupling constants. (d) The number γ versus t_H at $K = 0$ for different t_R/t_L , showing the enhancement of the Kondo temperature.

where K_H is the so called Hubbard part, occurring for short range Coulomb interaction, and $V_C < 0$ is a contribution stemming from long range Coulomb interaction [59]. Here, we consider small dots, for which the screening length is much larger than the DD size. The contribution V_C plays a crucial role in achieving a ST transition. Already at $B = 0$, the term V_C introduces a significant correction to K over a range of t_H , see K/K_H vs t_H in Fig. 1b. With applying the B -field, the absolute value of V_C first increases, whereas the value of K_H stays almost unaffected; both contributions are suppressed at $B \gtrsim B_0 = m c \omega_0 / |e|$, where $\hbar\omega_0$ is the one-dot energy spacing, and e and m are the electron charge and effective mass, *resp.* The ST transition occurs due to the orbital effect of the B -field at a value of B smaller than B_0 , when $|V_C| = K_H$ [59]. We neglect the Zeeman energy E_Z , assuming $T_K \gg E_Z$.

The metallic leads are described by $H_l = \sum_{\alpha k \sigma} \varepsilon_k c_{\alpha k \sigma}^\dagger c_{\alpha k \sigma}$, where $c_{\alpha k \sigma}^\dagger$ creates an electron-state with momentum k and spin σ in lead $\alpha = L, R$. The coupling between the DD and the leads is described by the tunneling Hamiltonian $H_T = \sum_{n \alpha k \sigma} (t_{\alpha n} c_{\alpha k \sigma}^\dagger d_{n \sigma} + \text{h.c.})$, with the tunneling amplitudes $t_{L,\pm} = t_L / \sqrt{2(1 \pm \mathcal{S})}$ and $t_{R,\pm} = \pm t_R / \sqrt{2(1 \pm \mathcal{S})}$. Here, \mathcal{S} is the overlap integral [59], and t_L, t_R describe the tunnel junctions at $t_H = 0$, with $t_L \geq t_R$ for definiteness. For the CB val-

ley, we integrate out the charge degree of freedom of the DD, with the help of the Schrieffer-Wolff transformation [163], and obtain the cotunneling Hamiltonian $H_{cot} = H_T[(i0^+ - \hat{L}_0)^{-1}H_T]$, where $\hat{L}_0 A \equiv [H_d + H_l, A]$ and H_d is the DD Hamiltonian. Next we concentrate on the states (2.1) and project out the higher lying energy levels by means of the mapping [154]

$$\begin{aligned} \sum_{\sigma\sigma'} d_{n\sigma}^\dagger \sigma_{\sigma\sigma'} d_{n'\sigma'} &= \mathbf{S}_+ \delta_{nn'} + \left(\frac{\phi_+}{2} \mathbf{S}_- + in\phi_- \mathbf{S}_L \times \mathbf{S}_R \right) \delta_{-nn'}, \\ \sum_{\sigma} d_{n\sigma}^\dagger d_{n'\sigma} &= \delta_{nn'} \left[1 - \frac{n}{2} \phi_+ \phi_- \left(\mathbf{S}_L \cdot \mathbf{S}_R - \frac{1}{4} \right) \right], \end{aligned} \quad (2.3)$$

where $\mathbf{S}_\pm = \mathbf{S}_L \pm \mathbf{S}_R$ and $\phi_\pm = \sqrt{2}(1 \pm \phi)/\sqrt{1 + \phi^2}$. The DD spin degrees of freedom are represented now by two spin 1/2 operators $\mathbf{S}_{L,R}$. The projected out energy levels stand at a significant energy distance $D_0 \simeq \min(\hbar\omega_0, U_H)$ from (2.1). With the help of the ‘‘poor man’s’’ scaling approach [136], we derive an effective Hamiltonian for the low energy physics of the DD. In this approach, the lead electrons at the cutoff energy D_0 are integrated out, and the cutoff energy is reduced to a new value $D = D_0 - dD$, which is eventually scaled down to the active region of the Fermi sea, i.e. to $D = cT$, with $c \gtrsim 1$. The Kondo correlations manifest themselves in a flow of the coupling constants entering the effective Hamiltonian

$$H_{\text{eff}} = H_l + K \mathbf{S}_L \cdot \mathbf{S}_R + \Delta H, \quad (2.4)$$

$$\begin{aligned} \Delta H &= \sum_{\alpha\alpha'} (J_{\alpha\alpha'} \mathbf{s}_{\alpha\alpha'} \cdot \mathbf{S}_+ + I_{\alpha\alpha'}^+ \mathbf{s}_{\alpha\alpha'} \cdot \mathbf{S}_- \\ &\quad + 2iI_{\alpha\alpha'}^- \mathbf{s}_{\alpha\alpha'} \cdot [\mathbf{S}_L \times \mathbf{S}_R] - V_{\alpha\alpha'} \rho_{\alpha\alpha'} \mathbf{S}_L \cdot \mathbf{S}_R), \end{aligned} \quad (2.5)$$

where $\mathbf{s}_{\alpha\alpha'} = \sum_{kk'\sigma\sigma'} c_{\alpha k\sigma}^\dagger (\sigma_{\sigma\sigma'}/2) c_{\alpha' k'\sigma'}$, and $\rho_{\alpha\alpha'} = \sum_{kk'\sigma} c_{\alpha k\sigma}^\dagger c_{\alpha' k'\sigma}$. The bare values of J, V, I^\pm are given by

$$J = \frac{2}{E_C} V^+, \quad I^\pm = \frac{\phi_\pm}{E_C} W^\pm, \quad V = \frac{\phi_+ \phi_-}{2E_C} V^-, \quad (2.6)$$

with matrices $V_{\alpha\alpha'}^\pm = t_{\alpha',+}^* t_{\alpha,+} \pm t_{\alpha',-}^* t_{\alpha,-}$, $W_{\alpha\alpha'}^\pm = t_{\alpha',-}^* t_{\alpha,+} \pm t_{\alpha',+}^* t_{\alpha,-}$, and with $E_C = 2E_+ E_- / (E_+ + E_-)$. Here, $E_\pm = E(N \pm 1) - E(N) \mp \mu$ is the CB addition/extraction energy, with $E(N)$ being the N -electron DD energy, and μ the Fermi energy. The scaling equations at $K = 0$ are best presented in a matrix form:

$$\begin{aligned} \dot{J} &= J^2 + (I^+)^2 - (I^-)^2, \quad \dot{V} = 2[I^-, I^+], \\ \dot{I}^\pm &= \{J, I^\pm\} + [V, I^\mp], \end{aligned} \quad (2.7)$$

where the dot denotes $d/d(\nu\mathcal{L})$, with ν being the lead density of states, and $\mathcal{L} = \ln(D_0/D)$. Here, we would like to note that a similar two-channel Kondo problem was recently dealt with in Refs. [153–155], in relation to the Kondo effect in a single vertical quantum dot [149]. Assuming conservation of the orbital symmetry in tunneling from dot to lead, the authors of Refs. [153–155] obtained a model, which in our

2.2. MODEL HAMILTONIAN

notations formally corresponds to $t_{\alpha n} = t_n \delta_{\alpha n}$. The flow of H_{eff} , governed by (2.7), can be analyzed in detail for the generic case, however the parameter space is too large to allow a comprehensible presentation. Remarkably, there is a simple physical picture behind the complicated and numerous scaling equations. It relies on two types of particle-hole symmetry (PHS), introduced in Ref. [164]. Arbitrarily rotating the lead space, one can search for the invariance of H_{eff} under $c_{\alpha k \sigma} \rightarrow \sigma c_{\alpha, -k, -\sigma}^\dagger$ (type I) or $c_{\alpha k \sigma} \rightarrow \sigma c_{-\alpha, -k, -\sigma}^\dagger$ (type II) transformation, where $\alpha \rightarrow -\alpha$ means $L/R \rightarrow R/L$. If one of such symmetries is found, then it is maintained by the equations (2.7) during the entire flow. The type I/II transformation reduces formally to $\mathbf{s}_{\alpha\alpha'} \rightarrow \mathbf{s}_{\pm\alpha', \pm\alpha}$ and $\rho_{\alpha\alpha'} \rightarrow 4\nu D \delta_{\alpha\alpha'} - \rho_{\pm\alpha', \pm\alpha}$ in Eq. (2.5), yielding

$$J = (J_0, J_x, 0, J_z), \quad I^+ = (I_0^+, I_x^+, 0, I_z^+), \quad I^- = (\bar{I}_0^-, \bar{I}_x^-, 0, \bar{I}_z^-), \quad V = (0, 0, \bar{V}_y, 0), \quad (\text{I})$$

$$J = (J_0, J_x, \bar{J}_y, 0), \quad I^+ = (I_0^+, I_x^+, \bar{I}_y^+, 0), \quad I^- = (\bar{I}_0^-, \bar{I}_x^-, I_y^-, 0), \quad V = (0, 0, 0, V_z), \quad (\text{II})$$

where $(A_0, A_x, A_y, A_z) \equiv A_0 + \sum_i A_i \sigma^i$, and $\bar{A}_k = 0$ for $\Delta H^* = \Delta H$ (time-reversal symmetry). From here on, we assume time-reversal symmetry in (2.5), which is the case for the considered DD setup,¹ since $t_{\alpha n}^* = t_{\alpha n}$. In a realistic system, as a rule, neither PHS holds, *e.g.*, for our DD, we have $J = (J_0, J_x, 0, J_z)$, $I^+ = (I_0^+, I_x^+, 0, I_z^+)$, $I^- = (0, 0, I_y^-, 0)$, and $V = (0, V_x, 0, V_z)$. The remarkable feature of equations (2.7) is that the fixed point of the type I symmetry is unstable with respect to a violation of PHS, whereas that of the type II symmetry is stable. This means that, if no PHS is present, the RG flow will evolve towards the type II symmetry in the low energy limit. The fixed point of the type I symmetry is characterized by two energy scales, given by $T_K^{(\pm)} = D_0 \exp(-1/\nu \tilde{J}_\pm)$, where $\tilde{J}_\pm = J_0 \pm I_0^+ + \sqrt{(J_x \pm I_x^+)^2 + (J_z \pm I_z^+)^2}$. For detached dots ($t_H = 0$), two spin-1/2 Kondo effects occur independently, with $\tilde{J}_\pm = 4t_{L/R}^2/E_C$. For tunnel-coupled dots ($t_H \neq 0$), the two Kondo effects compete and occur in two stages; however, at mirror symmetry², the two energy scales coincide: $\tilde{J}_+ = \tilde{J}_- = J_0 + \sqrt{J_x^2 + J_z^2 + (I_x^+)^2 + (I_z^+)^2}$, and we recover the Hamiltonian of the two-impurity Kondo model (2IKM), studied in Refs. [153,164]. The 2IKM is known to have a non-Fermi-liquid critical point at the exchange value $K_c \simeq 2.2 T_K$, separating the Kondo-screening phase ($K < K_c$) from the DD singlet phase ($K > K_c$) by a step-like transition in the scattering phase shift [164]. We obtain a signature of this critical point in the linear conductance for weakly coupled dots, see below. The fixed point of the type II symmetry is characterized by one single energy scale $T_K^{(0)} = D_0 \exp(-\gamma/\nu \tilde{J})$, where $\tilde{J} = J_0 + |J_x| + |I_0^+| + |I_x^+|$, and $\gamma \leq 1$ is a non-universal number. At $I_y^-, V_z \neq 0$, the flow asymptotes are universal and coincide with those obtained in Refs. [154, 155] for a single vertical dot: $J = (\tau^2 I, 0, 0, 0)$, $I^+ = (0, \sqrt{\tau/2} I, 0, 0)$, $iI^- = (0, 0, \sqrt{\tau/2} I, 0)$, $V = (0, 0, 0, \tau I)$, where $I = 1/2\nu \ln(D/T_K^{(0)})$ and $\tau = \frac{\sqrt{5}-1}{2}$. As pointed out in Ref. [155], this fixed point is rather delicate to achieve in a realistic

¹Eqs. (2.7) hold for arbitrary $t_{\alpha n}$ and can also describe a parallel (Aharonov-Bohm) geometry of the DD.

²At $t_L = t_R$, the Hamiltonian (2.4) is invariant under the mirror reflection: $\mathbf{S}_{L/R} \rightarrow \mathbf{S}_{R/L}$, $c_{L/R, k\sigma} \rightarrow c_{R/L, k\sigma}$.

system, since the approach to this universal ratio between the coupling constants is asymptotic and hence requires an infinitesimally weak coupling to the leads.

2.3 Kondo effect in the double dot

Next we turn to a discussion of the results for the DD. The RG flow terminates in a crossover region between the type I and type II PHS, *e.g.* as it is depicted in Fig. 1c. We associate two energy scales, $T_K^{(1,2)}$, with binding of two lead electrons, which screen the DD spins at $K = 0$. For weak inter-dot coupling ($\nu\tilde{J} \gg \phi_- t_R/t_L$), the two energy scales $T_K^{(1,2)}$ coincide with $T_K^{(\pm)}$ and the RG flow terminates in the neighborhood of the type I PHS, whereas for weak coupling to the leads ($\nu\tilde{J} \ll \phi_- t_R/t_L$), the two energy scales merge on $T_K^{(0)}$, and the RG flow terminates in the neighborhood of the type II PHS. We could numerically determine the largest energy scale, $T_K^{(1)}$, from equations (2.7) at the ST degeneracy point ($K = 0$). We find an exponential increase in $T_K^{(1)}$ as a function of the inter-dot coupling t_H . Using the definition $T_K^{(1)} = D_0 \exp(-\gamma/\nu\tilde{J})$, with $\tilde{J} = \frac{t_L^2}{EC} \left(\frac{2}{1-S^2} + \frac{\phi_+}{\sqrt{1-S^2}} \right)$, we plot γ vs t_H for different t_R/t_L in Fig. 1d. We choose \tilde{J} to normalize γ to $\gamma = 1$ at $t_R = 0$. From these results we can conclude that there are two physical phenomena responsible for the enhancement of the Kondo temperature at the ST transition in DDs. The first one is the hybridization of the DD orbital states combined with the overlap of the DD spin sites³. The definition of \tilde{J} includes this effect. The second phenomenon is more interesting, since it has to do with the cross-correlation between two Kondo clouds. At $t_H = 0$, each of the DD spins is screened by an independent Kondo cloud formed by the respective lead. For tunnel-coupled dots, a new possibility for Kondo correlations emerges, namely the processes which do not conserve the number of electrons in each channel. By choosing the two channels to be linear combinations of left and right leads, it can be shown that no rotation in the lead space makes the inter-channel current operator vanish. In addition, the strength of this minimal inter-channel coupling grows strongly under the RG flow (2.7). The 3rd and 4th terms in (2.5) are responsible for this new behavior. Such Kondo cross-correlations are present both in DDs and in single vertical dots studied in Refs. [153–155].

2.4 Signatures of the Kondo effect in transport

We present now the results for the transport through the DD at $t_L = t_R$. In lowest non-vanishing order in ΔH (Eq. (2.5)), the elastic and inelastic parts of the current

³As follows from (2.3), the spins $\mathbf{S}_{L,R}$ no longer reside in separate dots as the inter-dot tunneling is switched on.

2.4. SIGNATURES OF THE KONDO EFFECT IN TRANSPORT

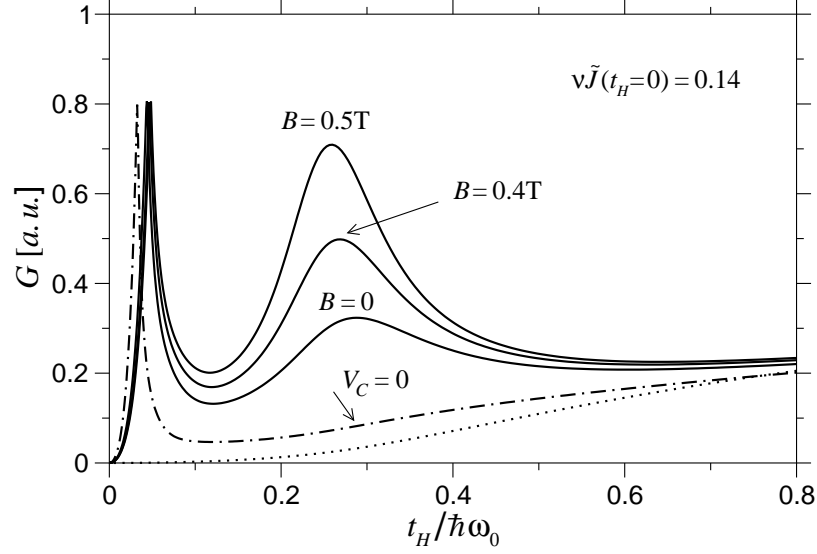


Figure 2.2: Linear G vs t_H at different B 's. The unitary limit of G is $2e^2/h$. Dotted line: cotunneling contribution. Dot-dashed line: G vs t_H with $V_C \rightarrow 0$ in (2.2).

are,

$$\mathcal{I}_{\text{el}} = \frac{e}{\hbar} \pi \nu^2 \left[J_{LR}^2 \langle \mathbf{S}_+^2 \rangle + V_{LR}^2 \left(\frac{9}{4} - \langle \mathbf{S}_+^2 \rangle \right) \right] \Delta\mu, \quad (2.8)$$

$$\mathcal{I}_{\text{inel}} = \frac{e}{\hbar \beta} \pi \nu^2 (I_{LR}^-)^2 g(\beta K) f(\beta K, \beta \Delta\mu), \quad \beta = 1/T, \quad (2.9)$$

where $\langle \mathbf{S}_+^2 \rangle = 6/(e^{\beta K} + 3)$, $\Delta\mu$ is the bias, $g(u) = (e^u + 1)/(e^u/3 + 1)$ accounts for the degeneracy of the excited level, and $f(u, v) = \frac{u \tanh(u/2) \sinh(v) + v[1 - \cosh(v)]}{\cosh(u) - \cosh(v)}$. The scaling equations (2.7) can be used to obtain the coupling constants in (2.8), (2.9) at $T \sim D \gg T_K^{(1)}, \Delta\mu$. The current scales as $\mathcal{I}(\mathcal{L}) = \mathcal{I}_K(\mathcal{L}) + \delta\mathcal{I}(0)$, where $\mathcal{I}_K = \mathcal{I}_{\text{el}} + \mathcal{I}_{\text{inel}}$, and $\delta\mathcal{I}$ stems from the potential scattering not present in the low-energy Hamiltonian (2.4). Using the cotunneling Hamiltonian, we find

$$\begin{aligned} \delta\mathcal{I} = & \frac{e}{\hbar} \pi \nu^2 \left[V_{LR}^2 \left(\frac{7}{4} - \langle \mathbf{S}_+^2 \rangle \right) + J_{LR}^2 \left(\frac{E_- - E_+}{E_- + E_+} \right)^2 - \right. \\ & \left. 2V_{LR} J_{LR} \frac{E_- - E_+}{E_- + E_+} (2 - \langle \mathbf{S}_+^2 \rangle) \right] \Delta\mu. \end{aligned} \quad (2.10)$$

In the cotunneling regime, $d\mathcal{I}/d\Delta\mu$ versus $\Delta\mu$ has a step at $\Delta\mu = \pm K$, for $T \ll |K|$; the step height is 3 times larger on the singlet side than on the triplet side. The linear conductance $G = e(d\mathcal{I}/d\Delta\mu)|_{\Delta\mu=0}$ as a function of t_H is plotted in Fig. 2. The dotted line shows the cotunneling conductance, calculated using unscaled coupling constants. The solid lines show a non-monotonous t_H -dependence of G with two peaks, resulting from Kondo correlations. The sharp peak at a small value of t_H

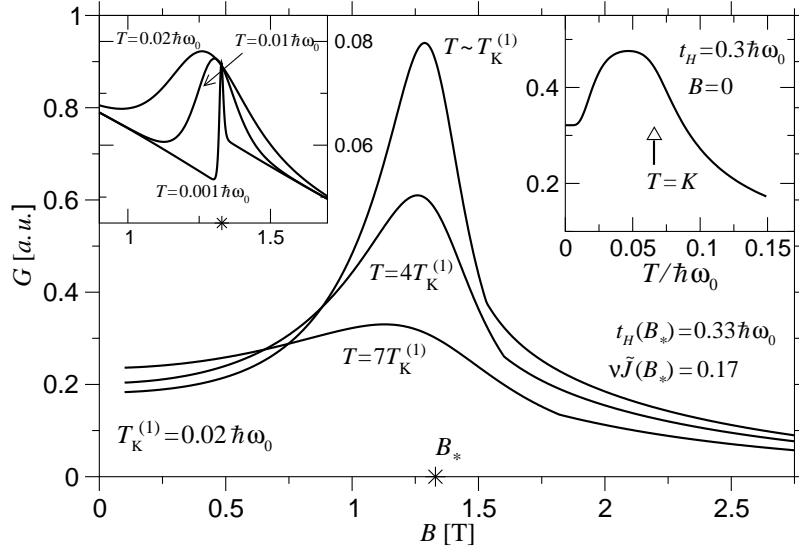


Figure 2.3: Linear G vs B at the ST transition. $K = 0$ occurs at $B_* \approx 1.3$ T, whereas $B_0 \approx 3.5$ T. Left inset: G with unscaled coupling constants (cotunneling G); parameters as in the main figure. Right inset: Linear G vs T , showing a maximum at $T \simeq K$.

has been studied in detail in Refs. [159, 160]. It occurs at $t_H \sim \sqrt{U_H T_K}$ due to the competition between the inter-dot singlet formation, with the exchange energy K , and the formation of two Kondo singlets, each with the exchange energy T_K . The transition between the two phases occurs discontinuously in the 2IKM [164] due to the type I PHS. In the context of the DD system, this non-Fermi-liquid behavior corresponds to a vanishing width of the sharp peak in Fig. 2. The closeness of the parameter ϕ to 1 at $K \simeq T_K$ allows the study of the 2IKM critical point in double quantum dots. The broad peak in G vs t_H occurs at the value of t_H , at which the effect of long range Coulomb interaction on the exchange K is significant, see Fig. 1b. Note that if $V_C = 0$ then this peak is absent, see the dot-dashed line in Fig. 2. The correction to K induced by V_C enhances the Kondo correlations such that the dip in Fig. 1b translates into the broad peak in Fig. 2. The broad peak is absent at $B = 0$, if the coupling to the leads is sufficiently weak such that $K \gg T_K^{(1)}$. However, applying a magnetic field pronounces the peak, provided long range Coulomb interaction is present. As a function of the B -field, the conductance G shows a peak at the ST transition, see Fig. 3. The peak height grows with lowering T for $T \gtrsim T_K^{(1)}$. It is interesting to note that the cotunneling conductance also has a peak at $K = 0$, of width $\Delta K \sim T$, due to the activation of $\mathcal{I}_{\text{inel}}$ at $|K| < T$, see left inset of Fig. 3. The signature of a ST Kondo effect is, therefore, not a peak in the conductance at $K = 0$, but rather the temperature dependence of this peak, and a conductance value close to the unitary limit $2e^2/h$. Finally, the temperature dependence of G for $K > 0$ has a maximum at $T \simeq K$, see right inset of Fig. 3. To the right of the maximum, the conductance decreases due to the decrease of Kondo correlations with increasing T ; to the left of the maximum, G decreases due to “freezing” of the inelastic component

2.4. SIGNATURES OF THE KONDO EFFECT IN TRANSPORT

(2.9) at $T < K$. This maximum can be used to estimate K from the temperature dependence of the linear conductance.

CHAPTER 2. KONDO EFFECT AND SINGLET-TRIPLET SPLITTING IN
COUPLED QUANTUM DOTS IN A MAGNETIC FIELD

Chapter 3

Transport through a double quantum dot in the sequential tunneling and cotunneling regimes

In this chapter, we study transport through a double quantum dot, both in the sequential tunneling and cotunneling regimes [91]. Using a master equation approach, we find that, in the sequential tunneling regime, the differential conductance G as a function of the bias voltage $\Delta\mu$ has a number of satellite peaks with respect to the main peak of the Coulomb blockade diamond. The position of these peaks is related to the interdot tunnel splitting and the singlet-triplet splitting. We find satellite peaks with both *positive* and *negative* values of differential conductance for realistic parameter regimes. Relating our theory to a microscopic (Hund-Mulliken) model for the double dot, we find a temperature regime for which the Hubbard ratio (=tunnel coupling over on-site Coulomb repulsion) can be extracted from $G(\Delta\mu)$ in the cotunneling regime. In addition, we consider a combined effect of cotunneling and sequential tunneling, which leads to new peaks (dips) in $G(\Delta\mu)$ inside the Coulomb blockade diamond below some temperature scales, which we specify.

3.1 Introduction

In recent years, there has been great interest in few-electron quantum dots, or so-called artificial atoms [16, 76]. The interest stems from a variety of fields, such as nano-electronics, spintronics, quantum computation, etc., which are all rapidly growing at present. Unlike real atoms, quantum dots can be locally manipulated by electrical gates and tuned to the regimes of interest such that in one and the same quantum dot one can realize a whole species of atomic-like electronic structures. Many of experimental investigations on the Kondo effect, Coulomb blockade effect, spin blockade effect, etc., have been performed in recent years owing to this tunability feature. Yet a not less important feature of quantum dots is the possibility to

architecture and control, to a great extent, the coupling to their surrounding, be it a dissipative environment, classical (gate) fields, or, in particular, other quantum dots. This makes quantum dots attractive for quantum computation [27].

A most promising candidate for a qubit (quantum bit) in solid state is the electron spin [27]. Confining electrons to quantum dots naturally defines the qubit as the *spin up* and *spin down* states of the dot, provided the dot contains an odd number of electrons. At the ultimate level of control over the electron charge, the quantum dot can be tuned to confine one single electron¹, thus implementing the artificial version of the hydrogen atom. This has been successfully achieved in recent years, first in vertical dots [67] and more recently also in lateral dots [168], due to a special design of top gates. Observation of shell filling of dot orbitals and the Hund’s rule in symmetric dots [67] indicates that the electron spin is a relevant degree of freedom in few-electron quantum dots and that achieving control over it should be feasible experimentally in the near future.

For quantum computation on an array of qubits [27, 118], both single-qubit and two-qubit gates are required. Two tunnel-coupled quantum dots represent the fundamental unit system where these quantum gates can be tested. A single-qubit gate is implemented as a rotation of the spin on the Bloch sphere. This can be realized if the magnetic field (or the effective g -factor) is locally controlled. On the other hand, the two-qubit gate requires formation of a non-local quantum-mechanical correlation between the qubits, known as entanglement. This can be achieved using the Heisenberg exchange interaction between the spins $H_{\text{spin}} = J\mathbf{S}_1 \cdot \mathbf{S}_2$, where $\mathbf{S}_{1,2}$ are spin-1/2 operators, and J is the exchange coupling constant. For instance, a $\pi/2$ -pulse of exchange J turns out to be a universal quantum gate [27, 59, 118], known as the “square root of swap gate”. Therefore, the exchange J plays as an important role for the two-qubit gate as the Zeeman splitting for the single-qubit gates. Moreover, exchange can also be used for single-spin rotations: exchange coupling the spin to some spin-ordered state like a nearby quantum Hall edge state, ferro- or antiferromagnets, etc.

The Zeeman splitting of a single electron in a quantum dot has been accessed in recent experiments [86, 87], by means of *dc* transport spectroscopy. The long-lived nature of the spin states has been tested in Ref. [86], using a pulsed relaxation measurement technique. This technique [84] uses a sequence of pulses, during which the electron is allowed to tunnel into an excited state of the quantum dot [85]. Relaxation from the excited state can be monitored in the average current versus the pulse timing, see Refs. [84] and [86] for details. The spin relaxation time T_1 was found to be larger than $50 \mu\text{s}$ at $B = 7.5 \text{ T}$ for single electron GaAs quantum dots [86, 90], thus, indicating that the spin states in quantum dots are long-lived.

On the other hand, the exchange J is yet to be accessed in experiments. The diffi-

¹Having one electron per dot is not a necessary condition for the spin qubit; an odd number of electrons can be as good [27, 167]. However, it is important that there are no low-lying excited states, *e.g.* with spin 3/2, which could restrain the adiabaticity of quantum gate operation and cause leakage from the spin-1/2 Hilbert space.

3.1. INTRODUCTION

culties in doing a transport spectroscopy of the double dot (DD) are primarily due to the small currents involved in the few-electron regime. Nevertheless, a DD with one electron per dot – an artificial H_2 molecule – has been realized recently [70, 71]. A complementary method of charge control was used in Ref. [70], which came with integrating the quantum dots with sensitive charge detectors [74, 75] — quantum point contacts (QPCs) placed nearby the quantum dots and tuned to the half pinch-off. Such a detector is capable of sensing a change in the dot charge by as little as a fraction of an electron [70]. Achieving control over the DD state is promising for performing further experiments and focusing on the transport properties in greater detail.

In this chapter, we show that the differential conductance G as well as the DD occupation number N allows one to extract the exchange constant J in the dc transport regime at a finite bias. We give a detailed analysis of the transport spectroscopy, considering separately (i) the sequential tunneling and (ii) cotunneling through the DD, as well as a combined effect of (i) and (ii), which we refer to as cotunneling-assisted sequential tunneling (iii). Our primary goal is to specify all features that can be seen in a dc transport spectroscopy and to seek ways to extract the DD parameters from transport setups which are experimentally accessible.

We begin with explaining the DD parameters in Sec. 3.2, for which we briefly review the Hund-Mulliken model for the DD [59] used throughout. Next, in Sec. 3.3, we consider sequential tunneling through the DD. Here, we calculate the tunneling rates using Fermi's golden rule and then we find the DD population probabilities ρ_p by solving the master equation in the stationary limit in Sec. 3.3.1. This solution allows us to specify the spectroscopic intervals over which ρ_p is constant as function of the applied bias $\Delta\mu$ at low temperatures. At the boundaries between these intervals, the probabilities ρ_p change step-wise. We calculate the sequential tunneling current in Sec. 3.3.2 and find that the differential conductance $G = edI/d\Delta\mu$ as a function of $\Delta\mu$ has peaks, as expected from the spectroscopic intervals of $\Delta\mu$. However, not all peaks are activated due to the sequential tunneling alone. We return to this question in Sec. 3.6 and show that a combined effect of sequential tunneling and cotunneling (cotunneling-assisted sequential tunneling) activates the missing peaks. We demonstrate that the peaks due to the sequential tunneling allow one to extract the exchange constant J and the tunnel splitting $2t_0$ of the DD in the I - V plot. Interestingly, we find that one of the peaks has a negative conductance, $G < 0$, for typical values of the DD parameters, which is a novel feature in transport through quantum dots. In Sec. 3.3.3, we consider charge detection via QPCs and show that the peaks occurring in G vs $\Delta\mu$ can also be monitored via the average number of electrons N on the DD.

In Secs. 3.4 and 3.5, we consider cotunneling through a Coulomb blockaded DD with one and two electrons, *resp.* We use again Fermi's golden rule (2nd order) to calculate the cotunneling rates and the master equation to obtain the population probabilities ρ_p . We show that from the competition of inelastic cotunneling into the same lead and inelastic cotunneling into the opposite lead a temperature regime of *strong heating*

results, where the DD population is determined by the applied bias $\Delta\mu$ and the DD parameters. We calculate the elastic and inelastic components of the current and show that the exchange J can be extracted also in the cotunneling regime. In the strong heating regime, additional parameters, such as the asymmetry η of coupling to the leads, and the DD *interaction* parameter ϕ , can be extracted from the transport measurement.

Finally, in Sec. 3.6, we consider a combined effect of sequential tunneling and cotunneling in the DD. The inelastic cotunneling induces a non-equilibrium population of the DD excited states. This results in a switching-on of the sequential tunneling transitions, which were forbidden to take place from the DD ground state, due to energy conservation. Here, again we find additional peaks or dips in G vs $\Delta\mu$ below certain temperature scales, which we specify. Some of the technical details are deferred to the App. A–C.

3.2 Energy spectrum of a double quantum dot

For definiteness we consider lateral quantum dots, which are formed by gating a two-dimensional electron gas (2DEG) under the surface of a substrate. The 2DEG is depleted in the regions under the gates and, with an appropriate gate design [168], one can achieve a depopulation of the dots down to 1 and 0 electrons per dot, while still allowing tunneling between the dots and the surrounding 2DEG. The low energy sector of a DD at occupation number $N = N_1 + N_2 = 1$ consists of two tunnel-split energy levels, which we label by the orbital quantum number n , with $n = +$ standing for the symmetric orbital and $n = -$ for the anti-symmetric one. The states of the DD with one electron can then be written as

$$|n, \sigma\rangle = d_{n\sigma}^\dagger |0\rangle, \quad (3.1)$$

where σ denotes the spin degeneracy of each level (we neglect the Zeeman splitting), $d_{n\sigma}^\dagger$ is the electron creation operator, and $|0\rangle$ is the DD state with zero electrons. The splitting between the two levels is given by $2t_0$, where t_0 is the interdot tunneling amplitude. We assume weak tunnel-coupling between the dots such that $t_0 \ll \hbar\omega_0$, where $\hbar\omega_0$ is the size-quantization energy of a single dot.

The two-electron spectrum can be obtained using the Hund-Mulliken method [59]. In this method, the single-particle states (3.1) are used to construct two-particle states. Obviously, there are 6 ways to distribute 2 electrons over 4 states. Using this truncated Hilbert space one can find the eigenstates of the DD Hamiltonian. The lowest energy states, one singlet state and 3 triplet states, are given by

$$\begin{aligned} |S\rangle &= \frac{1}{\sqrt{1+\phi^2}}(d_{+\uparrow}^\dagger d_{+\downarrow}^\dagger - \phi d_{-\uparrow}^\dagger d_{-\downarrow}^\dagger)|0\rangle, \\ |T_+\rangle &= d_{-\uparrow}^\dagger d_{+\uparrow}^\dagger |0\rangle, \quad |T_-\rangle = d_{-\downarrow}^\dagger d_{+\downarrow}^\dagger |0\rangle, \\ |T_0\rangle &= \frac{1}{\sqrt{2}}(d_{-\uparrow}^\dagger d_{+\downarrow}^\dagger + d_{-\downarrow}^\dagger d_{+\uparrow}^\dagger)|0\rangle. \end{aligned} \quad (3.2)$$

3.2. ENERGY SPECTRUM OF A DOUBLE QUANTUM DOT

The remaining excited states are separated by a substantial gap, see Eqs. (3.11) and (3.12) and the discussion therein. The energy splitting between the singlet and the triplet in Eq. (3.2), $J = E_{|T\rangle} - E_{|S\rangle}$, plays the role of the Heisenberg exchange interaction for the two electron spins in the DD,

$$H_{\text{spin}} = J\mathbf{S}_1 \cdot \mathbf{S}_2. \quad (3.3)$$

The *interaction* parameter ϕ , entering the singlet state in (3.2), is determined by a competition between tunneling and Coulomb interaction in the DD, and it can be calculated [115] (Hund-Mulliken method) to be

$$\phi = \sqrt{1 + \left(\frac{4t_H}{U_H}\right)^2} - \frac{4t_H}{U_H}, \quad (3.4)$$

where t_H and U_H are the so called extended inter-dot tunneling amplitude and on-site Coulomb repulsion, respectively [59]. We note that $t_H = t_0 + t_C \simeq t_0$, where t_C is a Coulomb contribution, which vanishes with detaching the dots ($t_0 \rightarrow 0$). To illustrate the meaning of ϕ , we also present the states (3.2) in terms of orbitals, which are mostly localized on one of the dots, see Appendix A. The double occupancy – the probability to find the two electrons in the same dot — for the singlet state is given by

$$D = \frac{(1 - \phi)^2}{2(1 + \phi^2)}. \quad (3.5)$$

Double occupancy is absent for the triplet states. The parameter ϕ also determines the entanglement between the two electrons in the singlet state. While ϕ can be used on its own as a measure of entanglement, we are presenting here a formula for the concurrence [116] of the singlet $|S\rangle$,

$$c = \frac{2\phi}{1 + \phi^2}. \quad (3.6)$$

The entanglement in the $|T_0\rangle$ state is maximal ($c = 1$) at all values of t_0 .

The energies of the considered DD states are given by

$$E_{|0\rangle} = 0, \quad (3.7)$$

$$E_{|n\sigma\rangle} = \tilde{\varepsilon} - nt_0, \quad (3.8)$$

$$E_{|S\rangle} = 2\tilde{\varepsilon} + U_{12} - J, \quad (3.9)$$

$$E_{|T\rangle} = 2\tilde{\varepsilon} + U_{12}, \quad (3.10)$$

where $\tilde{\varepsilon} \simeq \hbar\omega_0 - \tilde{V}_g$ and $U_{12} \simeq e^2/2C_{12}$, with \tilde{V}_g being the energy shift due to the common gate potential V_g (see Fig. 3.1) and C_{12} the mutual capacitance between the dots.

For small dots ($\hbar\omega_0 > U_H$), the next excited states are the following two singlets

$$|S1\rangle = \frac{1}{\sqrt{2}}(d_{-\uparrow}^\dagger d_{+\downarrow}^\dagger - d_{-\downarrow}^\dagger d_{+\uparrow}^\dagger)|0\rangle, \quad (3.11)$$

$$|S2\rangle = \frac{1}{\sqrt{1+\phi^2}}(\phi d_{+\uparrow}^\dagger d_{+\downarrow}^\dagger + d_{-\uparrow}^\dagger d_{-\downarrow}^\dagger)|0\rangle, \quad (3.12)$$

with $E_{|S1\rangle} \simeq E_{|S2\rangle} \simeq E_{|S\rangle} + U_H$. The states (3.2) together with (3.11) and (3.12) complete the resolution of unity for two electrons in the DD orbitals $n = \pm$. We note that the states (3.11) and (3.12) are separated in energy from the states (3.2) by $\delta\varepsilon \simeq U_H \gg J$, which ensures that the Hamiltonian (3.3) has room for adiabatic switching of the exchange J , see Ref. [118].

Finally, we note that according to the Hund-Mulliken method the exchange J consists of two components,

$$J = V_C + J_H, \quad (3.13)$$

where $V_C < 0$ is responsible for a singlet-triplet transition at a finite magnetic field, see Ref. [59], and

$$J_H = \frac{1}{2}\sqrt{U_H^2 + 16t_H^2} - \frac{1}{2}U_H \quad (3.14)$$

resembles the exchange constant obtained in the standard Hubbard model for on-site Coulomb repulsion. For weakly coupled quantum dots, we have $J_H \approx 4t_H^2/U_H$.

3.3 Sequential tunneling through the double dot

The setup we are considering is shown in Fig. 3.1a. Each dot is tunnel-coupled to a metallic lead via a point contact, forming a series lead-dot-dot-lead setup [for a parallel configuration see Refs. [169] and [170]]. The point contact in lateral structures has a smooth (wave-guide-like) potential, providing a number of lead modes (channels) that can couple to the dot. By constraining the point contact, the lead modes can be pinched off one by one, due to the transverse quantization in the contact region. When the last mode in each point contact is about to be pinched off, the structure shows Coulomb blockade (CB) effect at low temperatures. In this regime, the point contacts can be treated as tunnel junctions, with tunneling amplitudes t_L and t_R , for the left and right dot, respectively. The leads are then single-channel Fermi-liquid leads, which we describe by the Hamiltonian

$$H_{\text{leads}} = \sum_l H_l = \sum_l \sum_{k\sigma} \varepsilon_k c_{lk\sigma}^\dagger c_{lk\sigma}, \quad (3.15)$$

where $c_{lk\sigma}^\dagger$ creates an electron with momentum k (energy ε_k) and spin σ in lead $l = L, R$. The tunneling between the DD and the leads is described by the tunneling Hamiltonian

$$H_T = \sum_l H_T^l = \sum_l \sum_{nk\sigma} (t_{ln} c_{lk\sigma}^\dagger d_{n\sigma} + \text{h.c.}), \quad (3.16)$$

3.3. SEQUENTIAL TUNNELING THROUGH THE DOUBLE DOT

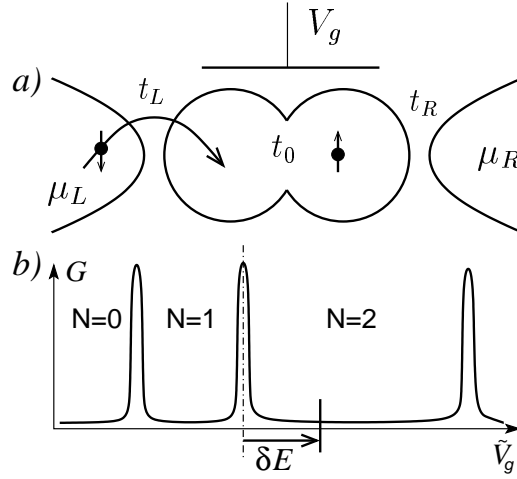


Figure 3.1: (a) Two coupled quantum dots, with the inter-dot tunneling amplitude t_0 , attached to metallic leads at different chemical potentials μ_L and $\mu_R = \mu_L - \Delta\mu$. The tunnel coupling between the dots and leads is characterized at $t_0 = 0$ by the tunneling amplitudes t_L and t_R . (b) A schematic plot of the linear ($\Delta\mu \rightarrow 0$) conductance G through the double dot (DD) as a function of the gate voltage \tilde{V}_g , showing the Coulomb blockade (CB) effect, with sequential-tunneling peaks and CB valleys. The number of electrons contained in the DD, $N = N_1 + N_2$, is fixed in the valleys between the peaks. The position away from the $N = 1, 2$ peak is defined by δE , which takes on negative (positive) values in the $N = 1$ ($N = 2$) CB valley.

with the tunneling amplitudes:

$$t_{L,\pm} = \frac{t_L}{\sqrt{2(1 \pm \mathcal{S})}}, \quad t_{R,\pm} = \pm \frac{t_R}{\sqrt{2(1 \pm \mathcal{S})}}. \quad (3.17)$$

Here, $\mathcal{S} \sim t_0/\hbar\omega_0$ is the overlap integral between the two dots orbital wave functions ($\mathcal{S} = \langle \varphi_L | \varphi_R \rangle$). Formulas (3.17) account for the hybridization of the DD orbitals at $2t_0 \lesssim \hbar\omega_0$ with the accuracy of the method of molecular orbitals (Hund-Mulliken method). The tunnel-coupling to the leads broadens the DD levels $n = \pm$, introducing the level width $\Gamma_n = \pi\nu(|t_{Ln}|^2 + |t_{Rn}|^2)$, where ν is the lead density of states (at the Fermi energy) per spin. For later convenience, we also use the notations: $\Gamma_l = \pi\nu|t_l|^2$, with $l = L, R$, and $\eta = |t_R|^2/|t_L|^2$. We assume $\Gamma_{\pm} \lesssim k_B T$, where T is the temperature, and k_B the Boltzmann constant.

The usual CB stability diagram [16, 76] for a DD represents a honeycomb structure of increased linear conductance plotted versus V_{g1}, V_{g2} — the gate voltages controlling dot 1 and 2, respectively. We are interested in the case when the two dots are similar, and therefore consider the diagonal of the stability diagram, $V_{g1} = V_{g2} = V_g$, in the vicinity of (1,1)-(1,0)-(0,1) triple point. However, we will be interested also in large applied bias voltages $\Delta\mu = \mu_L - \mu_R$, assuming that the bias voltage drop occurs on the structure as a whole and does not shift it away from the diagonal of the

stability diagram. The bias voltage $\Delta\mu$ can be applied in different ways, e.g. equally distributed between the left and right leads, or applied to one of the leads alone. To cover all possibilities, we assume the chemical potentials of the left and right leads to be respectively equal to:

$$\begin{aligned}\mu_L &= \mu + \Delta\mu_L, \\ \mu_R &= \mu - \Delta\mu_R,\end{aligned}\tag{3.18}$$

with $\Delta\mu_L + \Delta\mu_R = \Delta\mu$, and the bias-asymmetry parameter: $a = \Delta\mu_R/\Delta\mu_L$. The position in the CB is controlled by the common gate voltage V_g . In the linear regime ($\Delta\mu \rightarrow 0$) the conductance G as a function of V_g shows peaks at the degeneracy points of the chemical potential in the DD and in the leads, see Fig. 3.1*b*. We focus on the sequential tunneling peak, where the number of electrons in the DD fluctuates between $N = 1$ and $N = 2$. The degeneracy condition is given by: $E(2) - E(1) = \mu$, where $E(N)$ is the ground state energy of the DD with N electrons. We assume the singlet (3.9) to be the ground state for $N = 2$; therefore, $E(2) = E_{|S\rangle}$ and $E(1) = E_{|+, \sigma\rangle}$. The position in a CB valley is characterized by the addition/extraction energy: $E_{\pm}(N) = E(N \pm 1) - E(N) \mp \mu$. The distance away from the peak (in the scale of $\tilde{V}_g \propto V_g$) is measured by

$$\delta E = E_{|+, \sigma\rangle} - E_{|S\rangle} + \mu.\tag{3.19}$$

Positive (negative) values of δE correspond to positions in the $N = 2$ ($N = 1$) CB valley. The size of the $N = 1$ CB valley (distance between its 1st and 2nd CB peaks) is given by $E_+(1) + E_-(1) = U_{12} + 2t_0 - J$. The size of the $N = 2$ CB valley is of order of U_H ($U_H > U_{12}$).

The sequential tunneling through the DD is described by the golden rule rates:

$$W_{Mm}^l = \frac{2\pi}{\hbar} \sum_{\bar{n}, k\sigma} \left| \langle M; \bar{n} | c_{lk\sigma}^\dagger H_T^l | m; \bar{n} \rangle \right|^2 \delta(\varepsilon_k - E_{Mm}) \rho_{l, \bar{n}}^B,\tag{3.20}$$

$$W_{mM}^l = \frac{2\pi}{\hbar} \sum_{\bar{n}, k\sigma} \left| \langle m; \bar{n} | c_{lk\sigma} H_T^l | M; \bar{n} \rangle \right|^2 \delta(\varepsilon_k + E_{Mm}) \rho_{l, \bar{n}}^B,\tag{3.21}$$

where m stands for one of the states (3.1), and M for one of the states (3.2); W_{Mm}^l is the probability rate for the DD transition from m to M by exchanging an electron with the lead l ; $E_{Mm} = E_M - E_m$ with E_M, E_m being one of (3.7)–(3.10). The averaging in (3.20) and (3.21) is performed over the Fermi-sea states $|\bar{n}\rangle$ with the grand canonical density matrix $\rho_l^B = Z_l^{-1} \exp(-K_l/k_B T)$, where $Z_l = \text{Tr}_l \exp(-K_l/k_B T)$, $K_l = H_l - \mu_l \sum_{k\sigma} c_{lk\sigma}^\dagger c_{lk\sigma}$, and T is the temperature (we set $k_B = 1$ in what follows). In (3.20) and (3.21), we use the notations: $\rho_{l, \bar{n}}^B = \langle \bar{n} | \rho_l^B | \bar{n} \rangle$ and $|m; \bar{n}\rangle = |m\rangle |\bar{n}\rangle$. As a consequence of the thermal equilibrium in the leads, the rates (3.20) and (3.21) are related by the detailed-balance formula:

$$W_{mM}^l = W_{Mm}^l \exp[(E_{Mm} - \mu_l)/T].\tag{3.22}$$

3.3. SEQUENTIAL TUNNELING THROUGH THE DOUBLE DOT

We provide explicit expressions for the rates W_{Mm}^l in Appendix B.

It is convenient for the calculation to trace out the spin degeneracy in (3.1) and of the triplets Eq. (3.2). We map the degenerate levels onto non-degenerate ones, using the following replacement² [170]

$$\frac{1}{N_I} \sum_{\substack{i \in I \\ f \in F}} W_{fi} \rightarrow W_{FI}, \quad (3.23)$$

where N_I is the degeneracy of level I . Thus, from here on, we deal with 4 non-degenerate levels, denoted as $|+\rangle$, $|-\rangle$, $|S\rangle$, $|T\rangle$. The transition rates between these states, for $l = L$, are:

$$\begin{aligned} W_{S,+}^L &= \frac{2\pi}{\hbar} \nu \frac{|t_{L,+}|^2}{1+\phi^2} f(-\delta E - \Delta\mu_L), \\ W_{+,S}^L &= 2 \frac{2\pi}{\hbar} \nu \frac{|t_{L,+}|^2}{1+\phi^2} f(\delta E + \Delta\mu_L), \\ W_{S,-}^L &= \frac{2\pi}{\hbar} \nu \frac{\phi^2 |t_{L,-}|^2}{1+\phi^2} f(-\delta E - 2t_0 - \Delta\mu_L), \\ W_{-,S}^L &= 2 \frac{2\pi}{\hbar} \nu \frac{\phi^2 |t_{L,-}|^2}{1+\phi^2} f(\delta E + 2t_0 + \Delta\mu_L), \\ W_{T,+}^L &= \frac{3}{2} \frac{2\pi}{\hbar} \nu |t_{L,-}|^2 f(J - \delta E - \Delta\mu_L), \\ W_{+,T}^L &= \frac{2\pi}{\hbar} \nu |t_{L,-}|^2 f(-J + \delta E + \Delta\mu_L), \\ W_{T,-}^L &= \frac{3}{2} \frac{2\pi}{\hbar} \nu |t_{L,+}|^2 f(J - \delta E - 2t_0 - \Delta\mu_L), \\ W_{-,T}^L &= \frac{2\pi}{\hbar} \nu |t_{L,+}|^2 f(-J + \delta E + 2t_0 + \Delta\mu_L). \end{aligned} \quad (3.24)$$

Expressions for $l = R$ are obtained from above by substituting $L \rightarrow R$ and $\Delta\mu_L \rightarrow -\Delta\mu_R$. Here, $f(E) = 1/[1 + \exp(E/T)]$ is the Fermi function.

3.3.1 Master equation

Next, we use the rates (3.24) to calculate the probability ρ_p of finding the DD in a given energy level p , with $p \in \{|+\rangle, |-\rangle, |S\rangle, |T\rangle\}$. We apply the master equation approach, assuming for the temperature $T \gg \Gamma_{\pm}$. Thus, the population probability ρ_p satisfies the following equation

$$\dot{\rho}_p = \sum_{p'} (W_{pp'} \rho_{p'} - W_{p'p} \rho_p), \quad (3.25)$$

²This replacement is specific for the case when the population probability of a degenerate level is equally shared between its sub-levels.

with $W_{pp'}$ being the rate for the DD to transit from p' to p . In the stationary limit ($\dot{\rho} = 0$), we obtain explicitly

$$\begin{aligned} (W_{S,+} + W_{T,+}) \rho_+ &= W_{+,S} \rho_S + W_{+,T} \rho_T, \\ (W_{S,-} + W_{T,-}) \rho_- &= W_{-,S} \rho_S + W_{-,T} \rho_T, \\ (W_{+,S} + W_{-,S}) \rho_S &= W_{S,+} \rho_+ + W_{S,-} \rho_-, \\ (W_{+,T} + W_{-,T}) \rho_T &= W_{T,+} \rho_+ + W_{T,-} \rho_-, \end{aligned} \quad (3.26)$$

where we used the notation $W_{pp'} = W_{pp'}^L + W_{pp'}^R$. Only three of the equations (3.26) are linearly independent. Choosing any three of them, and using the normalization condition

$$\rho_+ + \rho_- + \rho_S + \rho_T = 1, \quad (3.27)$$

one can find the solution for ρ_p . However, it is convenient for the further discussion to describe the non-equilibrium stationary state in the DD by the following balance ratios:

$$\tau = \frac{\rho_S + \rho_T}{\rho_+ + \rho_-}, \quad (3.28)$$

$$\beta = \rho_T / \rho_S, \quad (3.29)$$

$$\gamma = \rho_- / \rho_+, \quad (3.30)$$

which give the population probability ρ_p of the DD states as

$$\begin{aligned} \rho_+ &= \frac{1}{(1 + \tau)(1 + \gamma)}, & \rho_- &= \frac{\gamma}{(1 + \tau)(1 + \gamma)}, \\ \rho_S &= \frac{\tau}{(1 + \tau)(1 + \beta)}, & \rho_T &= \frac{\tau\beta}{(1 + \tau)(1 + \beta)}. \end{aligned} \quad (3.31)$$

Expressions for τ , β , γ are given in Appendix B. In the linear bias regime, the DD is in thermodynamic equilibrium, and the occupation of the states is determined by the temperature T . For this regime, we find the equilibrium values:

$$\beta^T = 3 \exp(-J/T), \quad \gamma^T = \exp(-2t_0/T), \quad (3.32)$$

$$\tau^T = \frac{(1 + \beta^T) \exp(\delta E/T)}{2(1 + \gamma^T)}. \quad (3.33)$$

In the non-linear regime, the deviation from these equilibrium values due to the applied bias describe the *heating effect* in the DD. To simplify our further considerations we make the following realistic assumptions:

$$a) \quad |\delta E| > 2t_0 > J > 0, \quad (3.34)$$

$$b) \quad T \ll J, \quad 2t_0 - J, \quad |\delta E| - 2t_0. \quad (3.35)$$

For definiteness, we also assume a symmetric bias situation with $\Delta\mu_L = \Delta\mu_R = \Delta\mu/2$. Next, we consider the two following cases.

3.3. SEQUENTIAL TUNNELING THROUGH THE DOUBLE DOT

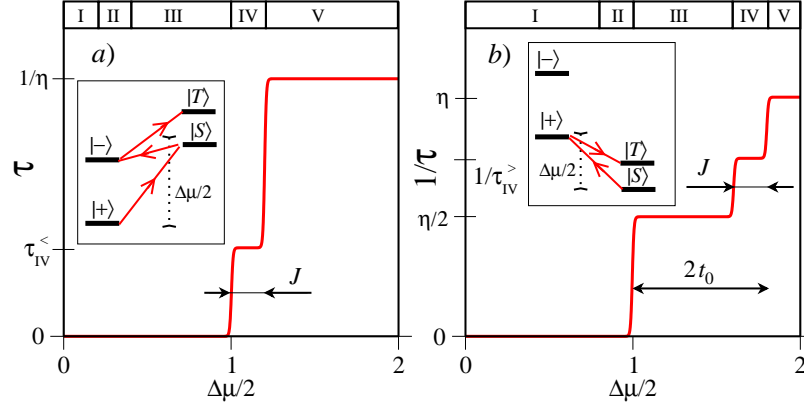


Figure 3.2: (a) The ratio $\tau = (\rho_S + \rho_T)/(\rho_+ + \rho_-)$ plotted versus $\Delta\mu/2 = \Delta\mu_{L,R}$ for $\delta E < 0$. (b) The inverse ratio $1/\tau$ versus $\Delta\mu/2$ for $\delta E > 0$. For both figures, we choose the units of energy such that $|\delta E| = 1$. We use the following parameters: $2t_0 = 0.8$, $J = 0.2$, $\mathcal{S} = 0.5$, and $\phi = 0.4$. The grids above the figures (a) and (b) show the division into the intervals (3.36) and (3.43), *resp.* The insets show the transitions which get switched on at $\Delta\mu/2 = |\delta E|$.

Sequential tunneling on the $N = 1$ CB valley side ($\delta E < 0$).

As mentioned in Sec. 3.2, the $N = 1$ CB valley has the size $U_{12} + 2t_0 - J$. We can estimate U_{12} for a lateral structure from the Hund-Mulliken method, neglecting screening effects from the top gates. We obtain³ $U_{12} \approx 2.7$ meV for GaAs quantum dots with $\hbar\omega_0 = 3$ meV coupled so that the distance between the dots centers is $\simeq 2a_B$, with $a_B = \sqrt{\hbar/m\omega_0}$ being the Bohr radius of one dot. For the on-site Coulomb repulsion we obtain $U_H \approx 4.5$ meV. The screening from the top gates, which depends on the design of the structure and on the thickness of the insulating layer between the 2DEG and top gates, reduces, in practice, the inter-dot Coulomb repulsion as compared to the on-site one. However, we still assume a sizable U_{12} such that $U_{12} \gtrsim 2t_0$, and thus we can neglect the contribution from the $N = 0, 1$ sequential-tunneling peak at $\Delta\mu/2 \simeq |\delta E| + J < (U_{12} + 2t_0 - J)/2$.

For further consideration it is convenient to divide the range of the applied bias into the following intervals:

- I. $0 < \Delta\mu/2 < |\delta E| - 2t_0$,
- II. $|\delta E| - 2t_0 < \Delta\mu/2 < |\delta E| - 2t_0 + J$,
- III. $|\delta E| - 2t_0 + J < \Delta\mu/2 < |\delta E|$,
- IV. $|\delta E| < \Delta\mu/2 < |\delta E| + J$,
- V. $|\delta E| + J < \Delta\mu/2$.

(3.36)

At temperatures satisfying (3.35), the solution of the master equation (3.26) is constant within each of these intervals. We plot the quantities (3.28), (3.29) and (3.30)

³ $V_- \equiv U_{12}$ in Ref. [59].

versus $\Delta\mu/2$ in Figs. 3.2a, 3.3a and 3.4a, respectively. The units of energy are chosen such that $|\delta E| = 1$. Fig. 3.2a shows the balance between the DD being in the sector with $N = 2$ electrons and the DD being in the sector with $N = 1$ electrons. At small bias voltages (I, II and III), the occupation of the $N = 2$ sector is suppressed as $\exp[-(|\delta E| - \Delta\mu/2)/T]$, because of the Coulomb blockade in the $N = 1$ valley. At the bias voltage $\Delta\mu/2 = |\delta E|$, the left lead chemical potential μ_L reaches the value of the DD $N = 2$ chemical potential. At this point the following sequence of transitions becomes possible:

$$|+\rangle \rightleftharpoons |S\rangle \rightleftharpoons |-\rangle \rightleftharpoons |T\rangle, \quad (3.37)$$

which changes the population probabilities ρ_p in the DD. It is important to note the difference between the intervals IV and V. In the interval V we get universal results: $\tau = 1/\eta$, $\beta = 3$, and $\gamma = 1$. This corresponds to setting $T \rightarrow \infty$ in Eq. (3.32) for β and γ , and recognizing that $(\rho_S + \rho_T) \sim \Gamma_L$ and $(\rho_+ + \rho_-) \sim \Gamma_R$, which yields $\tau = \Gamma_L/\Gamma_R = 1/\eta$ according to Eq. (3.28). In contrast, in the interval IV the plateau values of τ , β and γ depend on the DD parameters. For example, in Fig. 3.2a this non-universal value of τ is denoted by $\tau_{IV}^<$, and we find that

$$1/\tau_{IV}^< = \eta \left[1 + \frac{1 + 1/\phi^2 + 2\chi(2 + \phi^2)}{1 + 1/\phi^2 + 2\chi/3 + 8\eta/3(1 + \eta)} \right], \quad (3.38)$$

where $\chi = \Gamma_-/\Gamma_+ = (1 + \mathcal{S})/(1 - \mathcal{S})$. This ‘‘universality versus non-universality’’ depends on the way the sequence (3.37) is closed. For the interval IV, only the transition $|T\rangle \rightarrow |+\rangle$ is allowed, whereas the reverse transition is forbidden by energy conservation. For the interval V, however, the sequence is closed by $|T\rangle \rightleftharpoons |+\rangle$. We can express the fact that, for the regime on the plateau V, the results are universal by formulating a principle of detailed balance. For the rates entering the master equation (3.26), such a *non-equilibrium detailed-balance principle* can be written as follows

$$W_{S,\pm} = \frac{1}{2\eta} W_{\pm,S}, \quad (3.39)$$

$$W_{T,\pm} = \frac{3}{2\eta} W_{\pm,T}. \quad (3.40)$$

This suffices to obtain the universal result for τ , β and γ from the master equation (3.26).

For the Fig. 3.3a, we find that β changes from zero to a value $\beta_{IV}^<$ at the border between the intervals II and III. This is related to the fact that the transition $|S\rangle \rightarrow |-\rangle \rightarrow |T\rangle$ could occur, provided there was a non-vanishing population in the $N = 2$ sector. But since $\tau = 0$ for this interval, see Fig. 3.2a, this step-like change in β will not be observed in physical quantities. Interestingly, when the $N = 2$ sector acquires non-zero population at the border between the intervals III and IV, the ratio $\beta = \rho_T/\rho_S$ stays constant as a function of $\Delta\mu$ and T , for T satisfying (3.35). The value of $\beta_{IV}^<$ is given by

$$1/\beta_{IV}^< = \frac{1}{3} \left[1 + (1 + 1/\eta) \left(\chi + \frac{3}{2}(1 + 1/\phi^2) \right) \right], \quad (3.41)$$

3.3. SEQUENTIAL TUNNELING THROUGH THE DOUBLE DOT

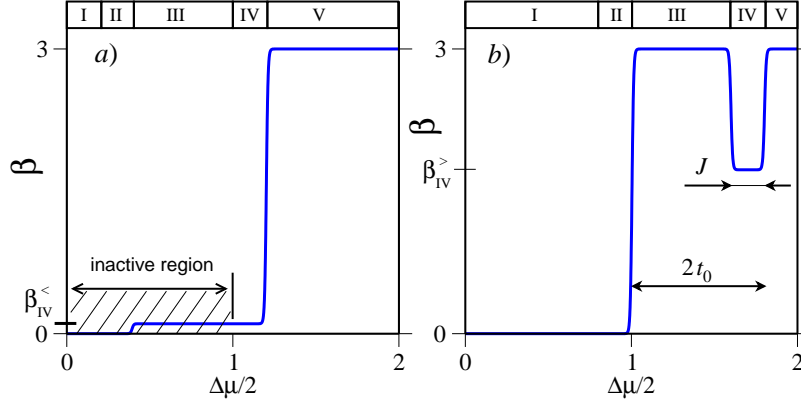


Figure 3.3: With the same parameters as in Fig. 3.2, the ratio $\beta = \rho_T / \rho_S$ versus $\Delta\mu/2$ for: (a) $\delta E < 0$ and (b) $\delta E > 0$. The shaded area in (a) shows the inactive region with no population of the $N = 2$ sector, see Fig. 3.2a. We note that this region can be active if a combined effect of sequential tunneling and cotunneling is considered, see Sec. 3.6.

and that of $\gamma_{IV}^<$, by

$$1/\gamma_{IV}^< = 1 + \frac{3}{2} \frac{1 + 1/\phi^2 + \chi(1 + \phi^2)}{\chi + \eta/(1 + \eta)}. \quad (3.42)$$

The population probability of each of the levels can be obtained from the formulas (3.31). We plot ρ_+ , ρ_- , ρ_S , and ρ_T on Fig. 3.5a for the above discussed situation.

Sequential tunneling on the $N = 2$ CB valley side ($\delta E > 0$).

Here, the relevant intervals of applied bias are:

$$\begin{aligned} \text{I.} & \quad 0 < \Delta\mu/2 < \delta E - J, \\ \text{II.} & \quad \delta E - J < \Delta\mu/2 < \delta E, \\ \text{III.} & \quad \delta E < \Delta\mu/2 < \delta E + 2t_0 - J, \\ \text{IV.} & \quad \delta E + 2t_0 - J < \Delta\mu/2 < \delta E + 2t_0, \\ \text{V.} & \quad \delta E + 2t_0 < \Delta\mu/2, \end{aligned} \quad (3.43)$$

and we assume $\delta E + 2t_0 < U_H/2$ such that the DD is not populated with 3 electrons while raising μ_L . We plot $1/\tau$, β and γ versus $\Delta\mu/2$ in Figs. 3.2b, 3.3b and 3.4b, respectively. At $\Delta\mu = 0$ the DD is in the $N = 2$ CB valley and as in the previous case a sizable change in the DD population occurs when $\Delta\mu/2 = \delta E$. At this point the chemical potential μ_R in the right lead is low enough such that an electron from the DD with $N = 2$ can occupy an empty place above the Fermi sea in the right lead. The following sequence of transition is immediately activated

$$|S\rangle \rightleftharpoons |+\rangle \rightleftharpoons |T\rangle, \quad (3.44)$$

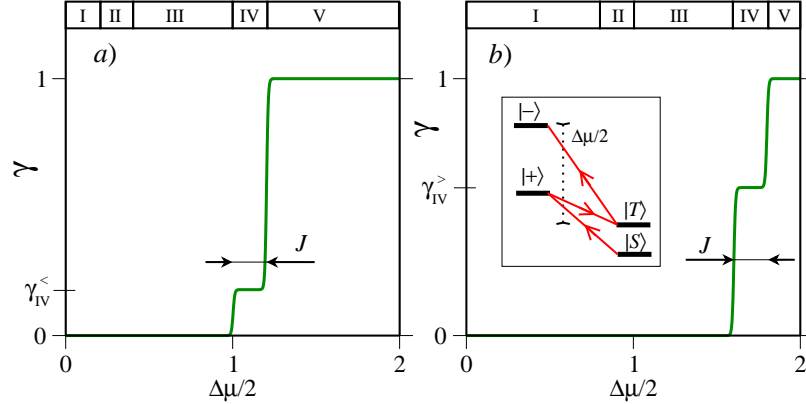


Figure 3.4: With the same parameters as in Fig. 3.2, the ratio $\gamma = \rho_-/\rho_+$ versus $\Delta\mu/2$ for: (a) $\delta E < 0$ and (b) $\delta E > 0$. The inset in (b) shows the sequence of transition which takes place at $\Delta\mu/2 \geq \delta E + 2t_0 - J$ (compare with the inset in Fig. 3.2b).

which yields universal values: $\tau = 2/\eta$, $\beta = 3$ and $\gamma = 0$, in the interval III. The corresponding principle of detailed balance is obtained if we disregard the level $|-\rangle$ in the master equation (3.26) and use (3.39) and (3.40) with $\pm \rightarrow +$. The left-to-right processes of the sequence (3.44) are illustrated in the inset to Fig. 3.2b. Yet two other changes in $1/\tau$ occur at $\Delta\mu = \delta E + 2t_0 - J$ and $\Delta\mu = \delta E + 2t_0$, see Fig. 3.2b. The value of $1/\tau$ on the plateau IV in Fig. 3.2b is given by

$$\tau_{\text{IV}}^> = \frac{1}{\eta} \left[1 + \frac{\chi(7 + 3\phi^2)/4 - 1/2}{3(1 + 1/\phi^2)/(1 + \eta) + 1 + \chi} \right]. \quad (3.45)$$

Fig. 3.3b shows that, in the interval IV, the triplet level loses its population probability relative to the singlet level, with the value of β being given by

$$1/\beta_{\text{IV}}^> = \frac{1}{3} \left[1 + \frac{2 + 3\chi(1 + \phi^2)}{2\chi + 3(1 + 1/\phi^2)/(1 + \eta)} \right]. \quad (3.46)$$

Just similarly to Sec. 3.3.1, we have here the following sequence of transitions

$$|S\rangle \rightleftharpoons |+\rangle \rightleftharpoons |T\rangle \rightleftharpoons |-\rangle, \quad (3.47)$$

which is closed in the interval IV by $|-\rangle \rightarrow |S\rangle$, and in the interval V by $|-\rangle \rightleftharpoons |S\rangle$. The latter results in $\tau = 1/\eta$, $\beta = 3$, and $\gamma = 1$, which is identical with the universal result in Sec. 3.3.1. The detailed balance for this case is also given by Eqs. (3.39) and (3.40). Finally, the non-universal value of γ in Fig. 3.4 is given by

$$1/\gamma_{\text{IV}}^> = 1 + \frac{2}{3} \frac{(1 + \eta)(1 + \chi)}{1 + 1/\phi^2}, \quad (3.48)$$

and we present each of the population probabilities ρ_p for the considered case in Fig. 3.5b.

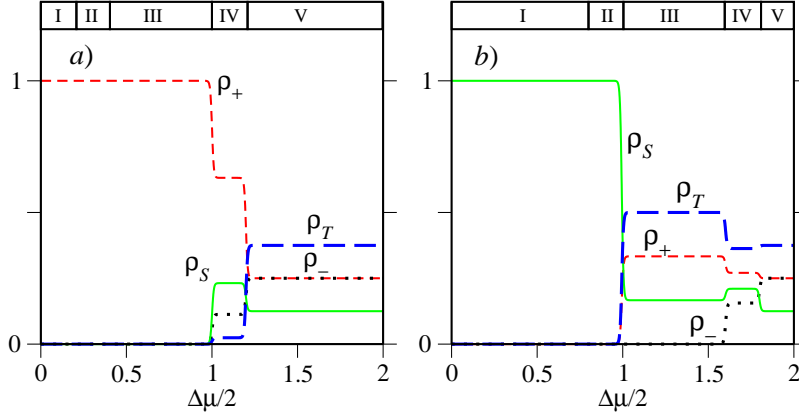


Figure 3.5: The population probabilities ρ_p versus $\Delta\mu/2$ calculated from Eqs. (3.31) with the values of τ , β and γ given by respectively Figs. 3.2, 3.3 and 3.4 for: (a) $\delta E = -1$ and (b) $\delta E = 1$.

3.3.2 Sequential tunneling current

Next, we show that the heating effects considered above show up in the transport spectroscopy. For this, we calculate the average current I through the DD at an applied bias voltage $\Delta\mu$. We consider both the $N = 1$ ($\delta E < 0$) and $N = 2$ ($\delta E > 0$) CB valley sides, as considered in Sec. 3.3.1. We show that the steps in the population probabilities ρ_p shown in Fig. 3.5 result in peaks in $dI/d\Delta\mu$ vs $\Delta\mu$.

The electron (particle) current, flowing from the DD into the lead l , reads

$$I^l = (W_{+,S}^l + W_{-,S}^l) \rho_S + (W_{+,T}^l + W_{-,T}^l) \rho_T - (W_{S,+}^l + W_{T,+}^l) \rho_+ - (W_{S,-}^l + W_{T,-}^l) \rho_-. \quad (3.49)$$

In the stationary regime described by (3.26), one has $I^L = -I^R \equiv I/|e|$. The differential conductance $G = e dI/d\Delta\mu$ as a function of δE and $\Delta\mu$ can be evaluated for different regimes of interest.

For the regime studied in Sec. 3.3.1, we can use a simplified formula for the current, namely

$$I/I_0^R = \frac{2}{1+\phi^2} \left(\frac{1}{1+\mathcal{S}} + \frac{\phi^2}{1-\mathcal{S}} \right) \rho_S + \frac{2}{1-\mathcal{S}^2} \rho_T, \quad (3.50)$$

where $I_0^R = |e|\Gamma_R/\hbar$. We plot G vs $\Delta\mu/2$ for $\delta E = -1$ in Fig. 3.6a. The main peak at $\Delta\mu/2 = |\delta E| = 1$ acquires a satellite peak at $\Delta\mu/2 = |\delta E| + J$, which for the given parameters has a larger amplitude than the main peak. The origin of the satellite peak is closely related to the heating effects discussed in Sec. 3.3.1. Eq. (3.50) shows that the changes in ρ_S and ρ_T as functions of $\Delta\mu$ are directly reflected in the current I .

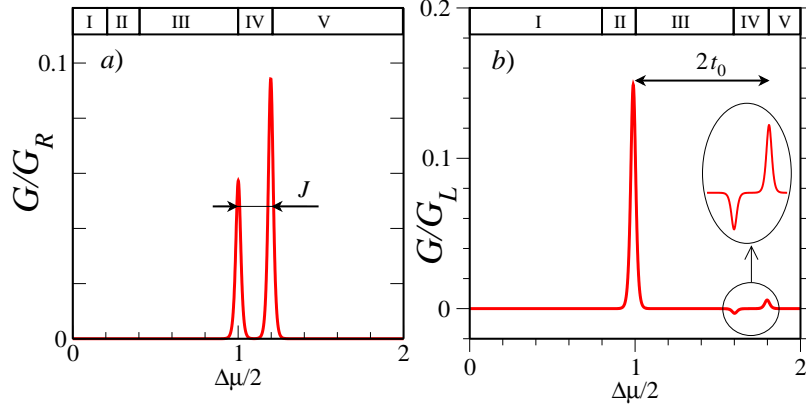


Figure 3.6: The bias dependence of the differential conductance G for: (a) $\delta E = -1$ and (b) $\delta E = 1$. The ordinate axis is scaled by $G_l = e^2\pi\nu|t_l|^2/\hbar T$. We use the same parameters as in Fig. 3.2 and with $t_L = t_R$ ($G_L = G_R$).

For the regime studied in Sec. 3.3.1, we can use a simplified formula for the current, namely

$$I/I_0^L = \left(\frac{1}{1+\mathcal{S}} \frac{1}{1+\phi^2} + \frac{3/2}{1-\mathcal{S}} \right) \rho_+ + \left(\frac{1}{1-\mathcal{S}} \frac{\phi^2}{1+\phi^2} + \frac{3/2}{1+\mathcal{S}} \right) \rho_-, \quad (3.51)$$

where $I_0^L = |e|\Gamma_L/\hbar$. We plot G vs $\Delta\mu/2$ for $\delta E = 1$ in Fig. 3.6b. The main peak at $\Delta\mu/2 = \delta E = 1$ acquires two satellite peaks at $\Delta\mu/2 = |\delta E| + 2t_0 - J$ and $\Delta\mu/2 = |\delta E| + 2t_0$. Interestingly, the first satellite peak has *negative* differential conductance for the given parameter values. Eq. (3.51) shows that the current I reflects the changes in ρ_+ and ρ_- as functions of $\Delta\mu$, discussed in Sec. 3.3.1. The negative value of G is due to the decrease of ρ_+ when going from the interval III to the interval IV (see Fig. 3.5b) and different tunnel coupling to the $n = +$ and $n = -$ energy levels. At the very origin of negative G lies the Coulomb interaction in the DD, which allows us to consider a truncated Hilbert space, namely, consisting of the states (3.1) and (3.2).

Using Eqs. (3.49) and (3.31), we calculate the differential conductance G for the whole range of variables δE and $\Delta\mu$. Fig. 3.7 shows a gray-scale plot of G for the case of symmetric biasing: $\Delta\mu_L = \Delta\mu_R = \Delta\mu/2$. The gray color corresponds to $G = 0$, the white (black) color corresponds to positive (negative) values of G . We note that the black line on Fig. 3.7 terminates at a satellite line ($\delta E = -t_0 + J$, $\Delta\mu/2 = t_0$), unlike the other two white (satellite) lines, which terminate at the main sequential-tunneling peaks. This can be attributed to the origin of the black line: change in the rate for *excited state* to *excited state* transition, see $|T\rangle \rightarrow |-\rangle$ in the inset of Fig. 3.4b (cf. inset of Fig. 3.2b). For $\Delta\mu/2 < t_0$, the transition $|T\rangle \rightarrow |-\rangle$ is blocked due to energy conservation. We note that “excited state to

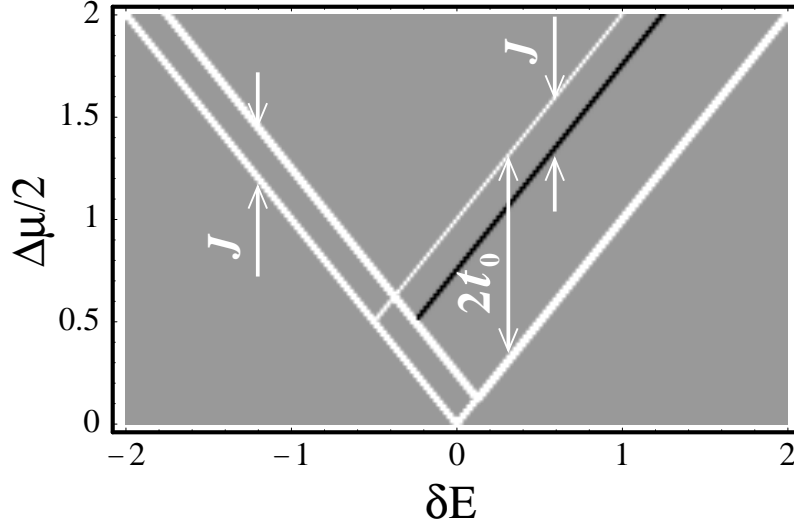


Figure 3.7: A gray scale plot of G versus δE and $\Delta\mu/2 = \Delta\mu_L = \Delta\mu_R$. The white (black) color corresponds to positive (negative) values of G ; gray stands for $G = 0$. Here, we use: $2t_0 = 1$, $J = 0.25$, $\mathcal{S} = 0.6$, $\phi = 0.3$ and $\eta = 1$.

excited state” sequential-tunneling satellite lines have been observed experimentally for single dots [85]. Finally, in Fig. 3.8, we present a gray-scale plot of G for the case of asymmetric biasing: $\Delta\mu_L = \Delta\mu$ and $\Delta\mu_R = 0$.

3.3.3 Charge detection via a QPC

Using quantum point contacts (QPCs) placed in the neighborhood of the quantum dots provides additional information about the DD [70]. Here, we consider the average charge on the DD, $\langle N \rangle = \rho_+ + \rho_- + 2(\rho_S + \rho_T)$. With the help of Eqs. (3.28) and (3.27) we relate $\langle N \rangle$ to the parameter τ as follows

$$\langle N \rangle = 1 + \frac{\tau}{1 + \tau}. \quad (3.52)$$

At a large bias voltage, corresponding to, *e.g.*, the interval V in Sec. 3.3.1, see Eq. (3.36), the DD occupation number fluctuates between 1 and 2, being on average $\langle N \rangle = 1 + 1/(1 + \eta)$, for $\Delta\mu > 0$. This relation can be used to find the asymmetry parameter $\eta = |t_R|^2/|t_L|^2$. In the case of symmetric coupling to the leads one has $\langle N \rangle = 1.5$. In the interval IV of Sec. 3.3.1, the average $\langle N \rangle$ assumes a non-universal value, determined by Eq. (3.38). This result can, in principle, be used to extract the overlap integral \mathcal{S} [or equivalently $\chi = \Gamma_-/\Gamma_+ = (1 + \mathcal{S})/(1 - \mathcal{S})$] in the case when the parameter ϕ is known, cf. Sec. 3.5. For symmetric coupling to the leads ($\eta = 1$) and in the limit of weakly coupled dots ($\phi \rightarrow 1$, $\mathcal{S} \rightarrow 0$), Eq. (3.38) yields $\tau = 1/3$, or equivalently $\langle N \rangle = 1.25$. This can be distinguished from the value $\langle N \rangle = 1.5$ in the interval V with the available sensitivity of QPCs, which is $\simeq 0.1 e$, see Ref. [70].

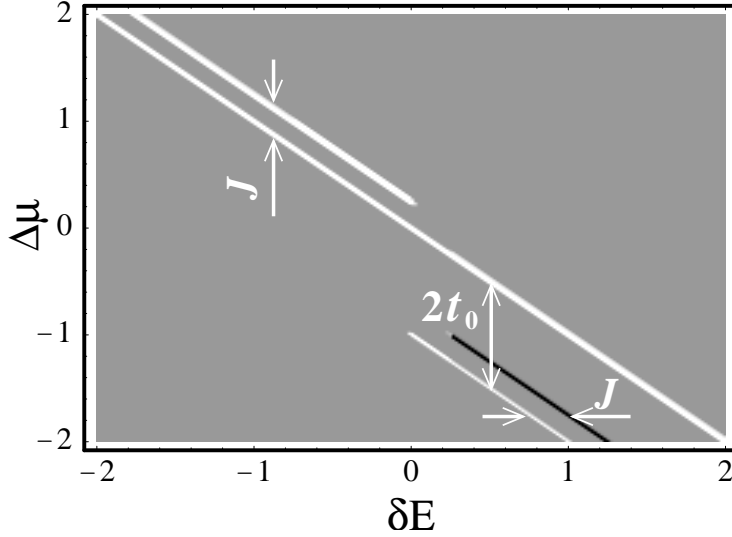


Figure 3.8: The same as in Fig. 3.7, but for asymmetric biasing: $\Delta\mu = \Delta\mu_L$, $\Delta\mu_R = 0$.

Thus, we conclude that the satellite peaks obtained for the differential conductance G in Sec. 3.3.2 (Figs. 3.7 and 3.8) can be also observed using QPCs.⁴ Next, we discuss the back action of the QPC on the DD.

The QPC detects the charge of the quantum dot via the electrostatic potential the dot induces in the QPC region. We consider the DD and one QPC close to the right dot. The term responsible for relaxation of the DD states is as follows⁵

$$\delta H_{QPC} = -\frac{1}{2}\delta\varepsilon(t) \sum_{n\sigma} d_{n,\sigma}^\dagger d_{-n,\sigma}, \quad (3.53)$$

where $\delta\varepsilon(t)$ is the fluctuating field of the QPC, with $\overline{\delta\varepsilon(t)} = 0$ (bar denotes average over the QPC degrees of freedom). The relaxation rate is given by [123]

$$W_{fi} = \frac{1}{4\hbar^2} \left| \langle f | \sum_{n\sigma} d_{n,\sigma}^\dagger d_{-n,\sigma} | i \rangle \right|^2 J(E_{if}/\hbar), \quad (3.54)$$

where $E_{if} = E_i - E_f$ is the transition energy. It follows from Eq. (3.54) that the QPC can induce relaxation only between the states $|+, \sigma\rangle$ and $|-, \sigma\rangle$; all other transitions are forbidden due to the spin and charge conservation in the Hamiltonian (3.53). The spectral function $J(\omega)$ is defined as follows

$$J(\omega) = \int_{-\infty}^{\infty} \overline{\delta\varepsilon(0)\delta\varepsilon(t)} e^{-i\omega t} dt. \quad (3.55)$$

⁴In order to extract χ , more sensitive measurements of charge are required. For the interval IV of Sec. 3.3.1, we find that $\delta\langle N \rangle \simeq (7/96)\delta\chi$, in the limit of weakly coupled dots ($\phi \simeq \chi \simeq 1$) and $\eta = 1$. Here, $\delta\langle N \rangle$ and $\delta\chi$ are the accuracies of measuring $\langle N \rangle$ and χ , *resp.*

⁵This term, Eq. (3.53), can be obtained from $H = \delta\varepsilon(t) \sum_{\sigma} \tilde{d}_{R,\sigma}^\dagger \tilde{d}_{R,\sigma}$, with the help of Eq. (A.1). More rigorously, the left dot counterpart should also be included, however, it merely redefines $\lambda_{l'}$ of Eq. (3.56).

3.4. COTUNNELING IN THE $N = 1$ COULOMB BLOCKADE VALLEY

The QPC field, $\delta\varepsilon(t) = \varepsilon(t) - \overline{\varepsilon(t)}$, is proportional to the charge density at the QPC,

$$\varepsilon(t) = \sum_{ll'kk'\sigma} \lambda_{ll'} e^{i(\tilde{\mu}_l - \tilde{\mu}_{l'})t} \tilde{c}_{lk\sigma}^\dagger(t) \tilde{c}_{l'k'\sigma}(t), \quad (3.56)$$

where the indices $l, l' = \mathcal{L}, \mathcal{R}$ denote the two leads of the QPC (not to be confused with the DD leads), $\tilde{\mu}_l$ is the chemical potential of lead l , $\tilde{\mu}_{\mathcal{L}} = \tilde{\mu}_{\mathcal{R}} + \Delta\tilde{\mu}$, and $\tilde{c}_{lk\sigma}^\dagger(t)$ creates a QPC electron. For $\omega, \Delta\mu/\hbar < \omega_c$, we have

$$J(\omega) = 4\pi\hbar\nu^2 (\lambda_{\mathcal{L}\mathcal{L}}^2 + \lambda_{\mathcal{R}\mathcal{R}}^2) \Theta(\hbar\omega) + 4\pi\hbar\nu^2 \lambda_{\mathcal{L}\mathcal{R}}^2 [\Theta(\hbar\omega + \Delta\tilde{\mu}) + \Theta(\hbar\omega - \Delta\tilde{\mu})], \quad (3.57)$$

where $\Theta(E) = E/(1 - \exp(-E/T))$, ν is the density of states per spin in the QPC, and ω_c is the high-frequency cutoff (order of bandwidth). Formula (3.54) is valid for weak coupling, *i.e.* $\nu\lambda_{ll'} \ll 1$. At $\hbar\omega, T \ll \Delta\tilde{\mu}$, Eq. (3.57) reduces to $J(0) = 4\pi\hbar\nu^2 \lambda_{\mathcal{L}\mathcal{R}}^2 |\Delta\tilde{\mu}|$, which formally coincides with $J(0) = \hbar\Gamma_d$ in the weak coupling limit, where Γ_d is the QPC decoherence rate for a single dot [171, 172]. We summarize here by writing down the non-zero relaxation rates due to the QPC:

$$\tilde{W}_{+-} = \frac{1}{4\hbar^2} J(2t_0/\hbar), \quad (3.58)$$

$$\tilde{W}_{-+} = \frac{1}{4\hbar^2} J(-2t_0/\hbar), \quad (3.59)$$

where we have already summed over the spin degeneracy, using the rule (3.23). We note that, for $|\Delta\tilde{\mu}| < 2t_0$, the rate \tilde{W}_{-+} is exponentially suppressed at low temperatures. The rates (3.58) and (3.59) describe relaxation of the DD due to, respectively, *excitation* and *annihilation* of an electron-hole pair in the QPC.

Including the rate \tilde{W}_{+-} into the balance equations (3.26) yields a correction, δN , to the average occupation number on the DD, $\langle N' \rangle = \langle N \rangle + \delta N$, where $\langle N \rangle$ is given by Eq. (3.52). In leading order in \tilde{W}_{+-} , the correction reads

$$\delta N = \frac{1}{(1 + \tau)^2} \frac{\gamma}{(1 + \gamma)^2} \frac{\tilde{W}_{+-}}{\tilde{W}_0}, \quad (3.60)$$

where $1/\tilde{W}_0$ is given by Eq. (B.4). Note that δN is proportional to γ and, therefore, vanishes in the interval III of Sec. 3.3.1, see Fig. 3.4b. In contrast, δN is finite in the interval V of Sec. 3.3.1. Thus, if N is measured in the interval III, its average value is given by $\langle N' \rangle = 1 + 1/(1 + \eta/2)$, see Fig. 3.2b and Eq. 3.52; whereas, if N is measured in the interval V, its average value is given by $\langle N' \rangle = 1 + 1/(1 + \eta) + \delta N$.

3.4 Cotunneling in the $N = 1$ Coulomb blockade valley

The CB valley with $N = 1$ has the width $E_-(1) + E_+(1) = U_{12} + 2t_0 - J$. Cotunneling dominates the conductance in the valley at $T \ll U_{12} + 2t_0 - J$. In a cotunneling

process [135], a lead electron (hole) coherently occupies the DD in a state with one extra (fewer) electron and is transferred to either lead, leaving the DD with the same energy (elastic cotunneling) or with a different energy (inelastic cotunneling). The cotunneling rate for a lead electron to go from lead l to lead l' and the DD to go from state m to state n is given by the golden rule rate [170]

$$w_{nm}(l', l) = \frac{2\pi}{\hbar} \sum_{\bar{m}\bar{n}} |\langle \mathbf{n} | T_{l'l} | \mathbf{m} \rangle|^2 \delta(E_{\mathbf{m}\mathbf{n}} + \Delta\mu_{ll'}) \rho_{\bar{m}}^B, \quad (3.61)$$

where $\Delta\mu_{ll'} = \mu_l - \mu_{l'}$ and $E_{\mathbf{m}\mathbf{n}} = E_{\mathbf{m}} - E_{\mathbf{n}}$. Here, we use the notation $E_{\mathbf{m}} = E_m + E_{\bar{m}}$ and $|\mathbf{m}\rangle = |m\rangle |\bar{m}\rangle$, where E_m and $|m\rangle$ denote the DD energy (3.8) and state (3.1), *resp.*; furthermore, $|\bar{m}\rangle$ is an eigenstate of $K_L + K_R$ with energy $E_{\bar{m}}$. The averaging in (3.61) is performed over the leads at thermal equilibrium with the density matrix $\rho_{\bar{m}}^B = \langle \bar{m} | \rho_L^B \otimes \rho_R^B | \bar{m} \rangle$. The stationary ($\omega \rightarrow 0$) cotunneling is described by the effective T-matrix amplitudes (second order perturbation theory)

$$T_{l'l} = - \sum_{\substack{n'k'\sigma' \\ nk\sigma}} t_{ln}^* t_{l'n'} \left(\frac{d_{n\sigma}^\dagger d_{n'\sigma'}}{E_-(1)} c_{lk\sigma} c_{l'k'\sigma'}^\dagger + \frac{d_{n'\sigma'} \mathbb{A} d_{n\sigma}^\dagger}{E_+(1)} c_{l'k'\sigma'}^\dagger c_{lk\sigma} \right), \quad (3.62)$$

where we assumed $J \ll E_+(1) \ll U_H$ and used $\mathbb{A} = |S\rangle \langle S| + \sum_i |T_i\rangle \langle T_i|$ to exclude virtual transitions to the states (3.11), (3.12). Formula (3.62) is valid for $\Delta\mu, T \ll E_{\pm}(1)$. Similarly, to Sec. 3.3 we trace out the spin degeneracy in (3.1), using the rule (3.23). The cotunneling rates can then be presented as follows

$$w_{nm}(l'l) = \frac{2\pi}{\hbar} \nu^2 \Theta(E_{mn} + \Delta\mu_{ll'}) \mathcal{M}_{nm}^{l'l}, \quad (3.63)$$

where $\Theta(E) = E / (1 - \exp(-E/T))$, and $\mathcal{M}_{nm}^{l'l}$ are given in Appendix C. The state of the DD is described by $\rho_+ = 1/(1 + \gamma)$ and $\rho_- = \gamma/(1 + \gamma)$, with

$$\gamma = \frac{w_{-+}}{w_{+-}} = \frac{\Theta(-2t_0 + \Delta\mu) + \Theta(-2t_0 - \Delta\mu) + (\eta + 1/\eta)\Theta(-2t_0)}{\Theta(2t_0 + \Delta\mu) + \Theta(2t_0 - \Delta\mu) + (\eta + 1/\eta)\Theta(2t_0)}, \quad (3.64)$$

where $w_{nm} = \sum_{l'l} w_{nm}(l', l)$. We note that this result is universal and does not depend on the number of virtual states taken into account. The cotunneling current [170] is given by

$$I = e \sum_{nm} w_{nm}^I \rho_m, \quad (3.65)$$

where $w_{nm}^I = w_{nm}(R, L) - w_{nm}(L, R)$. For $T \ll 2t_0$, we define the *elastic* and *inelastic* components of the current, $I = I_{\text{el}} + I_{\text{inel}}$, as follows

$$I_{\text{el}} = e w_{++}^I, \quad (3.66)$$

$$I_{\text{inel}} = e w_{-+}^I \rho_+ + e (w_{+-}^I + w_{--}^I - w_{++}^I) \rho_-, \quad (3.67)$$

3.5. COTUNNELING IN THE $N = 2$ COULOMB BLOCKADE VALLEY

where we used that $\sum_n \rho_n = 1$. We note that the component I_{el} is a linear function of $\Delta\mu$, whereas $dI_{inel}/d\Delta\mu$ has a step-like $\Delta\mu$ -dependence with the step at $\Delta\mu = 2t_0$.

Next, we consider the case of a highly asymmetric coupling to the leads, $(\eta+1/\eta) \gg 1$. For $\Delta\mu \gtrsim 2t_0$, there is a competition between two types of processes of inelastic cotunneling. One is the thermal equilibration of the DD, due to inelastic cotunneling into the same lead; and the second one is the heating effect of the DD, due to inelastic cotunneling from the left lead to the right lead, provided $\mu_L > \mu_R$. The strength of the former effect is proportional to $\exp(-2t_0/T)$, for $T \ll 2t_0$. The latter effect is proportional to $(T/2t_0)\eta/(1+\eta^2)$, for $\Delta\mu = 2t_0$. As a function of T , the crossover occurs at the energy scale $T_h = 2t_0/w(\eta+1/\eta)$, where $w(x) = \ln(x \ln(x \dots \ln(x)))$ for $x \geq e$. At $T \gg T_h$, the DD is in thermal equilibrium with $\gamma \equiv \rho_-/\rho_+ = \exp(-2t_0/T)$. At $T \simeq T_h$, the heating in the DD is governed by both types of processes, and the ratio γ depends on both T and $\Delta\mu$, as given by Eq. (3.64). At $T \ll T_h$, we are in the *strong* heating regime, dominated by processes of inelastic cotunneling from one lead to the other. Here, we have

$$\gamma = \begin{cases} \frac{\eta T}{2t_0(1+\eta)^2}, & |\Delta\mu - 2t_0| \ll T, \\ \frac{\Delta\mu - 2t_0}{\Delta\mu + 2t_0(1+\eta+1/\eta)}, & \Delta\mu - 2t_0 \gg T. \end{cases} \quad (3.68)$$

In this regime, we can extract the asymmetry parameter η , for $\Delta\mu - 2t_0 \gg T$, in the following way

$$\frac{4\eta}{(1+\eta)^2} = \frac{A}{1 - A \frac{\Delta\mu - 2t_0}{4t_0}}, \quad A \equiv -\frac{2t_0}{\Delta G} \frac{dG}{d\Delta\mu}, \quad (3.69)$$

where $\Delta G = G(\Delta\mu) - G(\infty)$. The value of $G(\infty)$ is the value of G at $\Delta\mu - 2t_0 \gg 2t_0(1+\eta)^2/\eta$. We note that Eq. (3.69) holds also for $\eta \simeq 1$, then the energy scale T_h coincides with $2t_0$.

3.5 Cotunneling in the $N = 2$ Coulomb blockade valley

The width of the $N = 2$ CB valley is of the order of U_H . The energy scale of interest here is the exchange $J \ll U_H$. Similarly to Sec. 3.4, we calculate the cotunneling rates with $N = 2$ electrons in the DD, using the formula (3.61) with $T_{l'l}$ given by

$$T_{l'l} = - \sum_{\substack{n'l'\sigma' \\ nk\sigma}} t_{ln}^* t_{l'n'} \left(\frac{d_{n\sigma}^\dagger d_{n'\sigma'}}{E_-(2)} c_{lk\sigma} c_{l'k'\sigma'}^\dagger + \frac{d_{n'\sigma'} d_{n\sigma}^\dagger}{E_+(2)} c_{l'k'\sigma'}^\dagger c_{lk\sigma} \right). \quad (3.70)$$

Here, we assumed $2t_0 \ll E_-(2)$ and the energy splitting in the $N = 3$ sector to be much smaller than $E_+(2)$ as well as $\Delta\mu, T \ll E_\pm(2)$. The DD states $|m\rangle, |n\rangle$ in

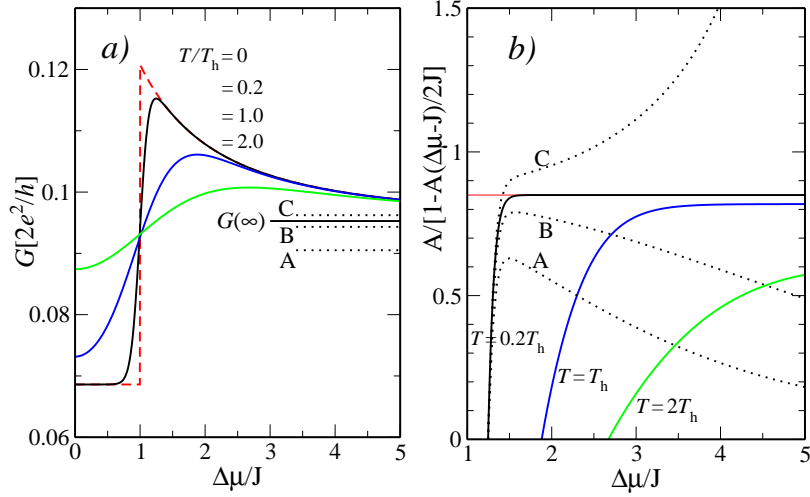


Figure 3.9: (a) Differential conductance G vs bias in the cotunneling regime for the $N = 2$ CB valley. The dashed curve corresponds to the asymptotic value of G at low temperatures. The solid curves are for a finite $T = (0.2, 1, 2)T_h$, where T_h is the characteristic temperature of the strong heating regime, see text. For the calculation we used: $\mathcal{S} = 0.6$, $\phi = 0.316$ ($T_h \simeq 0.23J$), $\eta = 1$, $E_-(2) = E_+(2) = E_C$, and $\Gamma_{L,R}/E_C = 0.1$. (b) The quantity $A/[1 - A(\Delta\mu - J)/2J]$, with $A \equiv -(J/\Delta G)(dG/d\Delta\mu)$, where $\Delta G = G(\Delta\mu) - G(\infty)$, is plotted for the three solid curves of $G(\Delta\mu)$ shown in Fig. 3.9a. The solid curve, corresponding to $T = 0.2T_h$, saturates with good precision at the value of $8/(2 + \kappa) = 2(1 - \phi)^2/(1 + \phi^2)$, whereas the other solid curves (not in the strong heating regime) have a smaller saturation value. The dotted curves A, B, and C, are plotted for the $T = 0.2T_h$ curve and correspond to choosing the value of $G(\infty)$ as shown in Fig. 3.9a by dotted horizontal segments. Only for a correct choice of $G(\infty)$ the curve has a plateau and saturates at a finite value.

(3.61) are now the singlet-triplet states (3.2) and the corresponding energies are taken from (3.9) and (3.10). After tracing out the spin degeneracy of the triplet (3.2), the cotunneling rates are given by Eq. (3.63) with $\mathcal{M}_{nm}^{\prime l}$ given in Appendix C.

The following discussion is similar to the one in Sec. 3.4. The heating effect of the DD is described by the ratio

$$\beta = \frac{w_{TS}}{w_{ST}} = \frac{3 \Theta(-J + \Delta\mu) + \Theta(-J - \Delta\mu) + \kappa \Theta(-J)}{\Theta(J + \Delta\mu) + \Theta(J - \Delta\mu) + \kappa \Theta(J)}, \quad (3.71)$$

where $\kappa = (\eta + 1/\eta)(1 + \phi)^2/(1 - \phi)^2$. The DD population probabilities are given by $\rho_S = 1/(1 + \beta)$ and $\rho_T = \beta/(1 + \beta)$. The formulas (3.65), (3.66) and (3.67) apply to this case also, provided we substitute the indices $+$ by S and $-$ by T . The differential conductance G , at $T \ll J$, has a step-like $\Delta\mu$ -dependence, with the step occurring at $\Delta\mu = J$. We plot G vs $\Delta\mu$ for different temperatures in Fig. 3.9a.

The strong heating regime was considered previously [118] for the case $\eta = 1$. We present the results for arbitrary η here. The energy scale of the *strong heating regime*

3.6. COTUNNELING-ASSISTED SEQUENTIAL TUNNELING

for $\kappa \gg 1$ is given by $T_h = J/w(\kappa)$, where the function $w(x)$ was introduced in Sec. 3.4. The asymptotes of β in the strong heating regime, $T \ll T_h$, are as follows

$$\beta = \begin{cases} \frac{3T}{J(2+\kappa)}, & |\Delta\mu - J| \ll T, \\ \frac{3(\Delta\mu - J)}{\Delta\mu + J(1+\kappa)}, & \Delta\mu - J \gg T. \end{cases} \quad (3.72)$$

For $\Delta\mu - J \gg T$, the following equality holds in the strong heating regime,

$$\frac{8}{2 + \kappa} = \frac{A}{1 - A \frac{\Delta\mu - J}{2J}}, \quad A \equiv -\frac{J}{\Delta G} \frac{dG}{d\Delta\mu}, \quad (3.73)$$

where $\Delta G = G(\Delta\mu) - G(\infty)$, with $G(\infty)$ given by G at $\Delta\mu - J \gg (2 + \kappa)J$. Eq. (3.73) allows us to extract κ , and hence, to extract the interaction parameter ϕ , provided the asymmetry parameter η is known (*e.g.* from a similar procedure as explained in Sec. 3.4). We illustrate how this procedure works in Fig. 3.9b. The r.h.s. of Eq. (3.73) is plotted for the curves in Fig. 3.9a. With lowering the temperature, the plateau value saturates at $8/(2 + \kappa)$, as one enters the strong heating regime; compare the three solid curves in Fig. 3.9b. If the value of $G(\infty)$ is not known, then one can proceed in the following way. Starting with a lower bound of $G(\infty)$, which can be *e.g.* $G(\infty) = 0$, a set of curves is plotted for values of $G(\infty)$ increased each time by an offset value. The curves can be divided into two classes: (i) curves which have no divergence for $\Delta\mu - J > T$, have a maximum, and saturate at zero; and (ii) curves which monotonically increase, or even diverge, for biases $\Delta\mu - J > T$ in the available (measured) range of $\Delta\mu$. The separatrix of these two classes has a monotonic dependence with a plateau at a non-zero value, and it corresponds to the asymptotic value of the cotunneling conductance $G(\infty)$. The dotted curves in Fig. 3.9b, denoted as A, B, and C, are plotted for values which might mistakenly be assigned to $G(\infty)$, and are related to the curve at $T = 0.2T_h$. The curves A and B belong to the class (i), and the curve C to the class (ii); the separatrix is the solid curve at $T = 0.2T_h$. The values of $G(\infty)$ taken for the curves A, B, and C, are shown in Fig. 3.9a by dotted lines, whereas the true value of $G(\infty)$ by a solid line. Next, assuming that the measurement of $G(\Delta\mu)$ has an error bar, we note that the value at the maximum in curves of class (i) provides a lower bound for $8/(2 + \kappa)$.

Finally, we note that the same physics holds true for the case $J < 0$ (triplet ground state), which can be realized by applying a magnetic field perpendicular to the 2DEG plane. Here, one should replace $J \rightarrow |J|$ and $\beta \rightarrow 9/\beta$ in (3.72), and $8/(2 + \kappa) \rightarrow 8/(6 + 3\kappa)$ in the l.h.s. of (3.73). Eq. (3.71) remains valid for this case.

3.6 Cotunneling-assisted sequential tunneling

In Sec. 3.3, we identified the spectroscopic intervals [Eqs. (3.36) and (3.43)] and found that peaks in tunneling spectroscopy can occur at the borders between these intervals, see Fig. (3.6). However, not all expected peaks are activated by the sequential

tunneling alone. Namely, no peaks are found in Fig. (3.6) for $\Delta\mu/2 < |\delta E|$. The reason for this is that the DD resides in its ground state until the first transition takes place, namely the “ground state-to-ground state” transition between $N = 1$ and $N = 2$, which takes place at $\Delta\mu/2 = \delta E$ for the symmetric biasing. On the other hand, we have shown in Secs. 3.4 and 3.5 that, at low temperatures, the inelastic cotunneling provides a substantial source of heating in the DD.

In this section we consider the interplay of sequential tunneling and cotunneling close to the sequential tunneling peaks at finite bias. We find that at low temperatures, $T \ll T_0$, the heating effect due to cotunneling provides population to the excited states, from which a subsequent sequential tunneling can occur. Such a *cotunneling-assisted sequential tunneling* produces new features (peaks/dips) in G versus $\Delta\mu$ and δE . The energy scale T_0 is given by $T_0 = 2t_0/\ln(2t_0/\Gamma_R)$ for the $N = 1$ CB side, and $T_0 = J/\ln(J/\Gamma_L)$ for the $N = 2$ CB side; here, we assumed symmetric biasing of the DD with $\Delta\mu_L = \Delta\mu/2 > 0$. For G versus $\Delta\mu$ we find a peak at $\Delta\mu/2 = |\delta E| - 2t_0 > 2t_0$ on the $N = 1$ CB valley side, as well as a peak/dip at $\Delta\mu/2 = |\delta E| - 2t_0 + J$. On the $N = 2$ CB valley side, we find a peak in G versus $\Delta\mu$ at $\Delta\mu/2 = |\delta E| - J > J$.

We proceed with considering the $N = 1$ CB valley side and for the sake of simplicity of the following expressions we assume $J \ll 2t_0 \ll U_{12}$, which corresponds to weakly coupled dots. We consider a position in the CB valley close to the $N = 1, 2$ sequential tunneling peak, $E_-(1) \gg E_+(1)$, but still far enough to be able to apply a bias $\Delta\mu > 2t_0$ and to have $E_+(1) - \Delta\mu_L > 2t_0$. Since $\Delta\mu_L$ is comparable to $-\delta E = E_+(1)$, the cotunneling rates obtained in Sec. 3.4 are not valid here and should be modified as to account for the energy dependence of the tunneling density of states in the bias window. We replace Eq. (3.62) by

$$\Gamma_{l'l} = - \sum_{\substack{n'k'\sigma' \\ nk\sigma}} t_{ln}^* t_{l'n'} \frac{d_{n'\sigma'} \mathbb{A} d_{n\sigma}^\dagger}{U_+^l} c_{l'k'\sigma'}^\dagger c_{lk\sigma}, \quad (3.74)$$

where $U_+^l = E(2) - E(1) - \mu_l$, and \mathbb{A} was defined below equation (3.62). Formula (3.74) is valid for $T \ll U_+^l$. Next, we calculate the cotunneling rates using the golden rule expression (3.61) and trace out the spin degeneracies according to Eq. (3.23). We obtain the cotunneling rates close to the sequential tunneling peak,

$$w_{nm}(l', l) = \frac{2\pi}{\hbar} \nu^2 \left(\frac{1}{U_+^l} - \frac{1}{U_+^{l'} + E_{mn}} \right) \tilde{\mathcal{M}}_{nm}^{l'l}, \quad (3.75)$$

for $E_{mn} + \Delta\mu_{l'l} > 0$, and $w_{nm}(l', l)$ suppressed by $\exp[(E_{mn} + \Delta\mu_{l'l})/T]$, for $E_{mn} + \Delta\mu_{l'l} < 0$. Here, we have assumed $T \ll 2t_0$ and $|E_{mn} + \Delta\mu_{l'l}| \gg T$. The quantities $\tilde{\mathcal{M}}_{nm}^{l'l}$ are obtained from $\mathcal{M}_{nm}^{l'l}$ in Appendix C by setting $U_- \rightarrow \infty$ and omitting the $1/U_+^2$ denominators. We note that the diagonal rates $w_{nn}(l, l)$ do not enter our further calculation, and hence the case $E_{mn} + \Delta\mu_{l'l} = 0$ refers only to the vicinity of $\Delta\mu = 2t_0$, where the value of the rate is proportional to T . For this case ($|E_{mn} + \Delta\mu_{l'l}| \ll U_+^l$), one can use the expressions derived in Sec. 3.4, setting $E_-(1) \gg E_+(1)$.

3.6. COTUNNELING-ASSISTED SEQUENTIAL TUNNELING

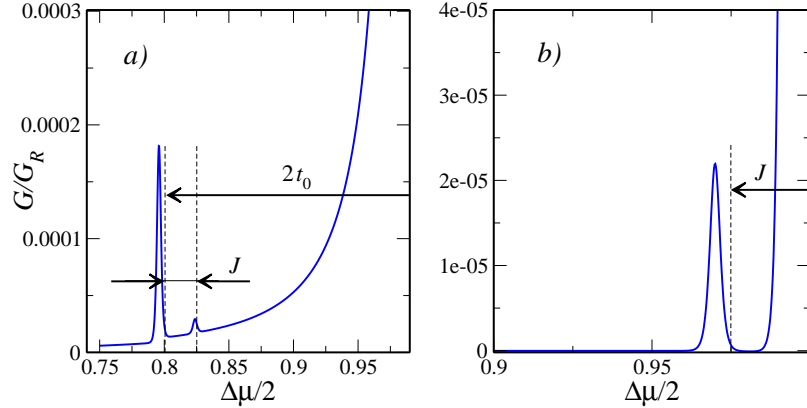


Figure 3.10: Differential conductance G versus bias for: (a) $\delta E = -1$ and (b) $\delta E = 1$. Here, we use the following parameters: $t_0 = 0.1$, $J = 0.025$, $S = 0.2$, $\phi = 0.6$, $\Gamma_L = \Gamma_R = 0.001$, $T = 0.001$, $\Delta\mu_{L,R} = \Delta\mu/2$. The conductance is scaled by $G_R = e^2\Gamma_R/\hbar T$ on both plots.

Next we solve the master equation, similar to Sec. 3.3.1, including also the cotunneling rates. We find that, on the $N = 1$ CB valley side, it suffices to take into account only the rates (3.75), *i.e.* between $|+\rangle$ and $|-\rangle$, and neglect the cotunneling between $|S\rangle$ and $|T\rangle$ (they give higher order correction). From the competition of the cotunneling rate w_{-+} and the sequential tunneling rate $W_{S,+}$ we deduce the energy scale $T_0 = 2t_0/\ln(2t_0/\nu t_R^2)$, valid for⁶ $\Delta\mu > 0$. For temperatures $T \ll T_0$, the ratio $\gamma = \rho_-/\rho_+$ is given by

$$\gamma = w_{-+} \left(w_{+-} + \frac{W_{+,S}W_{S,-}}{W_{+,S} + W_{-,S}} + \frac{W_{+,T}W_{T,-}}{W_{+,T} + W_{-,T}} \right)^{-1}. \quad (3.76)$$

This straightforwardly yields a non-vanishing population in the $N = 2$ sector,

$$\tau = \gamma \left(\frac{W_{S,-}}{W_{+,S} + W_{-,S}} + \frac{W_{T,-}}{W_{+,T} + W_{-,T}} \right), \quad (3.77)$$

with the balance between $|T\rangle$ and $|S\rangle$ given by

$$\beta = \frac{W_{T,-}(W_{+,S} + W_{-,S})}{W_{S,-}(W_{+,T} + W_{-,T})}. \quad (3.78)$$

The physical interpretation of equation (3.76) is as follows. In the bias range given by $U_+^L > 2t_0$, the occupation of the DD is determined by the cotunneling processes, with $\gamma = w_{-+}/w_{+-}$, see Sec. 3.4. For biases $\Delta\mu > 2t_0$, the population ρ_- increases with increasing bias, see (3.68), and can reach a value comparable to ρ_+ . A further increase of the bias brings us to the vicinity of the point $U_+^L = 2t_0$. Here, a new channel of relaxation opens, namely $|-\rangle \rightarrow |S\rangle \rightarrow |+\rangle$ (and also $|-\rangle \rightarrow |T\rangle \rightarrow |+\rangle$ at $U_+^L = 2t_0 - J$). Since the reversed sequence is forbidden due to energy conservation, the level $|-\rangle$ is emptied efficiently and one has $\rho_+ \approx 1$. A small non-equilibrium

⁶For $\Delta\mu < 0$, we have $T_0 = 2t_0/\ln(2t_0/\nu t_L^2)$.

population persists in the $N = 2$ sector and in the level $|-\rangle$. This allows for a sequential tunneling current from the excited DD states.

The current through the DD consists of two parts,

$$I = I^{\text{seq}} + I^{\text{cot}}, \quad (3.79)$$

where I^{seq} is the sequential-tunneling part given by Eq. (3.50) with $\rho_{S,T}$ calculated above. The cotunneling part I^{cot} can be calculated with Eq. (3.65) and the rates (3.75). Both terms, I^{seq} and I^{cot} in (3.79), contribute with the same order of magnitude to the current and differential conductance G . In Fig. 3.10a, we plot the bias dependence of G on the left-hand-side of the sequential-tunneling peak. The effect discussed above results in two features, namely (i) a peak at $\Delta\mu/2 = |\delta E| - 2t_0$, and (ii) a peak/dip at $\Delta\mu/2 = |\delta E| - 2t_0 + J$ (both positions are given for $T = 0$). The latter peak turns into a dip with increasing inter-dot coupling⁷. The positions of the peaks are temperature dependent. With increasing T both peaks shift to the left; the peak (i) shifts by $\delta\mu \propto T \ln[2t_0/\nu t_R^2(1 + 1/2\eta)]$ and it has a width of the same order of magnitude, the peak (ii) shifts by $\delta\mu \sim T$ and has width $\sim T$. This scaling behavior with varying $\Gamma_R = \pi\nu t_R^2$ results from the competition between the cotunneling rate w_{+-} and sequential tunneling rate $W_{S,-}$ in equation (3.76); for the peak (ii) it is not present. We note that the peak (ii) is solely due to $dI^{\text{seq}}/d\Delta\mu$, whereas the peak (i) is present in both $dI^{\text{seq}}/d\Delta\mu$ and $dI^{\text{cot}}/d\Delta\mu$.

Next, we proceed with considering the $N = 2$ CB valley side close to the $N = 1, 2$ peak ($E_-(2) \ll E_+(2)$). We assume $J \ll 2t_0 \ll U_H$, which is usually the case for double dots, and consider a position in the valley such that one can satisfy $\Delta\mu > J$ and $E_-(2) - \Delta\mu_R > J$. We follow a derivation close to the case discussed above. Instead of Eq. (3.74) we use

$$\Gamma_{ll} = - \sum_{\substack{n'k'\sigma' \\ nk\sigma}} t_{ln}^* t_{l'n'} \frac{d_{n\sigma}^\dagger \mathbb{A} d_{n'\sigma'}}{U_-^{l'}} c_{lk\sigma} c_{l'k'\sigma'}^\dagger, \quad (3.80)$$

where $U_-^l = E(1) - E(2) + \mu_l$ and $\mathbb{A} = \sum_{\sigma} |+, \sigma\rangle\langle+, \sigma|$. To calculate the golden rule rates we use Eq. (3.75) with $U_-^l \rightarrow U_+^{l'}$ and $\tilde{\mathcal{M}}_{nm}^{ll'}$ given in Appendix C. From solving the master equation we find results similar to Eqs. (3.76)–(3.78). Namely, we find that in the temperature regime $T \ll T_0$, with $T_0 = J/\ln(J/\nu t_L^2)$ for $\Delta\mu > 0$ and $T_0 = J/\ln(J/\nu t_R^2)$ for $\Delta\mu < 0$, the cotunneling rate w_{TS} provides non-equilibrium population to the state $|+\rangle$ for $U_-^R \lesssim J$, where $U_-^R = E_-(2) - \Delta\mu_R$. The ratio $\beta = \rho_T/\rho_S$ in this regime is as follows

$$\beta = w_{TS} \left(w_{ST} + \frac{W_{S,+} W_{+,T}}{W_{S,+} + W_{T,+}} \right)^{-1}. \quad (3.81)$$

⁷For the parameters used in Fig. 3.10, G has two peaks (and not a peak and a dip) on the $N = 2$ CB valley side for $\Delta\mu/2 > \delta E$.

3.7. CONCLUSIONS

The population in the $N = 1$ sector is determined by

$$\frac{1}{\tau} = \beta \left(\frac{W_{+,T}}{W_{S,+} + W_{T,+}} \right), \quad (3.82)$$

and belongs to the $|+\rangle$ state, *i.e.* $\gamma = 0$. The current through the DD is given by Eq. (3.79). The sequential tunneling part I^{seq} is given by Eq. (3.51), where one should assume $\rho_- = 0$, and $\rho_+ = 1/\tau \ll 1$ given by Eq. (3.82). The cotunneling part I^{cot} is given by Eq. (3.65), where one should use occupation probabilities determined by Eqs. (3.81) and (3.82), and cotunneling rates as discussed after Eq. (3.80). In Fig. 3.10*b*, we plot G vs $\Delta\mu/2 = \Delta\mu_R > 0$ on the left-hand-side of the sequential-tunneling peak. The new feature is a peak, which occurs at $\Delta\mu/2 = \delta E - J$ for $T = 0$. With increasing T , it moves to the left by an amount $\delta\mu \propto T \ln[J/\nu t_L^2(1 + \eta/2)]$, and has a width of the same order of magnitude. We note that the behavior of this peak is analogous to that of the peak (i) in the previously discussed case (see above).

To summarize, we have analyzed an effect originating from an interplay of sequential tunneling and (inelastic) cotunneling, and have specified the regimes where additional observable features in transport through a DD emerge.

3.7 Conclusions

We have analyzed theoretically the transport spectroscopy of a symmetric DD attached to leads in series. Our motivation was to find ways of characterizing the DD in dc transport measurements. For this, we have recast the main results of the Hund-Mulliken method [59], introducing a description of the DD in terms of a set of parameters, $\{t_0, J, \phi, \mathcal{S}, U_{12}, U_H, \hbar\omega_0\}$, which can be referred to in experiments as phenomenological parameters, see Sec. 3.2. Direct access to these parameters is necessary for building spin-based qubits using quantum dots, see Ref. [118]. Using a master equation approach, we have described the transport and the non-equilibrium probability distribution in the DD both in the sequential tunneling and cotunneling regimes. We have specified a number of “non-universal” regimes, which reveal information about these DD parameters. We summarize our main results below.

In the sequential tunneling regime, see Sec. 3.3, the differential conductance at a finite bias $G(\Delta\mu)$ has satellite peaks of sequential tunneling with respect to the main peaks of the CB diamond, see Figs. 3.7, 3.8, and 3.6. The exchange coupling constant J appears as a peak separation in $G(\Delta\mu)$ both on the $N = 1$ and $N = 2$ CB sides. The tunnel splitting $2t_0$ can be extracted from $G(\Delta\mu)$ on the $N = 2$ CB side, see Fig. 3.6. We note that if the two dots are detuned by some energy $\Delta E \lesssim 2t_0$, then one can replace $2t_0 \rightarrow \sqrt{4t_0^2 + \Delta E^2}$ for the transport spectroscopy of the DD.

In the cotunneling regime, see Secs. 3.4 and 3.5, the exchange coupling constant J can be observed on the $N = 2$ CB side as the bias value at which the inelastic cotunneling turns on. A step in $G(\Delta\mu)$ occurs at $|\Delta\mu| = |J|$. Similarly the tunnel splitting $2t_0$ can

be extracted from the $N = 1$ CB side. In Sec. 3.4 we have identified a *strong heating* regime where the bias dependence of $G(\Delta\mu)$ allows one to extract the asymmetry parameter $\eta = |t_R|^2/|t_L|^2$ on the $N = 1$ CB side. An additional relation involving η and ϕ can be obtained on the $N = 2$ CB side, see Sec. 3.4.

As an alternative to transport measurements we have considered the use of a charge detector (QPC) close to one of the dots, see Sec. 3.3.3. We found that measuring the average charge on the DD allows one to extract J and $2t_0$, similarly to the conductance measurements in the sequential tunneling regime. Moreover, additional relations between the DD parameters can be obtained with sensitive QPC measurements. We have also considered the back action of the QPC onto the DD and found that the QPC induces relaxation of the DD states with 1 electron. We accounted for this relaxation in the master equations in Sec. 3.3.3.

Finally, we have analyzed a combined mechanism of sequential tunneling and cotunneling, see Sec. 3.6. We found that inelastic cotunneling can provide non-equilibrium population probability to the excited DD states, which can then enable sequential tunneling via an excited DD state. Accounting for this effect results in additional satellite peaks in $G(\Delta\mu)$ at low temperatures.

Chapter 4

Phonon-induced decay of the electron spin in quantum dots

In this chapter, we study [90] spin relaxation and decoherence in a GaAs quantum dot due to the spin-orbit (SO) interaction. We derive an effective Hamiltonian which couples the electron spin to phonons or any other fluctuation of the dot potential. We show that the spin decoherence time T_2 is as large as the spin relaxation time T_1 , under realistic conditions. For the Dresselhaus and Rashba SO couplings, we find that, in leading order, the effective B -field can have only fluctuations transverse to the applied B -field. As a result, $T_2 = 2T_1$ for arbitrarily large Zeeman splittings, in contrast to the naively expected case $T_2 \ll T_1$. We show that the spin decay is drastically suppressed for certain B -field directions and ratios of SO coupling constants. Finally, for the spin-phonon coupling, we show that $T_2 = 2T_1$ for all SO mechanisms in leading order in the electron-phonon interaction.

4.1 Introduction

Phase coherence of spin in quantum dots (QDs) is of central importance for spin-based quantum computation in the solid state [4, 27]. Sufficiently long coherence times are needed for implementing quantum algorithms and error correction schemes. If the qubit is operated as a classical bit, its decay time is given by the spin relaxation time T_1 , which is the time of a spin-flip process. For quantum computation, however, the spin decoherence time T_2 — the lifetime of a coherent superposition of spin up and spin down states — must be sufficiently long. In semiconductor QDs, the spin coherence is limited by the dot *intrinsic* degrees of freedom, such as phonons, spins of nuclei, excitations on the Fermi surface (e.g. in metallic gates), fluctuating impurity states nearby the dot, electromagnetic fields, etc. It is well known (and experimentally verified) that the T_1 time of spin in QDs is extremely long, extending up to $100 \mu\text{s}$. The decoherence time T_2 , in its turn, is limited by both spin-flip and dephasing processes, and can be much smaller than T_1 , although its upper bound is

$T_2 \leq 2T_1$. Knowledge of the mechanisms of spin relaxation and decoherence in QDs can allow one to find regimes with the least spin decay.

Recently, the spin T_1 time in a one-electron GaAs QD was measured [86] by a pulsed relaxation measurement technique (PRMT) [84]. This technique was previously applied to detect triplet-to-singlet relaxation in a two-electron quantum dot [84], yielding a spin relaxation time of $200 \mu\text{s}$. Application of PRMT to Zeeman sub-levels became possible with resolving the Zeeman splitting in *dc* transport spectroscopy [86, 87], which required a magnetic field $B > 5 \text{ T}$. The results of Ref. [86] show that $T_1 > 50 \mu\text{s}$ at $B = 7.5 \text{ T}$ and 14 T , with no indication of a B -field dependence. Experimental values for the spin T_2 time in a single QD are not available yet, but an ESR scheme for its measurement has been proposed [131]. The ensemble spin decoherence time T_2^* was measured in *n*-doped GaAs bulk semiconductors [7], demonstrating coherent spin precession over times exceeding $T_2^* \sim 100 \text{ ns}$. This indicates that the decoherence time of a single spin is even larger, $T_2 \geq T_2^*$. However, the mechanisms of spin decoherence for extended and localized electrons are rather different, cf. Ref. [173].

Different mechanisms of spin relaxation in QDs have been considered, such as spin-phonon coupling via spin-orbit (SO) [89] or hyperfine interaction [127], and spin-nuclear coupling [59, 125, 126]. The SO mechanisms yield no spin decay at $B = 0$, due to the Kramers degeneracy of the dot states. Interestingly, for GaAs QDs, the orbital effect of B leads to no spin decay in lowest order in SO interaction [89, 174, 175]. This is due to the special form (linear in momentum) of the SO coupling in 2D. The leading order contribution is, thus, proportional to the Zeeman splitting and leads to long T_1 times in GaAs QDs varying strongly with the B -field [89]. However, previous theories [89] do not apply to the high values of B used in recent experiments [86], and thus, no comparison could be made so far. As for the nuclear mechanism, the electron spin decay can be suppressed by applying a B -field or by polarizing the nuclear system [59, 125].

In this chapter, we show that the spin T_2 time, caused by SO interaction in GaAs QDs, is as large as the spin T_1 time. We assume low temperatures, $T \ll \hbar\omega_0$, where $\hbar\omega_0$ is the dot size-quantization energy, and with no external noise in the applied B -field. We, thus, argue that the lower bound $T_1 \geq 50 \mu\text{s}$ established in Ref. [86] is, in fact, also a lower bound for T_2 . Furthermore, we show that the spin decay can be reduced by a special choice of direction of \mathbf{B} , if there is Rashba coupling.

4.2 Model Hamiltonian

The Hamiltonian describing the electron in a QD reads

$$H = H_d + H_Z + H_{SO} + U_{ph}, \quad (4.1)$$

$$H_d = \frac{p^2}{2m^*} + U(\mathbf{r}), \quad (4.2)$$

$$H_{SO} = \beta(-p_x\sigma_x + p_y\sigma_y) + \alpha(p_x\sigma_y - p_y\sigma_x), \quad (4.3)$$

$$H_Z = \frac{1}{2}g\mu_B\mathbf{B} \cdot \boldsymbol{\sigma}, \quad (4.4)$$

where $\mathbf{p} = -i\hbar\nabla + (e/c)\mathbf{A}(\mathbf{r})$ is the electron 2D kinetic momentum, $U(\mathbf{r})$ is the lateral confining potential, with $\mathbf{r} = (x, y)$, and $\boldsymbol{\sigma}$ are the Pauli matrices. The axes x and y point along the main crystallographic directions in the (001) plane of GaAs. The SO Hamiltonian (4.3) includes both the Dresselhaus SO coupling (β), due to the bulk inversion asymmetry of the GaAs lattice, and the Rashba SO coupling (α), due to asymmetry of the quantum well profile in the z -direction (structure inversion asymmetry). We consider here α and β as model parameters; for their microscopic derivation see, *e.g.*, Ref. [176]. The magnetic field $\mathbf{B} = B(\sin\theta\cos\varphi, \sin\theta\sin\varphi, \cos\theta)$ defines the spin quantization axis via the Zeeman term (4.4). The phonon potential is given by

$$U_{ph}(\mathbf{r}) = \sum_{\mathbf{q}j} \frac{F(q_z)e^{i\mathbf{q}\parallel\mathbf{r}}}{\sqrt{2\rho_c\omega_{qj}/\hbar}}(e\beta_{\mathbf{q}j} - iq\Xi_{\mathbf{q}j})(b_{-\mathbf{q}j}^\dagger + b_{\mathbf{q}j}),$$

where $b_{\mathbf{q}j}^\dagger$ creates an acoustic phonon with wave vector $\mathbf{q} = (\mathbf{q}\parallel, q_z)$, branch index j , and dispersion ω_{qj} ; ρ_c is the sample density [volume is set to unity in (4.5)]. Optical phonons play no role at the low energies considered here. The factor $F(q_z)$ in Eq. (4.5) equals unity for $|q_z| \ll d^{-1}$ and vanishes for $|q_z| \gg d^{-1}$, where d is the size of the quantum well along the z -axis. We take into account both piezo-electric ($\beta_{\mathbf{q}j}$) and deformation potential ($\Xi_{\mathbf{q}j}$) kinds of electron-phonon interaction [177]. Next, we derive an effective Hamiltonian for the low temperature ($T \ll \hbar\omega_0$) spin dynamics, relaxation and decoherence.

The electron spin couples to phonons due to the SO interaction (4.3). For typical GaAs QDs the SO length $\lambda_{SO} = \hbar/m^*\beta$ is much larger than the electron orbit size λ . The linear in λ/λ_{SO} contribution to the spin-phonon coupling is only due to a finite Zeeman splitting [89, 174, 175]. We consider a magnetic field B , for which the spin-phonon coupling dominates the spin decay. For simplicity we assume $m^*\beta^2 \ll g\mu_B B \ll \hbar\omega_0$. Using perturbation theory (or Schrieffer-Wolff transformation), we obtain¹ the effective Hamiltonian

$$H_{\text{eff}} = \frac{1}{2}g\mu_B(\mathbf{B} + \delta\mathbf{B}(t)) \cdot \boldsymbol{\sigma}, \quad (4.5)$$

$$\delta\mathbf{B}(t) = 2\mathbf{B} \times \boldsymbol{\Omega}(t), \quad (4.6)$$

¹In leading order in H_{SO} , we have $\tilde{H} \equiv e^S H e^{-S} = H_d + H_Z + U_{ph} + [S, U_{ph}]$, with S given by $[H_d + H_Z, S] = H_{SO}$. Then, $H_{\text{eff}} = \langle \psi | \tilde{H} | \psi \rangle$ up to a spin independent part.

where $\boldsymbol{\Omega}(t) = \langle \psi | [(\hat{L}_d^{-1} \boldsymbol{\xi}), U_{ph}(t)] | \psi \rangle$. Here, $|\psi\rangle$ is the electron orbital wave function, \hat{L}_d is the dot Liouvillean, $\hat{L}_d A = [H_d, A]$. The vector $\boldsymbol{\xi}$ has a simple form in the coordinate frame $x' = (x + y)/\sqrt{2}$, $y' = -(x - y)/\sqrt{2}$, $z' = z$ (see inset of Fig. 4.1), namely $\boldsymbol{\xi} = (y'/\lambda_-, x'/\lambda_+, 0)$, where $1/\lambda_{\pm} = m^*(\beta \pm \alpha)/\hbar$. Eq. (4.6) contains one of our main results: *in 1st order in SO interaction, there can be only transverse fluctuations of the effective magnetic field,² i.e. $\delta\mathbf{B}(t) \cdot \mathbf{B} = 0$* . This statement holds true for spin coupling to any fluctuations, be it the noise of a gate voltage or coupling to particle-hole excitations in a Fermi sea. Next, we consider the decay of the electron spin, $\mathbf{S} = \boldsymbol{\sigma}/2$, governed by Eq. (4.5).

4.3 Bloch equation

The phonons which are emitted or absorbed by the electron leave the dot during a time τ_c , $d/s \lesssim \tau_c \lesssim \lambda/s$, where s is the sound velocity. The electron spin decays over a much longer time span in typical structures, and, therefore, undergoes many uncorrelated scattering events. Then, the spin obeys the Bloch equation [123]

$$\langle \dot{\mathbf{S}} \rangle = \boldsymbol{\omega} \times \langle \mathbf{S} \rangle - \Gamma \langle \mathbf{S} \rangle + \boldsymbol{\Upsilon}, \quad (4.7)$$

where $\boldsymbol{\omega} = \omega \mathbf{l}$, with $\omega = g\mu_B B/\hbar$ and $\mathbf{l} = \mathbf{B}/B$. For a generic $\delta\mathbf{B}(t)$, in the Born-Markov approximation³ [123], we find $\Gamma_{ij} = \Gamma_{ij}^r + \Gamma_{ij}^d$, with

$$\begin{aligned} \Gamma_{ij}^r &= \delta_{ij} (\delta_{pq} - l_p l_q) J_{pq}^+(\omega) - (\delta_{ip} - l_i l_p) J_{pj}^+(\omega) \\ &\quad - \delta_{ij} \varepsilon_{kpq} l_k I_{pq}^-(\omega) + \varepsilon_{ipq} l_p I_{qj}^-(\omega), \end{aligned} \quad (4.8)$$

$$\Gamma_{ij}^d = \delta_{ij} l_p l_q J_{pq}^+(0) - l_i l_p J_{pj}^+(0), \quad (4.9)$$

where $J_{ij}^{\pm}(w) = \text{Re}[J_{ij}(w) \pm J_{ij}(-w)]$ and $I_{ij}^{\pm}(w) = \text{Im}[J_{ij}(w) \pm J_{ij}(-w)]$ are given by the spectral function

$$J_{ij}(w) = \frac{g^2 \mu_B^2}{2\hbar^2} \int_0^{+\infty} \langle \delta B_i(0) \delta B_j(t) \rangle e^{-iwt} dt. \quad (4.10)$$

The inhomogeneous part in Eq. (4.7) is given by

$$\begin{aligned} 2\Upsilon_i &= l_j J_{ij}^-(\omega) - l_i J_{jj}^-(\omega) + \varepsilon_{ipq} I_{pq}^+(\omega) \\ &\quad + \varepsilon_{iqk} l_k l_p [I_{pq}^+(\omega) - I_{pq}^+(0)], \end{aligned} \quad (4.11)$$

where ε_{ijk} is the anti-symmetric tensor (with Einstein summation convention) and we have assumed that $\langle \delta\mathbf{B}(t) \rangle = 0$. Eq. (4.7) describes spin decay in a number

²In the rotating frame, H_{SO} produces Zeeman-dependent fluctuations only transverse to \mathbf{B} . The fluctuations induced via orbital B effects can be along \mathbf{B} , but for H_{SO} linear in p they drop out since $\int p(t) dt = \text{const}$.

³Since $\tau_c \ll T_{1,2}$, the Markov approximation is well justified. For non-Markovian effects in the spin-boson model, see Ref. [178].

4.4. PHONON-INDUCED SPIN DECAY

of problems, such as electron scattering off impurities in bulk systems, nuclear spin scattering [123], etc. In our notation, the spin decay comes from the symmetric part of Γ , whereas the anti-symmetric part leads to a correction to $\boldsymbol{\omega}$ in Eq. (4.7). The tensor Γ^r describes spin decay due to processes of energy relaxation such as emission/absorption of a phonon. Therefore, the T_1 time is entirely determined by Γ^r , see Eq. (4.17). The tensor Γ^d can be non-zero only due to elastic scattering of spin, i.e. due to dephasing. Γ^d contributes to the decoherence time T_2 , and so does Γ^r . In many cases, however, the latter contribution is negligible, and Γ^d entirely dominates the spin decoherence [123]. This is in strong contrast to what we find here for an electron localized in a QD. To illustrate this, we first consider an example when Γ^d dominates the spin decoherence and then return to our case. A textbook example is $\langle \delta B_i(0) \delta B_j(t) \rangle = \bar{b}^2 \delta_{ij} \exp(-|t|/\tau_c)$. Choosing $\mathbf{l} = (0, 0, 1)$, we obtain from Eqs. (4.8) - (4.10) the non-zero elements: $\Gamma_{xx}^r = \Gamma_{yy}^r = \Gamma_{zz}^r/2 = \gamma_n^2 \bar{b}^2 \tau_c / (1 + \omega^2 \tau_c^2)$, and $\Gamma_{xx}^d = \Gamma_{yy}^d = \gamma_n^2 \bar{b}^2 \tau_c$, where $\gamma_n = g\mu_B/\hbar$. The longitudinal component $\langle S_z \rangle$ decays over the time $T_1 = \Gamma_{zz}^{-1} = 1/\Gamma_{zz}^r$. The transverse components decay over the time $T_2 = 1/(\Gamma_{xx}^r + \Gamma_{xx}^d)$. At $\omega \gg 1/\tau_c$, the contribution of Γ_{xx}^r to T_2 is negligible, and hence, $T_2 \ll T_1$. The latter relation has widely been quoted in the literature on quantum computing. In stark contrast to this example, we show now below that there are no *intrinsic* dephasing mechanisms for our case, which would justify this relation for the electron spin in GaAs QDs at $T \ll \hbar\omega_0$.

4.4 Phonon-induced spin decay

We start with calculating the spin decay due to the mechanism (4.6). Here, Γ_{ij}^d is identically zero, due to the transverse nature of the fluctuating field $\delta \mathbf{B}$. This can be inferred from Eqs. (4.9) and (4.10), noticing that each term in (4.9) contains $\mathbf{l} \cdot \delta \mathbf{B} = 0$. In order to calculate Γ_{ij}^r , we first find the main axes of the tensor $J_{ij}(w)$, see Eq. (4.10). $J_{ij}(w)$ is diagonal in the frame (X, Y, Z) (see inset of Fig. 4.1), which is obtained from (x', y', z) by a rotation with Euler angles φ' , θ , and χ . Here, the angles $\varphi' = \varphi - \pi/4$ and θ give \mathbf{B} in the frame (x', y', z) , and χ depends on the details of $U(\mathbf{r})$. It can be determined from $\langle \delta B_X \delta B_Y(t) \rangle = 0$. Assuming $U(\mathbf{r}) = U(r)$, we find⁴

$$\tan 2\chi = \frac{2(\lambda_+^2 - \lambda_-^2) l_{x'} l_{y'} l_z}{\lambda_+^2 (l_{y'}^2 - l_z^2 l_{x'}^2) + \lambda_-^2 (l_{x'}^2 - l_z^2 l_{y'}^2)}. \quad (4.12)$$

We now consider $U(r) = m^* \omega_0^2 r^2 / 2$ and evaluate $\boldsymbol{\Omega}(t)$ of Eq. (4.6) for the ground state $\psi(\mathbf{r}) = \exp(-r^2/2\lambda^2) / \lambda \sqrt{\pi}$, where $\lambda^{-2} = \hbar^{-1} \sqrt{(m^* \omega_0)^2 + (eB_z/2c)^2}$. Using⁵

$$y = \frac{-i}{\hbar m^* \omega_0^2} \hat{L}_d \left(p_y - \frac{eB_z}{\hbar c} x \right), \quad (4.13)$$

⁴We fix the quadrant of χ by requiring that the sign of $\sin 2\chi$ coincides with the one of the numerator of Eq. (4.12).

⁵A similar identity for x is obtained from Eq. (4.13) by replacing: $(x, y) \rightarrow (y, x)$ and $B_z \rightarrow -B_z$.

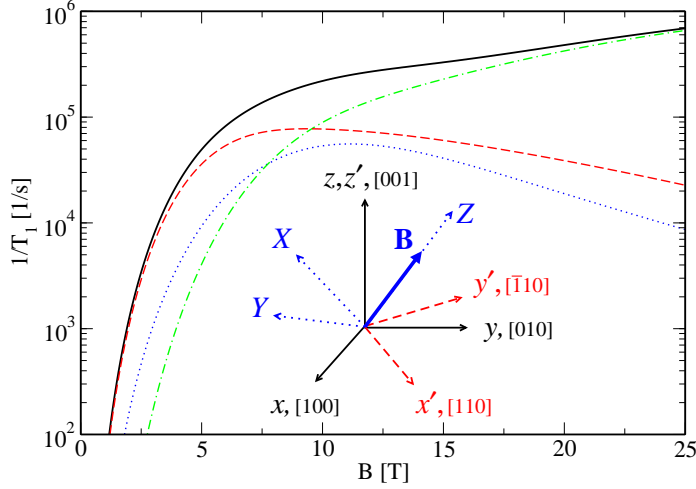


Figure 4.1: Solid curve: the relaxation rate $1/T_1$ of Eq. (4.19) as a function of an in-plane B for a GaAs QD with $\hbar\omega_0 = 1.1$ meV, $d = 5$ nm, $\lambda_{SO} = \hbar/m^*\beta = 1 \mu\text{m}$, and $\alpha = 0$. Dashed (dotted) curve: contribution of the piezo-electric mechanism ($\bar{\beta}_{j\vartheta}$) with transverse (longitudinal) phonons. Dot-dashed curve: contribution of the deformation potential mechanism ($\bar{\Xi}_j$). Note that $1/T_1 \propto 1/\lambda_{SO}^2$.

we find that $\Omega_{x'}$ follows from the r.h.s. of Eq. (4.5) with

$$\exp(i\mathbf{q}_{\parallel}\mathbf{r}) \rightarrow \frac{-iq_{y'}}{m^*\omega_0^2\lambda_-} \exp(-q_{\parallel}^2\lambda^2/4). \quad (4.14)$$

Further, $\Omega_{y'}$ is obtained in the same way, using (4.14) with the prefactor $q_{y'}/\lambda_- \rightarrow q_{x'}/\lambda_+$. Finally, we obtain

$$\begin{aligned} \text{Re}J_{XX}(w) &= \frac{\omega^2 w^3 (N_w + 1)}{(2\Lambda_+ m^* \omega_0^2)^2} \sum_j \frac{\hbar}{\pi \rho_c s_j^5} \int_0^{\pi/2} d\vartheta \sin^3 \vartheta \\ &\times e^{-(w\lambda \sin \vartheta)^2 / 2s_j^2} \left| F \left(\frac{|w|}{s_j} \cos \vartheta \right) \right|^2 \left(e^2 \bar{\beta}_{j\vartheta}^2 + \frac{w^2}{s_j^2} \bar{\Xi}_j^2 \right), \end{aligned} \quad (4.15)$$

where $N_w = (e^{\hbar w/T} - 1)^{-1}$, and s_j is the sound velocity for branch j . For GaAs, we use $s_1 = 4.73 \times 10^5$ cm/s and $s_2 = s_3 = 3.35 \times 10^5$ cm/s. Furthermore, $\bar{\Xi}_j = \delta_{j,1} \bar{\Xi}_0$ with $\bar{\Xi}_0 = 6.7$ eV, and $\bar{\beta}_{1,\vartheta} = 3\sqrt{2}\pi h_{14} \kappa^{-1} \sin^2 \vartheta \cos \vartheta$, $\bar{\beta}_{2,\vartheta} = \sqrt{2}\pi h_{14} \kappa^{-1} \sin 2\vartheta$, $\bar{\beta}_{3,\vartheta} = \sqrt{2}\pi h_{14} \kappa^{-1} (3 \cos^2 \vartheta - 1) \sin \vartheta$, with $h_{14} = -0.16$ C/m² and $\kappa = 13.1$. The effective SO length Λ_+ in Eq. (4.15) is given by

$$\frac{2}{\Lambda_{\pm}^2} = \frac{1 - l_{x'}^2}{\lambda_-^2} + \frac{1 - l_{y'}^2}{\lambda_+^2} \pm \sqrt{\left(\frac{1 - l_{x'}^2}{\lambda_-^2} + \frac{1 - l_{y'}^2}{\lambda_+^2} \right)^2 - \frac{4l_z^2}{\lambda_+^2 \lambda_-^2}}. \quad (4.16)$$

$\text{Re}J_{YY}(w)$ is obtained from Eq. (4.15) by substituting $\Lambda_+ \rightarrow \Lambda_-$, and $J_{ZZ}(w) = 0$. $\text{Im}J_{XX}(w)$ and $\text{Im}J_{YY}(w)$ are irrelevant for our discussion, see further. From

4.4. PHONON-INDUCED SPIN DECAY

Eq. (4.8), we obtain $\Gamma_{XX}^r = J_{YY}^+(\omega)$, $\Gamma_{YY}^r = J_{XX}^+(\omega)$, $\Gamma_{ZZ}^r = J_{XX}^+(\omega) + J_{YY}^+(\omega)$, $\Gamma_{XY}^r = -I_{YY}^-(\omega)$, $\Gamma_{YX}^r = I_{XX}^-(\omega)$. Since $\Gamma_{ij}/\omega \lesssim \omega\lambda^2/\omega_0\Lambda_{\pm}^2 \ll 1$, we can solve the secular equation iteratively.⁶ In the general case,

$$\frac{1}{T_1} := l_p l_q \Gamma_{pq} = \Gamma_{ZZ} = \Gamma_{ZZ}^r, \quad (4.17)$$

$$\frac{1}{T_2} := \frac{1}{2} (\delta_{pq} - l_p l_q) \Gamma_{pq} = \frac{1}{2} (\Gamma_{XX} + \Gamma_{YY}). \quad (4.18)$$

Then, the solution of Eq. (4.7) reads $\langle S_X(t) \rangle = S_{\perp} e^{-t/T_2} \sin(\omega t + \phi)$, $\langle S_Y(t) \rangle = S_{\perp} e^{-t/T_2} \cos(\omega t + \phi)$, and $\langle S_Z(t) \rangle = S_T + (S_Z^0 - S_T) e^{-t/T_1}$, with the thermodynamic value of spin being $\mathbf{S}_T = \mathbf{l} (\mathbf{l} \cdot \mathbf{\Upsilon}) T_1 = -(\mathbf{l}/2) \tanh(\hbar\omega/2k_B T)$, and the initial value $\langle \mathbf{S}(0) \rangle = (S_{\perp} \sin \phi, S_{\perp} \cos \phi, S_Z^0)$. For our special situation with purely transverse fluctuations ($\Gamma^d = 0$), we obtain

$$\frac{1}{T_1} = \frac{2}{T_2} = J_{XX}^+(\omega) + J_{YY}^+(\omega). \quad (4.19)$$

Keeping in mind the setup of Ref. [86], we plot $1/T_1$ as a function of B for $\theta = \pi/2$ and $\alpha = 0$ on Fig. 4.1 (solid curve). We find that $1/T_1$ has a plateau in a wide range of B -fields (cf. Ref. [86]), due to a crossover from the piezoelectric-transverse (dashed curve) to the deformation potential (dot-dashed curve) mechanism of electron-phonon interaction. For arbitrary φ , θ , and α , we have $1/T_1 = f/T_1(\theta = \pi/2, \alpha = 0)$ with

$$f = \frac{1}{\beta^2} [(\alpha^2 + \beta^2)(1 + \cos^2 \theta) + 2\alpha\beta \sin^2 \theta \sin 2\varphi] \quad (4.20)$$

Note that \sqrt{f} describes an ellipsoid in the frame (x', y', z) , i.e. $f = x'^2 + y'^2 + z^2$, with dimensionless x', y', z obeying $(x'/a)^2 + (y'/b)^2 + (z/c)^2 = 1$, where $a = 1 + \alpha/\beta$, $b = 1 - \alpha/\beta$, and $c = \sqrt{a^2 + b^2}$. Thus, if $\alpha = \beta$, then $b = 0$, i.e. $1/T_1$ *vanishes* if $\mathbf{B} \parallel y'$. The same is true for $\alpha = -\beta$ and $\mathbf{B} \parallel x'$. The case $\alpha = \pm\beta$ was considered previously for extended electron states in a two-dimensional electron gas (2DEG) [179]. Note that the Hamiltonian (4.1) conserves the spin component $\sigma_{y'(x')}$ for $\alpha = \beta$ ($\alpha = -\beta$) and $\mathbf{B} \parallel y'(x')$. This spin conservation results in T_1 being infinite to all orders in the SO Hamiltonian (4.3). At the same time, $1/T_2$ reduces to the next order contribution of (4.3). However, as we show below, a single-phonon process is inefficient in inducing dephasing and, therefore, $1/T_2$ can be non-zero only in the next order in electron-phonon interaction. Next, we note that a long lived spin state also occurs in a different GaAs structure, namely for a 2DEG grown in the (110) direction. Then, the normal to the 2DEG plane component of spin is conserved [180], provided $\alpha = 0$.

⁶The decay rates are defined by the secular equation: $\det \|\Gamma_{ij} - E\delta_{ij} + \varepsilon_{ijk}\omega_k\| = 0$, as the real part of E .

4.5 Other spin-orbit mechanisms

We discuss now other SO mechanisms. In Eq. (4.3), we omitted the so-called k^3 -terms of the Dresselhaus SO coupling [180], i.e. $H_{SO} \propto \hbar^{-2} \beta d^2 (\sigma_x \{p_x, p_y^2\} - \sigma_y \{p_y, p_x^2\})$. They are parametrically small ($d^2/\lambda^2 \ll 1$) in the 2D limit, compared to the retained ones. However, their contribution to the spin decay can be important, if $gm^*/m_0 \lesssim (d/\lambda)^2 \cos \theta$ and $\lambda^3 \lesssim d^2 \lambda_{SO}$, since the orbital effect of B contributes here in the first place. Otherwise, the orbital effect is given by the 2nd order contribution of (4.3), i.e. by $H_{SO}^{(2)} = -H_{SO} \hat{L}_d^{-1} H_{SO}$, and can be important, if $gm^*/m_0 \lesssim (\lambda/\lambda_{SO}) \cos \theta$. For in-plane B -fields, however, these mechanisms are negligible.

Additional spin decay mechanisms arise from the *direct* spin-phonon interaction [89]. The strain field produced by phonons couples to the electron spin via the SO interaction, resulting in the term $\Delta H' = (V_0/4) \varepsilon_{ijk} \sigma_i \{u_{ij}, p_k\}$, where p_i is the bulk kinetic momentum, u_{ij} is the phonon strain tensor, and $V_0 = 8 \times 10^7$ cm/s for GaAs. A similar mechanism occurs in a B -field, due to g -factor fluctuations caused by lattice distortion. This yields $\Delta H'' = \tilde{g} \mu_B \sum_{i \neq j} u_{ij} \sigma_i B_j$, where $\tilde{g} \approx 10$ for GaAs. The contribution of these mechanisms to the spin-flip rates in QDs has been estimated in Ref. [89]. Except for the $\alpha = \pm\beta$ cases discussed above, the direct mechanisms are usually negligible in QDs. Here, we find that such spin-phonon couplings do not violate the equality $T_2 = 2T_1$. For this, we note that $\Gamma_{ij}^d = 0$ for a generic $\delta B_i = \sum_{\mathbf{q}} M_i(\mathbf{q})(b_{-\mathbf{q}}^\dagger + b_{\mathbf{q}})$ in Eq. (4.5), if $q |M_i(\mathbf{q})|^2 \rightarrow 0$ at $q \rightarrow 0$. Obviously, this condition is satisfied for the direct spin-phonon mechanisms, since $u_{ij} = 0$ at $q = 0$. The same follows for the Hamiltonian (4.1) with the phonon potential (4.5) and an arbitrary H_{SO} ; the physical explanation is that the potential of long-wave phonons is constant over the dot size and, thus, commutes with H_{SO} . Finally, we note that, at temperatures $T \sim \hbar\omega_0$, there can be dephasing mechanisms [181], which can result in $T_2 \ll T_1$.

4.6 Conclusions

In conclusion, we have shown that the decoherence time T_2 of an electron spin in a GaAs QD is as large as the relaxation time T_1 for the spin decay based on SO mechanisms.

Chapter 5

Spin relaxation at the singlet-triplet transition in a quantum dot

In this chapter, we study electron spin relaxation due to spin-orbit interaction and phonon emission in a quantum dot with Coulomb interaction. We account for the Coulomb interaction using a special type of variational method, which turns into a controlled perturbation-theory expansion in the limits of weak and strong Coulomb interaction. We focus on the lowest in energy singlet and triplet levels of the quantum dot and calculate the relaxation rates in this subspace as a function of magnetic field in the vicinity of singlet-triplet transition.

5.1 Introduction

The spin dynamics of electrons in semiconducting nanostructures has become of central interest in recent years [3, 4]. It is desirable to understand the mechanisms which limit the spin phase coherence of electrons, in particular in GaAs semiconductors, which have been shown [7] to exhibit unusually long spin decoherence times T_2 exceeding 100 ns. Besides the spin states in quantum dots are considered to be promising for physical realization of the quantum computation algorithm [27]. Quantum computation requires coherent coupling between the dots, the coherence to be preserved on sufficiently long time scales. That makes it relevant to provide a complete theoretical estimation of the typical spin decoherence time of the electron in the QD. One of the important question is the calculation of T_1 time, i.e. the time of the spin relaxation. The first theoretical investigation of the spin relaxation in a quantum dot was done in Ref. [183], see also related Refs. [174, 175, 182, 184]. The spin-flip processes were considered within the one-electron approach. It was shown that the spin relaxation of the electrons localized in the dots differs strikingly from that of the delocalized electrons. The most effective mechanisms in the 2D case are

related to the broken inversion symmetry, either in the elementary crystal cell or at the heterointerface. Those are described by the spin-orbit terms in the electron Hamiltonian [180, 186] that are linear in the two-dimensional electron momentum, see below. As it was shown in Refs. [174, 183] these terms can be removed in the case of localized electrons by some spin-dependent unitary transformation. As a result, the contribution to the spin flip rate proportional to the second power of the spin-orbit coupling constant appears only if one takes into account the finite Zeeman splitting in the electron spectrum. This results in unusually low spin-flip rates. These theoretical predictions were verified experimentally, see Refs. [64, 84–86, 187, 189].

The natural question arises: to which extent these results survive for a situation when electrons interact? We consider a quantum dot (either lateral or vertical) which contains two electrons interacting through Coulomb interaction. As is known the ground state of this system is a singlet for the external orbital magnetic field which is lower than some critical value (several tesla) and for larger values of magnetic field the ground state becomes a triplet. Thus the singlet-triplet splitting can be easily tuned. Transitions between singlet and triplet states accompanied, for example, by the phonon emission involve necessarily spin flips. Thus the experimental investigation of the transition rate between these two states provides the natural probe of the spin-flip mechanisms in a quantum dot [84].

In this work we show that the conclusion obtained for a one-particle problem holds also for an interacting problem, i.e. the effect of the spin-orbit interaction cancels in the lowest order in the spin-orbit coupling constant β in the absence of the Zeeman field¹. Thus the term in the transformed Hamiltonian linear in the spin-orbit coupling constant is necessarily proportional to the Zeeman energy E_Z . As a result, the energy gap which determines the anticrossing of singlet and some triplet states is very small, it is given by the quantity $E_Z(\lambda/\lambda_{SO})$, where $\lambda/\lambda_{SO} \ll 1$ is the ratio of the dot lateral size λ and the spin-orbit length $\lambda_{SO} = \hbar/m^*\beta$. This is the reason for a very strong suppression of the spin-flip rate in the neighborhood of the anticrossing point. Indeed, the wave functions of singlet and triplet states are orthogonal and since the corresponding wave vectors of the phonons involved in the transition are much smaller than the inverse dot size, the matrix element of the phonon-assisted transition contains very small form-factor. On the other hand, when the current gap between the singlet and triplet states becomes large (away from the anticrossing point) then the wave vectors of the phonons involved are large compared to the dot lateral size and the rate decreases again. As a result, the corresponding curve has a non-monotonic form with two maxima at the gap values $\approx \hbar s/\lambda$ corresponding to the phonon wave vectors approximately equal to the inverse dot size, here s is the speed of sound. Note strong variation (by many orders of magnitude) of the spin-flip rate in a narrow interval of the gap (i.e. of the orbital magnetic field value) and a small value of the rate itself, for example, up to seconds in the neighborhood of the

¹This fact is not surprising and can be anticipated from the very beginning since the Coulomb interaction operator being spin independent commutes with the unitary operator mentioned above. The lack to observe such a cancellation was the reason for the wrong results obtained in Ref. [188].

anticrossing point.

5.2 Model Hamiltonian

We consider two interacting electrons in a quantum dot described by the Hamiltonian

$$H_0 = H_d + H_{SO} + H_Z, \quad (5.1)$$

$$H_d = \sum_{i=1,2} \left(\frac{p_i^2}{2m^*} + \frac{m^*\omega_0^2}{2} r_i^2 \right) + \frac{e^2}{\kappa|\mathbf{r}_1 - \mathbf{r}_2|}, \quad (5.2)$$

$$H_{SO} = \sum_{i=1,2} [\beta(-p_i^x \sigma_i^x + p_i^y \sigma_i^y) + \alpha(p_i^x \sigma_i^y - p_i^y \sigma_i^x)], \quad (5.3)$$

$$H_Z = \frac{1}{2} g \mu_B \mathbf{B} \cdot (\boldsymbol{\sigma}_1 + \boldsymbol{\sigma}_2), \quad (5.4)$$

where $\mathbf{r}_j = (x_j, y_j)$ is the j -th electron radius-vector and $\mathbf{p}_j = -i\hbar\partial/\partial\mathbf{r}_j + (e/c)\mathbf{A}(\mathbf{r}_j)$ is the kinetic momentum, with $\mathbf{A}(x_j, y_j) = (-y_j, x_j)B_z/2$ being the vector-potential; $\boldsymbol{\sigma}_j = (\sigma_j^x, \sigma_j^y, \sigma_j^z)$ are Pauli matrices. The spin-orbit coupling is given by the Hamiltonian (5.3), where the term proportional to β originates from the bulk Dresselhaus spin-orbit coupling, which is due to the absence of inversion symmetry in the GaAs lattice; the term proportional to α represents the Rashba spin-orbit coupling, which can be present in quantum wells if the confining potential (in our case along the z -axis) is asymmetric. The axes x and y point along the main crystallographic directions in the (001) plane of GaAs. The magnetic field $\mathbf{B} = B(\cos\varphi \sin\theta, \sin\varphi \sin\theta, \cos\theta)$ determines the spin quantization axis and the magnitude of the Zeeman splitting, $E_Z = g\mu_B B$, where g is the electron g -factor in GaAs. The orbital effect of \mathbf{B} is given by the component $B_z = B \cos\theta$ entering in $\mathbf{A}(\mathbf{r})$, and it allows one to control the singlet-triplet splitting $E_{ST} = E_{ST}(B_z)$.

We consider the acoustic phonons as a major source of orbital fluctuations in the quantum dot. The potential of acoustic phonons reads

$$U_{\text{ph}}(\mathbf{r}_1, \mathbf{r}_2) = \sum_{\mathbf{q}j} \frac{F(q_z)}{\sqrt{2\rho_c\omega_{\mathbf{q}j}/\hbar}} (e\beta_{\mathbf{q}j} - iq\Xi_{\mathbf{q}j}) \times (e^{i\mathbf{q}\parallel\mathbf{r}_1} + e^{i\mathbf{q}\parallel\mathbf{r}_2}) (b_{-\mathbf{q}j}^\dagger + b_{\mathbf{q}j}), \quad (5.5)$$

where $b_{\mathbf{q}j}^\dagger$ creates an acoustic phonon with wave vector $\mathbf{q} = (\mathbf{q}\parallel, q_z)$, branch index j , and dispersion $\omega_{\mathbf{q}j}$; ρ_c is the sample density [volume is set to unity in (5.5)]. The factor $F(q_z)$ equals unity for $|q_z| \ll d^{-1}$ and vanishes for $|q_z| \gg d^{-1}$, where d is the width of the 2D layer. We take into account both the piezo-electric ($\beta_{\mathbf{q}j}$) and deformation potential ($\Xi_{\mathbf{q}j}$) kinds of electron-phonon interaction [177].

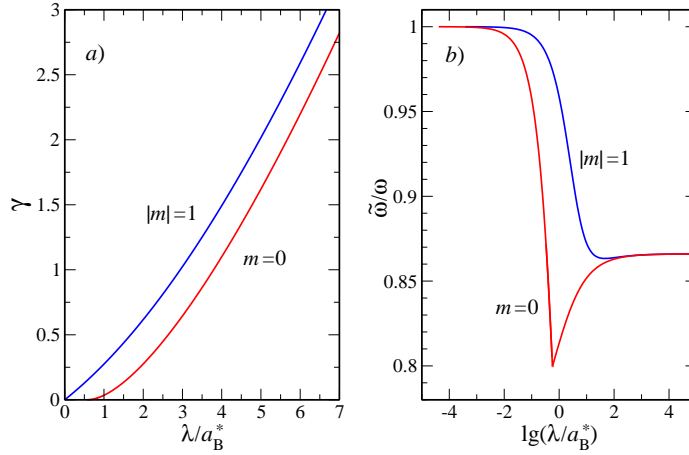


Figure 5.1: a) The variational parameters γ as a functions of the Coulomb interaction strength λ/a_B^* for the singlet $m = 0$ and the triplet $|m| = 1$ states. b) The ratio $\tilde{\omega}/\omega$ as a function of $\lg(\lambda/a_B^*)$ for $m = 0$ and $|m| = 1$. To find γ and $\tilde{\omega}/\omega$ we minimize the ground state energy in Eq.(5.13), see Appendix D for details.

5.3 Energy spectrum and wave functions

We consider here the Schrödinger equation $H_d|\mathbf{n}\rangle = E_{\mathbf{n}}|\mathbf{n}\rangle$, with H_d given in Eq. (5.2), and find the energies and wave functions of two interacting electrons. We use of the separation of variables in the Schrödinger equation in terms of the center of mass, $\mathbf{R} = (\mathbf{r}_1 + \mathbf{r}_2)/2$, and the relative motion, $\mathbf{r} = \mathbf{r}_1 - \mathbf{r}_2$, coordinates. The wave functions can then be written as $|\mathbf{n}\rangle = |NM\rangle|nm\rangle$, with

$$|NM\rangle = R_{NM}(R)e^{iM\varphi_R}/\sqrt{2\pi}, \quad M = 0, \pm 1, \pm 2, \dots, \quad (5.6)$$

$$|nm\rangle = \mathcal{R}_{nm}(r)e^{im\varphi_r}/\sqrt{2\pi}, \quad m = 0, \pm 1, \pm 2, \dots, \quad (5.7)$$

where φ_R and φ_r are the polar angles of \mathbf{R} and \mathbf{r} , *resp.* Note that $\mathbf{r}_1 \leftrightarrow \mathbf{r}_2$ corresponds to $\varphi_r \rightarrow \varphi_r + \pi$. Thus, $m = 0, \pm 2, \pm 4, \dots$ refers to singlet states (symmetric orbital wave function), and $m = \pm 1, \pm 3, \pm 5, \dots$, to triplet states (antisymmetric orbital wave function). The radial component in Eq. (5.6) reads

$$R_{NM}(R) = \sqrt{\frac{2N!}{(N + |M|)!}} \frac{R^{|M|}}{\Lambda^{|M|+1}} L_N^{|M|} (R^2/\Lambda^2) e^{-R^2/2\Lambda^2}, \quad (5.8)$$

where $L_N^{|M|}$ is a Laguerre polynomial ($N = 0, 1, 2, \dots$) and $\Lambda = \sqrt{\hbar/2m^*\omega}$, with $\omega = \sqrt{\omega_0^2 + \omega_c^2}/4$ and the cyclotron frequency $\omega_c = eB_z/m^*c$. The radial component in Eq. (5.7) is given by $\mathcal{R}_{nm}(r) = f_{nm}(r)/\sqrt{r}$, where the function $f_{nm}(r)$ obeys the Schrödinger equation $\mathcal{H}_m f_{nm}(r) = \varepsilon_{nm} f_{nm}(r)$, with the Hamiltonian

$$\mathcal{H}_m = \frac{\hbar^2}{m^*} \left(-\frac{\partial^2}{\partial r^2} + \frac{m^2 - 1/4}{r^2} + \frac{1}{a_B^* r} \right) + \frac{m^* \omega^2}{4} r^2, \quad (5.9)$$

5.3. ENERGY SPECTRUM AND WAVE FUNCTIONS

where $a_B^* = \hbar^2 \kappa / m^* e^2$ is the Bohr radius and $r = |\mathbf{r}_1 - \mathbf{r}_2|$. The functions $f_{nm}(r)$ obey the boundary conditions $f_{nm}(0) = f_{nm}(\infty) = 0$, and are normalized as follows

$$\int_0^\infty f_{nm}(r) f_{n'm}(r) dr = \delta_{nn'}. \quad (5.10)$$

The energy spectrum of the Hamiltonian (5.2) is given by

$$E_{NMnm} = \hbar\omega (2N + |M| + 1) + \frac{\hbar\omega_c}{2} (M + m) + \varepsilon_{nm}, \quad (5.11)$$

where ε_{nm} are the eigenvalues of \mathcal{H}_m in Eq. (5.9). Note that the quantum number m enters in \mathcal{H}_m as a parameter. We apply a variational method to find the ground state of \mathcal{H}_m for each m . For this, we consider first a Hamiltonian $\tilde{\mathcal{H}}_m$, similar to Eq. (5.9), but with $1/a_B^* r \rightarrow \gamma/r^2$ and with $\omega \rightarrow \tilde{\omega}$. From the solution of the Schrödinger equation for $\tilde{\mathcal{H}}_m$, we obtain a complete set of functions

$$\begin{aligned} \tilde{f}_{nm}(r) &= \sqrt{\frac{2\Gamma(n+1+\sqrt{m^2+\gamma})}{n!\Gamma^2(1+\sqrt{m^2+\gamma})}} r^{1/2+\sqrt{m^2+\gamma}} \\ &\quad \times e^{-r^2/2\tilde{\lambda}^2} {}_1F_1\left(-n, 1+\sqrt{m^2+\gamma}; r^2/\tilde{\lambda}^2\right), \end{aligned} \quad (5.12)$$

where $n = 0, 1, 2, \dots$, $\tilde{\lambda} = \sqrt{2\hbar/m^*\tilde{\omega}}$, $\Gamma(z)$ is the gamma function, and ${}_1F_1(a, b; z)$ is the confluent hypergeometric function of the first kind; $\gamma \geq 0$ and $\tilde{\omega}$ are variational parameters. Next, we evaluate the ground state energy of the Hamiltonian (5.9), using $\tilde{f}_{0m}(r)$ as a trial wave function, *i.e.* we calculate $\varepsilon_{0m} = \langle \tilde{f}_{0m} | \mathcal{H}_m | \tilde{f}_{0m} \rangle$ and obtain

$$\begin{aligned} \varepsilon_{0m} &= \hbar\tilde{\omega} \left(1 + \frac{m^2 + \gamma/2}{\sqrt{m^2 + \gamma}} + \frac{\tilde{\lambda}}{2a_B^*} \frac{\Gamma(1/2 + \sqrt{m^2 + \gamma})}{\Gamma(1 + \sqrt{m^2 + \gamma})} \right. \\ &\quad \left. + \left(1 + \sqrt{m^2 + \gamma} \right) \frac{\omega^2 - \tilde{\omega}^2}{2\tilde{\omega}^2} \right). \end{aligned} \quad (5.13)$$

Minimizing ε_{0m} in Eq. (5.13) with respect to γ and $\tilde{\omega}$, we obtain the ground state energy and wave function of \mathcal{H}_m within this variational method. In the absence of Coulomb interaction ($a_B^* = \infty$), the eigenfunctions of the Hamiltonian (5.9) are the functions $f_{nm}(r)$ in Eq. (5.12), with $\gamma = 0$ and $\tilde{\omega} = \omega$. With increasing the strength of the Coulomb interaction, the parameter $\tilde{\omega}$ varies non-monotonically and approaches the value $\tilde{\omega} = \sqrt{3}\omega/2$ in the limit of strong Coulomb interaction ($\tilde{\lambda}/a_B^* \gg 1$). At the same time, the parameter γ increases monotonically and tends to infinity with increasing the strength of the Coulomb interaction; the leading order term of the asymptotic expansion of γ reads $\gamma = (3/4)(\lambda/2a_B^*)^{4/3}$, where $\lambda = \sqrt{2\hbar/m^*\omega}$. A detailed analysis of the dependence of $\tilde{\omega}$ and γ on the Coulomb interaction strength λ/a_B^* is given in Appendix D. In Fig. 5.1, we plot γ and $\tilde{\omega}/\omega$ as functions of λ/a_B^* and $\log_{10}(\lambda/a_B^*)$, respectively, both for the singlet state $m = 0$ and the triplet states $m = \pm 1$. Note that, for the singlet state $m = 0$, the parameters γ and $\tilde{\omega}$ behave

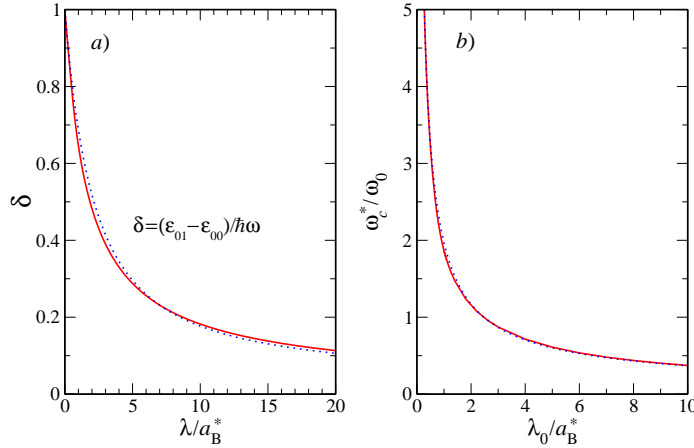


Figure 5.2: *a)* The parameter δ as a function of the Coulomb interaction strength λ/a_B^* . The dotted curve shows δ calculated according to Eq. (5.15). *b)* The singlet-triplet degeneracy occurs at a magnetic field B_z^* ($E_{TS} = 0$). This figure shows the corresponding ω_c^*/ω_0 as a function of λ_0/a_B^* , where $\omega_c^* = eB_z^*/m^*c$ and $\lambda_0 = \sqrt{2\hbar/m^*\omega_0}$. The dotted curve corresponds to the fitting function in Eq. (5.16)

non-analytically at the point $\lambda/a_B^* = \xi_c \approx 0.57$, where ξ_c is given in Eq. (D.5). Nonetheless, the energy of the $m = 0$ state, calculated according to Eq. (5.13), is a smooth function of λ/a_B^* , i.e. it has a continuous first derivative with respect to λ/a_B^* .

Now we focus on the singlet-triplet transition, between the singlet state $|\psi_S\rangle = |0000\rangle$ and the triplet state $|\psi_T\rangle = |000, -1\rangle$, which occurs with applying an orbital magnetic field B_z in the presence of the Coulomb interaction (the Zeeman interaction is set to zero here). Using Eq. (5.11), we obtain for the singlet-triplet splitting ($E_{TS} \equiv E_T - E_S$)

$$E_{TS} = \frac{\hbar}{2}\delta\sqrt{\omega_c^2 + 4\omega_0^2} - \frac{\hbar\omega_c}{2}, \quad (5.14)$$

where $\omega_c = eB_z/m^*c$ and $\delta = (\epsilon_{01} - \epsilon_{00})/\hbar\omega$. The Coulomb interaction enters in $\delta = \delta(\lambda/a_B^*)$ and, for vanishing strength of the Coulomb interaction, we have $\delta(0) = 1$. Furthermore, in leading order, we have $\delta = 1 - \sqrt{\pi}\lambda/4a_B^*$, for $\lambda/a_B^* \ll 1$, and $\delta = \frac{1}{2}(2a_B^*/\lambda)^{2/3}$, for $\lambda/a_B^* \gg 1$. A crossover formula for δ reads

$$\delta(\lambda/a_B^*) = \frac{\sqrt{1 + c(\lambda/a_B^*)^{3/2}}}{(1 + b\lambda/a_B^*)^{17/12}}, \quad (5.15)$$

where $b = \frac{3}{17}\sqrt{\pi} \approx 0.31$ and $c = 2^{-2/3}b^{17/6} \approx 0.023$. In Fig. 5.2(a), we plot the parameter δ as a function of λ/a_B^* , calculated with the help of Eq. (5.13) (solid curve) and as given by the fitting function (5.15) (dotted curve). Formula (5.15) is exact in the limits of weak and strong Coulomb interaction, and is accurate within 7% in the crossover region ($b^{-1} \lesssim \lambda/a_B^* \lesssim c^{-2/3}$). According to Eq. (5.14), if $\delta = 1$,

5.3. ENERGY SPECTRUM AND WAVE FUNCTIONS

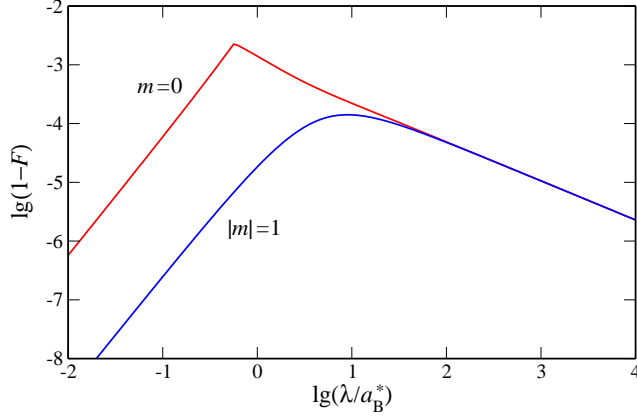


Figure 5.3: Infidelity $1 - F$ of the ground state of \mathcal{H}_m for $|m| = 0, 1$, see Eq. (5.21).

the singlet-triplet transition does not occur for arbitrary large B_z , i.e. there is no singlet-triplet transition without Coulomb interaction.

The singlet-triplet transition takes place at $B_z = B_z^*$, due to the orbital effect of \mathbf{B} , in the presence of Coulomb interaction. For strong Coulomb interaction, we have $\delta \ll 1$ and the singlet-triplet transition occurs at a small value of B_z , $B_z^* \ll \omega_0 m^* c / e$, and thus, one can neglect the magnetic field dependence in λ and δ . In this case, the degeneracy field is given by $B_z^* = 2\delta\omega_0 m^* c / e$, or equivalently by $\omega_c^* = \omega_0 (2a_B^* / \lambda_0)^{2/3}$, where $\omega_c^* = eB_z^* / m^* c$ and $\lambda_0 = \sqrt{2\hbar / m^* \omega_0}$. For weak Coulomb interaction, the singlet-triplet degeneracy occurs at $\omega_c^* = 2\pi^{-1/3} \omega_0 (2a_B^* / \lambda_0)^{2/3}$. In Fig. 5.2(b), we plot the ratio ω_c^* / ω_0 as a function of a_B^* / λ_0 ; the dotted curve corresponds to using the following crossover function

$$\frac{\omega_c^*}{\omega_0} = \left[1 + \left(\frac{2}{\pi^{1/3}} - 1 \right) \mathcal{F}(\lambda_0 / a_B^*) \right] \left(\frac{\lambda_0}{2a_B^*} \right)^{-2/3}, \quad (5.16)$$

where $\mathcal{F}(x) = (1 + 0.11x^2) / (1 + 0.3x^{4/3})^2$.

We discuss now the accuracy of our variational method. We rewrite Eq. (5.9) in the following form

$$\mathcal{H}_m = \tilde{\mathcal{H}}_m + V, \quad (5.17)$$

where $\tilde{\mathcal{H}}_m$ has the eigenvalues $\tilde{\varepsilon}_{nm} = \hbar\tilde{\omega}(2n + 1 + \sqrt{m^2 + \gamma})$ and the eigenfunctions given in Eq. (5.12). The perturbation

$$V = \frac{\hbar^2}{m^*} \left(\frac{1}{a_B^* r} - \frac{\gamma}{r^2} \right) + \frac{m^*}{4} (\omega^2 - \tilde{\omega}^2) r^2, \quad (5.18)$$

is expected to be “small” when the variational method works, with “small” meaning that the off-diagonal matrix elements of V are much smaller than the level spacing (the diagonal part of V needs not be small). We can show that indeed $V \ll \tilde{\mathcal{H}}_m$ in the case $\lambda / a_B^* \ll 1$, and also in the case $\lambda / a_B^* \gg 1$ for transitions involving the ground

state. As for intermediate strengths of the Coulomb interaction ($\lambda/a_B^* \sim 1$), there is no small parameter in the problem, which can justify the assumption $V \ll \tilde{\mathcal{H}}_m$. Nonetheless, we calculate the matrix elements of V (see Appendix E) between the ground and excited states, and find that they are numerically small, as compared to the level spacing $2\hbar\tilde{\omega}$. In particular, we find that the matrix element $\langle \tilde{f}_{1m} | V | \tilde{f}_{0m} \rangle$ is identically zero, if the variational parameter $\tilde{\omega}$ minimizes the energy of the ground state in Eq. (5.13) [see also Eq. (D.1)]. Furthermore, we determine an upper bound on the absolute value of any of the remaining matrix elements ($n \geq 2$). We find that, in both $m = 0$ and $|m| = 1$ cases, the matrix element $\langle \tilde{f}_{2,m} | V | \tilde{f}_{0m} \rangle$ has the largest value in the crossover region $\lambda/a_B^* \sim 1$. If measured in terms of the level spacing $2\hbar\tilde{\omega}$, this upper bound is approximately 0.1 and 0.03, for the $m = 0$ and $|m| = 1$ cases, respectively. Next, we characterize the accuracy of our variational method in terms of the fidelity

$$F = \left| \langle \Psi | \tilde{\Psi} \rangle \right|^2, \quad (5.19)$$

where $\Psi(r) \equiv f_{0m}(r)$ is the exact ground state of H_m , and $\tilde{\Psi}(r) \equiv \tilde{f}_{0m}(r)$ is the corresponding wave function calculated with the help of the variational method. We estimate the fidelity, using the perturbation theory expansion [122]

$$f_{0m}(r) = \tilde{f}_{0m}(r) + \sum_{n=1}^{\infty} \frac{\langle \tilde{f}_{nm} | V | \tilde{f}_{0m} \rangle}{\tilde{\varepsilon}_{0m} - \tilde{\varepsilon}_{nm}} \tilde{f}_{nm}(r) + \dots, \quad (5.20)$$

where we retain terms up to the second order in V (not shown). Thus, we obtain the infidelity

$$1 - F = \frac{1}{2} \sum_{n=2}^{\infty} \left| \frac{\langle \tilde{f}_{nm} | V | \tilde{f}_{0m} \rangle}{2n\hbar\tilde{\omega}} \right|^2, \quad (5.21)$$

where we dropped the $n = 1$ term, due to its zero contribution. The matrix elements $V_{nn'} \equiv \langle \tilde{f}_{nm} | V | \tilde{f}_{n'm} \rangle$ are calculated in Appendix E. In Fig. 5.3, we plot $\lg(1 - F)$ as a function of $\lg(\lambda/a_B^*)$ for $|m| = 0, 1$. Figure 5.3 shows that our variational method is fairly accurate, even in the crossover region $\lambda/a_B^* \sim 1$. Finally, we note that in Eqs. (5.20) and (5.21) we did not include the diagonal part of V in the energy denominators. More accurately, one has to take this part into account as well, since V_{nn} can be comparable to the level spacing $\hbar\tilde{\omega}$. However, it turns out that the difference $V_{nn} - V_{00} \geq 0$ monotonically increases with n in the whole range of λ/a_B^* . Therefore, when we replaced $2n\hbar\tilde{\omega} \rightarrow 2n\hbar\tilde{\omega} + V_{nn} - V_{00}$ in Eq. (5.21), we obtained only an insignificant reduction of $1 - F$ for $\lambda/a_B^* \sim 1$ on the scale of Fig. 5.3 (not shown).

5.4 Matrix elements of H_{SO}

The spin-orbit Hamiltonian H_{SO} in Eq. (5.3) connects different spin components and orbital wave functions. The matrix elements of H_{SO} read

$$\langle \mathbf{n}\mathbf{s} | H_{SO} | \mathbf{n}'\mathbf{s}' \rangle = i(E_{\mathbf{n}} - E_{\mathbf{n}'}) \sum_{j=1,2} \langle \mathbf{n} | \boldsymbol{\xi}_j | \mathbf{n}' \rangle \cdot \langle \mathbf{s} | \boldsymbol{\sigma}_j | \mathbf{s}' \rangle, \quad (5.22)$$

where $E_{\mathbf{n}}$ and $|\mathbf{n}\rangle = |NMnm\rangle$ are, respectively, the eigenenergies and eigenfunctions of H_d (see Sec. 5.3), and \mathbf{s} stands for the spin quantum numbers of two electrons. The vector $\boldsymbol{\xi}_j$ has a simple form in the coordinate frame: $x' = (x + y)/\sqrt{2}$, $y' = -(x - y)/\sqrt{2}$, $z' = z$, namely

$$\boldsymbol{\xi}_j = (y'_j/\lambda_-, x'_j/\lambda_+, 0), \quad (j = 1, 2), \quad (5.23)$$

where $\lambda_{\pm} = \hbar/m^*(\beta \pm \alpha)$ are the spin-orbit lengths. To obtain Eq. (5.22), we used the definition of momentum, $\mathbf{p}_j = (im^*/\hbar)[H_d, \mathbf{r}_j]$, with H_d given in Eq. (5.2). Note that, due to the linear in p form of H_{SO} , the matrix elements (5.22) vanish at the point of singlet-triplet degeneracy².

The spin states of two electrons $|\mathbf{s}\rangle$ are the singlet (S) and triplet (T) states:

$$|S\rangle = \frac{1}{\sqrt{2}}(|\uparrow\downarrow\rangle - |\downarrow\uparrow\rangle), \quad (5.24)$$

$$|T_+\rangle = |\uparrow\uparrow\rangle, \quad |T_-\rangle = |\downarrow\downarrow\rangle, \quad (5.25)$$

$$|T_0\rangle = \frac{1}{\sqrt{2}}(|\uparrow\downarrow\rangle + |\downarrow\uparrow\rangle), \quad (5.26)$$

where, arrows in the first (second) place denote the spin state of the first (second) electron. Using the representation in terms of $\mathbf{R} = (\mathbf{r}_1 + \mathbf{r}_2)/2$ and $\mathbf{r} = \mathbf{r}_1 - \mathbf{r}_2$, we write

$$\sum_{j=1,2} \boldsymbol{\xi}_j \cdot \boldsymbol{\sigma}_j = \boldsymbol{\xi}^R \cdot \boldsymbol{\Sigma} + \frac{1}{2} \boldsymbol{\xi}^r \cdot \boldsymbol{\sigma}, \quad (5.27)$$

where $\boldsymbol{\Sigma} = \boldsymbol{\sigma}_1 + \boldsymbol{\sigma}_2$ and $\boldsymbol{\sigma} = \boldsymbol{\sigma}_1 - \boldsymbol{\sigma}_2$, and also $\boldsymbol{\xi}^R = (\boldsymbol{\xi}_1 + \boldsymbol{\xi}_2)/2$ and $\boldsymbol{\xi}^r = \boldsymbol{\xi}_1 - \boldsymbol{\xi}_2$. Then, it is easy to see that the following matrix elements vanish

$$\langle S | H_{SO} | S \rangle = \langle T_0 | H_{SO} | T_0 \rangle = \langle T_+ | H_{SO} | T_- \rangle = 0. \quad (5.28)$$

Next, since the operator $\boldsymbol{\Sigma}$ is nonzero only in the triplet subspace and $\boldsymbol{\sigma}$ only between the singlet and triplets, all matrix elements of H_{SO} in the triplet subspace are proportional to $\boldsymbol{\xi}^R$, and those connecting singlet and triplet are proportional to $\boldsymbol{\xi}^r$. For a magnetic field along $\mathbf{l} = \mathbf{B}/B$, we thus have

$$\langle \mathbf{n}T_{\pm} | H_{SO} | \mathbf{n}'T_{\pm} \rangle = \pm 2i(E_{\mathbf{n}} - E_{\mathbf{n}'}) \langle \mathbf{n} | \boldsymbol{\xi}^R | \mathbf{n}' \rangle \cdot \mathbf{l}, \quad (5.29)$$

$$\langle \mathbf{n}T_{\pm} | H_{SO} | \mathbf{n}'T_0 \rangle = 2i\sqrt{2}(E_{\mathbf{n}} - E_{\mathbf{n}'}) \langle \mathbf{n} | \boldsymbol{\xi}^R | \mathbf{n}' \rangle \cdot (\mathbf{X} \mp i\mathbf{Y}), \quad (5.30)$$

²In the presence of Zeeman interaction, this should be understood as the degeneracy of the states $|S\rangle$ and $|T_0\rangle$.

where \mathbf{X} , \mathbf{Y} and $\mathbf{Z} \equiv \mathbf{l}$ are unit vectors of a coordinate frame with \mathbf{Z} along the spin quantization axis. One possible choice of \mathbf{X} and \mathbf{Y} is: $\mathbf{X} = (\sin \varphi', -\cos \varphi', 0)$ and $\mathbf{Y} = (\cos \varphi' \cos \theta, \sin \varphi' \cos \theta, -\sin \theta)$, where $\varphi' = \varphi - \pi/4$ and we wrote vectors in the frame (x', y', z) . Note that for the vector \mathbf{l} in this frame we have $\mathbf{l} = (\cos \varphi' \sin \theta, \sin \varphi' \sin \theta, \cos \theta)$. The matrix elements of $\boldsymbol{\xi}^R$ can be easily evaluated using the wave functions in Eqs. (5.6) and (5.8). To avoid extra phase factors due to the $(\pi/4)$ -rotation in going from (x, y, z) to (x', y', z) , we replace $\varphi_R \rightarrow \varphi_{R'}$ and $\varphi_r \rightarrow \varphi_{r'}$ in Eqs. (5.6) and (5.7), respectively. Thus, e.g., we have $R_{\pm} \equiv R_{x'} \pm iR_{y'} = Re^{\pm i\varphi_{R'}}$ and $|NM\rangle = R_{nm}(R)e^{iM\varphi_{R'}}/\sqrt{2\pi}$. Then, the matrix elements $\langle NM|\boldsymbol{\xi}^R|N'M'\rangle$ of the vector

$$\boldsymbol{\xi}^R = \left(i\frac{R_- - R_+}{2\lambda_-}, \frac{R_- + R_+}{2\lambda_+}, 0 \right) \quad (5.31)$$

are given in terms of the following matrix elements,

$$\begin{aligned} \langle NM|R_{\pm}|N'M'\rangle &= \Lambda\delta_{M,M'\pm 1} \left(\delta_{N,N'}\sqrt{N + \frac{|M| + |M'| + 1}{2}} - \right. \\ &\quad \left. \delta_{N+|M|,N'+|M'|}\sqrt{\frac{N + N' + 1}{2}} \right). \end{aligned} \quad (5.32)$$

In particular, for the ground state $N' = M' = 0$, we have non-zero only $\langle 0, \pm 1|R_{\pm}|00\rangle = \Lambda$, which yields

$$\langle NM|\boldsymbol{\xi}^R|00\rangle = \sum_{\pm} \frac{\Lambda}{2}\delta_{N,0}\delta_{M,\pm 1} (\mp i\lambda_-^{-1}, \lambda_+^{-1}, 0). \quad (5.33)$$

Next, we calculate the remaining three matrix elements of H_{SO} in Eq. (5.22). They connect the singlet and triplet states, and therefore, the second term in Eq. (5.27) contributes here. We obtain

$$\langle \mathbf{n}T_0|H_{SO}|\mathbf{n}'S\rangle = i(E_{\mathbf{n}} - E_{\mathbf{n}'})\langle \mathbf{n}|\boldsymbol{\xi}^r|\mathbf{n}'\rangle \cdot \mathbf{l}, \quad (5.34)$$

$$\langle \mathbf{n}T_{\pm}|H_{SO}|\mathbf{n}'S\rangle = \mp \frac{i}{\sqrt{2}}(E_{\mathbf{n}} - E_{\mathbf{n}'})\langle \mathbf{n}|\boldsymbol{\xi}^r|\mathbf{n}'\rangle \cdot (\mathbf{X} \mp i\mathbf{Y}), \quad (5.35)$$

where \mathbf{X} and \mathbf{Y} have been defined above. Analogously to the previous case, we express $\boldsymbol{\xi}^r$ in terms of $r_{\pm} = r_{x'} \pm ir_{y'}$,

$$\boldsymbol{\xi}^r = \left(i\frac{r_- - r_+}{2\lambda_-}, \frac{r_- + r_+}{2\lambda_+}, 0 \right), \quad (5.36)$$

which allows us to evaluate $\langle nm|\boldsymbol{\xi}^r|n'm'\rangle$, provided we know $\langle nm|r_{\pm}|n'm'\rangle$. Using the wave function in Eq. (5.7), we obtain

$$\langle nm|r_{\pm}|n'm'\rangle = \delta_{m,m'\pm 1} \int_0^{\infty} r \tilde{f}_{nm}(r) \tilde{f}_{n'm'}(r) dr, \quad (5.37)$$

5.4. MATRIX ELEMENTS OF H_{SO}

where we recalled that $\mathcal{R}_{nm}(r) = \tilde{f}_{nm}(r)/\sqrt{r}$, with $\tilde{f}_{nm}(r)$ given in Eq. (5.12). The function $\tilde{f}_{nm}(r)$ contains the variational parameters γ and $\tilde{\omega}$, which are determined from the minimum of the ground state energy of \mathcal{H}_m in Eq. (5.9), for each $|m|$ independently. Therefore, apart from the explicit dependence on $|m|$ in Eq. (5.12), the function $\tilde{f}_{nm}(r)$ depends on $|m|$ also via γ and $\tilde{\lambda} \sim \sqrt{1/\tilde{\omega}}$. In what follows, we provide γ and $\tilde{\lambda} \sim \sqrt{1/\tilde{\omega}}$ with an index m . We thus rewrite Eq. (5.12) in the following form

$$\tilde{f}_{nm}(r) = \sqrt{\frac{2\Gamma(n+t_m)}{n!}} \frac{r^{t_m-1/2}}{\Gamma(t_m)\tilde{\lambda}_m^{t_m}} \exp\left(\frac{-r^2}{2\tilde{\lambda}_m^2}\right) {}_1F_1\left(-n, t_m; r^2/\tilde{\lambda}_m^2\right), \quad (5.38)$$

where $t_m = 1 + \sqrt{m^2 + \gamma_m}$ and $\tilde{\lambda}_m = \sqrt{2\hbar/m^*\tilde{\omega}_m}$. Then, evaluating the integral in Eq. (5.37), we obtain

$$\begin{aligned} \langle nm|r_{\pm}|n'm'\rangle &= \lambda_{mm'}\delta_{m,m'\pm 1} \sqrt{\frac{\Gamma(n+t_m)\Gamma(n'+t_{m'})}{n!n'\Gamma(t_m)\Gamma(t_{m'})}} \times \\ &F_2\left(\frac{1+t_m+t_{m'}}{2}; -n, -n'; t_m, t_{m'}; \frac{2\tilde{\lambda}_{m'}^2}{\tilde{\lambda}_m^2 + \tilde{\lambda}_{m'}^2}, \frac{2\tilde{\lambda}_m^2}{\tilde{\lambda}_{m'}^2 + \tilde{\lambda}_m^2}\right), \end{aligned} \quad (5.39)$$

where $F_2(\alpha; \beta, \beta'; \gamma, \gamma'; x, y)$ is a hypergeometric function of two variables, see below. In Eq. (5.39), we used the notation

$$\lambda_{mm'} = \frac{\tilde{\lambda}_m^{1+t_m}\tilde{\lambda}_{m'}^{1+t_{m'}}}{\sqrt{\Gamma(t_m)\Gamma(t_{m'})}} \left(\frac{2}{\tilde{\lambda}_m^2 + \tilde{\lambda}_{m'}^2}\right)^{\frac{1+t_m+t_{m'}}{2}} \Gamma\left(\frac{1+t_m+t_{m'}}{2}\right). \quad (5.40)$$

We note that the diagonal part of $\lambda_{mm'}$ gives the average distance between the electrons in a state with $n = 0$,

$$\langle r \rangle_m \equiv \lambda_{mm} = \tilde{\lambda}_m \frac{\Gamma(3/2 + \sqrt{m^2 + \gamma_m})}{\Gamma(1 + \sqrt{m^2 + \gamma_m})}. \quad (5.41)$$

In particular, for strong Coulomb interaction, we have $\langle r \rangle_m = \tilde{\lambda}_m \gamma_m^{1/4} = \lambda(\lambda/2a_B^*)^{1/3}$, in the leading asymptotic order of $\lambda/a_B^* \gg 1$.

The function $F_2(\alpha; \beta, \beta'; \gamma, \gamma'; x, y)$ used in Eq. (5.39) is defined by the series

$$F_2(\alpha; \beta, \beta'; \gamma, \gamma'; x, y) = \sum_{k,l=0}^{\infty} \frac{(\alpha)_{k+l}(\beta)_k(\beta')_l}{(\gamma)_k(\gamma')_l k! l!} x^k y^l, \quad (5.42)$$

where $(x)_k = \Gamma(x+k)/\Gamma(x)$ is the Pochhammer symbol, and the variables x and y should obey the condition $|x|+|y| < 1$ to guarantee convergence. In our case, however, we have $x = 2\tilde{\lambda}_{m'}^2/(\tilde{\lambda}_m^2 + \tilde{\lambda}_{m'}^2)$ and $y = 2\tilde{\lambda}_m^2/(\tilde{\lambda}_{m'}^2 + \tilde{\lambda}_m^2)$, which gives $|x|+|y| = 2 > 1$. Nevertheless, the series in Eq. (5.42) contains a finite number of terms, and thus converges. Indeed, since the second and third arguments of $F_2(\alpha; \beta, \beta'; \gamma, \gamma'; x, y)$ in

Eq. (5.39) are negative integers, $\beta = -n$ and $\beta' = -n'$, the Pochhammer symbols $(\beta)_k$ and $(\beta')_l$ in Eq. (5.42) are identically zero for $k > n$ and $l > n'$, and thus, the summation in Eq. (5.42) ends at $k = n$ and $l = n'$.

Finally, we note that, in particular, for $n = n' = 0$, Eq. (5.39) gives

$$\langle 0m|r_{\pm}|0m'\rangle = \lambda_{mm'}\delta_{m,m'\pm 1}. \quad (5.43)$$

In the absence of Coulomb interaction, Eq. (5.39) reduces to a simpler expression, as given in Eq. (5.32), but with capital letters replaced by lower-case ones.

5.5 Electron states with spin-orbit interaction

Using the results of Sections 5.3 and 5.4, we proceed now to construct a perturbation theory in the vicinity of the singlet-triplet transition. We assume that the spin-orbit interaction in the quantum dot is weak. As we show below, the small parameter of our perturbation theory is given by the average distance between the electrons in the dot divided by the spin-orbit length, $\langle r \rangle_m / \lambda_{SO} \ll 1$, where $\langle r \rangle_m$ is given in Eq. (5.41) and λ_{SO} is the smallest absolute value of $\lambda_{\pm} = \hbar / m^*(\beta \pm \alpha)$. Next, we consider separately the case of zero and finite Zeeman interaction.

5.5.1 Case of zero Zeeman interaction ($g = 0$)

We consider the Hamiltonian $H = H_d + H_{SO}$. In this case, the matrix elements of the spin-orbit interaction vanish at the singlet-triplet degeneracy point, see Eq. (5.22), and we can use perturbation theory for the non-degenerate case [122] up to a close vicinity of the singlet-triplet degeneracy point. We have to make sure only that, within each degenerate multiplet, such as a triplet, the basis states are chosen correctly. For this, we write down the correction to the dot Hamiltonian in the second order of H_{SO} ,

$$\begin{aligned} \Delta H^{(2)} &= \frac{1}{2} \left[\left(\hat{L}_d^{-1} H_{SO} \right), H_{SO} \right] \\ &= \frac{\hbar}{m^* \lambda_- \lambda_+} \sum_j (x_j p_{jy} - y_j p_{jx}) \sigma_{jz}, \end{aligned} \quad (5.44)$$

where $\hat{L}_d A = [H_d, A]$ for $\forall A$, and the z -axis is perpendicular to the plane of the 2DEG. Going to the relative coordinates in Eq. (5.44) and neglecting transitions between levels which never intersect, we obtain

$$\Delta H^{(2)} \simeq \frac{\hbar^2}{2m^* \lambda_- \lambda_+} \left[\ell_z^R + \ell_z^r + \frac{eB_z}{\hbar c} \left(R^2 + \frac{r^2}{4} \right) \right] \Sigma_z, \quad (5.45)$$

where $\ell_z^R = -i\partial/\partial\varphi_R$ and $\ell_z^r = -i\partial/\partial\varphi_r$ and we have used the cylindrical gauge $\mathbf{A}(\mathbf{r}) = \frac{1}{2}[\mathbf{B} \times \mathbf{r}]$. Equation (5.45) gives a spin-orbit induced spin-splitting of the dot

5.5. ELECTRON STATES WITH SPIN-ORBIT INTERACTION

energy levels. This splitting can be viewed as an effective Zeeman energy which sets the quantization axis along the [001] crystallographic direction. The terms which we neglected in Eq. (5.45) are proportional to $\sigma_z = \sigma_{1z} - \sigma_{2z}$ and thus violate the symmetry of a Zeeman interaction. However, since these terms are purely off-diagonal, their contribution goes to higher orders.

The leading order correction to the two-electron wave function can be easily found using the matrix elements of H_{SO} calculated in Section 5.4. We choose the unit vectors \mathbf{X} , \mathbf{Y} and $\mathbf{Z} \equiv \mathbf{l}$ to point along the axes x' , y' and z , respectively (this fixes our spin measurement frame). The singlet and triplet states in the first order of H_{SO} then become,

$$\begin{aligned} |SNMnm\rangle' &= |SNMnm\rangle + |NM\rangle \frac{\sqrt{2}m^*}{\hbar} \times \\ &\quad \sum_{n'} \{ |n', m-1\rangle (|T_+\rangle\alpha + |T_-\rangle\beta) \langle n', m-1|r_-|nm\rangle + \\ &\quad |n', m+1\rangle (|T_-\rangle\alpha + |T_+\rangle\beta) \langle n', m+1|r_+|nm\rangle \}, \end{aligned} \quad (5.46)$$

$$\begin{aligned} |T_{\pm}NMnm\rangle' &= |T_{\pm}NMnm\rangle - |SNM\rangle \frac{\sqrt{2}m^*}{\hbar} \times \\ &\quad \sum_{n'} \{ |n', m \pm 1\rangle \alpha \langle n', m \pm 1|r_{\pm}|nm\rangle + \\ &\quad |n', m \mp 1\rangle \beta \langle n', m \mp 1|r_{\mp}|nm\rangle \} \pm |T_0nm\rangle \frac{2\sqrt{2}m^*}{\hbar} \times \\ &\quad \sum_{N'} \{ |N', M \pm 1\rangle \alpha \langle N', M \pm 1|R_{\pm}|NM\rangle + \\ &\quad |N', M \mp 1\rangle \beta \langle N', M \mp 1|R_{\mp}|NM\rangle \}, \end{aligned} \quad (5.47)$$

$$\begin{aligned} |T_0NMnm\rangle' &= |T_0NMnm\rangle + |nm\rangle \frac{2\sqrt{2}m^*}{\hbar} \times \\ &\quad \sum_{N'} \{ |N'M+1\rangle (|T_-\rangle\alpha - |T_+\rangle\beta) \langle N', M+1|R_+|NM\rangle - \\ &\quad |N'M-1\rangle (|T_+\rangle\alpha - |T_-\rangle\beta) \langle N', M-1|R_-|NM\rangle \}. \end{aligned} \quad (5.48)$$

We note that Eqs. (5.46), (5.47) and (5.48) can be rewritten in the following general form

$$|\mathbf{ns}\rangle' = (1 - S) |\mathbf{ns}\rangle, \quad (5.49)$$

$$S = i\boldsymbol{\xi}^R \cdot \boldsymbol{\Sigma} + \frac{i}{2}\boldsymbol{\xi}^r \cdot \boldsymbol{\sigma} = i \sum_{j=1,2} \boldsymbol{\xi}_j \cdot \boldsymbol{\sigma}_j, \quad (5.50)$$

which can be viewed as a spin-dependent gauge transformation $|\mathbf{ns}\rangle' = \exp(-S)|\mathbf{ns}\rangle$ in leading order of S . We note that this transformation is identical to that used for a single-electron quantum dot [90, 175, 183, 185], with the only difference that we sum over electrons here. Using the states in Eq. (5.49), it is easy to see that the

matrix elements of any scalar potential, such as, e.g., the electron-phonon interaction in Eq. (5.5), are diagonal in the spin index,

$$\langle \mathbf{ns} | e^S U_{\text{ph}}(\mathbf{r}_1, \mathbf{r}_2) e^{-S} | \mathbf{n}' \mathbf{s}' \rangle = (U_{\text{ph}})_{\mathbf{nn}'} \delta_{ss'}, \quad (5.51)$$

because S in Eq. (5.50), being a function of coordinates only, commutes with scalar potentials. Thus, the spin degrees of freedom in the quantum dot decouple from all scalar potential fluctuations in the first order of H_{SO} . Next, we discuss the validity of this statement for quantum dots of arbitrary shape.

We arrived at Eqs. (5.49) and (5.50) by considering the harmonic confining potential. For this confining potential and any other one possessing a center of inversion in the (x, y) -plane, the diagonal in orbit part

$$S_{\mathbf{ns}, \mathbf{ns}'} = i \sum_j (\boldsymbol{\xi}_j)_{\mathbf{nn}} \cdot (\boldsymbol{\sigma}_j)_{\mathbf{ss}'} \quad (5.52)$$

is identically zero for all orbital states $|\mathbf{n}\rangle$, or it can be made so by shifting the origin of coordinates. This allowed us to choose the quantization axis for all orbital levels equally (along z), as required by the interaction (5.45). We now consider a dot confining potential of an arbitrary shape, for which $S_{\mathbf{ns}, \mathbf{ns}'}$ in Eq. (5.52) is not necessarily zero. We also allow for an arbitrary number of electrons in the quantum dot. As we show below, the transformation (5.49) takes then the form

$$|\mathbf{ns}\rangle' = (1 - S_Q) e^{-S_P} |\mathbf{ns}\rangle, \quad (5.53)$$

where S_P and S_Q are some operators, respectively, diagonal and off-diagonal in the Hilbert space of H_d , i.e. $\mathcal{P}S_P = S_P$ and $\mathcal{Q}S_Q = S_Q$, with $\mathcal{Q} = 1 - \mathcal{P}$ and $\mathcal{P}A = \sum_{\mathbf{n}} A_{\mathbf{nn}} |\mathbf{n}\rangle \langle \mathbf{n}|$ for $\forall A$. Here, we assume for simplicity that the Hamiltonian H_d has no orbital degeneracies (otherwise one had to regroup the sets \mathbf{n} and \mathbf{s} such that $E_{\mathbf{n}}$ were non-degenerate). We start with writing down the following formally exact equality of the Schrieffer-Wolff transformation,

$$e^S (H_d + H_{SO}) e^{-S} = H_d + \Delta H, \quad (5.54)$$

where $S = -S^\dagger$ is chosen such that $\mathcal{P}\Delta H = \Delta H$. The Hamiltonian $H' = H_d + \Delta H$ is diagonal in the basis of H_d and has the same energy spectrum as the Hamiltonian $H = H_d + H_{SO}$; the latter is diagonal in a basis related by $\exp(-S)$ to the basis of H_d . Since in our case $\mathcal{P}H_{SO} = 0$ and thus $\Delta H = o(H_{SO}^2)$, it follows from Eq. (5.54) that $[H_d, S] = H_{SO}$ in leading order of H_{SO} . In matrix form, the latter equation reads

$$(E_{\mathbf{n}} - E_{\mathbf{n}'}) S_{\mathbf{ns}, \mathbf{n}'\mathbf{s}'} = i (E_{\mathbf{n}} - E_{\mathbf{n}'}) \sum_j (\boldsymbol{\xi}_j)_{\mathbf{nn}'} \cdot (\boldsymbol{\sigma}_j)_{\mathbf{ss}'}, \quad (5.55)$$

where we used Eq. (5.22) for matrix elements of H_{SO} . Clearly, for $E_{\mathbf{n}} \neq E_{\mathbf{n}'}$, we obtain from Eq. (5.55) that $S_{\mathbf{ns}, \mathbf{n}'\mathbf{s}'} = i \sum_j (\boldsymbol{\xi}_j)_{\mathbf{nn}'} \cdot (\boldsymbol{\sigma}_j)_{\mathbf{ss}'}$, which coincides with what one obtains from Eq. (5.50). Further, we note that the fully diagonal part $S_{\mathbf{ns}, \mathbf{ns}}$ are

5.5. ELECTRON STATES WITH SPIN-ORBIT INTERACTION

unimportant phases and we do not discuss it here. The diagonal in orbit part $S_{\text{ns,ns}'}$ remains undefined by Eq. (5.55), because the perturbation H_{SO} does not lift the spin degeneracy in the first order ($\mathcal{P}H_{SO} = 0$). Next, we split the transformation (5.54) into a product, $\exp(-S) = (1 - S_{\mathcal{Q}}) \exp(-S_{\mathcal{P}})$, where we retain only the leading order of $S_{\mathcal{Q}}$. For $S_{\mathcal{Q}}$, we again have $[H_d, S_{\mathcal{Q}}] = H_{SO}$, which now gives

$$S_{\mathcal{Q}} = (1 - \mathcal{P}) \sum_j i \boldsymbol{\xi}_j \cdot \boldsymbol{\sigma}_j, \quad (5.56)$$

where the factor $(1 - \mathcal{P})$ zeroes out the diagonal in orbit part. Note that $S_{\mathcal{Q}}$ does not generally commute with scalar potentials and, unless $S_{\mathcal{P}}$ can be chosen such as in Eq. (5.52), there can be, in principle, spin relaxation in the first order of H_{SO} . As we have seen above the spin splitting in the dot occurs in the second or higher orders of H_{SO} and is formally given by ΔH in Eq. (5.54). The operator $S_{\mathcal{P}}$ is chosen such that ΔH is diagonal in the spin subspace of each orbital level. Therefore, $S_{\mathcal{P}}$ depends on the details of H_d , i.e. on the confining potential and the number of electrons in the quantum dot. Next we briefly discuss ΔH for the two-electron case considered in this chapter.

The fine structure of a two-electron quantum dot in the absence of orbital degeneracy (such as singlet-triplet degeneracy) is described by a Hamiltonian of the following form

$$\Delta H = \mathbf{A} \cdot \boldsymbol{\Sigma} + \sum_{\mu\nu} B_{\mu\nu} \Sigma_\mu \Sigma_\nu, \quad (5.57)$$

where A_μ and $B_{\mu\nu} = B_{\nu\mu}$ are operators diagonal in the orbital space of H_d . In Eq. (5.57), we did not include energy shifts of the singlet levels, since they are negligible on the scale of the dot level spacing. On the same reason, we also neglect the triplet shifts by setting $\sum_\mu B_{\mu\mu} = 0$. The term $\mathbf{A} \cdot \boldsymbol{\Sigma}$ in Eq. (5.57) can be viewed as a spin-orbit induced Zeeman interaction. In leading order, \mathbf{A} is perpendicular to the 2DEG and can be found from Eq. (5.45), which remains valid also in this case. On average \mathbf{A} has the following magnitude

$$\langle A \rangle = \frac{\hbar\omega_c}{4\lambda_- \lambda_+} \sum_{j=1,2} \langle r_j^2 \rangle, \quad (5.58)$$

where $\langle \dots \rangle$ denotes averaging over many orbital levels. Note that \mathbf{A} vanishes at zero magnetic field due to time reversal symmetry. The remaining terms (second order in $\boldsymbol{\Sigma}$) in Eq. (5.57) describe on-site spin anisotropy. For a given triplet level, we can choose a coordinate frame in which $\langle \mathbf{n} | B_{\mu\nu} | \mathbf{n} \rangle \sim \delta_{\mu\nu}$, and since $\sum_\mu B_{\mu\mu} = 0$, there remain only two independent components of $B_{\mu\nu}$. We note that $B_{\mu\nu}$ is of higher order in H_{SO} than \mathbf{A} ; however, since the spin anisotropy interaction is time-reversal invariant, $B_{\mu\mu} \Sigma_\mu^2$ are the only terms left at zero magnetic field.

We now discuss the relevance of the fine structure to the spin relaxation. We have seen above that the spin-orbit interaction can induce spin splitting in the quantum dot, and for quantum dots without center of inversion in the (x, y) -plane this results

in spin coupling to potential fluctuations in the first order of H_{SO} . We mention first several cases when this coupling does not result in spin relaxation in the two-electron quantum dot (still assuming $g = 0$).

(i) There can be no relaxation between singlet and triplet states in the first order of H_{SO} without Zeeman interaction. This is because $S_{\mathbf{ns},\mathbf{ns}'}$ in Eq. (5.52) is effectively zero whenever a singlet state is involved, and then we come back to Eqs. (5.49), (5.50) and (5.51), resulting in no spin decay. Indeed, the left-hand side of Eq. (5.52) can be rewritten as follows

$$\mathcal{P} \sum_{j=1,2} i\xi_j \cdot \sigma_j = i\mathcal{P}\xi^R \cdot \Sigma, \quad (5.59)$$

where we used the symmetry with respect to exchange of electrons. In a transition involving a singlet state, the operator Σ gives zero. Thus, $S_{\mathbf{ns},\mathbf{ns}'} \sim \Sigma$ is effectively zero. As a result, the singlet state is block-diagonal in coupling to scalar potential fluctuations [cf. Eq. (5.51)], i.e. a singlet can relax only to a singlet.

(ii) There can be no relaxation between spin states belonging to one and the same orbital level in the first order of H_{SO} without Zeeman interaction. This is obvious since $\mathcal{P}[S_Q, U_{\text{ph}}] = 0$, see Eq. (5.51) with $S \rightarrow S_Q$.

After (i) and (ii) we are now left only with transitions between triplet states of different orbital levels. Let the triplet states be fine-split with some characteristic energy Δ_{fs} . This fine splitting can be calculated from the Hamiltonian (5.57), using coupling constants obtained from the perturbation theory expansion of Eq. (5.54). However, for the sake of making a simple argument here, we assume Δ_{fs} to be an independent parameter. Clearly, if $\Delta_{\text{fs}} = 0$, we are free to construct any linear combination of states within a triplet; so we can recover Eqs. (5.49), (5.50) and (5.51), which yield no spin relaxation. To be more rigorous, we formulate an additional condition when there is no spin decay in the first order of H_{SO} .

(iii) If the orbital relaxation time τ is much shorter than \hbar/Δ_{fs} , then the spin relaxation between triplet states belonging to different orbital levels is suppressed. To explain this result, we note that, provided $\Delta_{\text{fs}} < \hbar/\tau$, we can choose to work with the states in Eqs. (5.49) and (5.50) instead of the true eigenstates (5.53), because the internal evolution of the states (5.49), being due to the fine structure splitting Δ_{fs} , is slower than the lifetime τ . Then, since the states (5.49) undergo no spin relaxation, the spins can be considered as decoupled from the potential fluctuations on the time scale \hbar/Δ_{fs} . As a result, the spin relaxation occurs in the second or higher orders of H_{SO} .

Finally, we conclude that spin relaxation in the first order of H_{SO} and without Zeeman interaction is possible only between spin triplet states belonging to different orbital levels and only if $\Delta_{\text{fs}} > \hbar/\tau$. The interaction which causes spin relaxation is proportional to $(\xi_{\mathbf{nn}}^R - \xi_{\mathbf{mm}}^R) \cdot \Sigma$, where \mathbf{n} and \mathbf{m} denote the involved orbital states. We do not consider this mechanism in further detail here, since it refers to an asymmetric quantum dot, which goes beyond our model.

5.5.2 Case of finite Zeeman interaction ($g \neq 0$)

We consider now the Hamiltonian $H = H_d + H_Z + H_{SO}$ in the vicinity of a singlet-triplet transition. We assume the Zeeman splitting $E_Z = g\mu_B B$ to be large compared to both the fine structure splitting Δ_{fs} and the level broadening \hbar/τ . This allows us to set the spin quantization axis along the applied magnetic field \mathbf{B} . In Section 5.5.1, we found the wave functions of two electrons in the quantum dot for the case without Zeeman interaction. It is convenient now to use these functions as basis states for studying the effect of Zeeman interaction. We perform the following unitary transformation [175, 183, 185], $\tilde{H} = e^{S_Q}(H_d + H_Z + H_{SO})e^{-S_Q}$, with S_Q given in leading order in Eq. (5.56). After this transformation, a basis state $|\mathbf{ns}\rangle$, associated with the Hamiltonian \tilde{H} , will correspond to the basis state $|\mathbf{ns}'\rangle = (1 - S_Q)|\mathbf{ns}\rangle$, associated with the Hamiltonian $H = H_d + H_Z + H_{SO}$. In the first order of H_{SO} , it is straightforward to obtain

$$\tilde{H} = H_d + H_Z + H_Z^{SO}, \quad (5.60)$$

$$H_Z^{SO} = E_Z \sum_j [\mathbf{l} \times \mathcal{Q}\boldsymbol{\xi}_j] \cdot \boldsymbol{\sigma}_j, \quad (5.61)$$

where $\mathbf{l} = \mathbf{B}/B$, $E_Z = g\mu_B B$, and \mathcal{Q} zeroes out the diagonal part of $\boldsymbol{\xi}_j$. Below, we consider the harmonic confining potential, for which we achieve $\mathcal{Q}\boldsymbol{\xi}_j = \boldsymbol{\xi}_j$ by choosing the origin of coordinates in the dot center. In Eq. (5.61), we can rewrite the sum over two electrons in terms of the relative coordinates,

$$\sum_j [\mathbf{l} \times \boldsymbol{\xi}_j] \cdot \boldsymbol{\sigma}_j = [\mathbf{l} \times \boldsymbol{\xi}^R] \cdot \boldsymbol{\Sigma} + \frac{1}{2} [\mathbf{l} \times \boldsymbol{\xi}^r] \cdot \boldsymbol{\sigma}. \quad (5.62)$$

The first term on the right-hand side of Eq. (5.62) admixes only triplet states with different orbital wave functions, and therefore, we can take it into account by means of perturbation theory for the non-degenerate case. In contrast, the second term on the right-hand side of Eq. (5.62) is *strong* at the singlet-triplet transition, since it connects singlet and triplet states which are degenerate. For this terms, we use below perturbation theory for the degenerate case [122]. The matrix elements of H_Z^{SO} in Eq. (5.61), therefore, read

$$\langle \mathbf{n}T_{\pm} | H_Z^{SO} | \mathbf{n}'T_0 \rangle = \mp 2i\sqrt{2}E_Z \langle \mathbf{n} | \boldsymbol{\xi}^R | \mathbf{n}' \rangle \cdot (\mathbf{X} \mp i\mathbf{Y}), \quad (5.63)$$

$$\langle \mathbf{n}T_{\pm} | H_Z^{SO} | \mathbf{n}'S \rangle = i\sqrt{2}E_Z \langle \mathbf{n} | \boldsymbol{\xi}^r | \mathbf{n}' \rangle \cdot (\mathbf{X} \mp i\mathbf{Y}), \quad (5.64)$$

$$\langle \mathbf{n}T_0 | H_Z^{SO} | \mathbf{n}'S \rangle = \langle \mathbf{n}T_- | H_Z^{SO} | \mathbf{n}'T_+ \rangle = 0 \quad (5.65)$$

where \mathbf{X} and \mathbf{Y} are unit vectors in the plane perpendicular to the applied magnetic field \mathbf{B} (see Sec. 5.4). Note that, according to Eq. (5.65), there is no admixture between any singlet $|S\rangle$ and triplet $|T_0\rangle$ states, as well as between any triplet states: $|T_+\rangle$ and $|T_-\rangle$. This will have an effect on the spin relaxation rates in Sec. 5.6.2, where the corresponding rates for the transitions $S \leftrightarrow T_0$ and $T_- \leftrightarrow T_+$ are found to be zero in leading order in spin-orbit interaction. Next, we use Eqs. (5.63) and

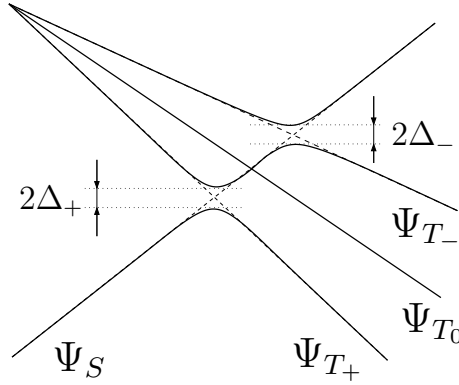


Figure 5.4: Sketch of the singlet-triplet transition in a quantum dot with spin-orbit interaction. The triplet level splits in three due to the Zeeman interaction. The singlet $|\Psi_S\rangle$ undergoes avoided crossing with the triplets $|\Psi_{T_\pm}\rangle$, with the splittings Δ_\pm given in Eq. (5.68). At the same time, the degeneracy of $|\Psi_S\rangle$ and $|\Psi_{T_0}\rangle$ at the transition point is not lifted.

(5.64) to find the two-electron wave functions for the lowest in energy singlet-triplet transition in the quantum dot.

We consider first a close vicinity of the singlet-triplet transition, where the contribution of *strong* matrix elements is dominant. Substituting Eq. (5.36) into Eqs. (5.63)–(5.65) and using Eq. (5.43), we obtain for $|\Psi_S\rangle = |0000S\rangle$ and $|\Psi_{T_{0,\pm}}\rangle = |000, -1, T_{0,\pm}\rangle$ the following expression

$$\langle \Psi_{T_\pm} | H_Z^{SO} | \Psi_S \rangle = \frac{iE_Z \lambda_{1,0}}{\sqrt{2}} \left[\left(\pm \frac{\cos \theta}{\lambda_-} - \frac{1}{\lambda_+} \right) \cos \varphi' + i \left(\frac{1}{\lambda_-} \mp \frac{\cos \theta}{\lambda_+} \right) \sin \varphi' \right], \quad (5.66)$$

$$\langle \Psi_{S,T_\pm} | H_Z^{SO} | \Psi_{T_0} \rangle = \langle \Psi_{T_+} | H_Z^{SO} | \Psi_{T_-} \rangle = 0, \quad (5.67)$$

where we used the convention for \mathbf{X} and \mathbf{Y} given below Eq. (5.30). Next, introducing $\Delta_\pm \equiv |\langle \Psi_{T_\pm} | H_Z^{SO} | \Psi_S \rangle|$, we obtain

$$\Delta_\pm = E_Z \frac{\lambda_{1,0}}{\sqrt{2}} \sqrt{\frac{1 - l_{x'}^2}{\lambda_-^2} + \frac{1 - l_{y'}^2}{\lambda_+^2} \mp \frac{2l_z}{\lambda_- \lambda_+}}, \quad (5.68)$$

where we made use of the components of $\mathbf{l} = (\cos \varphi' \sin \theta, \sin \varphi' \sin \theta, \cos \theta)$ to represent the angular dependence of Δ_\pm . The Coulomb interaction enters in Eqs. (5.66) and (5.68) via the quantity $\lambda_{1,0}$, which is defined in Eq. (5.40). Note that, approximately, we have $\lambda_{1,0} \approx \langle r \rangle$. And since the Coulomb repulsion increases $\langle r \rangle$, see Eq. (5.41), we expect a stronger effect of the spin-orbit interaction in quantum dots with a larger ratio λ/a_B^* .

The singlet-triplet transition is shown schematically in Fig. 5.4. The triplet level is split in three by the Zeeman interaction: $E_{T_0} = E_T$ and $E_{T_\pm} = E_T \mp E_Z$. The avoided

5.5. ELECTRON STATES WITH SPIN-ORBIT INTERACTION

crossing of the singlet state $|\Psi_S\rangle$ with the triplets $|\Psi_{T_\pm}\rangle$ occurs due to the interaction H_Z^{SO} , with the matrix elements given in Eq. (5.66). The splitting energies are the doubled Δ_\pm in Eq. (5.68). Note that the degeneracy of the singlet state with the triplet $|\Psi_{T_0}\rangle$ at the transition point is not lifted. This degeneracy, however, can be lifted in higher orders of H_{SO} . Next, we consider the interaction between the states: $|\Psi_S\rangle$, $|\Psi_{T_+}\rangle$, and $|\Psi_{T_-}\rangle$. And since the state $|\Psi_{T_0}\rangle$ couples to neither of these states, see Eq. (5.62) and the discussion thereafter, we disregard it for the time being here. Writing the wave function in the form

$$|\Psi\rangle = a|\Psi_S\rangle + b|\Psi_{T_+}\rangle + c|\Psi_{T_-}\rangle, \quad (5.69)$$

we obtain the following set of equations

$$\begin{pmatrix} E_S - E & W_{ST_+} & W_{ST_-} \\ W_{T_+S} & E_{T_+} - E & 0 \\ W_{T_-S} & 0 & E_{T_-} - E \end{pmatrix} \begin{pmatrix} a \\ b \\ c \end{pmatrix} = 0, \quad (5.70)$$

where W_{ST_\pm} stands for $\langle\Psi_S|H_Z^{SO}|\Psi_{T_\pm}\rangle$. The characteristic equation reads

$$E_S - E - \frac{\Delta_+^2}{E_{T_+} - E} - \frac{\Delta_-^2}{E_{T_-} - E} = 0, \quad (5.71)$$

where $E_{T_\pm} = E_T \mp E_Z$, and E_S and E_T are the energies of singlet $|\Psi_S\rangle$ and triplet state $|\Psi_{T_0}\rangle$, respectively. Since $\Delta_\pm \ll E_Z$, we can solve Eq. (5.71) in the secular approximation. Setting in turn Δ_- and Δ_+ to zero in Eq. (5.71), we find the following expressions, for the lower (+) and upper (-) solid curves in Fig. 5.4,

$$E_\pm = \frac{1}{2} \left[E_{T_\pm} + E_S \mp \sqrt{(E_{T_\pm} - E_S)^2 + 4\Delta_\pm^2} \right]. \quad (5.72)$$

Next, multiplying Eq. (5.71) by $(E_{T_+} - E)(E_{T_-} - E)$ and dividing the obtained polynomial by $E^2 - (E_+ + E_-)E + E_+E_-$, we obtain in leading order the solution for the S-shaped curve in Fig. 5.4,

$$E_0 = E_T + \frac{1}{2} \sqrt{(E_{T_+} - E_S)^2 + 4\Delta_+^2} - \frac{1}{2} \sqrt{(E_{T_-} - E_S)^2 + 4\Delta_-^2}. \quad (5.73)$$

Finally, the wave function of a level with the energy $E = E_\pm, E_0$ is given by Eq. (5.69), with the coefficients

$$b = \frac{\langle\Psi_{T_+}|H_Z^{SO}|\Psi_S\rangle}{E - E_{T_+}} a, \quad c = \frac{\langle\Psi_{T_-}|H_Z^{SO}|\Psi_S\rangle}{E - E_{T_-}} a, \quad (5.74)$$

$$a = \left[1 + \frac{\Delta_+^2}{(E - E_{T_+})^2} + \frac{\Delta_-^2}{(E - E_{T_-})^2} \right]^{-1/2}. \quad (5.75)$$

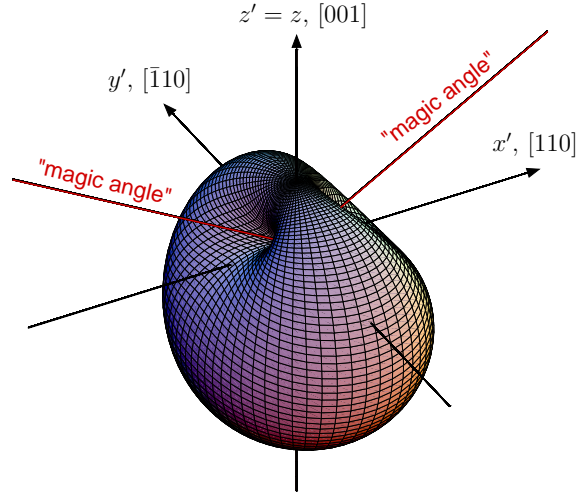


Figure 5.5: Angular dependence of the splitting Δ_+ as given by Eq. (5.68), evaluated for $\lambda_+/\lambda_- = 2$. The direction in space corresponds to the spin-quantization axis, given by $\mathbf{l} = \mathbf{B}/B$. At the “magic angles”, the value of Δ_+ equals zero. The angular dependence of the splitting Δ_- in Eq. (5.68) is obtained from this figure by reflecting it in the (x', y') -plane. Note that the circular symmetry of the quantum dot was essential for obtaining this angular dependence.

Equation (5.69) together with Eqs. (5.72)–(5.75) allows one to calculate transitions between quantum dot levels under the action of a perturbation. As a perturbation, in the next Section, we consider the electron-phonon interaction.

Now, we return to Eq. (5.68) and consider the particular case when the magnetic field \mathbf{B} is perpendicular to the 2DEG plane ($\theta = 0, \pi$). Then, according to Eq. (5.68), we have $\Delta_+ = \sqrt{2}E_Z\lambda_{1,0}m^*|\alpha|/\hbar$ and $\Delta_- = \sqrt{2}E_Z\lambda_{1,0}m^*|\beta|/\hbar$. These expressions, in principle, allow one to access the Rashba (Dresselhaus) coupling constant α (β) separately in a measurement of Δ_+ (Δ_-). We do not exclude here a direct measurement of the splittings $2\Delta_{\pm}$ in transport spectroscopy of quantum dots. However, for GaAs quantum dots, this requires a fairly low electron temperature and applied bias voltage, as well as a large magnetic field. To give an estimate, we assume typical GaAs values: $\lambda_{1,0} = 100$ nm for the inter-electron distance, $\hbar/m^*\beta = 8$ μ m for the spin-orbit length, and a magnetic field $B = 10$ T (with $g = -0.44$); as a result, we obtain $2\Delta_- \approx 20$ μ eV. A different possibility to access Δ_{\pm} is to measure the spin relaxation times and to deduce the strength of the spin-orbit interaction therefrom, see further.

Equation (5.68) has a strong dependence on the direction of $\mathbf{l} = \mathbf{B}/B$. For some angles — “magic angles” — the effect of the spin-orbit interaction vanishes. From Eq. (5.68), we find that $\Delta_+ = 0$ for $\cos\theta = \lambda_-/\lambda_+$ and $\varphi' = 0, \pi$, provided $|\lambda_+| > |\lambda_-|$. Alternatively, if $|\lambda_-| > |\lambda_+|$, we find that $\Delta_+ = 0$ for $\cos\theta = \lambda_+/\lambda_-$ and $\varphi' = \pi/2, 3\pi/2$. Similarly for Δ_- , we have the same expressions, but with $\cos\theta \rightarrow -\cos\theta$. In Fig. 5.5, we plot the angular dependence of Δ_+ given in Eq. (5.68), calculated for

5.5. ELECTRON STATES WITH SPIN-ORBIT INTERACTION

the ratio $\lambda_+/\lambda_- = 2$. A similar figure can be obtained also for Δ_- in Eq. (5.68), by reflecting Fig. 5.5 in the (x, y) -plane. Clearly, the “magic angles” can be used to determine the relative strength between the Rashba (α) and Dresselhaus (β) coupling constants (recall that $1/\lambda_{\pm} = m^*(\beta \pm \alpha)/\hbar$).

The angular dependence of the splittings Δ_{\pm} in Eq. (5.68) is specific to the circular symmetry of the harmonic confining potential used above. In the opposite extreme case, when the two-electron wave functions can be chosen real (or their imaginary parts due to B_z are negligible) we obtain $\Delta_+ = \Delta_-$ and

$$\Delta_{\pm} = \sqrt{2}E_Z \sqrt{\frac{\bar{r}_{y'}^2}{\lambda_-^2} + \frac{\bar{r}_{x'}^2}{\lambda_+^2} - \left(\frac{\bar{r}_{y'}}{\lambda_-} l_{x'} + \frac{\bar{r}_{x'}}{\lambda_+} l_{y'} \right)^2}, \quad (5.76)$$

where $\bar{\mathbf{r}} = \langle \psi_T | \mathbf{r} | \psi_S \rangle$ is the dipolar matrix element (not to be confused with $\langle r \rangle$), which we assume to be real. We note that this corresponds to a quantum dot elongated in one direction, or to a double quantum dot. The singlet-triplet transition can occur in this case at a value of B_z much smaller than the characteristic confining magnetic field. Then, the imaginary part of $\bar{\mathbf{r}}$ is negligible. Note that Eq. (5.76) can be rewritten in the form $\Delta_{\pm} = \sqrt{2}E_Z \sqrt{(\bar{r}_{y'}/\lambda_-)^2 + (\bar{r}_{x'}/\lambda_+)^2} \sqrt{1 - \cos^2(\varphi' - \varphi_0) \sin^2 \theta}$, with φ_0 satisfying $\tan \varphi_0 = \bar{r}_{x'} \lambda_- / \bar{r}_{y'} \lambda_+$. Then, it is easy to see that Eq. (5.76) describes a doughnut (or more precisely a *horn torus*) with the rotation axis at $\varphi' = \varphi_0$ and $\theta = \pi/2$, see Fig. 5.6. In this case, the “magic angle” coincides with the rotation axis of the torus. Knowing the rotation axis, one can find the relative strength of α and β , provided the asymmetry of the quantum dot in the directions x' and y' is known. In Fig. 5.6, we plotted the angular dependence of Δ_{\pm} assuming $\bar{r}_{y'} \lambda_+ / \bar{r}_{x'} \lambda_- = 2$.

Now, we return to the *weak* matrix elements in Eqs. (5.63) and (5.64). These are the matrix elements other than those given in Eq. (5.66). As before, we consider the lowest in energy singlet and triplet levels. In some cases, the contribution of the weak matrix elements to the wave functions can be comparable to, or even dominating over, the contribution of the strong ones. For example, away from the singlet-triplet transition, the energy $E_{TS} = E_T - E_S$ becomes comparable to the excitation energies of other excited states in the quantum dot (the closest would be the state $|000, -2, S\rangle$). In this case, the admixture of such excited states to the wave functions of the singlet and triplet under consideration can be as large as the mutual admixture within the singlet-triplet subspace due to the strong matrix elements. Another case is when the direction of \mathbf{B} is at the “magic angle” or in its vicinity. Then, the strong matrix elements vanish and the weak ones dominate. Below, we take into account the weak matrix elements by means of perturbation theory for the non-degenerate case. It is convenient to proceed as we did in Section 5.5.1, performing a Schrieffer-Wolff transformation on the Hamiltonian.

We return now to Eq. (5.60) and separate the weak matrix elements from the Hamil-

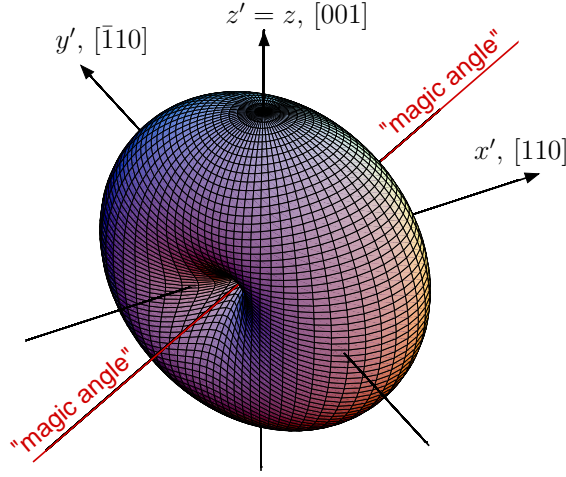


Figure 5.6: Opposite to Fig. 5.5, we plot here the angular dependence of the splittings Δ_{\pm} (with $\Delta_{+} = \Delta_{-}$) as given by Eq. (5.76), which describes a quantum dot without circular symmetry. The degree of asymmetry needs to be large enough, such that in a magnetic field causing the singlet-triplet transition the imaginary part of $\bar{\mathbf{r}} = \langle \psi_T | \mathbf{r} | \psi_S \rangle$ to be negligible. For the plot we assumed $\bar{r}_{y'} \lambda_{+} / \bar{r}_{x'} \lambda_{-} = 2$.

tonian into a perturbation,

$$\tilde{H} = \tilde{H}_0 + \tilde{V}_w, \quad (5.77)$$

$$\tilde{H}_0 = H_d + H_Z + \mathcal{P}_{ST} H_Z^{SO}, \quad (5.78)$$

$$\tilde{V}_w = (1 - \mathcal{P}_{ST}) H_Z^{SO}, \quad (5.79)$$

where \mathcal{P}_{ST} projects onto the singlet-triplet subspace, $\mathcal{P}_{ST} A = \sum_{\mu\nu} A_{\mu\nu} |\mu\rangle \langle \nu|$, with $\mu, \nu \in (\Psi_S, \Psi_{T_{\pm}}, \Psi_{T_0})$ and $\forall A$. Note that all the strong matrix elements are included into \tilde{H}_0 , whereas all the weak ones into \tilde{V}_w . We retain the *tilde* mark over the Hamiltonian to denote the Schrieffer-Wolff transformation performed at the beginning of this Section. In that transformation, we excluded the spin-orbit interaction H_{SO} from the Hamiltonian, using the transformation matrix S_Q in Eq. (5.56). Now we change the basis a second time, performing this time a Schrieffer-Wolff transformation which excludes the perturbation \tilde{V}_w from the Hamiltonian (5.77). Thus, we transform \tilde{H} to $\tilde{H}' = (1 + S_w) \tilde{H} (1 - S_w)$, with $S_w \ll 1$ obeying $[\tilde{H}_0, S_w] = \tilde{V}_w$. After this transformation, we obtain $\tilde{H}' = \tilde{H}_0$ in leading order of the spin-orbit interaction. At the same time, by doing this transformation, we correct the basis states to take into account the perturbation \tilde{V}_w in leading order.

Considering now the phonon potential $U_{\text{ph}}(\mathbf{r}_1, \mathbf{r}_2, t)$, we apply the same unitary transformations, $\tilde{U}'_{\text{ph}} = (1 + S_w) \tilde{U}_{\text{ph}} (1 - S_w)$, and obtain in leading order

$$U_{\text{ph}} \rightarrow U_{\text{ph}} + [S_w, U_{\text{ph}}]. \quad (5.80)$$

Note that the first Schrieffer-Wolff transformation, $\tilde{U}_{\text{ph}} = (1 + S_Q) U_{\text{ph}} (1 - S_Q)$, does not affect the phonon potential (or any other scalar potential), provided we consider

5.5. ELECTRON STATES WITH SPIN-ORBIT INTERACTION

a parabolic dot confinement, or one with a center of inversion (see Sec. 5.5.1). Furthermore, for an arbitrary dot confinement, we have shown in Sec. 5.5.1 that $S_{\mathcal{Q}}$ can effectively be replaced by S given in Eq. (5.50), provided we consider spin relaxation between singlet and triplet, or between triplet states of the same triplet level. Under these restrictions, we set $S_{\mathcal{Q}} \rightarrow S$ and arrive at Eq. (5.80) in the general case as well; note that S in Eq. (5.50) commutes with scalar potentials.

The transformation matrix S_w in the leading order of H_Z^{SO} formally reads

$$S_w = \frac{1 - \mathcal{P}_{ST}}{\hat{L}_d + \hat{L}_Z} H_Z^{SO}, \quad (5.81)$$

where $\hat{L}_d A = [H_d, A]$ and $\hat{L}_Z A = [H_Z, A]$, for $\forall A$. We note that Eq. (5.80) has been derived to describe transitions only within the subspace \mathcal{P}_{ST} , consisting of singlet and triplet states under consideration. If relaxation processes between other excited states are being considered, then \mathcal{P}_{ST} should span those excited states. Equation (5.81) is general to an arbitrary shape of the dot confinement and in matrix form it is given by

$$\langle \mathbf{ns} | S_w | \mathbf{n}'\mathbf{s}' \rangle = \frac{\langle \mathbf{ns} | H_Z^{SO} | \mathbf{n}'\mathbf{s}' \rangle}{E_{\mathbf{ns}} - E_{\mathbf{n}'\mathbf{s}'}}, \quad (5.82)$$

provided one of the states $|\mathbf{ns}\rangle$ and $|\mathbf{n}'\mathbf{s}'\rangle$ lies outside of the subspace \mathcal{P}_{ST} , and $\langle \mathbf{ns} | S_w | \mathbf{n}'\mathbf{s}' \rangle = 0$, otherwise. We note that, away from the singlet-triplet transition ($E_{ST} \gg \Delta_{\pm}$), separation of matrix elements into strong and weak is not required: one can treat all matrix elements of H_Z^{SO} by means of non-degenerate perturbation theory. This amounts then to replacing $\mathcal{P}_{ST} \rightarrow \mathcal{P}$ in Eq. (5.81) or, equivalently, to excluding only identical states ($\mathbf{ns} \neq \mathbf{n}'\mathbf{s}'$) in Eq. (5.82).

Next, we note that Eq. (5.82) can already be used to find the spin-phonon coupling, by calculating the matrix elements of $[S_w, U_{\text{ph}}]$, see Eq. (5.80). This requires knowledge about the dot energy spectrum and wave functions, and finding the matrix forms of S_w and U_{ph} in the Hilbert space of H_d . Often, however, it is convenient to have an explicit expression for S_w in terms of differential operators. Then, one evaluates the commutator $[S_w, U_{\text{ph}}]$ explicitly and calculates the matrix elements of the resultant expression only between the singlet and triplet states under consideration.

We consider now our harmonic quantum dot and obtain an expression for S_w . As before, we are interested in the subspace \mathcal{P}_{ST} , consisting of a singlet and triplet with the orbital wave functions $|\psi_S\rangle = |0000\rangle$ and $|\psi_T\rangle = |000, -1\rangle$, respectively. For simplicity, we assume small Zeeman splittings, $E_Z \ll \hbar\omega_0$, which is usually the case for GaAs quantum dots. Thus, neglecting the Liouvillean \hat{L}_Z in the denominator of Eq. (5.81) and going to the relative coordinates, we rewrite Eq. (5.81) as follows

$$S_w = E_Z \left\{ \frac{1}{\hat{L}_d} [\mathbf{l} \times \boldsymbol{\xi}^R] \cdot \boldsymbol{\Sigma} + \frac{1 - \mathcal{P}_{ST}}{2\hat{L}_d} [\mathbf{l} \times \boldsymbol{\xi}^r] \cdot \boldsymbol{\sigma} \right\}, \quad (5.83)$$

where we used Eq. (5.61) and the fact that $\mathcal{P}_{ST} \boldsymbol{\xi}^R = 0$ for the considered singlet-triplet subspace. Considering the first term in Eq. (5.83), we proceed in a way similar

to Ref. [90]. Namely, we express the coordinates entering in $\boldsymbol{\xi}^R$ in terms of the commutator of the Hamiltonian with the momentum operator. For a particle j we have the identities (solely for harmonic confinement)

$$x_j = \frac{-i}{\hbar m^* \omega_0^2} \hat{L}'_d \left(p_{jx} + \frac{e}{c} B_z y_j \right), \quad (5.84)$$

$$y_j = \frac{-i}{\hbar m^* \omega_0^2} \hat{L}'_d \left(p_{jy} - \frac{e}{c} B_z x_j \right), \quad (5.85)$$

where $\mathbf{p}_j = -i\hbar\partial/\partial\mathbf{r}_j + (e/c)\mathbf{A}(\mathbf{r}_j)$ and \hat{L}'_d is the Liouvillean of H_d in Eq. (5.2) without the Coulomb interaction term. Since the Coulomb interaction does not couple to the center of mass coordinate $\mathbf{R} = (\mathbf{r}_1 + \mathbf{r}_2)/2$, we can use Eqs. (5.84) and (5.85) to obtain

$$R_x = \frac{-i}{2\hbar m^* \omega_0^2} \hat{L}_d \left(P_x + \frac{2e}{c} B_z R_y \right), \quad (5.86)$$

$$R_y = \frac{-i}{2\hbar m^* \omega_0^2} \hat{L}_d \left(P_y - \frac{2e}{c} B_z R_x \right), \quad (5.87)$$

where $\mathbf{P} = -i\hbar\partial/\partial\mathbf{R} + (2e/c)\mathbf{A}(\mathbf{R})$ and \hat{L}_d is the Liouvillean of H_d in Eq. (5.2). Next, substituting the explicit form of $\boldsymbol{\xi}^R = (R_y/\lambda_-, R_x/\lambda_+, 0)$ into Eq. (5.83) and using Eqs. (5.86) and (5.87), we cancel out the Liouvillean \hat{L}_d in the first term of Eq. (5.83), thus, obtaining

$$\frac{E_Z}{\hat{L}_d} [\mathbf{l} \times \boldsymbol{\xi}^R] \cdot \boldsymbol{\Sigma} = \frac{-E_Z}{2m^* \omega_0^2} [\mathbf{l} \times \mathbf{D}^R] \cdot \boldsymbol{\Sigma} + f(\mathbf{R}), \quad (5.88)$$

$$\mathbf{D}^R = (\lambda_-^{-1} \partial/\partial R_y, \lambda_+^{-1} \partial/\partial R_x, 0), \quad (5.89)$$

where $f(\mathbf{R})$ is a function of coordinates, which is irrelevant here since it commutes with scalar potentials. Equation (5.88) with the definition (5.89) give us the explicit operator form of the first term of S_w in Eq. (5.83).

As for the second term in Eq. (5.83), there are two complications arising. One is the presence of the Coulomb interaction, which couples to the relative coordinate $\mathbf{r} = \mathbf{r}_1 - \mathbf{r}_2$, and the second one is the projector $1 - \mathcal{P}_{ST}$, which excludes the contribution of the strong matrix elements. In the presence of Coulomb interaction, we derive the following identities

$$r_x \left(1 - \frac{\lambda_0^4}{2a_B^* r^3} \right) = \frac{-2i}{\hbar m^* \omega_0^2} \hat{L}_d \left(p_x + \frac{e}{2c} B_z r_y \right), \quad (5.90)$$

$$r_y \left(1 - \frac{\lambda_0^4}{2a_B^* r^3} \right) = \frac{-2i}{\hbar m^* \omega_0^2} \hat{L}_d \left(p_y - \frac{e}{2c} B_z r_x \right), \quad (5.91)$$

where $\lambda_0 = \sqrt{2\hbar/m^* \omega_0}$ and $\mathbf{p} = -i\hbar\partial/\partial\mathbf{r} + (e/2c)\mathbf{A}(\mathbf{r})$. Clearly, the right-hand side in each of Eqs. (5.90) and (5.91) gives zero at the singlet-triplet degeneracy point for the matrix element taken between the singlet and triplet orbital states. As a

5.5. ELECTRON STATES WITH SPIN-ORBIT INTERACTION

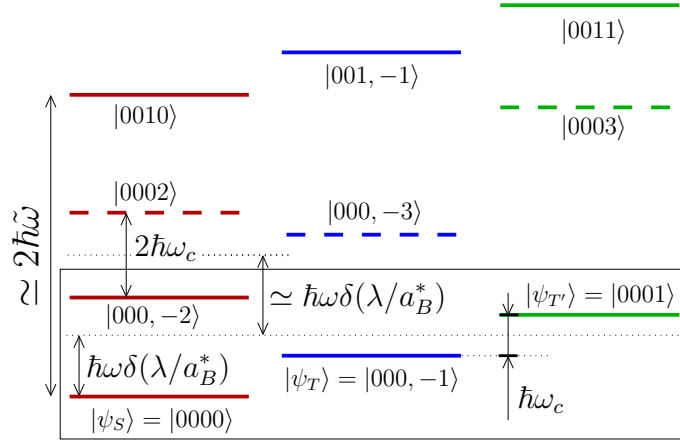


Figure 5.7: Sketch of several lowest energy levels in the quantum dot, showing the relevant energy scales. The box encloses the energy levels used to make an approximation in Eq. (5.92). The levels represented by dashed segments are unimportant due to the selection rule $\Delta m = 0, \pm 1$.

by-product, we thus obtain an exact equality, which we defer to Appendix F. Here, however, we are interested in the opposite case. Due to the projector $1 - \mathcal{P}_{ST}$ in the second term of Eq. (5.83), the singlet-triplet degeneracy has little effect on S_w . Therefore, we can use Eqs. (5.90) and (5.91), with some approximations, to express \mathbf{r} in terms of the commutator $[H_d, \mathbf{p}]$, similarly to how we did above for \mathbf{R} .

We consider first the case of no orbital magnetic field ($B_z = 0$). Then, Eqs. (5.90) and (5.91) have a particular simple form and can be rewritten as follows

$$\frac{1}{\hat{L}_d} \mathbf{r} \left(1 - \frac{\lambda_0^4}{2a_B^* r^3} \right) = \frac{-2}{m^* \omega_0^2} \frac{\partial}{\partial \mathbf{r}}, \quad (5.92)$$

where we have multiplied both sides by \hat{L}_d^{-1} . Next, we make the following approximation: we replace r^3 in the denominator of Eq. (5.92) by some effective value r_{eff}^3 . To determine r_{eff} , we require that the operators $\hat{L}_d^{-1} \mathbf{r} / r^3$ and $\hat{L}_d^{-1} \mathbf{r} / r_{\text{eff}}^3$ have on average equal quantum fluctuations in the low energy Hilbert subspace. Mathematically, we require that

$$\langle \psi_\alpha | \frac{1}{\hat{L}_d} \mathbf{r} | \psi_\beta \rangle \simeq \frac{1}{r_{\text{eff}}^3} \langle \psi_\alpha | \frac{1}{\hat{L}_d} \mathbf{r} | \psi_\beta \rangle, \quad (5.93)$$

for all singlet-triplet pairs (α, β) enclosed in the rectangular box in Fig. 5.7. In Fig. 5.7, we show different energy levels in the quantum dot and the relevant energy scales (for clarity, we show also the orbital splittings due to B_z). Due to the circular symmetry of the dot, the levels represented by dashed segments in Fig. 5.7 can be disregarded, since their quantum number m differs by more than ± 1 from the lowest singlet and triplet. Note that the selection rule in Eq. (5.92) reads $\Delta m = 0, \pm 1$. Furthermore, the Coulomb interaction reduces efficiently the energy spacing between levels with one and the same quantum number n . Therefore, for the considered lowest

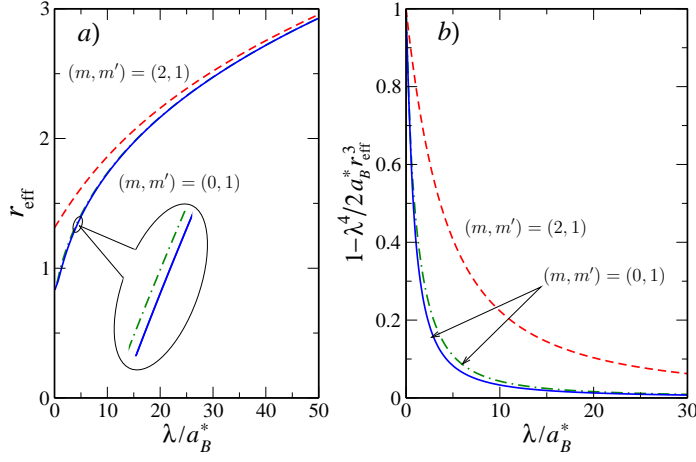


Figure 5.8: (a) The parameter r_{eff} (in units of λ) as a function of the Coulomb interaction strength λ/a_B^* , for $(m, m') = (0, 1)$ (solid and dash-dotted curves) and $(m, m') = (2, 1)$ (dashed curves). The difference between the solid curve, given by Eq. (5.96), and dash-dotted curve, given by Eq. (5.94), stems from the infidelity of our variational method. (b) Similarly to (a), the factor $1 - \lambda^4/2a_B^* r_{\text{eff}}^3$ as a function of λ/a_B^* .

singlet and triplet, the contribution of levels with $n = 0$ is dominant in the limit of strong Coulomb interaction. Using the singlet and triplet wave functions found in Sec. 5.3, we obtain from Eq. (5.93) an explicit expression for r_{eff} ,

$$r_{\text{eff}} \simeq \frac{\sqrt{2\tilde{\lambda}_m \tilde{\lambda}_{m'}}}{\sqrt{\tilde{\lambda}_m^2 + \tilde{\lambda}_{m'}^2}} \left[\frac{\Gamma(3/2 + \frac{x_m + x_{m'}}{2})}{\Gamma(\frac{x_m + x_{m'}}{2})} \right]^{1/3}, \quad (5.94)$$

where $x_m = \sqrt{m^2 + \gamma_m}$, and the quantum numbers m and m' refer to the singlet and triplet states enclosed in the box of Fig. 5.7. Recalling that $\tilde{\lambda}_m$ and γ_m are even functions of m , we have that $|m| = 0, 2$ and $|m'| = 1$ in Eq. (5.94). Using either $(0, 1)$ or $(2, 1)$ in place of (m, m') in Eq. (5.94) is within the accuracy of our approximation. For definiteness, we choose $(m, m') = (0, 1)$.

A different method to find r_{eff} relies on the commutation relation $\partial/\partial \mathbf{r} = -(m^*/2\hbar^2)\hat{L}_d \mathbf{r}$, present at $B_z = 0$. Substituting this expression in the right-hand side of Eq. (5.92), we obtain the following exact relation at $B_z = 0$

$$\begin{aligned} & \left[1 - \frac{(\varepsilon_{nm} - \varepsilon_{n'm'})^2}{\hbar^2 \omega_0^2} \right] \int_0^\infty r f_{nm}(r) f_{n'm'}(r) dr = \\ & = \frac{\lambda_0^4}{2a_B^*} \int_0^\infty \frac{1}{r^2} f_{nm}(r) f_{n'm'}(r) dr, \end{aligned} \quad (5.95)$$

where $m' = m \pm 1$, and ε_{nm} and $f_{nm}(r)$ are, respectively, the exact eigenvalues and eigenfunctions of the Hamiltonian \mathcal{H}_m in Eq. (5.9). Substituting $n = n' = m = 0$

5.5. ELECTRON STATES WITH SPIN-ORBIT INTERACTION

and $m' = 1$ in Eq. (5.95), we obtain for r_{eff} the following relation

$$\frac{1}{r_{\text{eff}}^3} = \frac{2a_B^*}{\lambda_0^4} (1 - \delta^2), \quad (5.96)$$

where $\delta = (\varepsilon_{01} - \varepsilon_{00})/\hbar\omega$ was introduced in Sec. 5.3 (note that $\lambda = \lambda_0$ and $\omega = \omega_0$ at $B_z = 0$). In Fig. 5.8(a), we plot r_{eff} as a function of λ/a_B^* using Eq. (5.96) (solid curve). If we use Eq. (5.94) with $(m, m') = (0, 1)$ to determine r_{eff} , we obtain a different (but numerically very close) result, see the dash-dot curve in Fig. 5.8(a). The difference stems from the fact that our variational method, developed in Sec. 5.3, is not exact. Note that Eq. (5.94) relies on precise knowledge of wave functions, whereas Eq. (5.96) relies on precise knowledge of energy spectrum. To avoid discrepancy in the future, we choose to work with r_{eff} given by Eq. (5.96). This is also convenient because δ can be calculated using the approximate crossover function (5.15). Finally, the dashed line in Fig. 5.8(a) represents r_{eff} obtained from Eq. (5.94) with $(m, m') = (2, 1)$. This shows the accuracy of our approximation, see also Fig. 5.8(b).

Using Eq. (5.96) for r_{eff} and replacing $r^3 \rightarrow r_{\text{eff}}^3$ in Eq. (5.92), we thus obtain (at $B_z = 0$)

$$\frac{1}{\hat{L}_d} \mathbf{r} = \frac{-2}{m^* \delta^2 \omega_0^2} \frac{\partial}{\partial \mathbf{r}}, \quad (5.97)$$

where the effect of the Coulomb interaction is represented by a single parameter, $\delta = \delta(\lambda/a_B^*)$. Clearly, Eq. (5.97) can be interpreted in the following way: the Coulomb interaction in the quantum dot renormalizes the level spacing, resulting in replacing $\hbar\omega_0 \rightarrow \hbar\omega_0 \delta(\lambda/a_B^*)$ as compared to the non-interacting case. However, this is roughly the case only for the subset of levels with different quantum numbers m and with $N = M = n = 0$, see Fig. 5.7. These are the levels we have taken into account when making the approximation in Eq. (5.92). In addition, however, there is also a ladder of levels, for each m , differing only in n and having a level spacing $\simeq 2\hbar\tilde{\omega}$. At strong Coulomb interaction, the two energy scales are different, $\hbar\tilde{\omega} \gg \hbar\omega\delta$, and Eq. (5.97), being proportional to $\partial/\partial \mathbf{r} = -(m^*/2\hbar^2)\hat{L}_d \mathbf{r}$, tends to overestimate the contribution of excited states with $n > 0$.

To exclude the contribution of excited states with $n > 0$ at strong Coulomb interaction, we integrate over the radial coordinate r in Eq. (5.97). Going to the polar coordinates, $(r_x, r_y) = r(\cos \varphi_r, \sin \varphi_r)$, we use the expression

$$\frac{\partial}{\partial r_x} \pm i \frac{\partial}{\partial r_y} = e^{\pm i\varphi_r} \left(\frac{\partial}{\partial r} \pm \frac{i}{r} \frac{\partial}{\partial \varphi_r} \right), \quad (5.98)$$

and suppress the quantum fluctuations of the operators $\partial/\partial r$ and $1/r$. As a result, we obtain

$$\frac{1}{\hat{L}_d} (r_x \pm ir_y) \simeq \frac{\mp i 2e^{\pm i\varphi_r}}{m^* \delta^2 \omega_0^2} \left\langle \frac{1}{r} \right\rangle \frac{\partial}{\partial \varphi_r}, \quad (5.99)$$

where we can further approximate $\langle 1/r \rangle$ by $1/r_{\text{eff}}$. Next, we implement the projector $1 - \mathcal{P}_{ST}$ in Eq. (5.99) by eliminating one of its sign components. For example, if we

are calculating $\langle \psi_S | [S_w, U_{\text{ph}}] | \psi_T \rangle$, then we can set to zero the upper sign component in Eq. (5.99), and if we are calculating $\langle \psi_T | [S_w, U_{\text{ph}}] | \psi_S \rangle$, then we can set to zero the lower sign component.

At finite orbital magnetic field, Eq. (5.99) can be generalized to include terms proportional to B_z . However, due to the projector $1 - \mathcal{P}_{ST}$, the orbital magnetic field dependence becomes inessential, since the matrix elements which diverge at the singlet-triplet degeneracy point are excluded. Therefore, we use Eq. (5.99) as an estimate for the contribution of weak matrix elements both at $B_z = 0$ and at $B_z \lesssim \omega_0 m^* c / e$; the accuracy of our approximation does not permit accounting for B_z .

Assuming that $\langle \psi_S | [S_w, U_{\text{ph}}] | \psi_T \rangle$ is being evaluated ($\langle \psi_T | [S_w, U_{\text{ph}}] | \psi_S \rangle$ can then be obtained by complex conjugation), we obtain finally the following expression for the second term in Eq. (5.83),

$$E_Z \frac{1 - \mathcal{P}_{ST}}{2\hat{L}_d} [\mathbf{l} \times \boldsymbol{\xi}^r] \cdot \boldsymbol{\sigma} = \frac{-E_Z}{m^* \omega_0^2 \delta^2} [\mathbf{l} \times \mathbf{D}^r] \cdot \boldsymbol{\sigma}, \quad (5.100)$$

$$\mathbf{D}^r = \left(\frac{1}{\lambda_-}, \frac{-i}{\lambda_+}, 0 \right) \frac{e^{-i\varphi_r}}{2r_{\text{eff}}} \frac{\partial}{\partial \varphi_r}. \quad (5.101)$$

The sum of Eqs. (5.88) and (5.100) gives us an explicit expression for S_w used in the next section to calculate $\langle \psi_S | [S_w, U_{\text{ph}}] | \psi_T \rangle$.

5.6 Phonon-induced spin relaxation

The relaxation and decoherence of the spin degrees of freedom in the quantum dot are well described by the Bloch-Wangsness-Redfield theory [123]. In that theory, the time evolution of a system's density matrix $\rho_{\alpha\alpha'}(t)$ is governed by a set of linear differential equations, known as the Redfield equations,

$$\frac{d}{dt} \rho_{\alpha\alpha'}(t) = -i\omega_{\alpha\alpha'} \rho_{\alpha\alpha'}(t) + \sum_{\beta\beta'} R_{\alpha\alpha'\beta\beta'} \rho_{\beta\beta'}(t), \quad (5.102)$$

where $R_{\alpha\alpha'\beta\beta'} = (R_{\alpha'\alpha\beta'\beta})^*$ is constant in time and $\omega_{\alpha\alpha'} = (E_\alpha - E_{\alpha'})/\hbar$, with E_α being the energy of level α . These equations can be derived microscopically under the assumption that the system is coupled weakly to its bath (Born approximation) and that the bath correlation time τ_c — the time over which the bath loses the “memory” about its state — is much shorter than the times considered in Eq. (5.102) (Markov approximation). These two approximations combined are known as the Born-Markov approximation.

In the case of phonons, the correlation time τ_c is given by the time it takes a phonon to traverse the quantum dot, $\tau_c = \lambda/s$, where s is the speed of sound in the sample. For single-electron quantum dots, the spin-phonon coupling [90] is parametrically small, compared to the bare interaction $U_{\text{ph}}(\mathbf{r})$, by a product of two factors: $E_z/\hbar\omega_0 \ll 1$

5.6. PHONON-INDUCED SPIN RELAXATION

and $\lambda/\lambda_{SO} \ll 1$. This makes the Born-Markov approximation for the phonon-induced spin decay easy to validate in typical structures [90]. For example, in GaAs quantum dots, the experimentally measured spin relaxation times are in the range [64, 88] $T_1 \simeq (10 - 10^4) \mu\text{s}$, while the phonon correlation time is always much shorter, $\tau_c \simeq 10 \text{ ps}$. Moreover, the phonon-phonon correlation function decays rapidly in time. This can be explained as follows: once a phonon is emitted it leaves the quantum dot during the time τ_c and does not come back. The decay law for the phonon-phonon correlation function depends on the wave function of the electron in the quantum dot, and can be as fast as a Gaussian decay law. Of course, we ignore here phonon reflection and localization, which can be controlled by the sample geometry. The small parameter $\tau_c/T_{1,2} \ll 1$ gives room also for an intermediate time scale Δt , such that $\tau_c \ll \Delta t \ll T_{1,2}$. The time Δt is the smallest time resolution allowed by the Bloch-Wangsness-Redfield theory in Eq. (5.102). During the time Δt the phonon fluctuations average out ($\Delta t \gg \tau_c$), while the spin decay has not occurred yet ($\Delta t \ll T_{1,2}$). It is at this time scale, when the coherent influence of the phonon potential via the spin-orbit and Zeeman interactions appears as a decay mechanism for the electron spin [90]. Finally, we note that Eq. (5.102) is valid even in the classical limit of $U_{\text{ph}}(\mathbf{r})$, when there are many phonons in the sample, as long as Δt exists.

In the case of two electrons in the quantum dot, the dot size λ in the estimate above is replaced by the average inter-electron distance $\langle r \rangle$, which is larger due to the Coulomb repulsion between the electrons. This enhances the effect of the spin-orbit interaction and can result in shorter lifetimes compared to the single-electron case. However, in typical structures the Coulomb interaction is not that strong and usually $\langle r \rangle \sim \lambda$. Therefore, the estimate given above for the single-electron quantum dot does not change significantly in the case of a two-electron quantum dot. This agrees also with the fact that measurements of the singlet-triplet relaxation find long lifetimes [84] $\gtrsim 200 \mu\text{s}$.

In the Born-Markov approximation, the Redfield tensor acquires the form

$$R_{\alpha\alpha'\beta\beta'} = \Gamma_{\beta'\alpha'\alpha\beta}^+ + \Gamma_{\beta'\alpha'\alpha\beta}^- - \delta_{\alpha'\beta'} \sum_{\gamma} \Gamma_{\alpha\gamma\gamma\beta}^+ - \delta_{\alpha\beta} \sum_{\gamma} \Gamma_{\beta'\gamma\gamma\alpha'}^-, \quad (5.103)$$

given in terms of different correlators of the system-bath interaction U_{int} ,

$$\Gamma_{\alpha\alpha'\beta\beta'}^+ = \int_0^{\infty} \frac{dt}{\hbar^2} e^{-i\omega_{\beta\beta'}t} \overline{\langle \alpha | U_{\text{int}}(t) | \alpha' \rangle \langle \beta | U_{\text{int}} | \beta' \rangle}, \quad (5.104)$$

$$\Gamma_{\alpha\alpha'\beta\beta'}^- = \int_0^{\infty} \frac{dt}{\hbar^2} e^{-i\omega_{\alpha\alpha'}t} \overline{\langle \alpha | U_{\text{int}} | \alpha' \rangle \langle \beta | U_{\text{int}}(t) | \beta' \rangle}. \quad (5.105)$$

Here, the bar denotes averaging over the bath degrees of freedom and $|\alpha\rangle$ is a state of the system. The time dependence of $U_{\text{int}}(t)$ is with respect to the bath only, $U_{\text{int}}(t) = \exp(iH_B t/\hbar) U_{\text{int}} \exp(-iH_B t/\hbar)$, where H_B is the Hamiltonian of the bath. In the expressions above it is assumed that $\overline{U_{\text{int}}(t)} = 0$.

By definition, the two types of correlators in Eqs. (5.104) and (5.105) are related to each other by $(\Gamma_{\alpha\alpha'\beta\beta'}^+)^* = \Gamma_{\beta'\beta\alpha'\alpha}^-$, which guarantees that $\rho(t)$ preserves its hermiticity in time. The form of Eq. (5.103) also guarantees that the normalization condition $\sum_{\alpha} \rho_{\alpha\alpha}(t) = 1$ is not changed by the time evolution. One can check this by verifying that $\sum_{\alpha} R_{\alpha\alpha\beta\beta'} = 0$. An additional requirement on $\rho(t)$ is that it evolves in time obeying the rule of “completely positive maps”, which is to say that $\rho(t)$ can be expressed in terms of $\rho(t')$ at $t' < t$ using an expression of the form $\rho(t) = \sum_n O_n \rho(t') O_n^\dagger$, where $\{O_n\}$ is a set of linear operators obeying the normalization condition $\sum_n O_n O_n^\dagger = 1$. This poses a constrain on the time evolution of $\rho(t)$. It is known that in some cases Eq. (5.102) with $R_{\alpha\alpha'\beta\beta'}$ given in Eq. (5.103) does not support complete positivity of $\rho(t)$. To guarantee complete positivity, one has to show that Eq. (5.102) can be cast into the so-called Lindblad form,

$$\begin{aligned} \frac{d}{dt}\rho(t) = & -\frac{i}{\hbar} [H_S, \rho(t)] \\ & + \frac{1}{2} \sum_J \left\{ [L_J \rho(t), L_J^\dagger] + [L_J, \rho(t) L_J^\dagger] \right\}, \end{aligned} \quad (5.106)$$

where $\{L_J\}$ is a set of linear operators, and H_S is a Hermitian operator, representing the system (possibly renormalized by the system-bath interaction U_{int}).

The Fermi “golden rule” transition probabilities are reproduced as a particular case of Eqs. (5.104) and (5.105),

$$\Gamma_{\alpha\beta} = \Gamma_{\beta\alpha\alpha\beta}^+ + \Gamma_{\beta\alpha\alpha\beta}^-, \quad (5.107)$$

where $\Gamma_{\alpha\beta}$ is the probability per unit time to transit from state β to state α . For the rates $\Gamma_{\alpha\beta}$ the time integral can be extended to $-\infty$ in the lower bound, which significantly eases the calculation. Thus, one can use the expression

$$\Gamma_{\alpha\beta} = \int_{-\infty}^{+\infty} \frac{dt}{\hbar^2} e^{-i\omega_{\alpha\beta}t} \overline{\langle \beta | U_{\text{int}}(t) | \alpha \rangle \langle \alpha | U_{\text{int}} | \beta \rangle}. \quad (5.108)$$

In our case, the system-bath interaction is given by

$$U_{\text{int}}(t) = U_{\text{ph}}(t) + [S_w, U_{\text{ph}}(t)], \quad (5.109)$$

where S_w was expressed in terms of differential operators in the previous section. The commutator term in Eq. (5.109) originates from the Schrieffer-Wolff transformation, performed in the previous section to account for the contribution of the weak matrix elements. The time dependence of the phonon potential $U_{\text{ph}}(t)$ is governed by the Hamiltonian of free phonons,

$$H_B \equiv H_{\text{ph}} = \sum_{\mathbf{qj}} \hbar\omega_{\mathbf{qj}} \left(b_{\mathbf{qj}}^\dagger b_{\mathbf{qj}} + 1/2 \right), \quad (5.110)$$

which includes three branches of acoustic phonons. The optical phonons can be neglected, since usually $E_{ST}, E_Z < \hbar\omega_{\text{opt}}$, where $\hbar\omega_{\text{opt}}$ is the energy of optical phonons.

5.6. PHONON-INDUCED SPIN RELAXATION

The acoustic phonon potential can be rewritten in terms of the relative coordinates as follows

$$U_{\text{ph}}(\mathbf{R}, \mathbf{r}, t) = \sum_{\mathbf{q}j} M_{\mathbf{q}j} F(q_z) e^{i\mathbf{q}\parallel\mathbf{R}} \cos(\mathbf{q}\parallel\mathbf{r}/2) \times [b_{-\mathbf{q}j}^\dagger(t) + b_{\mathbf{q}j}(t)], \quad (5.111)$$

$$M_{\mathbf{q}j} = \sqrt{\frac{2\hbar}{\rho_c \omega_{\mathbf{q}j}}} (e\beta_{\mathbf{q}j} - iq\Xi_{\mathbf{q}j}), \quad (5.112)$$

where $b_{\mathbf{q}j}(t) = b_{\mathbf{q}j} \exp(-i\omega_{\mathbf{q}j}t)$ gives the time dependence mentioned above for $U_{\text{ph}}(t)$. The averaging over the bath, denoted by *bar* in Eqs. (5.104) and (5.105), is a thermodynamic mean value, evaluated with the statistical operator of free phonons:

$$\rho_{\text{ph}} = Z_{\text{ph}}^{-1} e^{-H_{\text{ph}}/T}, \quad (5.113)$$

where T is the temperature ($k_B = 1$) and Z_{ph} is the phonon partition function. At low temperatures, $T \ll E_{ST}, E_Z$, there are nearly no phonons available to scatter the dot spins. Nevertheless, spin relaxation can occur even at $T = 0$ due phonon emission from the dot. In this case, the dot relaxes from an excited state to the ground state, and the excitation energy is carried away by a phonon.

The states $|\alpha\rangle$ in Eqs. (5.104) and (5.105) are the lowest singlet and triplet states of the two-electron quantum dot. In Section 5.5.2, we have shown how these states transform, due to a combined effect of the spin-orbit and Zeeman interactions. In particular, the singlet state $|\Psi_S\rangle$ undergoes avoided crossings with the triplet states $|\Psi_{T_+}\rangle$ and $|\Psi_{T_-}\rangle$ at the singlet-triplet transition, see Fig. 5.4. In what follows, we calculate the relaxation and decoherence rates for transitions between the quantum dot eigenstates, using the system-bath interaction (5.109) and the definitions (5.104), (5.105) and (5.108).

5.6.1 Secular approximation

The Redfield equations (5.102) are significantly simplified if there is a separation of time scales between coherent evolution and decay of quantum states: $\omega_{\alpha\alpha'} \gg R_{\alpha\alpha'\beta\beta'}$ for $\alpha \neq \alpha'$. The coherent evolution takes place, in our case, on the time scales of \hbar/E_{ST} and \hbar/E_Z . The decay of $\rho_{\alpha\alpha'}(t)$ to the thermal equilibrium density matrix takes place on the time scale of spin relaxation/decoherence, which is of the order of $\hbar/\Gamma_{\alpha\beta}$ for our phonon-induced decay. For a wide range of parameters we have $\Gamma_{\alpha\beta} \ll E_{ST}, E_Z$, which allows us to apply the secular approximation.

In the secular approximation, one decouples the high frequency dynamics of the density matrix from the low frequency one. A systematic way to do this is to write down algebraic equations corresponding to the set (5.102). Thus, searching for solutions of

the form $\rho_{\alpha\alpha'}(t) = \rho_{\alpha\alpha'} \exp(-i\Omega t)$, where Ω is a complex frequency, we arrive at

$$\sum_q (\Omega_{pq}^{(0)} - \Omega\delta_{pq} + iR_{pq}) \rho_q = 0, \quad (5.114)$$

$$\det \|\Omega_{pq}^{(0)} - \Omega\delta_{pq} + iR_{pq}\| = 0. \quad (5.115)$$

Here, we used a two-index notation for the Redfield tensor $R_{p,q} \equiv R_{\alpha\alpha',\beta\beta'}$, with $p = (\alpha, \alpha')$ and $q = (\beta, \beta')$. Note that p takes on N^2 values, where N is the number of states taken into account ($\alpha = 1, 2, \dots, N$). The free evolution part $\Omega_{pq}^{(0)}$ has the form

$$\Omega_{\alpha\alpha'\beta\beta'}^{(0)} = (\delta_{\beta'\alpha'}(H_S)_{\alpha\beta} - \delta_{\alpha\beta}(H_S)_{\beta'\alpha'}) / \hbar \quad (5.116)$$

$$= \omega_{\alpha\alpha'}\delta_{\alpha\beta}\delta_{\alpha'\beta'} \equiv \omega_p\delta_{pq}, \quad (5.117)$$

where the first line is generic to any basis of states. Equations (5.114) and (5.115) resemble the problem of standard perturbation theory, in which the role of the unperturbed wave function is played by the density matrix ρ_p and the role of the energy of an unperturbed level is played by the transition frequency $\omega_p = \omega_{\alpha\alpha'}$. If a frequency ω_p is non-degenerate, i.e. there exists no other transition frequency in the system with the same value, then one can easily find the solutions for the corresponding eigenvector $\hat{\rho}_p$ and eigenvalue Ω_p :

$$\hat{\rho}_p = \hat{\rho}_p + \sum_{q \neq p} \frac{iR_{qp}}{\omega_p - \omega_q} \hat{\rho}_q + \dots, \quad (5.118)$$

$$\Omega_p = \omega_p + iR_{pp} + \sum_{q \neq p} \frac{i^2 R_{pq}R_{qp}}{\omega_p - \omega_q} + \dots \quad (5.119)$$

Here, we used the notation $\hat{\rho}_{\alpha\alpha'} = |\alpha\rangle\langle\alpha'|$ to denote the eigenvectors of the unperturbed density matrix ($\hat{\rho}_p \equiv \hat{\rho}_{\alpha\alpha'}$). Equation (5.118) is defined up to an arbitrary non-zero factor, since $\hat{\rho}_p$ needs not be normalized. The time dynamics of the eigenvector $\hat{\rho}_p$ is given by $\hat{\rho}_p(t) = \hat{\rho}_p \exp(-i\Omega_p t)$. Further, since the frequency Ω_p in Eq. (5.119) has in general an imaginary part, the eigenvector $\hat{\rho}_p(t)$ will decay after some time τ_p , given by $1/\tau_p = -\text{Im}[\Omega_p]$. Thus, we find the decoherence time, up to second order,

$$\frac{1}{\tau_{\alpha\alpha'}} = -R'_{\alpha\alpha'\alpha\alpha'} + \sum_{\substack{\beta \neq \alpha \\ \beta' \neq \alpha'}} \frac{2\text{Re}[R'_{\alpha\alpha'\beta\beta'}R''_{\beta\beta'\alpha\alpha'}]}{\omega_{\alpha\alpha'} - \omega_{\beta\beta'}} + \dots, \quad (5.120)$$

where we used the following notations:

$$R'_{\alpha\alpha'\beta\beta'} = (R_{\alpha\alpha'\beta\beta'} + R_{\beta'\beta\alpha'\alpha}) / 2, \quad (5.121)$$

$$R''_{\alpha\alpha'\beta\beta'} = (R_{\alpha\alpha'\beta\beta'} - R_{\beta'\beta\alpha'\alpha}) / 2i. \quad (5.122)$$

Note that $R_{pq} = R'_{pq} + iR''_{pq}$, with hermitian $R'_{pq} = (R'_{qp})^*$ and $R''_{pq} = (R''_{qp})^*$.

5.6. PHONON-INDUCED SPIN RELAXATION

A different interesting case occurs when a non-zero transition frequency ω_{p_1} coincides accidentally with another transition frequency $\omega_{p_2} = \omega_{p_1}$, or when the two frequencies are close to each other, $|\omega_{p_1} - \omega_{p_2}| \lesssim |R_{p_1 p_2}|$. The secular approximation, in lowest order, is then carried out by solving two coupled equations of the type (5.114), for the two considered transition frequencies (ω_{p_2} and ω_{p_1}). Higher orders of $R_{pq}/\omega_p \ll 1$ can be taken into account by replacing $R_{pq} \rightarrow \mathcal{R}_{pq}$ in Eq. (5.114), with

$$\mathcal{R}_{pp'} = R_{pp'} + i \sum_{q \neq p_1, p_2} \frac{R_{pq} R_{qp'}}{\omega_p - \omega_q} + \dots, \quad (5.123)$$

where $p, p' \in (p_1, p_2)$. Retaining terms, up to second order in R_{pq} , we find two eigenvectors $\hat{\varrho}_{p\pm}$ and eigenvalues $\Omega_{p\pm}$,

$$\hat{\varrho}_{p\pm} = c_{p_1}^{\pm} \left(\hat{\rho}_{p_1} + \sum_{q \neq p_1, p_2} \frac{i R_{qp}}{\omega_{p_1} - \omega_q} \hat{\rho}_q + \dots \right) + c_{p_2}^{\pm} \left(\hat{\rho}_{p_2} + \sum_{q \neq p_1, p_2} \frac{i R_{qp}}{\omega_{p_2} - \omega_q} \hat{\rho}_q + \dots \right), \quad (5.124)$$

$$\Omega_{p\pm} = \frac{1}{2} (\omega_{p_1} + \omega_{p_2} + i \mathcal{R}_{p_1 p_1} + i \mathcal{R}_{p_2 p_2}) \mp \frac{1}{2} \sqrt{(\omega_{p_1} - \omega_{p_2} + i \mathcal{R}_{p_1 p_1} - i \mathcal{R}_{p_2 p_2})^2 - 4 \mathcal{R}_{p_1 p_2} \mathcal{R}_{p_2 p_1}}, \quad (5.125)$$

where the coefficients $c_{p_1}^{\pm}$ and $c_{p_2}^{\pm}$ are related to each other by $c_{p_1}^{\pm}/c_{p_2}^{\pm} = i \mathcal{R}_{p_1 p_2} / (\Omega_{p\pm} - \omega_{p_1} - i \mathcal{R}_{p_1 p_1})$. As before, Eq. (5.124) has no normalization condition, except that $|c_{p_1}|^2 + |c_{p_2}|^2 \neq 0$. The time dynamics of the eigenvector $\hat{\varrho}_{p\pm}$ is given by $\hat{\varrho}_{p\pm}(t) = \hat{\varrho}_{p\pm} \exp(-i \Omega_{p\pm} t)$. Thus, as before the decoherence time is given by $1/\tau_{p\pm} = -\text{Im}[\Omega_{p\pm}]$. For simplicity, we consider further the degeneracy point $\omega_{p_1} = \omega_{p_2}$ and assume that $R_{p_1 p_1} = R_{p_2 p_2}$. Then, the decoherence times are given by

$$\frac{1}{\tau_{p\pm}} = -R'_{p_1 p_1} \pm \text{Re} \sqrt{R_{p_1 p_2} R_{p_2 p_1}}, \quad (5.126)$$

where we retained only the first term in Eq. (5.123). For the solution to be physical, the decoherence rates have to be non-negative, $1/\tau_{p\pm} \geq 0$, which is satisfied if $-R'_{p_1 p_1} \geq \pm \text{Re} \sqrt{R_{p_1 p_2} R_{p_2 p_1}}$. An interesting case occurs when the equality sign holds in the latter expression. Then, one of the rates (5.126) equals zero, whereas the other one is doubled ($1/\tau = -2R'_{p_1 p_1}$). In spite of our hypothetical consideration, this example indicates that at the degeneracy point ($\omega_{p_2} = \omega_{p_1}$) interference effects can create an eigenvector with a long decoherence time.

Before we proceed further with the remaining part of Eq. (5.114), we discuss first the meaning of Eqs. (5.118) and (5.124). These equations represent a transformation, which connects the operators $\hat{\varrho}$ and $\hat{\rho}$ with each other. This transformation can, in general, be written as follows

$$\hat{\varrho}_p = \sum_q c_{pq} \hat{\rho}_q, \quad (5.127)$$

where c_{pq} are complex numbers. The matrix c_{pq} needs not be unitary, but it must have an inverse: $\sum_l c_{pl}c_{lq}^{-1} = \delta_{pq}$, where c_{pq}^{-1} denotes the inverse matrix. Note that, if $c_{pq} \equiv c_{\alpha\alpha'\beta\beta'}$ can be presented as follows: $c_{\alpha\alpha'\beta\beta'} = \bar{c}_{\alpha\beta}\bar{c}_{\alpha'\beta'}^*$, where $\bar{c}_{\alpha\beta}$ is a unitary matrix, then the transformation (5.127) reduces to a basis change of the system Hamiltonian H_S , which is well known in perturbation theory [122] when a perturbation is added to H_S . However, in the general case, Eq. (5.127) does not reduce to a basis change (renormalization) of the system Hamiltonian. It is, actually, not necessary to prescribe any physical meaning to the transformation Eq. (5.127) and to the eigenvectors $\hat{\rho}_p$. The eigenvectors $\hat{\rho}_p$ merely allow us to find the time dynamics of the unperturbed eigenvectors $\hat{\rho}_p$, given as

$$\hat{\rho}_p(t) = \sum_{qq'} e^{-i\Omega_q t} c_{pq}^{-1} c_{qq'} \hat{\rho}_{q'}. \quad (5.128)$$

Further, using the operator form of the density matrix,

$$\rho = \sum_{\alpha\alpha'} \rho_{\alpha\alpha'} |\alpha\rangle\langle\alpha'| = \sum_p \rho_p \hat{\rho}_p, \quad (5.129)$$

we change representation,

$$\sum_p \rho_p \hat{\rho}_p(t) \longrightarrow \sum_p \rho_p(t) \hat{\rho}_p, \quad (5.130)$$

and obtain

$$\rho_p(t) = \sum_{qq'} e^{-i\Omega_q t} c_{q'q}^{-1} c_{qp} \rho_{q'}. \quad (5.131)$$

Note that, at $t = 0$, we have $\rho_p(0) = \rho_p$, which gives us the initial condition on $\rho_p(t)$. We also remark that, in general, the time evolution of a matrix element $\rho_{\alpha\alpha'}(t)$ is governed by more than one decoherence/relaxation time, as it follows from Eq. (5.131). However, for a ‘‘stand alone’’ transition frequency, as considered in Eqs. (5.118)–(5.120), there is only one decoherence time in the lowest order.

Now, we consider the remaining, zero-frequency, part of Eq. (5.114). For simplicity, we assume that there are no degenerate energy levels in the system, i.e. the equality $\omega_{\alpha\alpha'} = 0$ means also $\alpha = \alpha'$. Then, in the lowest order, we arrive at the Pauli master equation,

$$\begin{aligned} \frac{d}{dt} \rho_{\alpha\alpha}(t) &= \sum_{\beta} R_{\alpha\alpha\beta\beta} \rho_{\beta\beta}(t) \\ &= \sum_{\beta} [\Gamma_{\alpha\beta} \rho_{\beta\beta} - \Gamma_{\beta\alpha} \rho_{\alpha\alpha}], \end{aligned} \quad (5.132)$$

or equivalently, at the following secular equation,

$$\sum_{\beta} (\Omega \delta_{\alpha\beta} - i R_{\alpha\alpha\beta\beta}) \rho_{\beta\beta} = 0, \quad (5.133)$$

$$\det \|\Omega \delta_{\alpha\beta} - i R_{\alpha\alpha\beta\beta}\| = 0, \quad (5.134)$$

5.6. PHONON-INDUCED SPIN RELAXATION

where $R_{\alpha\alpha\beta\beta} = \Gamma_{\alpha\beta} - \delta_{\alpha\beta} \sum_{\gamma} \Gamma_{\gamma\alpha}$. One of the solutions of Eq. (5.134) is $\Omega = 0$, which corresponds to the stationary density matrix at $t \rightarrow \infty$. This solution exists always, since $\det \| R_{\alpha\alpha\beta\beta} \| \equiv 0$ due to the property $\sum_{\alpha} R_{\alpha\alpha\beta\beta} = 0$. For simplicity, we assume now that the rank of the matrix $R_{\alpha\alpha\beta\beta}$ equals $N - 1$, which physically means that there are no *stable* (arbitrarily long lived) excited states in the system, and thus, the stationary state is unique for arbitrary initial conditions. For a bath at thermal equilibrium, the relaxation rates obey the detailed balance equation,

$$\Gamma_{\alpha\beta} = \Gamma_{\beta\alpha} \exp\left(\frac{E_{\beta} - E_{\alpha}}{T}\right), \quad (5.135)$$

which alone is sufficient to obtain the eigenvector of Eq. (5.133) corresponding to $\Omega = 0$,

$$\hat{\rho}_T = \sum_{\alpha} e^{-E_{\alpha}/T} |\alpha\rangle\langle\alpha|. \quad (5.136)$$

Comparing the latter expression to Eq. (5.127) we obtain $c_{T,\alpha\alpha'} = \delta_{\alpha\alpha'} \exp(-E_{\alpha}/T)$, and by imposing the normalization condition on the density matrix (5.131) for an arbitrary initial condition $\rho_{\alpha\alpha'}$, we find $c_{\alpha\alpha',T}^{-1} = \delta_{\alpha\alpha'} Z_S^{-1}$, where $Z_S = \sum_{\alpha} \exp(-E_{\alpha}/T)$ is the system partition function. Using the expressions for $c_{T,\alpha\alpha'}$ and $c_{\alpha\alpha',T}^{-1}$ in Eq. (5.131) and assuming that $\exp(-i\Omega_q t)$ vanishes at $t \rightarrow \infty$ for all q , except $q = T$ ($\Omega_T = 0$), we recover the equilibrium distribution function

$$\rho_{\alpha\alpha'}(\infty) = \delta_{\alpha\alpha'} Z_S^{-1} e^{-E_{\alpha}/T}. \quad (5.137)$$

The remaining $N - 1$ solutions of Eq. (5.134) depend on the rates $\Gamma_{\alpha\beta}$. In what follows, we calculate these rates for the two-electron quantum dot.

5.6.2 Relaxation rates

The Hilbert space of our system is spanned by $N = 4$ states: $|\Psi_S\rangle$, $|\Psi_{T_+}\rangle$, $|\Psi_{T_-}\rangle$ and $|\Psi_{T_0}\rangle$. At zero Zeeman splitting ($E_Z = 0$), these states are the eigenstates of the Schrieffer-Wolff-transformed Hamiltonian describing the quantum dot, see Sec. 5.5.1, and we find no spin relaxation within this subspace in the first order (2nd order for rates) of H_{SO} , as already mentioned in Sec. 5.5.1. The absence of spin relaxation is now obvious, since for $E_Z = 0$ we have $U_{\text{int}} = U_{\text{ph}}$, and the relaxation rates $\Gamma_{\alpha\beta}$ in Eq. (5.108) vanish for $\alpha \neq \beta$ due to spin conservation. Higher order in H_{SO} processes will be considered later, but, for now, we note that $\Gamma_{\alpha\beta} = \mathcal{O}(H_{SO}^4)$ at $E_Z = 0$.

At a finite Zeeman splitting ($E_Z \neq 0$), the singlet and triplet states are intermixed by the interaction H_Z^{SO} , given in Eq. (5.61). In Sec. 5.5.2, we found the eigenstates and the renormalized energy levels of the quantum dot at $E_Z \neq 0$, using methods of both degenerate and non-degenerate perturbation theory to treat different (*strong* and *weak*) matrix elements of H_Z^{SO} . As a result, we obtained from the degenerate perturbation theory the renormalized energy levels, given in Eqs. (5.72) and (5.73),

and the eigenstates in Eq (5.69) with the coefficients in Eq. (5.75). From the non-degenerate perturbation theory, in its turn, we have derived an effective interaction U_{int} , given in Eq. (5.109), where the second term takes into account the weak matrix elements of H_Z^{SO} .

To keep our derivation simple, we first take into account only the strong matrix elements of H_Z^{SO} , thus letting $U_{\text{int}} = U_{\text{ph}}$. This should give us most of the dominant relaxation rates, except for some special cases, e.g. B -field direction at a “magic angle”, which we address later on. In the case considered now, the triplet state $|\Psi_{T_0}\rangle$ decouples from the rest of the states, thus forming a stable state in this approximation, with $\Gamma_{\alpha T_0} = \Gamma_{T_0 \alpha} = 0$ for $\alpha \neq T_0$. This state is, in fact, metastable, since in our subsequent consideration we find non-zero relaxation rates for $|\Psi_{T_0}\rangle$ due to the weak matrix elements of H_Z^{SO} , see below. However, for now, it is convenient to disregard the state $|\Psi_{T_0}\rangle$, thus considering only $N = 3$ states: $|\Psi_0\rangle$, $|\Psi_+\rangle$ and $|\Psi_-\rangle$, which are linear combinations of the singlet $|\Psi_S\rangle$ and two triplets $|\Psi_{T\pm}\rangle$ shown in Eq. (5.69). Then, it is straightforward to obtain the matrix elements of U_{int} ,

$$\begin{aligned} \langle \Psi_\alpha | U_{\text{int}} | \Psi_\beta \rangle &= a_\alpha a_\beta [\langle \psi_S | U_{\text{ph}} | \psi_S \rangle - \langle \psi_T | U_{\text{ph}} | \psi_T \rangle] \\ &\quad + \delta_{\alpha\beta} \langle \psi_T | U_{\text{ph}} | \psi_T \rangle, \end{aligned} \quad (5.138)$$

where $\alpha = 0, \pm$ labels the considered eigenstates, and $|\psi_{S(T)}\rangle$ is the singlet (triplet) orbital wave function. The coefficients a_α read

$$a_\alpha = \left[1 + \frac{\Delta_+^2}{(E_\alpha - E_{T_+})^2} + \frac{\Delta_-^2}{(E_\alpha - E_{T_-})^2} \right]^{-1/2}, \quad (5.139)$$

where $E_\alpha = E_0, E_\pm$ are the exact solutions of Eq. (5.71). The last term in Eq. (5.138) is irrelevant for our further discussion, since we consider only $\Gamma_{\alpha\beta}$ with $\alpha \neq \beta$. Thus, from the first line in Eq. (5.138), we see that the spin relaxation is owing to the difference $|\psi_S(\mathbf{r}_1, \mathbf{r}_2)|^2 - |\psi_T(\mathbf{r}_1, \mathbf{r}_2)|^2$. This difference turns out to be largest for a quantum dot without Coulomb interaction (see below), and almost vanishes in a double quantum dot due to the strong effect of the Coulomb repulsion.

Using the wave functions found in Sec. 5.3, we evaluate next the following form-factor

$$\begin{aligned} \mathcal{F}_{ST}(q_{\parallel}) &= \langle \psi_S | e^{i\mathbf{q}_{\parallel}\mathbf{R}} \cos(\mathbf{q}_{\parallel}\mathbf{r}/2) | \psi_S \rangle \\ &\quad - \langle \psi_T | e^{i\mathbf{q}_{\parallel}\mathbf{R}} \cos(\mathbf{q}_{\parallel}\mathbf{r}/2) | \psi_T \rangle. \end{aligned} \quad (5.140)$$

For the wave functions $|\psi_S\rangle = |0000\rangle$ and $|\psi_T\rangle = |000, -1\rangle$, we obtain

$$\begin{aligned} \mathcal{F}_{ST}(q_{\parallel}) &= e^{-\frac{1}{4}q_{\parallel}^2\Lambda^2} \left[e^{-\frac{1}{16}q_{\parallel}^2\tilde{\lambda}_0^2} {}_1F_1 \left(-\sqrt{\gamma_0}, 1; \frac{q_{\parallel}^2\tilde{\lambda}_0^2}{16} \right) \right. \\ &\quad \left. - e^{-\frac{1}{16}q_{\parallel}^2\tilde{\lambda}_1^2} {}_1F_1 \left(-\sqrt{1+\gamma_1}, 1; \frac{q_{\parallel}^2\tilde{\lambda}_1^2}{16} \right) \right], \end{aligned} \quad (5.141)$$

5.6. PHONON-INDUCED SPIN RELAXATION

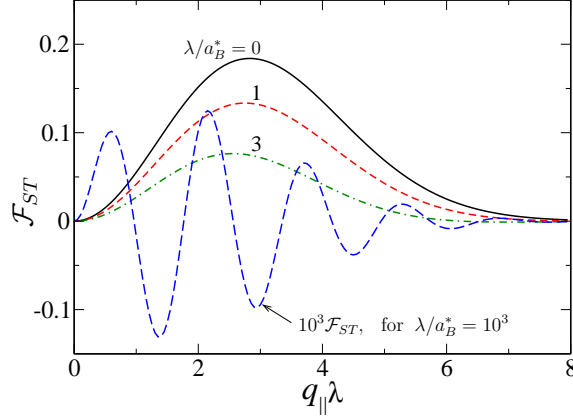


Figure 5.9: The form-factor $\mathcal{F}_{ST}(q_{\parallel})$ for $\lambda/a_B^* = 0, 1, 3$, as well as $10^3 \mathcal{F}_{ST}(q_{\parallel})$ for $\lambda/a_B^* = 10^3$.

where γ_m and $\tilde{\lambda}_m$, with $m = 0, 1$, are the variational parameters found in Appendix D. In the absence of Coulomb interaction ($\gamma_m = 0$ and $\tilde{\lambda} = \lambda$), Eq. (5.141) reduces to the following expression ($\lambda/a_B^* = 0$)

$$\mathcal{F}_{ST}(q_{\parallel}) = \frac{\hbar q_{\parallel}^2}{8m^* \omega} e^{-\frac{\hbar q_{\parallel}^2}{4m^* \omega}}, \quad (5.142)$$

where we used that $\lambda = \sqrt{2\hbar/m^* \omega}$ and $\Lambda = \sqrt{\hbar/2m^* \omega}$. Note that the function $\mathcal{F}_{ST}(q_{\parallel})$ in Eq. (5.142) has a single scale, $q_{\parallel} \sim \sqrt{4m^* \omega/\hbar}$. For strong Coulomb interaction, however, we find that $\mathcal{F}_{ST}(q_{\parallel})$ has two scales; an additional scale arises due to the Coulomb interaction and it is given by $q_{\parallel} \sim 1/\langle r \rangle$, where $\langle r \rangle = \lambda(\lambda/2a_B^*)^{1/3}$. In the limit $\lambda/a_B^* \gg 1$, we find $\mathcal{F}_{ST}(q_{\parallel})$ from Eq. (5.140) for both $q_{\parallel} \ll 1/\langle r \rangle$ and $q_{\parallel} \gg 1/\langle r \rangle$, and then match the two asymptotes into the following crossover function ($\lambda/a_B^* \gg 1$)

$$\mathcal{F}_{ST}(q_{\parallel}) = \frac{q_{\parallel} a_B^*}{3} J_1\left(\frac{q_{\parallel} \langle r \rangle}{2}\right) e^{-\frac{(1+\sqrt{3})\hbar q_{\parallel}^2}{8\sqrt{3}m^* \omega}}, \quad (5.143)$$

where $\langle r \rangle = \lambda(\lambda/2a_B^*)^{1/3}$ and $J_1(x)$ is a Bessel function of the first kind. We check numerically that Eq. (5.143) coincides with Eq. (5.141) in the whole range of q_{\parallel} for $\lambda/a_B^* \gg 1$. By comparing Eq. (5.143) to Eq. (5.142), we find that the magnitude of the function $\mathcal{F}_{ST}(q_{\parallel})$, in its maximum, scales as $(a_B^*/\lambda)^{7/6} \ll 1$, in the limit of strong Coulomb interaction. In Fig. 5.9, we plot $\mathcal{F}_{ST}(q_{\parallel})$ as a function of $q_{\parallel} \lambda$ for $\lambda/a_B^* = 0, 1, 3$, showing the suppression of $\mathcal{F}_{ST}(q_{\parallel})$ with increasing the Coulomb interaction strength. In addition, we also plot $10^3 \mathcal{F}_{ST}(q_{\parallel})$ for $\lambda/a_B^* = 10^3$, which shows that $\mathcal{F}_{ST}(q_{\parallel})$ oscillates on the scale $q_{\parallel} \sim 1/\langle r \rangle$, see also Eq. (5.143).

Next, we find the relaxation rates $\Gamma_{\alpha\beta}$ by substituting Eq. (5.138) into Eq. (5.108)

and averaging over phonons at thermal equilibrium,

$$\Gamma_{\alpha\beta} = 2a_\alpha^2 a_\beta^2 \omega_{\beta\alpha} (1 + N_{\omega_{\beta\alpha}}) \sum_j \int_0^{\pi/2} d\vartheta \frac{\sin \theta}{\pi \hbar \rho_c s_j^3} \left| F \left(\frac{\omega_{\beta\alpha}}{s_j} \cos \vartheta \right) \right|^2 \times \mathcal{F}_{ST} \left(\frac{\omega_{\beta\alpha}}{s_j} \sin \vartheta \right) \left(e^2 \bar{\beta}_{j,\vartheta}^2 + \delta_{j,1} \Xi_0^2 \frac{\omega_{\beta\alpha}^2}{s_j^2} \right), \quad (5.144)$$

where a_α is given in Eq. (5.139), $\omega_{\beta\alpha} = (E_\beta - E_\alpha)/\hbar$ is the transition frequency, and $N_w = (e^{\hbar w/T} - 1)^{-1}$. In deriving Eq. (5.144), we assumed a linear phonon dispersion relation, $\omega_{\mathbf{q}j} = s_j q$, and a transition frequency $\omega_{\beta\alpha}$ smaller than the Debye energy. We neglect optical phonon modes, since the characteristic transition energies in GaAs quantum dots do not exceed, typically, 1 meV. In Eq. (5.144), we also used the following notations:

$$\begin{aligned} \bar{\beta}_{1,\vartheta} &= 3\sqrt{2}\pi h_{14} \kappa^{-1} \sin^2 \vartheta \cos \vartheta, \\ \bar{\beta}_{2,\vartheta} &= \sqrt{2}\pi h_{14} \kappa^{-1} \sin 2\vartheta, \\ \bar{\beta}_{3,\vartheta} &= \sqrt{2}\pi h_{14} \kappa^{-1} (3 \cos^2 \vartheta - 1) \sin \vartheta, \end{aligned} \quad (5.145)$$

where the expressions for $\bar{\beta}_{2,\vartheta}$ and $\bar{\beta}_{3,\vartheta}$ depend on the choice of the transverse polarizations, while the quantity $\bar{\beta}_{2,\vartheta}^2 + \bar{\beta}_{3,\vartheta}^2$ is invariant. Below, we distinguish between three contributions of phonons in the relaxation rate (5.144),

$$\Gamma_{\alpha\beta} = \Gamma_{\alpha\beta}^{\text{DP}} + \Gamma_{\alpha\beta}^{\text{PEL}} + \Gamma_{\alpha\beta}^{\text{PET}}, \quad (5.146)$$

where $\Gamma_{\alpha\beta}^{\text{DP}}$ comes from the longitudinal ($j = 1$) phonon mode, interacting via the deformation potential mechanism (Ξ_0), $\Gamma_{\alpha\beta}^{\text{PEL}}$ comes from the longitudinal ($j = 1$) phonon mode, interacting via the piezoelectric mechanism (h_{14}), and $\Gamma_{\alpha\beta}^{\text{PET}}$ is the sum of contributions of transverse ($j = 2, 3$) phonon modes, interacting via the piezoelectric mechanism (h_{14}).

Since, in our approximation, the triplet state $|\Psi_{T_0}\rangle$ is infinitely long lived, we need to consider only three non-trivial relaxation rates: $\Gamma_{0,+}$, $\Gamma_{-,0}$, and $\Gamma_{-,+}$. Other rates are either zero or can be found using Eq. (5.135). As it follows from Eq. (5.144), any relaxation rate $\Gamma_{\alpha\beta}$ is proportional to $a_\alpha^2 a_\beta^2$. This factor is entirely determined by the combined effect of spin-orbit and Zeeman interactions, while the other factors in Eq. (5.144) stem from the particular form of the phonon potential (5.112). Thus, it is convenient to analyze $a_\alpha^2 a_\beta^2$ separately, since it describes the main effect of the spin-orbit interaction in the relaxation rate. For a weak spin-orbit interaction ($\lambda/\lambda_{SO} \ll 1$), the avoided crossing splittings Δ_\pm are small compared to the Zeeman energy, $\Delta_\pm \ll E_Z$. If, in addition, Δ_+ and Δ_- do not differ significantly from each other ($\Delta_\pm \gg \Delta_\mp^2/E_Z$), then the product $a_\alpha^2 a_\beta^2$ can be approximated by the following expressions:

$$2a_0^2 a_\pm^2 = \frac{\Delta_\pm^2}{J_\pm^2 + 4\Delta_\pm^2} \left(1 \pm \frac{J_\mp}{\sqrt{J_\mp^2 + 4\Delta_\mp^2}} \right), \quad (5.147)$$

$$4a_+^2 a_-^2 = \left(1 + \frac{J_+}{\sqrt{J_+^2 + 4\Delta_+^2}} \right) \left(1 - \frac{J_-}{\sqrt{J_-^2 + 4\Delta_-^2}} \right), \quad (5.148)$$

5.6. PHONON-INDUCED SPIN RELAXATION

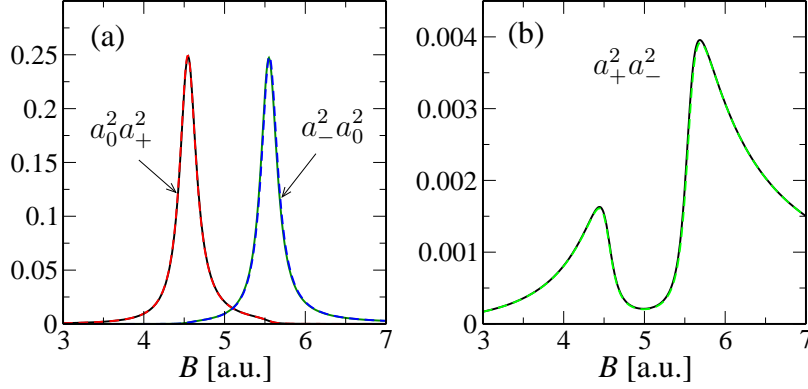


Figure 5.10: The factor $a_\alpha^2 a_\beta^2$, which multiplies the relaxation rate (5.144), plotted as a function B for the following cases: (a) $a_0^2 a_+^2$ and $a_-^2 a_0^2$, and (b) $a_+^2 a_-^2$. For the plot we used the following model parameters (in arbitrary units): $\Delta_+ = 0.15E_Z$, $\Delta_- = 0.1E_Z$, $E_S = 0$, $E_{T_\pm} = 10 - 2B \mp E_Z$, and $E_Z = 0.2B$.

where $J_\pm = E_{T_\pm} - E_S$. Equation (5.147) gives us a Lorentzian line-shape for $a_0^2 a_\pm^2$ in the vicinity of $J_\pm = 0$. We plot $a_0^2 a_\pm^2$ as a function of B in Fig. 5.10(a). Note that $a_0^2 a_\pm^2 \simeq 1/4$ at $J_\pm = 0$. In contrast, $a_+^2 a_-^2$ is suppressed compared to $a_0^2 a_\pm^2$ in the region between the avoided crossings ($E_{T_+} \leq E_S \leq E_{T_-}$), see Fig. 5.10(b). The quantity $a_+^2 a_-^2$ has two maxima, occurring close to the points where $J_\pm = 0$. The maximum at $J_\pm = 0$ scales down as $\sim \Delta_\mp^2/E_Z^2$ with decreasing Δ_\mp/E_Z . Furthermore, away from the singlet-triplet transition region, the quantity $a_0^2 a_+^2$ is suppressed for $E_S > E_{T_-}$ due to the factor in parentheses in Eq. (5.147). Thus, here, we have $a_+^2 a_0^2 \simeq (\Delta_+ \Delta_- / J_+ J_-)^2$ in contrast to $a_-^2 a_0^2 \simeq \Delta_-^2 / J_-^2$ and $a_+^2 a_-^2 \simeq \Delta_+^2 / J_+^2$. Similarly, on the other side of the singlet-triplet transition region ($E_S < E_{T_+}$), the quantity $a_0^2 a_-^2$ is suppressed, and we have $a_-^2 a_0^2 \simeq (\Delta_+ \Delta_- / J_+ J_-)^2$ in contrast to $a_+^2 a_0^2 \simeq \Delta_+^2 / J_+^2$ and $a_+^2 a_-^2 \simeq \Delta_-^2 / J_-^2$.

Next, we proceed with the phonon factor in Eq. (5.144), *i.e.* we consider $\Gamma_{\alpha\beta}/a_\alpha^2 a_\beta^2 (1 + N_{\omega_{\beta\alpha}})$ as a function of $\omega_{\beta\alpha}$. The spin-orbit interaction enters in this part only as a renormalization of the transition frequency $\omega_{\beta\alpha}$. It is, therefore, convenient to study this part of the rate as a function of $\omega_{\beta\alpha}$; note that $\omega_{\beta\alpha}$ is also the frequency of the emitted phonon. For simplicity, we assume $T = 0$, which allows only spontaneous emission of phonons from the quantum dot ($N_{\omega_{\beta\alpha}} = 0$). Thus, dropping the factor $a_\alpha^2 a_\beta^2 (1 + N_{\omega_{\beta\alpha}})$ from Eq. (5.144) and considering each term of the sum over j separately, we are left with an integration of a product of two form-factors and some trigonometric functions. This integration introduces several scales for the frequency $\omega_{\beta\alpha}$. Namely, from the form-factor $F(q_z)$, we obtain the scale $\omega_{\beta\alpha} \sim s_j/d$ and, from the form-factor $\mathcal{F}_{ST}(q_{||})$, we obtain, in general, two scales: $\omega_{\beta\alpha} \sim s_j/\lambda$ and $\omega_{\beta\alpha} \sim s_j/\langle r \rangle$. As a result, the integral in Eq. (5.144) can be taken analytically only for specific regimes. In Fig. 5.11, we show schematically the phonon factor $\Gamma_{\alpha\beta}/a_\alpha^2 a_\beta^2 (1 + N_{\omega_{\beta\alpha}})$ as a function of $\omega_{\beta\alpha}$ calculated numerically for the deformation potential mechanism and a strong Coulomb interaction in the quantum dot

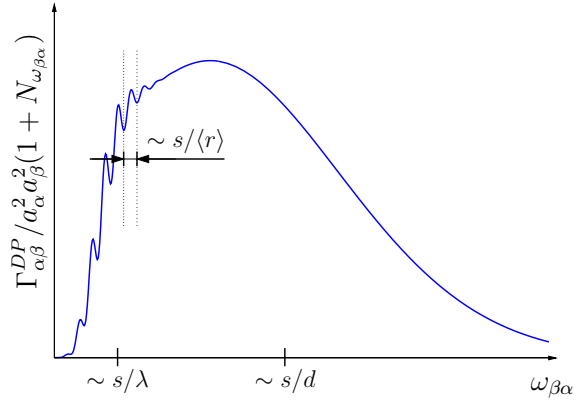


Figure 5.11: The phonon factor of the relaxation rates as a function of the phonon frequency $\omega_{\beta\alpha}$, plotted for the deformation potential mechanism and a strong Coulomb interaction in the quantum dot ($\lambda/a_B^* = 10^3$). The function contains three parameters: s/λ , s/d , and $s/\langle r \rangle$, where $s = s_1$ is the speed of sound.

($\lambda/a_B^* = 10^3$). The oscillatory part of the phonon factor is not present for weak and intermediate strengths of the Coulomb interaction, which is usually the case in the experiment.

Finally, we plot the relaxation rates $\Gamma_{+,-}$, $\Gamma_{+,0}$, and $\Gamma_{0,-}$ in Fig. 5.12, calculated for a GaAs quantum dot parameters. The relaxation rate $\Gamma_{+,-}$ is strongly suppressed around the singlet-triplet transition ($B_* \simeq 2.5$ T). The relaxation rates $\Gamma_{+,0}$, and $\Gamma_{0,-}$ have similar line-shape centered at different positions, however, the relaxation rate $\Gamma_{0,-}$ is larger due to the overall $\sim B^2$ enhancement of the coupling strength.

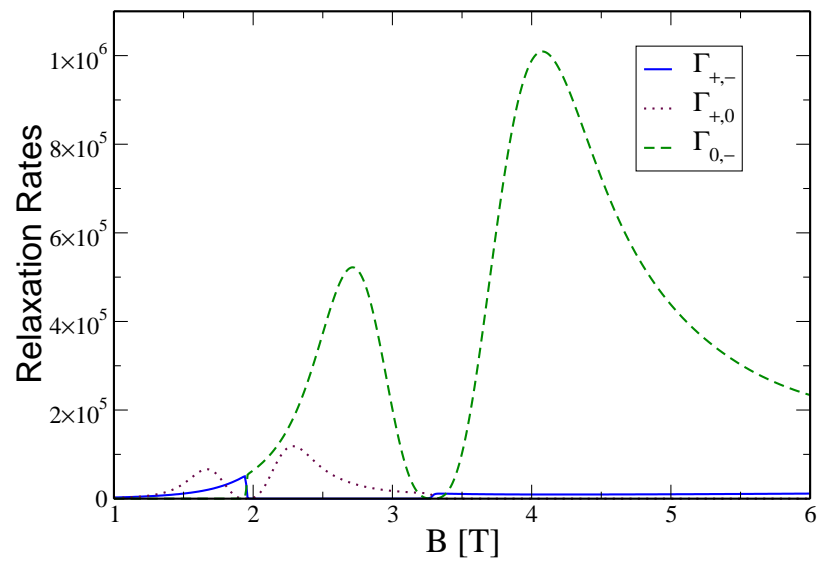


Figure 5.12: The relaxation rates $\Gamma_{+,-}$, $\Gamma_{+,0}$, and $\Gamma_{0,-}$ as a function of the magnetic field in the vicinity of the singlet-triplet transition.

CHAPTER 5. SPIN RELAXATION AT THE SINGLET-TRIPLET
TRANSITION IN A QUANTUM DOT

Chapter 6

Spin decay in a quantum dot coupled to a quantum point contact

In this chapter, we consider a mechanism of spin decay for the electron spin in the quantum dot (QD) due to its coupling to a nearby functioning quantum point contact (QPC). The coupling of spin to charge is achieved by means of the spin-orbit interaction at a finite Zeeman splitting. We calculate microscopically the coupling constants of the effective Hamiltonian and make prediction about the magnitude of the QPC-induced spin relaxation/decoherence rate in a realistic system. We find that, for some specific orientations of the setup with respect to the crystallographic axes, the spin relaxation/decoherence rate vanishes, while the charge sensitivity of the QPC is not changed. This can be used in experiments to avoid QPC-induced spin decay in read-out schemes.

6.1 Introduction

Solid state based quantum information processing is a rapidly developing field which aims at realizing and scaling up a quantum computer. Recent progress in nanotechnology has enabled us to access the electron spin in semiconductors [3, 4, 6], whereas electron spin in a QD has been proposed as a promising quantum object to implement a qubit due to its long coherence time [27]. Full control over the coherence time of the electron spin is thus a crucial point in spin-based qubit proposals. On the other hand, as a part of a quantum computer, read-out systems play an essential role in determining the final result of the computation. However, read-out devices, in general, affect the spin state of the system. Quantum point contacts (QPCs) which are used as charge detectors, in particular, couple to the spin via the spin-orbit interaction. For small GaAs QDs, the spin-orbit length ($\approx 8 \mu\text{m}$) is much larger than the dot

size (≈ 50 nm) and the spin-orbit interaction can often be neglected, however it is desirable to estimate how small it is and to minimize its effect.

Nowadays, experimentalists have reached the regimes where they can easily manipulate the number of electrons in QDs by electrical gates [70]. Furthermore, they managed to resolve the Zeeman splitted sublevels [86] and measure the spin relaxation time (T_1) up to 0.85 ms at an in-plane magnetic field of 8 T [64, 189]. In these types of experiments, they use a QPC near the QD as a charge detector by measuring the conductance of the QPC as a function of the number of electrons in the QD. The shot noise in the QPC affects the electron charge in the QD via the Coulomb interaction, and therefore, it can couple to the electron spin as well, via the spin-orbit interaction. While charge relaxation/decoherence in a QD due to a nearby functioning QPC has been studied before [171, 172], we show that the same charge fluctuations in the QPC introduce spin relaxation/decoherence by means of the spin-orbit and Zeeman interactions. Finally as a qubit, in addition to a long T_1 time, we need to have a sufficiently long T_2 for the electron spin in the QD. Although there are several proposals to measure decoherence time of electron spin in a QD (see e.g. Ref. [131, 132, 190]), it has not yet been achieved experimentally. However, it has been shown [90] that the spin-orbit interaction is inefficient in causing pure dephasing in QDs, and the decoherence time T_2 takes the maximal value $T_2 = 2T_1$, in the absence of other couplings to the electron spin.

In this chapter, we first derive an effective Hamiltonian for spin dynamics in the QD which contains a transverse (with respect to the external magnetic field) fluctuating field. We show that this read-out system speeds up the spin relaxation/decoherence rate and derive a similar expression, as in Ref. [90], for the T_1 and T_2 ; however, there are some regimes in which this effect vanishes (in the first order in spin-orbit interaction). The relaxation time is then highly dependent on the QPC orientation on the substrate, the distance between the QPC and the QD, the direction of the applied magnetic field and so on. Although this effect is, generally, smaller than other relaxation/relaxation mechanisms (e.g. coupling of spin to phonons [90] or nuclear spins [130]), it is still measurable with the current setups under certain conditions. The following results could be of interest to experimentalists to avoid QPC-induced spin decay due to their read-out systems.

6.2 Quantum dot coupled to a QPC

We consider an electron in a QD and a nearby functioning QPC (Fig. 1). To model this system, we treat QPC as a one dimensional object coupled capacitively to the electron confined in the QD. It is also assumed that there is only one electron inside the dot which can be assured by the measured current in QPC. The Hamiltonian

6.3. EFFECTIVE HAMILTONIAN

describing this coupled system reads $H = H_d + H_Z + H_{SO} + H_Q + H_{Qd}$, where

$$H_d = \frac{p^2}{2m^*} + U(\mathbf{r}), \quad (6.1)$$

$$H_{SO} = \beta(-p_x\sigma_x + p_y\sigma_y) + \alpha(p_x\sigma_y - p_y\sigma_x), \quad (6.2)$$

$$H_Z = \frac{1}{2}g\mu_B\mathbf{B} \cdot \boldsymbol{\sigma} = \frac{1}{2}E_Z\mathbf{n} \cdot \boldsymbol{\sigma}, \quad (6.3)$$

$$H_Q = \sum_{lk\sigma} \epsilon_k \bar{C}_{lk\sigma}^\dagger \bar{C}_{lk\sigma}, \quad (6.4)$$

$$H_{Qd} = \sum_{l'l'k'\sigma} \eta_{ll'}(\mathbf{r}) \bar{C}_{lk\sigma}^\dagger \bar{C}_{l'k'\sigma}. \quad (6.5)$$

Here, Q refers to the QPC and d to the dot, $\mathbf{p} = -i\hbar\nabla + (e/c)\mathbf{A}(\mathbf{r})$ is the electron 2D momentum, $U(\mathbf{r})$ is the lateral confining potential, with $\mathbf{r} = (x, y)$, and $\boldsymbol{\sigma}$ are the Pauli matrices. The 2DEG is perpendicular to the z direction and the spin-orbit Hamiltonian H_{SO} in Eq.(6.2) includes both Rashba (α), due to asymmetry of the quantum well profile in the z direction, and Dresselhaus (β) spin-orbit couplings, due to the bulk inversion of the GaAs lattice. The Zeeman interaction H_Z in Eq. (6.3) introduces a spin quantization axis along $\mathbf{n} = \mathbf{B}/B = (\cos\varphi \sin\vartheta, \sin\varphi \sin\vartheta, \cos\vartheta)$. The QPC consists of two leads coupled via a tunnel barrier and is described by the Hamiltonian H_Q , where $\bar{C}_{lk\sigma}^\dagger$, with $l = L, R$, creates an electron incident from lead l , with wave vector k and spin σ . We use the *bar* sign (e.g. over the operator $\bar{C}_{lk\sigma}$) to denote the scattering states in the absence of the electron on the QD. The Hamiltonian H_{Qd} in Eq. (6.5) describes the coupling between the quantum dot electron and the QPC electrons, the coupling being given by the screened Coulomb interaction

$$\eta_{ll'}(\mathbf{r}) = \langle \bar{l}k | \frac{e^2}{\kappa |\mathbf{r} - \mathbf{R}|} \tilde{\delta}(\mathbf{R} - \mathbf{a}) | \bar{l}'k' \rangle, \quad (6.6)$$

where \mathbf{R} refers to the location of the electrons in the QPC, κ is the dielectric constant of GaAs and we ignore the k -dependence of η . We describe the screening by a static screening factor $\tilde{\delta}(\mathbf{R} - \mathbf{a})$, which is a sharply peaked function with a width given by the screening length λ_{scr} , where the vector \mathbf{a} gives the location of the QPC (see Fig.1).

6.3 Effective Hamiltonian

The quantum dot electron spin couples to charge fluctuations in the QPC via the spin-orbit Hamiltonian (6.2). The charge fluctuations are caused by electrons passing through the QPC. To derive an effective Hamiltonian for the coupling of spin to charge fluctuations, we perform a Schrieffer-Wolff transformation, $\tilde{H} = \exp(S)H \exp(-S)$ [191], and exclude the spin-orbit Hamiltonian in leading order. We thus require that $[H_d + H_Z, S] = H_{SO}$, under the condition $\lambda_d \ll \lambda_{SO}$, where λ_d is the quantum dot size and $\lambda_{SO} = \hbar/m^*(|\beta| + |\alpha|)$ is the shortest spin-orbit length. The transformed

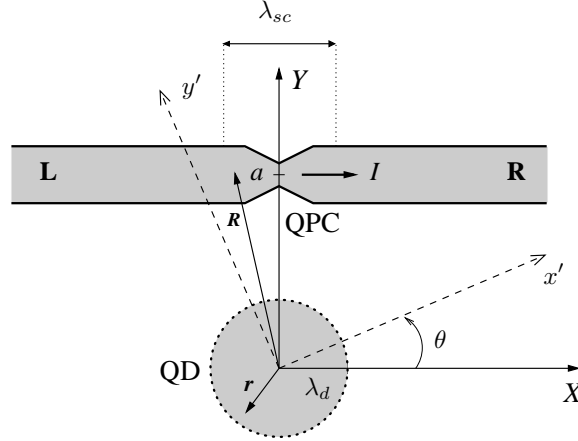


Figure 6.1: Schematic of the coupled QD and QPC. The (X, Y) frame gives the setup orientation (left and right leads) with respect to the crystallographic directions $x' \equiv [110]$ and $y' \equiv [\bar{1}10]$. The QD has a radius λ_d and is located at a distance a from the QPC. The vector \mathbf{R} shows the QPC electrons and \mathbf{r} refers to the coordinate of the electron in the QD. The noise of the QPC current I perturbs the electron spin on the QD via the spin-orbit interaction.

Hamiltonian is then given by

$$\tilde{H} = H_d + H_Z + H_Q + H_{Qd} + [S, H_{Qd}]. \quad (6.7)$$

$$S = \frac{1}{\hat{L}_d + \hat{L}_Z} H_{SO} = \frac{1}{\hat{L}_d} \sum_{m=0}^{+\infty} \left(-\frac{\hat{L}_Z}{\hat{L}_d} \right)^m H_{SO}, \quad (6.8)$$

where \hat{L} is Liouville superoperator for a given Hamiltonian defined by $\hat{L}A \equiv [H, A]$. For a harmonic confinement $U(r) = \frac{1}{2}m^*\omega_0^2 r^2$ we have

$$\frac{1}{\hat{L}_d} p_j = \frac{im^*}{\hbar} r_j, \quad (6.9)$$

$$\frac{1}{\hat{L}_d} r_j = \frac{1}{i\hbar m^* \omega_0^2} p_j \quad (j = x, y), \quad (6.10)$$

whence we can write the spin-orbit interaction in a more useful way

$$H_{SO} = i\hat{L}_d(\boldsymbol{\sigma} \cdot \boldsymbol{\xi}), \quad (6.11)$$

where $\boldsymbol{\xi}$ is a vector in the 2DEG and has a simple form in the coordinate frame $x' = (x + y)/\sqrt{2}$, $y' = (y - x)/\sqrt{2}$, $z' = z$, namely, $\boldsymbol{\xi} = (y'/\lambda_-, x'/\lambda_+, 0)$, where $\lambda_{\pm} = \hbar/m^*(\beta \pm \alpha)$ are the spin-orbit lengths. In addition, we have the following relations for the Zeeman Liouvillian

$$\hat{L}_Z^m(\boldsymbol{\sigma} \cdot \boldsymbol{\xi}) = iE_Z^m[\mathbf{n} \times \boldsymbol{\xi}] \cdot \boldsymbol{\sigma}, \quad m \text{ odd} > 0 \quad (6.12)$$

$$\hat{L}_Z^m(\boldsymbol{\sigma} \cdot \boldsymbol{\xi}) = E_Z^m[\mathbf{n} \times (\mathbf{n} \times \boldsymbol{\xi})] \cdot \boldsymbol{\sigma}, \quad m \text{ even} > 0. \quad (6.13)$$

6.3. EFFECTIVE HAMILTONIAN

The last term in Eq. (6.7) gives the coupling of the dot spin to the charge fluctuations in the QPC and the approximate expression (to first order in spin-orbit interaction) for S in Eq. (6.8) can be derived by using the above relations

$$-iS = \boldsymbol{\xi} \cdot \boldsymbol{\sigma} + [\mathbf{n} \times \boldsymbol{\xi}_1] \cdot \boldsymbol{\sigma} - [\mathbf{n} \times [\mathbf{n} \times \boldsymbol{\xi}_2]] \cdot \boldsymbol{\sigma} \quad (6.14)$$

$$\boldsymbol{\xi}_1 = ((\alpha_1 p_{y'} + \alpha_2 x')/\lambda_-, (\alpha_1 p_{x'} - \alpha_2 y')/\lambda_+, 0), \quad (6.15)$$

$$\boldsymbol{\xi}_2 = ((\beta_1 p_{x'} + \beta_2 y')/\lambda_-, (-\beta_1 p_{y'} + \beta_2 x')/\lambda_+, 0), \quad (6.16)$$

$$\alpha_1 = \frac{\hbar}{m^*} E_Z \frac{E_Z^2 - (\hbar\omega_0)^2}{(E_Z^2 - E_+^2)(E_Z^2 - E_-^2)}, \quad (6.17)$$

$$\alpha_2 = \frac{E_Z \hbar\omega_c (\hbar\omega_0)^2}{(E_Z^2 - E_+^2)(E_Z^2 - E_-^2)}, \quad (6.18)$$

$$\beta_1 = \frac{\hbar}{m^*} \frac{E_Z^2 \hbar\omega_c}{(E_Z^2 - E_+^2)(E_Z^2 - E_-^2)}, \quad (6.19)$$

$$\beta_2 = E_Z^2 \frac{(\hbar\omega_c)^2 + (\hbar\omega_0)^2 - E_Z^2}{(E_Z^2 - E_+^2)(E_Z^2 - E_-^2)}, \quad (6.20)$$

where $E_Z = g\mu_B B$ is the Zeeman splitting and $E_{\pm} = \hbar\omega \pm \hbar\omega_c/2$, with $\omega = \sqrt{\omega_0^2 + \omega_c^2}/4$ and $\omega_c = eB_z/m^*c$. Here, we assume that $E_{\pm} - E_Z \gg E_Z \lambda_d/\lambda_{SO}$, which ensures that our QD is a well defined spin qubit. This approximation is well justified because the typical size of QD is much smaller than the spin-orbit length. Next we consider low temperatures and biases, $T, \Delta\mu \ll \hbar\omega_0$, (to insure that only the ground state is populated so that its Zeeman sublevels constitute a two level system) and average over the dot ground state in Eq. (6.7). We obtain, using Eqs. (6.9-6.13), the following effective spin Hamiltonian

$$H_{\text{eff}} = \frac{1}{2} g\mu_B [\mathbf{B} + \delta\mathbf{B}(t)] \cdot \boldsymbol{\sigma}, \quad (6.21)$$

where we have gone to the interaction picture with the leads Hamiltonian $H'_Q = H_Q + \langle H_{Qd} \rangle_d$ and omitted a spin-independent part. Here and below, we use $\langle \dots \rangle_d$ to denote averaging over the dot ground state. Note that H'_Q describes the QPC, while it is electrostatically influenced by the QD with one electron in the ground state. Obviously, H'_Q can be rewritten in the same form as H_Q in Eq. (6.4), but with a different scattering phase in the scattering states. To denote the new scattering states, we omit the *bar* sign in our notations. The effective fluctuating magnetic field $\delta\mathbf{B}(t)$ in Eq. (6.21) is then given by

$$\begin{aligned}
 \delta \mathbf{B}(t) &= 2\mathbf{B} \times [\boldsymbol{\Omega}_1(t) + \mathbf{n} \times \boldsymbol{\Omega}_2(t)], & (6.22) \\
 \boldsymbol{\Omega}_1 &= \frac{e\hbar^2\gamma_1}{m^*} (\lambda_-^{-1}\boldsymbol{\mathcal{E}}_{y'}, \lambda_+^{-1}\boldsymbol{\mathcal{E}}_{x'}, 0), \\
 \boldsymbol{\Omega}_2 &= \frac{e\hbar^2\gamma_2}{m^*} (-\lambda_-^{-1}\boldsymbol{\mathcal{E}}_{x'}, \lambda_+^{-1}\boldsymbol{\mathcal{E}}_{y'}, 0), \\
 \gamma_1 &= \frac{m^*}{\hbar E_Z} \alpha_1 = \frac{E_Z^2 - (\hbar\omega_0)^2}{(E_+^2 - E_Z^2)(E_-^2 - E_Z^2)}, \\
 \gamma_2 &= \frac{m^*}{\hbar E_Z} \beta_1 = \frac{E_Z \hbar\omega_c}{(E_+^2 - E_Z^2)(E_-^2 - E_Z^2)}.
 \end{aligned}$$

Here we have introduced an electric field acting on the QPC electrons,

$$\boldsymbol{\mathcal{E}} = \frac{1}{e} \langle \nabla H_{Qd} \rangle_d = \sum_{l'k'k\sigma} \boldsymbol{\varepsilon}_{l'k'} C_{lk\sigma}^\dagger C_{l'k'\sigma}. \quad (6.23)$$

where $\boldsymbol{\varepsilon}_{l'k'} = e^{-1} \langle \nabla \eta_{l'k'}(\mathbf{r}) \rangle_d$ and the operator $C_{l'k'\sigma}$ corresponds to scattering states in the leads with the dot being occupied by one electron (H'_Q is diagonal in $C_{l'k'\sigma}$). As a first result, we note that the fluctuating quantum field $\delta \mathbf{B}(t)$ is transverse with respect to the (classical) applied magnetic field \mathbf{B} (*cf.* Ref. [90]). The magnetic field fluctuations here originate from orbital fluctuations that couple to the electron spin via the spin-orbit interaction. The absence of time reversal symmetry, which is removed by the Zeeman interaction, is crucial for this coupling. We assume no fluctuations in the external magnetic field \mathbf{B} . The dot electron spin couples to a bath of fermions, in contrast to the Ref. [90] where the bath was bosonic.

To calculate the coupling constants $\boldsymbol{\varepsilon}_{l'k'}$ in eq. (6.23), it is convenient to first integrate over the coordinates of the dot electron. We thus obtain $\boldsymbol{\mathcal{E}}(\mathbf{R}) = \boldsymbol{\mathcal{E}}_0(\mathbf{R}) \tilde{\delta}(\mathbf{R} - \mathbf{a})$, where \mathbf{R} refers to the location of the electrons in the QPC and the bare (unscreened) electric field is given by

$$\boldsymbol{\mathcal{E}}_0(\mathbf{R}) = \frac{e}{\kappa} \left\langle \frac{\mathbf{R} - \mathbf{r}}{|\mathbf{R} - \mathbf{r}|^3} \right\rangle_d = \frac{e\mathbf{R}}{\kappa R^3} \left(1 + \frac{3}{4} \frac{\lambda_d^2}{R^2} + \dots \right). \quad (6.24)$$

Here, we have assumed a parabolic confinement for the electron in QD, set the origin of coordinates in the dot center ($\langle \mathbf{r} \rangle_d = 0$) and averaged with the dot wave function $\Psi_d(\mathbf{r}) = \exp(-r^2/2\lambda_d^2)/\lambda_d\sqrt{\pi}$ which is the ground state of a symmetric harmonic potential in two dimensions. While we choose a very special form for the ground state wave function, this does not affect substantially the final result, the relaxation time T_1 . This is because any circularly symmetric wave function leads to the same form for $\boldsymbol{\mathcal{E}}_0(\mathbf{R})$ except that it just alters the second term in eq. (6.24) which is very small compare to the first term (about one hundredth) and negligible. The same kind of argument applies to the asymmetric wave functions. The coupling constants in Eq. (6.23) read $\boldsymbol{\varepsilon}_{l'k'} = \langle lk | \boldsymbol{\mathcal{E}}(\mathbf{R}) | l'k' \rangle$, where $|lk\rangle$ denote the scattering states in the leads and we neglect the k dependence in $\boldsymbol{\varepsilon}_{l'k'}$.

6.4 Relaxation time T_1

To proceed further, we construct the scattering states [192] out of the exact wave functions of the electron in the potential of the QPC tunnel barrier. While this is a generic method, we consider for simplicity a δ -potential tunnel barrier, $V(X) = (m^*/\hbar^2 \varkappa)\delta(X)$ where \varkappa gives the strength of the delta potential. In the QPC, electrons come from the left (right) lead, “feel” the tunnel barrier potential and are being transmitted or reflected, for which the electron wave functions in the even and odd channels are given by

$$\psi_e(X) = \sqrt{2} \begin{cases} \cos(kX + \phi), & X < 0, \\ \cos(kX - \phi), & X > 0, \end{cases} \quad (6.25)$$

$$\psi_o(X) = \sqrt{2} \sin kX \quad (6.26)$$

where $\phi = \arctan(\varkappa/k)$ and the sample size is set to unity. Note that $\phi = \pi/2 - \delta$, where $\delta \equiv \delta_e - \delta_o$ is the relative scattering phase between even and odd channels. The transmission through the QPC is related to ϕ by $\mathcal{T} = \cos^2 \phi$. We construct the scattering states in the following way

$$\begin{pmatrix} \psi_{sc}^L \\ \psi_{sc}^R \end{pmatrix} = \mathcal{U} \begin{pmatrix} \psi_e \\ \psi_o \end{pmatrix}, \quad \mathcal{U} = \frac{1}{2i} \begin{pmatrix} e^{i\delta} & -1 \\ e^{i\delta} & 1 \end{pmatrix}. \quad (6.27)$$

Up to a global phase, Eq. (6.27) is valid for any tunnel barrier with mirror symmetry.

We now calculate the matrix elements of $\boldsymbol{\mathcal{E}}(\mathbf{R})$ using the wave functions (6.25) and (6.26). Two interesting regimes are studied here : (i) $\lambda_{scr} \ll k_F^{-1} \ll a$ and (ii) $k_F^{-1} \ll \lambda_{scr} \ll a$, where λ_{scr} is the screening length in the QPC leads. In case (i), we set $\tilde{\delta}(\mathbf{R} - \mathbf{a}) = 2b\lambda_{scr}\delta(\mathbf{R} - \mathbf{a})$, with b being the QPC width in the transverse direction. By calculating the matrix elements of $\boldsymbol{\varepsilon}$ in the eigenstates of the potential barrier, we obtain

$$\boldsymbol{\varepsilon}_{ee} = \frac{4\lambda_{scr}}{\kappa} \mathcal{T} \boldsymbol{\mathcal{E}}_0(\mathbf{a}), \quad \boldsymbol{\varepsilon}_{oo} = \boldsymbol{\varepsilon}_{eo} = 0, \quad (6.28)$$

where we used the odd and even eigenbases and $\int dY |\Phi(Y)|^2 \delta(Y - a) = 1/b$, with $\Phi(Y)$ being the QPC wave function in the transverse direction. Going to the Left-Right basis, which is more suitable for studying transport phenomena, we obtain

$$\begin{pmatrix} \boldsymbol{\varepsilon}_{LL} & \boldsymbol{\varepsilon}_{LR} \\ \boldsymbol{\varepsilon}_{RL} & \boldsymbol{\varepsilon}_{RR} \end{pmatrix} = \frac{1}{4} \boldsymbol{\varepsilon}_{ee} \begin{pmatrix} 1 & 1 \\ 1 & 1 \end{pmatrix}. \quad (6.29)$$

Note that, in this case, we have $\boldsymbol{\varepsilon}_{ll'} \propto \mathcal{T}$, see Eqs. (6.28) and (6.29).

In case (ii), we set $\tilde{\delta}(\mathbf{R} - \mathbf{a}) = \Theta(X + \lambda_{sc}) - \Theta(X - \lambda_{sc})$, where $\Theta(X)$ is the step function, and obtain in leading order of $1/k_F\lambda_{sc}$

$$\boldsymbol{\varepsilon}_{ee} = \boldsymbol{\varepsilon}_{oo} = \frac{2e\lambda_{sc}}{\kappa a^2} \left(1 + \frac{3\lambda_d^2}{4a^2} - \frac{\lambda_{sc}^2}{a^2} + \dots \right) \mathbf{e}_Y, \quad (6.30)$$

$$\boldsymbol{\varepsilon}_{eo} = \frac{e\lambda_{sc}^2 \cos \delta}{\kappa a^3} \left(1 + \frac{3\lambda_d^2}{4a^2} - \frac{3\lambda_{sc}^2}{4a^2} + \dots \right) \mathbf{e}_X, \quad (6.31)$$

where \mathbf{e}_Y is a unit vector parallel to \mathbf{a} and \mathbf{e}_X is a unit vector perpendicular to \mathbf{a} (see Fig. 6.1). Going as before to the Left-Right basis, we obtain

$$\begin{pmatrix} \varepsilon_{LL} & \varepsilon_{LR} \\ \varepsilon_{RL} & \varepsilon_{RR} \end{pmatrix} = \frac{1}{4} \begin{pmatrix} \varepsilon_{ee} - 2\varepsilon_{eo} \cos \delta & 2i\varepsilon_{eo} \sin \delta \\ -2i\varepsilon_{eo} \sin \delta & \varepsilon_{ee} + 2\varepsilon_{eo} \cos \delta \end{pmatrix}. \quad (6.32)$$

Note that, in this case, we have $\varepsilon_{LR} \propto \sqrt{\mathcal{T}(1-\mathcal{T})}$, see Eqs. (6.31) and (6.32) in agreement with the result in Ref. [171]. Next we use the effective Hamiltonian (6.21) to calculate the relaxation rate (in secular approximation [90]) $1/T_1 = n_i n_j \Gamma_{ij}$, where the spin decay rate tensor Γ_{ij} can be expressed in terms of the spectral functions and n_i denote the components of the unit vector in the same direction of the applied magnetic field (see below). For a generic $\delta \mathbf{B}(t)$ (with $\langle \delta \mathbf{B}(t) \rangle = 0$), in the Born-Markov approximation we have $\Gamma_{ij} = \Gamma_{ij}^r + \Gamma_{ij}^d$ (r and d refer to the relaxation and dephasing, respectively), with [90]

$$\begin{aligned} \Gamma_{ij}^r &= \delta_{ij}(\delta_{pq} - n_p n_q) J_{pq}^+(\omega) - (\delta_{ip} - n_i n_p) J_{pj}^+(\omega) \\ &\quad - \delta_{ij} \epsilon_{kpq} n_k I_{pq}^-(\omega) + \epsilon_{ipq} n_p I_{qj}^-(\omega), \end{aligned} \quad (6.33)$$

$$\Gamma_{ij}^d = \delta_{ij} n_p n_q J_{pq}^+(0) - n_i n_p J_{pj}^+(0), \quad (6.34)$$

where $J_{ij}^\pm(w) = \text{Re}[J_{ij}(w) \pm J_{ij}(-w)]$ and $I_{ij}^\pm(w) = \text{Im}[J_{ij}(w) \pm J_{ij}(-w)]$ are given by the spectral function

$$J_{ij}(w) = \frac{g^2 \mu_B^2}{2\hbar^2} \int_0^{+\infty} \langle \delta B_i(0) \delta B_j(t) \rangle e^{-iwt} dt, \quad (6.35)$$

where ϵ_{ijk} is the antisymmetric tensor. In spite of its complicated form, it turns out that only the diagonal elements of Γ_{ij} contribute to the relaxation rate. Note that Γ_{ij}^d is identically zero, because of the transverse nature of the fluctuating magnetic field ($n_i \delta B_i(t) = 0$), and the second and the fourth terms on the RHS of Eq. (6.33) are nonzero but do not contribute to the relaxation rate for the same reason (contraction of n_i with J_{ik} gives zero). As a result we obtain

$$\begin{aligned} \frac{1}{T_1} &= 2\pi \hbar \nu^2 (M_{LL} + M_{RR}) F(E_Z) + \\ &\quad 2\pi \hbar \nu^2 M_{LR} [F(E_Z + \Delta\mu) + F(E_Z - \Delta\mu)], \end{aligned} \quad (6.36)$$

where $\nu = 1/2\pi \hbar v_F$ is the density of states per spin and mode in the lead, $F(x) = x \coth(x/2T)$ and the coefficients M_{lr} read

$$\begin{aligned} M_{lr} &= \boldsymbol{\omega}^{lr} \cdot \boldsymbol{\omega}^{rl} - (\mathbf{n} \cdot \boldsymbol{\omega}^{lr}) (\mathbf{n} \cdot \boldsymbol{\omega}^{rl}), \\ \boldsymbol{\omega}^{lr} &= \boldsymbol{\Omega}_1^{lr} + \mathbf{n} \times \boldsymbol{\Omega}_2^{lr}, \\ \boldsymbol{\Omega}_1^{lr} &= \frac{e\hbar\gamma_1 E_Z}{m^*} (\lambda_-^{-1} \varepsilon_{y'}^{lr}, \lambda_+^{-1} \varepsilon_{x'}^{lr}, 0), \\ \boldsymbol{\Omega}_2^{lr} &= \frac{e\hbar\gamma_2 E_Z}{m^*} (-\lambda_-^{-1} \varepsilon_{x'}^{lr}, \lambda_+^{-1} \varepsilon_{y'}^{lr}, 0), \end{aligned} \quad (6.37)$$

6.5. CONCLUSIONS

where Ω_i^{lr} , $i = 1, 2$ are matrix elements of Ω_i operators with respect to the leads.

To estimate the relaxation time, we use reasonable experimental parameters (the data belong to GaAs QDs) similar to those used in Ref. [64] and a large bias $E_Z \ll \Delta\mu \ll \hbar\omega_0$ which simply means that only the second term in Eq. (6.36) appreciably contribute to the relaxation rate. To calculate the relaxation rate we do not consider the first term in Eq. (6.36) because there are other sources which make the same contribution (such as electron-hole excitations in the leads) and only the second term is purely due to the QPC. Therefore Eq. (6.36) reduces to

$$\frac{1}{T_1} = 4\pi\hbar\nu^2 M_{LR}\Delta\mu, \quad E_Z \ll \Delta\mu \ll \hbar\omega_0. \quad (6.38)$$

We now consider an in plane magnetic field (15 T) which leads to $\Omega_2 = 0$ ($\gamma_2 = 0$) and, for simplicity, assume that it is directed in one of the spin-orbit axis (say x'). In this special case we obtain the following expression (provided $k_F^{-1} \ll \lambda_{\text{scr}} \ll a$, see Fig.6.1)

$$M_{LR} \simeq \frac{e^4\hbar^2\lambda_{sc}^2\cos^2\theta}{4m^{*2}\kappa^2a^6\lambda_+^2} \frac{E_Z^2}{(\hbar^2\omega_0^2 - E_Z^2)^2} \mathcal{T}(1 - \mathcal{T}). \quad (6.39)$$

Note that when $\theta = \pi/2$, the relaxation rate in this case is zero where θ is the angle between X and x' reference frames. For a QPC located at 300 nm from the center of the QD, the relaxation time is approximately 100 ms which is highly dependent on a ($1/T_1 \propto a^{-6}$).

At low temperatures and large bias voltage, the relaxation rate is linear in bias voltage and quadratic in Zeeman energy. However, the relaxation rate would generally be zero in the first order of spin-orbit interaction, if we apply the magnetic field in some specific directions. This can be easily seen from Eq. (6.32) where the matrix elements M_{lr} identically vanish for certain values of the setup parameters.

6.5 Conclusions

In conclusion, we have shown that charge read-out devices (e.g. a nearby QPC) increase spin relaxation/decoherence rate in a QD due to the spin-orbit interaction (both Rashba and Dresselhaus). Thanks to the transversal nature of the fermionic fluctuating field $\delta\mathbf{B}(t)$, we found that for this relaxation/decoherence mechanism $T_2 = 2T_1$. Finally, we showed how to calculate this rate microscopically and minimize this effect by tuning certain (geometrical and engineering) parameters of the setup. Our results can be used in experiments to avoid QPC-induced spin decay in read-out schemes.

Chapter 7

Measurement efficiency and n -shot read out of spin qubits

In this chapter, we consider electron spin qubits in quantum dots and define a measurement efficiency e to characterize reliable measurements via n -shot read outs [193]. We propose various implementations based on a double dot and quantum point contact (QPC) and show that the associated efficiencies e vary between 50% and 100%, allowing single-shot read out in the latter case. We model the read out microscopically and derive its time dynamics in terms of a generalized master equation, calculate the QPC current and show that it allows spin read out under realistic conditions.

7.1 Introduction

The read out of a qubit state is of central importance for quantum information processing [17]. In special cases, the qubit state can be determined in a single measurement, referred to as single shot read out. In general, however, the measurement needs to be performed not only once but n times, where n depends on the qubit, the efficiency e of the measurement device, and on the tolerated inaccuracy (infidelity) α . In the first part of this chapter, we analyze such n -shot read outs for general qubit implementations and derive a lower bound on n in terms of e and α . We then turn to spin-based qubits and GaAs quantum dots [27, 63] and analyze their n -shot read out based on a spin-charge conversion and charge measurement via quantum point contacts.

7.1.1 n -shot read out and measurement efficiency e

How many times n do the preparation and measurement need to be performed until the state of the qubit is known with some given infidelity α (n -shot read out)? We consider a well-defined qubit, i.e., we take only a two-dimensional qubit Hilbert space

into account and exclude leakage to other degrees of freedom. We define a set of positive operator-valued measure (POVM) operators [166], $E_{A_0} = p_0 |0\rangle\langle 0| + (1 - p_1) |1\rangle\langle 1|$ and $E_{A_1} = (1 - p_0) |0\rangle\langle 0| + p_1 |1\rangle\langle 1|$, where p_0 and p_1 are probabilities. These operators describe measurements with outcomes A_0 and A_1 , *resp.* They are positive and $E_{A_0} + E_{A_1} = 1$. This model of the measurement process can be pictured as follows. First, the qubit is coupled to some other device (e.g., to a reference dot, see below). Then this coupled system is measured and thereby projected onto some internal state. That state is accessed via an external “pointer” observable \hat{A} [166] (e.g., a particular charge distribution, a time-averaged current, or noise). We assume that only two measurement outcomes are possible, either A_0 or A_1 , which are classically distinguishable¹. For initial qubit state $|0\rangle$ the expectation value is $\langle \hat{A} \rangle_0 = p_0 A_0 + (1 - p_0) A_1$, while for initial state $|1\rangle$ it is $\langle \hat{A} \rangle_1 = (1 - p_1) A_0 + p_1 A_1$. Let us take an initial qubit state $|0\rangle$ and consider a single measurement. With probability p_0 , the measurement outcome is A_0 which one would interpret as “qubit was in state $|0\rangle$ ”. However, with probability $1 - p_0$, the outcome is A_1 and one might incorrectly conclude that “qubit was in state $|1\rangle$ ”. Conversely, the initial state $|1\rangle$ leads with probability p_1 to A_1 and with $1 - p_1$ to A_0 . We now determine n for a given α , for a qubit either in state $|0\rangle$ or $|1\rangle$ (no superposition allowed²). For an accurate read out we need, roughly speaking, that $\langle \hat{A} \rangle_0$ and $\langle \hat{A} \rangle_1$ are separated by more than the sum of the corresponding standard deviations. More precisely [194], we consider a parameter test of a binomial distribution of the measurement outcomes, one of which is A_0 with probability p . The null hypothesis is that the qubit is in state $|0\rangle$, thus $p = p_0$. The alternative is a qubit in state $|1\rangle$, thus $p = 1 - p_1$. For sufficiently large n , namely $n p_{0,1}(1 - p_{0,1}) > 9$, one can approximate the binomial with a normal distribution³. The state of the qubit can then be determined with significance level (“infidelity”) α for

$$n \geq z_{1-\alpha}^2 \left(\frac{1}{e} - 1 \right), \quad (7.1)$$

$$e = \left(\sqrt{p_0 p_1} - \sqrt{(1 - p_0)(1 - p_1)} \right)^2, \quad (7.2)$$

with the quantile (critical value) $z_{1-\alpha}$ of the standard normal distribution function, $\Phi(z_{1-\alpha}) = 1 - \alpha = \frac{1}{2} [1 + \text{erf}(z_{1-\alpha}/\sqrt{2})]$. We interpret e as *measurement efficiency*. Indeed, it is a single parameter $e \in [0, 1]$ which tells us if n -shot read out is possible.

¹In other words, we assume a sufficient signal-to-noise ratio of the apparatus to distinguish the measurement outcome A_0 from A_1 .

²For a qubit in an arbitrary superposition $\alpha |0\rangle + \beta |1\rangle$, the expectation value of the measurement is $\langle \hat{A} \rangle = |\alpha|^2 \langle \hat{A} \rangle_0 + |\beta|^2 \langle \hat{A} \rangle_1$, which allows to determine $|\alpha|^2$ and $|\beta|^2 = 1 - |\alpha|^2$. (To measure the phase $\arg \alpha/\beta$, first some single qubit rotations need to be performed.) In order to differentiate a given $|\alpha|^2$ from a value $|\alpha'|^2$, a sufficient n is given by Eqs. (7.1) and (7.2) after replacing $p_0 \rightarrow |\alpha|^2 p_0 + (1 - |\alpha|^2)(1 - p_1)$ and $p_1 \rightarrow 1 - |\alpha'|^2 p_0 - (1 - |\alpha'|^2)(1 - p_1)$.

³If n is small, one can use Clopper-Pearson confidence intervals. However, if read out of one state is perfect, say $p_0 = 1$, we can no longer approximate with a normal distribution, even for large n . In that case, finding A_0 as outcome n times in a row, even if the qubit is $|1\rangle$, i.e., read out fails, occurs with probability $(1 - p_1)^n$. Thus, $n \geq \log(\alpha)/\log(1 - e)$ is sufficient for read out.

7.1. INTRODUCTION

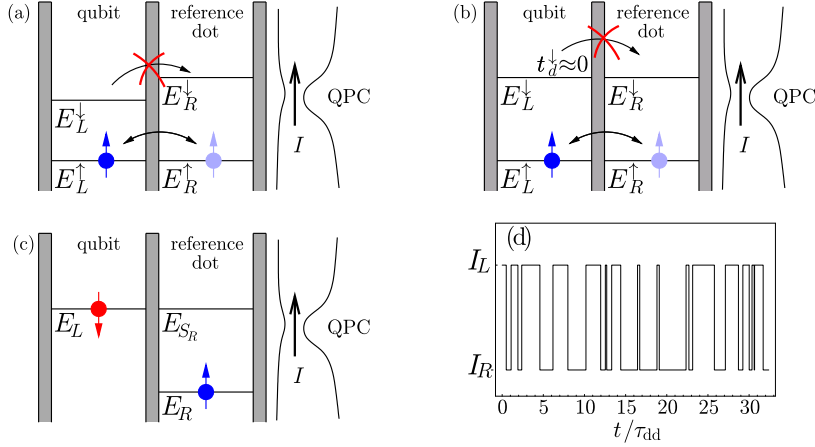


Figure 7.1: Electron spin read-out setup consisting of a double dot. The right “reference” dot is coupled capacitively to a QPC shown on the right. (a) Read out using different Zeeman splittings. For \uparrow , the electron tunnels between the two dots. For \downarrow , tunneling is suppressed by the detuning and the stationary state has a large contribution of the left dot since it has lower energy. This allows single-shot read out, i.e., $e = 100\%$. (b) Spin-dependent tunneling amplitudes, $t_d^\downarrow < t_d^\uparrow$, also enable efficient read out. (c) Read out with the singlet state. Tunneling of spin \uparrow to the reference dot is blocked due to the Pauli principle. (d) Schematic current vs. time during a single measurement. Here, τ_{dd} is the time scale for tunneling and we assume $\Gamma_{tot} > t_d$, i.e., that the tunneling events can be resolved in the current.

For $p_0 = p_1 = 1$, the efficiency is maximal, $e = 100\%$, and single-shot read out is possible ($n = 1$). Conversely, for $p_1 = 1 - p_0$ (e.g., $p_0 = p_1 = \frac{1}{2}$), the state of the qubit cannot be determined, not even for an arbitrarily large n , and the efficiency is $e = 0\%$. For the intermediate regime, $0\% < e < 100\%$, the state of the qubit is known after several measurements, with n satisfying Eq. (7.1).

7.1.2 Visibility v

When coherent oscillations between $|0\rangle$ and $|1\rangle$ are considered, the amplitude of the oscillating signal is $|\langle \hat{A} \rangle_1 - \langle \hat{A} \rangle_0|$, i.e., smaller than the value $|A_1 - A_0|$ by a factor of $v = |p_0 + p_1 - 1|$. Thus, we can take v as a measure of the visibility of the coherent oscillations. With v and the shift of the oscillations, $s = \frac{1}{2}(p_1 - p_0) = \frac{1}{2}(\langle \hat{A} \rangle_0 + \langle \hat{A} \rangle_1 - A_0 - A_1)/(A_1 - A_0)$, we can get e . We find the general relation $v^2 \leq e \leq v$, where the left inequality becomes exact for $p_0 = p_1$ and the right for $p_0 = 1$ or $p_1 = 1$. Further, for every $0 < \epsilon < 1$ we can take $p_0 = \frac{1}{2}$ and $p_1 = \frac{1}{2} + \frac{\epsilon}{2}$, thus $e < \epsilon v$. Hence, given these natural interpretations of e and v , we see that somewhat unexpectedly the efficiency can be much smaller than the visibility (of course, $e = 0 \Leftrightarrow v = 0$).

7.2 Single spin read out

We now discuss several concrete read-out setups and their measurement efficiency. We consider a promising qubit, which is an electron spin confined in a quantum dot [27,63]. For the read out of such a spin qubit, the time scale is limited by the spin-flip time T_1 , which has a lower bound of $\approx 100 \mu\text{s}$ [84,86] (while T_2 is not of relevance here). One setup proposed in Ref. [27] is read out via a neighboring paramagnetic dot, where the qubit spin nucleates formation of a ferromagnetic domain. This leads to $p_0 = p_1 = \frac{3}{4}$ and thus $e = 25\%$. Another idea is to transfer the qubit information from spin to charge [27,63,131,165,195]. For this, we propose to couple the qubit dot to a second (“reference”) dot⁴ and discuss several possibilities how that coupling can be made spin-dependent, see also Fig. 7.1. The resulting charge distribution on the double dot will then depend on the qubit spin state and can be detected by coupling the double dot to an electrometer, such as a quantum point contact (QPC) [70,74], see Fig. 7.1 (or, alternatively, a single-electron transistor [196]).

7.2.1 Read out with different Zeeman splittings

First, we propose a setup where efficiencies up to 100 % can be reached, see Fig. 7.1a. We take a double dot with different Zeeman splittings, $\Delta_z^{L,R} = E_{L,R}^\downarrow - E_{L,R}^\uparrow$, in each dot and consider a single electron on the double dot. For initial qubit state $|\uparrow\rangle$, the electron can tunnel from state $|L_\uparrow\rangle \hat{=} \uparrow_L \circlearrowright_R$ to state $|R_\uparrow\rangle \hat{=} \circlearrowleft_L \uparrow_R$ and vice versa, and analogously for qubit state $|\downarrow\rangle$. We consider time scales shorter than T_1 , thus the states with different spins are not coupled. Next, we define the detunings $\varepsilon_{\uparrow,\downarrow} = E_L^{\uparrow,\downarrow} - E_R^{\uparrow,\downarrow}$, which are different for the up and down states, $\varepsilon_\downarrow - \varepsilon_\uparrow = \Delta_z^L - \Delta_z^R \neq 0$. The stationary state of the double dot depends on $\varepsilon_{\uparrow,\downarrow}$ and so does the QPC current $\bar{I}_{\uparrow,\downarrow}$ [we show this below, see Eq. (7.6) and \bar{I}_{incoh}]. Therefore, initial states $|\uparrow\rangle$ and $|\downarrow\rangle$ can be identified through distinguishable stationary currents, $\bar{I}_\uparrow \neq \bar{I}_\downarrow$, thus $e = 100\%$ and single-shot read out is possible.

7.2.2 Spin-dependent tunneling

Spin-dependent tunneling provides another read-out scheme, see Fig. 7.1b, which we describe with spin-dependent tunneling amplitudes $t_d^{\uparrow,\downarrow}$. For $t_d^\downarrow \ll t_d^\uparrow$, only spin \uparrow tunnels onto the reference dot while tunneling of spin \downarrow is suppressed. We assume the same Zeeman splitting in both dots and resonance $\varepsilon = 0$. It turns out [Eq. (7.6)] that $\bar{I}_{\uparrow,\downarrow}$ depends on $t_d^{\uparrow,\downarrow}$ and thus the state of the qubit can be measured. However, the decay to the stationary state is quite slow in case the qubit is $|\downarrow\rangle$, due to the suppressed tunneling amplitude t_d^\downarrow . Since the difference in charge distribution

⁴Instead of a reference dot, the qubit dot can be coupled to a lead. To ensure that only electrons with, say, spin \downarrow can tunnel, one can use spin-polarized leads or a Zeeman splitting on the dot and properly tuned energy levels [131].

between qubit $|\uparrow\rangle$ and $|\downarrow\rangle$ is larger at short timescales, it can thus be advantageous to measure the time-dependent current (discussed toward the end).

7.2.3 Read out with Pauli principle

We now consider the case where the reference dot contains initially an electron in spin up ground state, see Fig. 7.1c. We assume gate voltages such that there are either two electrons on the right dot or one electron on each dot. Thus, we consider the 5 dimensional Hilbert space $|S_R\rangle \hat{=} \bigcirc_L \bigcirc_R$, $|\uparrow\downarrow\rangle \hat{=} \bigcirc_L \bigcirc_R$, $|\downarrow\uparrow\rangle \hat{=} \bigcirc_L \bigcirc_R$, $|T_+\rangle \hat{=} \bigcirc_L \bigcirc_R$, $|T_-\rangle \hat{=} \bigcirc_L \bigcirc_R$. We define the “delocalized” singlet $|S_{LR}\rangle = (|\uparrow\downarrow\rangle - |\downarrow\uparrow\rangle)/\sqrt{2}$ and the triplet $|T_0\rangle = (|\uparrow\downarrow\rangle + |\downarrow\uparrow\rangle)/\sqrt{2}$. In the absence of tunneling, the corresponding energies are $E_{S_R} = 2\epsilon_R + U$ and $E_{S_{LR}} = E_{T_{0,\pm}} = \epsilon_L + \epsilon_R$ with charging energy U and single particle energies $\epsilon_{L,R}$. We can neglect states with two electrons on the qubit dot and the triplet states with two electrons on the reference dot, since they have a much larger energy (their admixture due to tunneling is small). We denote the state with an “extra” electron on the right dot as $|R\rangle \equiv |S_R\rangle$ with corresponding QPC current I_R . For state $|L\rangle \equiv |S_{LR}\rangle$ and for all triplet states, $|T_{0,\pm}\rangle$, the current is I_L . When tunneling is switched on and the qubit is initially in state $|\uparrow\rangle$, tunneling to the reference dot is blocked due to the Pauli exclusion principle [134]. Thus, the double dot will remain in the (stationary) state $|T_+\rangle\langle T_+|$ and the current in the quantum dot remains $\langle I \rangle = I_L$ (a so-called non-demolition measurement). On the other hand, for an initial qubit state $|\downarrow\rangle$, the initial state of the double dot is $|\downarrow\uparrow\rangle = (|T_0\rangle - |S_{LR}\rangle)/\sqrt{2}$. The contribution $|S_{LR}\rangle$ of this superposition is tunnel coupled to $|S_R\rangle$ and will decay to the stationary state $\bar{\rho}$ with corresponding QPC current \bar{I} (see below for an explicit evaluation). In contrast, the triplet contribution $|T_0\rangle$ is not tunnel-coupled to $|S_R\rangle$ due to spin conservation and does not decay. In total, the density matrix of the double dot decays into the stationary value $\frac{1}{2}(|T_0\rangle\langle T_0| + \bar{\rho})$. For $\varepsilon = 0$, the ensemble-averaged QPC current for qubit $|\downarrow\rangle$ is $\langle I \rangle = \frac{1}{2}(I_L + \bar{I}) \approx \frac{1}{4}(3I_L + I_R)$ and can thus be distinguished from I_L for qubit $|\uparrow\rangle$. However, in a single run of such a measurement, an initial qubit $|\downarrow\rangle$ decays either into $|T_0\rangle\langle T_0|$ or into $\bar{\rho}$, with 50% probability each. Since $|T_0\rangle\langle T_0|$ and $|T_+\rangle\langle T_+|$ lead to the same QPC current I_L , these two states are not distinguishable within this read-out scheme and single-shot read-out is not possible. The read out can now be described with the POVM model given above, with $|\uparrow\rangle \equiv |0\rangle$ and $|\downarrow\rangle \equiv |1\rangle$ and $A_\uparrow = I_L$; $A_\downarrow = \bar{I}$; $p_\uparrow = 1$; and $p_\downarrow = \frac{1}{2}$. Thus, the *measurement efficiency* is $e = 50\%$, i.e., to achieve a fidelity of $1 - \alpha = 99\%$, we need $n \geq 7$ read outs.

An analogous read out is possible if the ground state of the reference dot is a triplet, say $|RT_+\rangle \hat{=} \bigcirc_L \bigcirc_R$ which is lower than the other triplets ($|RT_{0,-}\rangle$, $|RT_-\rangle$) due to Zeeman splitting. Again, we assume that the reference dot is initially $|\uparrow\rangle$. First, for a qubit state $|\uparrow\rangle$ and at resonance, $\varepsilon = 0$, tunneling into $|RT_+\rangle$ always occurs and $p_\uparrow = 1$. Second, the qubit state $|\downarrow\rangle$ has an increased energy by the Zeeman splitting Δ_z and is thus at resonance with $|RT_0\rangle$ (which has also an increased energy). If the double dot is not projected onto the singlet (in 50% of the cases), tunneling onto

the reference dot will also occur, i.e., $p_1 = \frac{1}{2}$. Thus, when one detects an additional charge on the reference dot, the initial state of the qubit is not known. We find again $e = 50\%$.

7.3 Read-out model

So far we have introduced various spin read out schemes and the corresponding measurement efficiencies. In order to evaluate the signal strength $A_0 - A_1$ for these schemes, we now calculate the stationary charge distribution $\bar{\rho}$ and QPC current \bar{I} for the case when the electron can tunnel coherently between the two dots (as a function of the detuning and the tunnel coupling). We describe the read-out setup with the Hamiltonian $H = H_d + V_d + H_{\text{QPC}} + V$. Here, H_{QPC} contains the energies of the (uncoupled) Fermi leads of the QPC. Further, H_d describes the double dot in the absence of tunneling, including orbital and electrostatic charging energies, $H_d |n\rangle = E_n |n\rangle$. It thus contains $\varepsilon = E_L - E_R$, the detuning of the tunneling resonance. The inter-dot tunneling Hamiltonian is defined as $V_d = t_d(|R\rangle \langle L| + |L\rangle \langle R|)$. (Note that for tunneling between $|S_{LR}\rangle$ and $|S_R\rangle$, t_d is $\sqrt{2}$ times the one-particle tunneling amplitude, since both states $|\uparrow\downarrow\rangle$ and $|\downarrow\uparrow\rangle$ are involved). V is a tunneling Hamiltonian describing transport through the QPC. The tunneling amplitudes, t_L^Q and t_R^Q , will be influenced by electrostatic effects, in particular by the charge distribution on the double dot. Thus, we model the measurement of the dot state via the QPC with $V = \left(t_L^Q |L\rangle \langle L| + t_R^Q |R\rangle \langle R| \right) \sum (c_{\text{in}}^\dagger c_{\text{out}} + \text{h.c.})$ [197–199]. Here, c_{in}^\dagger and c_{out}^\dagger create electrons in the incoming and the outgoing leads of the QPC, where the sum is taken over all momentum and spin states. We derive the master equation for the reduced density matrix ρ of the double dot. We use standard techniques and make a Born-Markov approximation⁵ in V [200]. We allow for an arbitrary inter-dot tunnel coupling, i.e., we keep V_d exactly, with energy splitting $E = \sqrt{4t_d^2 + \varepsilon^2}$ in the eigenbasis of $H_d + V_d$. We obtain the master equation⁶

$$\dot{\rho}_L = -\dot{\rho}_R = 2t_d \text{Im}[\rho_{RL}], \quad (7.3)$$

$$\begin{aligned} \dot{\rho}_{RL} = & \left[it_d + t_d \frac{\Gamma_Q \varepsilon}{E^2} (g_\Sigma - 2g_0) \right] (\rho_R - \rho_L) \\ & - \frac{t_d \Gamma_Q}{\Delta\mu} - (\kappa \Gamma_Q + \Gamma_i - i\varepsilon) \rho_{RL}, \end{aligned} \quad (7.4)$$

⁵We map the two-level system $\{|L\rangle, |R\rangle\}$ onto a pseudo spin $\frac{1}{2}$ with Hamiltonian $H(t) = \frac{1}{2}\varepsilon\sigma_z + t_d\sigma_x + X(t)\sigma_z + \frac{1}{2}(t_L^Q + t_R^Q)V_{\text{QPC}}(t)$. The fluctuations due to the QPC are $X(t) = \frac{1}{2}(t_L^Q - t_R^Q)V_{\text{QPC}}(t)$ with $V_{\text{QPC}}(t) = e^{iH_{\text{QPC}}t}V_{\text{QPC}}e^{-iH_{\text{QPC}}t}$.

⁶We define $\mathbf{P} = \frac{1}{2}\text{Tr}\rho\boldsymbol{\sigma}$ and write the master equation in the standard Bloch notation, $\dot{\mathbf{P}} = \boldsymbol{\omega} \times \mathbf{P} + \Gamma'(\mathbf{P} - \mathbf{P}_0)$, with $\boldsymbol{\omega} = (2t_d, 0, 0)$ and $\Gamma'\mathbf{a} = (0, -t_d\Gamma_Q/\Delta\mu - t_d\Gamma_Q(g_\Sigma - 2g_0)\varepsilon/E^2, \varepsilon + t_d\Gamma_Q/\Delta\mu) \times \mathbf{a} + \Gamma\mathbf{a}$, where Γ is symmetric with elements $\Gamma_{xy} = \Gamma_{yx} = -t_d\Gamma_Q/\Delta\mu$; $\Gamma_{xz} = \Gamma_{zx} = \Gamma_{xy} - t_d\Gamma_Q(g_\Sigma - 2g_0)\varepsilon/E^2$; $\Gamma_{yy} = -\Gamma_Q(1 + g_\Sigma) + \Gamma_Q(g_\Sigma - 2g_0)\varepsilon^2/E^2$; $\Gamma_{xx} = 2\Gamma_{xy} + \Gamma_{yy}$; $\Gamma_{yz} = \Gamma_{zy} = \Gamma_{zz} = 0$. Finally, $P_{0x} = P_{0y} = 0$ and $P_{0z} = [t_d\Gamma_Q(2t_d + \varepsilon)/(1 + g_\Sigma)\Delta\mu^2 - \Gamma_{xy}]/\Gamma_{xz}$.

7.3. READ-OUT MODEL

for $\rho_n = \langle n|\rho|n\rangle$ and $\rho_{RL} = \langle R|\rho|L\rangle$. In comparison to previous work [197–199], we find an additional term, $-t_d \Gamma_Q/\Delta\mu$, which comes from treating V_d exactly. We find that the current through the QPC is $I_L = 2\pi\nu^2 e \Delta\mu |t_L^Q|^2$ for state $|L\rangle$ and analogously I_R for state $|R\rangle$, and we choose $I_L, I_R \geq 0$. Here, $\Delta\mu > 0$ is the applied bias across the QPC and ν is the DOS at the Fermi energy of the leads connecting to the QPC. We define $g_{\pm} = g(\Delta\mu \pm E)$, $g_{\Sigma} = g_+ + g_-$ and $g_0 = g(\Delta\mu)$ with $g(x) = x/\Delta\mu(e^{x/kT} - 1)$. The values $g_{\pm, \Sigma, 0}$ vanish for $\Delta\mu \pm E > kT$. In this case, the decay rate due to the current assumes the known value [197–199], $\Gamma_Q = (\sqrt{T_L} - \sqrt{T_R})^2 / 2e$. Generally, the factor $\kappa = 1 + (4t_d^2 g_{\Sigma} + 2\varepsilon^2 g_0)/E^2$ accounts for additional relaxation/dephasing due to particle hole excitations, induced, e.g., by thermal fluctuations of the QPC current. For almost equal currents, $I_{L,R} = I(1 \pm \frac{1}{2}x)$, we have $\Gamma_Q = Ix^2/8e + O(x^4)$. Finally, by introducing the phenomenological rate Γ_i we have allowed for some intrinsic charge dephasing, which occurs on the time scale of nanoseconds [201]. For an initial state in the subspace $\{|L\rangle, |R\rangle\}$, we find the stationary solution of the double dot,

$$\bar{\rho} = \left(\frac{1}{2} - \frac{\eta\varepsilon}{2\Delta\mu}\right) |L\rangle\langle L| + \left(\frac{1}{2} + \frac{\eta\varepsilon}{2\Delta\mu}\right) |R\rangle\langle R| - \frac{\eta t_d}{\Delta\mu} (|R\rangle\langle L| + |L\rangle\langle R|), \quad (7.5)$$

where $\eta = \Gamma_Q/[\Gamma_Q(1+g_{\Sigma})+\Gamma_i]$. Positivity of $\bar{\rho}$ is satisfied since $\eta \leq \Delta\mu/E$. The time decay to $\bar{\rho}$ is described by three rates, given as the roots of $P(\lambda) = \lambda^3 + 2\Gamma_{\text{tot}}\lambda^2 + (E^2 + \Gamma_{\text{tot}}^2)\lambda + 4t_d^2[\Gamma_{\text{tot}} + \Gamma_Q(g_{\Sigma} - 2g_0)\varepsilon^2/E^2]$, with $\Gamma_{\text{tot}} = \kappa\Gamma_Q + \Gamma_i$. The stationary current through the QPC is given by $\bar{I} = \bar{\rho}_L I_L + \bar{\rho}_R I_R + 2e t_d \lambda (\Gamma_Q/\Delta\mu) \text{Re } \bar{\rho}_{RL}$ and thus becomes

$$\bar{I} = \frac{I_L + I_R}{2} + \eta \frac{\varepsilon}{2\Delta\mu} (I_R - I_L) - \eta \lambda \frac{2e \Gamma_Q t_d^2}{\Delta\mu^2}, \quad (7.6)$$

where $\lambda = 1 - \Delta\mu(g_- - g_+)/E$. We note that η quantifies the effect of the detuning ε on the QPC current. To reach maximal sensitivity, $\eta = 1$, we need $I_R \lesssim I_L/10$ for $I \sim 1 \text{ nA}$ and $\Gamma_i \sim 10^9 \text{ s}^{-1}$. In linear response, the current becomes

$$\begin{aligned} \bar{I} = & \frac{I_L + I_R}{2} + \frac{\varepsilon}{E} \tanh \frac{E}{2T} \left[1 - \frac{\Gamma_i \Delta\mu}{\Gamma_Q E} \tanh \frac{E}{2T} \right] \frac{I_R - I_L}{2} - \frac{2e t_d^2 \Gamma_Q}{E^2} \left[1 - \frac{E}{T} \sinh \frac{E}{T} \right] + \\ & \frac{e t_d^2 \Gamma_i \Delta\mu}{E^3 \cosh^2(E/T)} \left[\sinh \frac{E}{T} - \frac{E}{T} \right] \left[1 - \frac{\Gamma_i \Delta\mu}{\Gamma_Q E} \tanh \frac{E}{2T} \right]. \end{aligned} \quad (7.7)$$

Note that the second term in Eq. (7.6) depends on ε , a property which can be used for read out, as we have discussed above. For example, for different Zeeman splittings and $\varepsilon_{\uparrow, \downarrow} = \pm \Delta\mu/2$, $\Gamma_i = 10^9 \text{ s}^{-1}$, $I_L = 1 \text{ nA}$, and $I_R = 0$, the current difference is $\bar{I}_{\downarrow} - \bar{I}_{\uparrow} = 0.4 \text{ nA}$, which reduces to 0.05 nA for $I_R = 0.5 \text{ nA}$. However, typical QPC currents currently reachable are $I_L = 10 \text{ nA}$ and $I_R = 9.9 \text{ nA}$, i.e., the relaxation of the double dot due to the QPC is suppressed, $\eta < 10^{-3}$, and other relaxation channels become important.

7.3.1 Incoherent tunneling

So far, we have discussed coherent tunneling. We can also take incoherent tunneling into account, e.g., phonon assisted tunneling, by introducing relaxation rates in Eqs. (7.3),(7.4). For example, for detailed balance rates and neglecting coherent tunneling, we find the stationary current $\bar{I}_{\text{incoh}} = \frac{1}{2}(I_L + I_R) + \frac{1}{2}(I_R - I_L) \tanh(\varepsilon/2kT)$ (which becomes I_R for $\varepsilon > kT$). The QPC current again depends on ε and can be used for spin read out. The current can also be measured on shorter time scales as we discuss now.

7.3.2 Read out with time-dependent currents

Read out with time-dependent currents is possible if there is sufficient time to distinguish I_L from I_R between two tunneling events to or from the reference dot, i.e., we consider $\Gamma_{\text{tot}} > t_d$. In this incoherent regime, the tunneling from qubit to reference dot occurs with a rate W_{\uparrow} or W_{\downarrow} , depending on the qubit state, with, say, $W_{\downarrow} \ll W_{\uparrow}$. Such rates arise from spin-dependent tunneling, $t_d^{\uparrow,\downarrow}$, or from different Zeeman splittings and tuning to tunneling resonance for, say, qubit $|\uparrow\rangle$ while qubit $|\downarrow\rangle$ is off-resonant, see Figs. 7.1a and 7.1b. For read out, the electron is initially on the left dot and the QPC current is I_L . Then, if the electron tunnels onto the reference dot within time t and thus changes the QPC current to I_R , such a change would be interpreted as qubit in state $|\uparrow\rangle$, otherwise as qubit $|\downarrow\rangle$. For calculating the measurement efficiency e , we note that $p_{\uparrow} = p_0 = 1 - e^{-tW_{\uparrow}}$ and $p_{\downarrow} = p_1 = e^{-tW_{\downarrow}}$ (with this type of read out, W_{\downarrow} corresponds to a loss of the information, i.e., describes “mixing” [202]). We then maximize e by choosing a suitable t and find efficiencies $e \gtrsim 50\%$ for $W_{\uparrow}/W_{\downarrow} \gtrsim 8.75$ and $e \gtrsim 90\%$ for $W_{\uparrow}/W_{\downarrow} \gtrsim 80$.

A more involved read out is to measure the current through the QPC at different times. The current as function of time switches between the values I_L and I_R , i.e., shows telegraph noise, as sketched in Fig. 7.1d. Since the frequency of these switching events (roughly W_{\uparrow} or W_{\downarrow}) depends on the spin, the QPC noise reveals the state of the qubit. Finally, at times of the order of the spin relaxation time T_1 , the information about the qubit is lost. At each spin flip, the switching frequency changes ($W_{\uparrow} \leftrightarrow W_{\downarrow}$), which thus provides a way to measure T_1 .

7.4 Conclusions

In conclusion, we have given the criterion when n -shot measurements are possible and have introduced the measurement efficiency e . For electron spin qubits, we have proposed several read-out schemes and have found efficiencies up to 100%, which allow single-shot read out. Other schemes, which are based on the Pauli principle, have a lower efficiency, $e = 50\%$.

Chapter 8

Shot noise in transport through a double quantum dot close to the Kondo regime

8.1 Introduction

Spin-flip processes in a spin 1/2 quantum dot attached to leads result in a renormalization of the single-particle transmission coefficient \mathcal{T} , giving rise to the Kondo effect [139, 140] below the Kondo temperature T_K . Theoretical studies on shot noise in this system are available [203–205], and show that the noise S obeys qualitatively the same formula as for noninteracting electrons but with a renormalized \mathcal{T} . Here, we consider a system where the spin fluctuations (that are enhanced near the Kondo regime) strongly affect the noise, resulting in some cases in super-Poissonian noise – a result which cannot be obtained from the “non-interacting” formula.

We consider two lateral quantum dots (DD), connected in series between two metallic leads via tunnel contacts, see inset of Fig. 8.1*a*. The dots are tuned into the Coulomb blockade regime, each dot having a spin 1/2 ground state. The low energy sector of the DD consists of a singlet $|S\rangle$ and a triplet $|T\rangle \equiv \{|T_+\rangle, |T_0\rangle, |T_-\rangle\}$, with the singlet-triplet splitting K . The Kondo effect in this system has been studied extensively [115, 152, 158–160]. Two peculiar features in the linear conductance G have been found: a peak in G vs the inter-dot tunnel coupling t_H (see Fig. 8.1*a*), revealing the non-Fermi-liquid critical point of the two-impurity Kondo model (2IKM) [164]; and a peak in G vs an applied perpendicular magnetic field B (see Fig. 8.1*b*), as a result of the singlet-triplet Kondo effect at $K = 0$ [115].

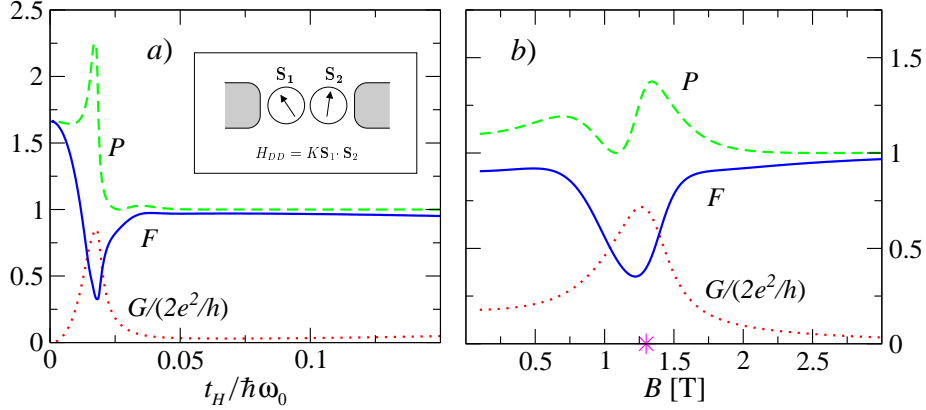


Figure 8.1: (a) Linear conductance G (dotted line), Fano factor (solid line), and the factor P (dashed line), in vicinity of the 2IKM critical point. Inset: DD setup. (b) Similar to (a), but in the vicinity of the singlet-triplet Kondo effect (“*” denotes $K = 0$).

8.2 From scattering matrix to a stochastic model

The problem of shot noise in DDs with Kondo effect is rather involved. Here we propose a phenomenological approach. For bias $\Delta\mu \gg T_K, K$, the scattering problem can be formulated in terms of the following scattering matrix

$$\begin{aligned}
 s = & \begin{pmatrix} r_S & t_S \\ t_S & r_S \end{pmatrix} |S\rangle \langle S| + \begin{pmatrix} r_T & t_T \\ t_T & r_T \end{pmatrix} |T\rangle \langle T| \\
 & + \begin{pmatrix} r_{TS} & t_{TS} \\ t_{TS} & r_{TS} \end{pmatrix} |T\rangle \langle S| + \begin{pmatrix} r_{ST} & t_{ST} \\ t_{ST} & r_{ST} \end{pmatrix} |S\rangle \langle T|, \quad (8.1)
 \end{aligned}$$

where $t_{i(j)}$ and $r_{i(j)}$ are the transmission and reflection amplitudes. The spin fluctuations in the DD cause fluctuations in the transmission through the DD. The dominant mechanism for shot noise is qualitatively described by the following stochastic model

$$f(t) = [f_1(t)(1 - F(t)) + f_2(t)F(t)] \left(1 - \left|\dot{F}(t)\right|\right) + f_3(t) \left|\dot{F}(t)\right|, \quad (8.2)$$

where $f_i(t) = 0, 1$ is a white noise ($i = 1, 2, 3$) with $\langle f_i(t) \rangle = \bar{f}_i$ and $\langle f_i(t)f_i(0) \rangle - \bar{f}_i^2 = \bar{f}_i(1 - \bar{f}_i)\delta(t/\Delta t)$, and $F(t) = 0, 1$ is a telegraph noise with $\bar{F} = \beta/(1 + \beta)$ and $\langle F(t)F(0) \rangle - \bar{F}^2 = \beta \exp(-ct)/(1 + \beta)^2$, for $t \geq 0$. In this model, the time t is discretized in intervals of $\Delta t = h/2\Delta\mu$. The derivative $\dot{F}(t)$ takes values $0, \pm 1$. The function $f_{1(2)}(t)$ describes tunnelling through the DD, with the DD staying in the singlet (triplet) state, while $f_3(t)$ describes tunnelling accompanied by the DD transition between singlet and triplet. The relation to formula (8.1) is given by: $\bar{f}_1 = |t_S|^2 = 1 - |r_S|^2$, $\bar{f}_2 = |t_T|^2 = 1 - |r_T|^2$, and $f_3 = |t_{ST}|^2/(|t_{ST}|^2 + |r_{ST}|^2) = |t_{TS}|^2/(|t_{TS}|^2 + |r_{TS}|^2)$. The telegraph noise is described by two parameters: $\beta = w_{12}/w_{21}$ and $c = w_{12} + w_{21}$, where w_{ij} is the probability to go from i to j .

8.3 Results

The quantity of interest is the Fano factor $F = S/e|I|$. For a single-channel non-interacting system, one has $F = 1 - \mathcal{T}$. In order to show the effect of interaction, we introduce the factor $P = F/(1 - \mathcal{T})$. The noise power at zero frequency is then given by $S = 2eI_{\text{imp}}\mathcal{T}(1 - \mathcal{T})P$, where $I_{\text{imp}} = 2e\Delta\mu/h$. For the average transmission probability we obtain

$$\mathcal{T} \equiv \langle f \rangle = \frac{\bar{f}_1 + \beta\bar{f}_2}{1 + \beta} + \frac{\beta c\Delta t}{(1 + \beta)^2} (2\bar{f}_3 - \bar{f}_1 - \bar{f}_2). \quad (8.3)$$

The noise can be calculated as $S = 2eI_{\text{imp}}S_f$, with $S_f = \mathcal{T}(1 - \mathcal{T}) + \Delta S_f$, where

$$\begin{aligned} \Delta S_f = & \frac{2\beta}{(1 - q)(1 + \beta)^2} \left\{ q(\bar{f}_1 - \bar{f}_2)^2 + \frac{c\Delta t(\bar{f}_1 - \bar{f}_2)}{(1 + \beta)} \times \right. \\ & [\bar{f}_3(\beta - 1)(q + 1) + \bar{f}_1(1 - \beta q) + \bar{f}_2(q - \beta)] + \\ & \left. \frac{(c\Delta t)^2}{4} [(2\bar{f}_3 - \bar{f}_1 - \bar{f}_2)^2 - (\bar{f}_1 - \bar{f}_2)^2] \right\}, \quad (8.4) \end{aligned}$$

with $q = \exp(-c\Delta t)$. The factor P is then given by $P = 1 + \Delta S_f/(\mathcal{T} - \mathcal{T}^2)$. Deviations of P from $P = 1$ show the effect of interactions in the DD. We plot the Fano factor and the factor P for a DD on Fig. 8.1. The results show that the spin fluctuations affect the shot noise in the regions where $K \lesssim T_K$. A peculiar feature in P is found both at the 2IKM critical point (Fig. 8.1a) and at the point of the singlet-triplet Kondo effect (Fig. 8.1b).

For $\Delta\mu \ll T_K$ the DD spin is screened, and correlations between two electrons passing through the DD occur only via virtual excitations of the Kondo state. The shot noise is expected to qualitatively obey the non-interacting formula with the renormalized \mathcal{T} .

CHAPTER 8. SHOT NOISE IN TRANSPORT THROUGH A DOUBLE
QUANTUM DOT CLOSE TO THE KONDO REGIME

Appendix A

Double dot states in the L - R basis

Using the definition

$$d_{n\sigma} = \frac{1}{\sqrt{2}} \left(\tilde{d}_{L\sigma} + n\tilde{d}_{R\sigma} \right), \quad (\text{A.1})$$

we rewrite (3.2) in terms of the new operators $\tilde{d}_{l\sigma}$ as follows

$$\begin{aligned} |S\rangle &= \frac{1}{2\sqrt{1+\phi^2}} \left\{ (1+\phi)(\tilde{d}_{L\uparrow}^\dagger \tilde{d}_{R\downarrow}^\dagger - \tilde{d}_{L\downarrow}^\dagger \tilde{d}_{R\uparrow}^\dagger) + \right. \\ &\quad \left. (1-\phi)(\tilde{d}_{L\uparrow}^\dagger \tilde{d}_{L\downarrow}^\dagger + \tilde{d}_{R\uparrow}^\dagger \tilde{d}_{R\downarrow}^\dagger) \right\} |0\rangle, \\ |T_+\rangle &= \tilde{d}_{L\uparrow}^\dagger \tilde{d}_{R\uparrow}^\dagger |0\rangle, \quad |T_-\rangle = \tilde{d}_{L\downarrow}^\dagger \tilde{d}_{R\downarrow}^\dagger |0\rangle, \\ |T_0\rangle &= \frac{1}{\sqrt{2}} (\tilde{d}_{L\uparrow}^\dagger \tilde{d}_{R\downarrow}^\dagger + \tilde{d}_{L\downarrow}^\dagger \tilde{d}_{R\uparrow}^\dagger) |0\rangle. \end{aligned} \quad (\text{A.2})$$

Similarly, for (3.11) and (3.12) we have

$$|S1\rangle = \frac{1}{\sqrt{2}} (\tilde{d}_{L\uparrow}^\dagger \tilde{d}_{L\downarrow}^\dagger - \tilde{d}_{R\uparrow}^\dagger \tilde{d}_{R\downarrow}^\dagger) |0\rangle, \quad (\text{A.3})$$

$$\begin{aligned} |S2\rangle &= \frac{1}{2\sqrt{1+\phi^2}} \left\{ (\phi-1)(\tilde{d}_{L\uparrow}^\dagger \tilde{d}_{R\downarrow}^\dagger - \tilde{d}_{L\downarrow}^\dagger \tilde{d}_{R\uparrow}^\dagger) + \right. \\ &\quad \left. (1+\phi)(\tilde{d}_{L\uparrow}^\dagger \tilde{d}_{L\downarrow}^\dagger + \tilde{d}_{R\uparrow}^\dagger \tilde{d}_{R\downarrow}^\dagger) \right\} |0\rangle. \end{aligned} \quad (\text{A.4})$$

Appendix B

Sequential tunneling rates

The sequential tunneling rates W_{Mm}^l calculated according to the formula (3.20) are:

$$\begin{aligned}W_{\langle S|+, \uparrow \rangle}^l &= \frac{2\pi}{\hbar} \nu \frac{|t_{l,+}|^2}{1+\phi^2} f(E_{|S} - E_{|+, \uparrow} - \mu_l) , \\W_{\langle S|+, \downarrow \rangle}^l &= \frac{2\pi}{\hbar} \nu \frac{|t_{l,+}|^2}{1+\phi^2} f(E_{|S} - E_{|+, \downarrow} - \mu_l) , \\W_{\langle S|-, \uparrow \rangle}^l &= \frac{2\pi}{\hbar} \nu \frac{\phi^2 |t_{l,-}|^2}{1+\phi^2} f(E_{|S} - E_{|-, \uparrow} - \mu_l) , \\W_{\langle S|-, \downarrow \rangle}^l &= \frac{2\pi}{\hbar} \nu \frac{\phi^2 |t_{l,-}|^2}{1+\phi^2} f(E_{|S} - E_{|-, \downarrow} - \mu_l) , \\W_{\langle T_+|+, \uparrow \rangle}^l &= \frac{2\pi}{\hbar} \nu |t_{l,-}|^2 f(E_{|T_+} - E_{|+, \uparrow} - \mu_l) , \\W_{\langle T_+|+, \downarrow \rangle}^l &= 0 , \\W_{\langle T_+|-, \uparrow \rangle}^l &= \frac{2\pi}{\hbar} \nu |t_{l,+}|^2 f(E_{|T_+} - E_{|-, \uparrow} - \mu_l) , \\W_{\langle T_+|-, \downarrow \rangle}^l &= 0 , \\W_{\langle T_-|+, \uparrow \rangle}^l &= 0 , \\W_{\langle T_-|+, \downarrow \rangle}^l &= \frac{2\pi}{\hbar} \nu |t_{l,-}|^2 f(E_{|T_-} - E_{|+, \downarrow} - \mu_l) , \\W_{\langle T_-|-, \uparrow \rangle}^l &= 0 ,\end{aligned}$$

$$\begin{aligned}
 W_{\langle T_- | -, \downarrow \rangle}^l &= \frac{2\pi}{\hbar} \nu |t_{l,+}|^2 f(E_{|T_-} - E_{|-, \downarrow} - \mu_l), \\
 W_{\langle T_0 | +, \uparrow \rangle}^l &= \frac{2\pi}{\hbar} \nu \frac{|t_{l,-}|^2}{2} f(E_{|T_0} - E_{|+, \uparrow} - \mu_l), \\
 W_{\langle T_0 | +, \downarrow \rangle}^l &= \frac{2\pi}{\hbar} \nu \frac{|t_{l,-}|^2}{2} f(E_{|T_0} - E_{|+, \downarrow} - \mu_l), \\
 W_{\langle T_0 | -, \uparrow \rangle}^l &= \frac{2\pi}{\hbar} \nu \frac{|t_{L+}|^2}{2} f(E_{|T_0} - E_{|-, \uparrow} - \mu_l), \\
 W_{\langle T_0 | -, \downarrow \rangle}^l &= \frac{2\pi}{\hbar} \nu \frac{|t_{L+}|^2}{2} f(E_{|T_0} - E_{|-, \downarrow} - \mu_l),
 \end{aligned}$$

where $f(E) = 1/[1 + \exp(E/k_B T)]$. The rates for the reverse transitions can be obtained from above expressions by replacing $f(E) \rightarrow 1 - f(E)$, satisfying (3.22).

Solving (3.26) and (3.27), we find for (3.28), (3.29), and (3.30) the following expressions:

$$\tau = \frac{(W_{T,-}W_{-,S} + W_{-,T}W_{S,-})(W_{S,+} + W_{T,+}) + (W_{S,+}W_{+,T} + W_{T,+}W_{+,S})(W_{T,-} + W_{S,-})}{(W_{+,S}W_{S,-} + W_{-,S}W_{S,+})(W_{+,T} + W_{-,T}) + (W_{+,T}W_{T,-} + W_{-,T}W_{T,+})(W_{+,S} + W_{-,S})}, \quad (\text{B.1})$$

$$\beta = \frac{W_{T,+}W_{+,S}(W_{S,-} + W_{T,-}) + W_{T,-}W_{-,S}(W_{S,+} + W_{T,+})}{W_{+,T}W_{S,+}(W_{S,-} + W_{T,-}) + W_{-,T}W_{S,-}(W_{S,+} + W_{T,+})}, \quad (\text{B.2})$$

$$\gamma = \frac{W_{-,S}W_{S,+}(W_{+,T} + W_{-,T}) + W_{-,T}W_{T,+}(W_{+,S} + W_{-,S})}{W_{+,S}W_{S,-}(W_{+,T} + W_{-,T}) + W_{+,T}W_{T,-}(W_{+,S} + W_{-,S})}. \quad (\text{B.3})$$

The rate \tilde{W}_0 entering Eq. (3.60) is given by

$$\tilde{W}_0^{-1} = \frac{(W_{S+} - W_{S-})(W_{+T} + W_{-T}) + (W_{T+} - W_{T-})(W_{+S} + W_{-S})}{W_{+S}W_{S-}(W_{+T} + W_{-T}) + W_{+T}W_{T-}(W_{+S} + W_{-S})}. \quad (\text{B.4})$$

Appendix C

Cotunneling rates

The cotunneling rates for the $N = 1$ CB valley are given in Eq. (3.63), with $\mathcal{M}_{nm}^{\prime l}$ given by

$$\begin{aligned} \mathcal{M}_{++}^{RL} &= \left(\frac{1}{U_-^2} + \frac{1}{1+\phi^2} \frac{1}{U_- U_+} + \frac{1}{(1+\phi^2)^2} \frac{1}{U_+^2} \right) 2 |t_{L+} t_{R+}|^2 + \\ &\quad \frac{3 |t_{L-} t_{R-}|^2}{2U_+^2} - \frac{3}{U_- U_+} \Re(t_{R+}^* t_{R-} t_{L+} t_{L-}^*), \end{aligned} \quad (\text{C.1})$$

$$\begin{aligned} \mathcal{M}_{--}^{RL} &= \left(\frac{1}{U_-^2} + \frac{\phi^2}{1+\phi^2} \frac{1}{U_- U_+} + \frac{\phi^4}{(1+\phi^2)^2} \frac{1}{U_+^2} \right) 2 |t_{L-} t_{R-}|^2 + \\ &\quad \frac{3 |t_{L+} t_{R+}|^2}{2U_+^2} - \frac{3}{U_- U_+} \Re(t_{R+}^* t_{R-} t_{L+} t_{L-}^*), \end{aligned} \quad (\text{C.2})$$

$$\begin{aligned} \mathcal{M}_{+-}^{RL} &= \left(\frac{2}{U_-^2} + \frac{3}{U_- U_+} + \frac{3}{2U_+^2} \right) |t_{L-} t_{R+}|^2 + \frac{2\phi^2 |t_{L+} t_{R-}|^2}{(1+\phi^2)^2 U_+^2} - \\ &\quad \frac{2\phi \Re(t_{R+}^* t_{R-} t_{L+} t_{L-}^*)}{(1+\phi^2) U_- U_+}, \end{aligned} \quad (\text{C.3})$$

where $U_- = E_-(1)$ and $U_+ = E_+(1)$, and \Re is real part. For \mathcal{M}_{+-}^{RL} , change $t_{l+} \rightleftharpoons t_{l-}$ in Eq. (C.3); for \mathcal{M}_{nm}^{RR} , set $L \rightarrow R$.

The cotunneling rates for the $N = 2$ Coulomb blockade valley (singlet-triplet cotunneling rates) are given in Eq. (3.63), with $\mathcal{M}_{nm}^{\prime l}$ given by

$$\mathcal{M}_{SS}^{RL} = 2 \left| \left(\frac{\phi^2}{U_+} - \frac{1}{U_-} \right) \frac{t_{L+}^* t_{R+}}{1+\phi^2} + \left(\frac{1}{U_+} - \frac{\phi^2}{U_-} \right) \frac{t_{L-}^* t_{R-}}{1+\phi^2} \right|^2, \quad (\text{C.4})$$

$$\mathcal{M}_{TT}^{RL} = \left[\left(\frac{U_+ + U_-}{U_+ U_-} \right)^2 + \frac{1}{2} \left(\frac{U_+ - U_-}{U_+ U_-} \right)^2 \right] |t_{L+}^* t_{R+} + t_{L-}^* t_{R-}|^2, \quad (\text{C.5})$$

$$\mathcal{M}_{ST}^{RL} = \left(\frac{U_+ + U_-}{U_+ U_-} \right)^2 \frac{|t_{L+}^* t_{R-} + \phi t_{L-}^* t_{R+}|^2}{1+\phi^2} = \frac{1}{3} \mathcal{M}_{TS}^{LR}, \quad (\text{C.6})$$

where $U_- = E_-(2)$ and $U_+ = E_+(2)$.

To calculate the cotunneling rates $w_{nm}(l', l)$, close to the sequential tunneling peak on the $N = 2$ CB valley side, one can use Eq. (3.75) with $U_-^l \rightarrow U_+^{l'}$, and with $\tilde{\mathcal{M}}_{nm}^{l'l}$ given by

$$\tilde{\mathcal{M}}_{SS}^{RL} = \frac{2|t_{L+}t_{R+}|^2}{(1 + \phi^2)^2}, \quad (\text{C.7})$$

$$\tilde{\mathcal{M}}_{TT}^{RL} = \frac{3}{2}|t_{L-}t_{R-}|^2, \quad (\text{C.8})$$

$$\tilde{\mathcal{M}}_{ST}^{RL} = \frac{|t_{L+}t_{R-}|^2}{1 + \phi^2} = \frac{1}{3}\tilde{\mathcal{M}}_{TS}^{LR}. \quad (\text{C.9})$$

The cotunneling is allowed at $E_{mn} + \Delta\mu_W > 0$, and forbidden due to energy conservation at $E_{mn} + \Delta\mu_W < 0$.

Appendix D

Variational parameters $\tilde{\omega}$ and γ

Equating to zero the derivatives of ε_{0m} in Eq. (5.13) with respect to $\tilde{\omega}$ and γ , we obtain two equations

$$(1+x)y^4 - 1 - \frac{m^2}{x} - y \frac{\lambda}{2a_B^*} \frac{\Gamma(1/2+x)}{x\Gamma(x)} = 0, \quad (\text{D.1})$$

$$x^2y^4 - m^2 - xy \frac{\lambda}{a_B^*} \frac{\Gamma(1/2+x)}{\Gamma(x)} [\Psi(1+x) - \Psi(1/2+x)] = 0, \quad (\text{D.2})$$

where $x = \sqrt{m^2 + \gamma}$, $y = \tilde{\lambda}/\lambda = \sqrt{\omega/\tilde{\omega}}$, and $\Psi(x)$ is the digamma function. Solving Eqs. (D.1) and (D.2) with respect to x and y gives the variational parameters γ and $\tilde{\omega}$ as functions of the Coulomb interaction strength λ/a_B^* .

We consider first the case $m = 0$. For weak Coulomb interaction ($\lambda/a_B^* \ll 1$), we expand Eq. (D.2) in terms of $x \ll 1$ and obtain

$$x = \frac{2 \ln 2 - \pi^{-1/2} y^3 a_B^* / \lambda}{4 \ln^2 2 + \pi^2 / 3}. \quad (\text{D.3})$$

Note that, for $\lambda/a_B^* < y^3/2\sqrt{\pi} \ln 2$, Eq. (D.3) gives $x < 0$, whereas by definition $x = \sqrt{\gamma} \geq 0$. In this case, the minimum of energy in Eq. (5.13) is achieved at $\gamma = 0$ and thus, Eq. (D.2) should be replaced by $x = 0$ for $\lambda/a_B^* \leq y^3/2\sqrt{\pi} \ln 2$. Setting $x = 0$ in Eq. (D.1), we obtain an equation for y ,

$$y^4 - \frac{\sqrt{\pi}}{2} \frac{\lambda}{a_B^*} y - 1 = 0, \quad (\text{D.4})$$

which is valid for $\lambda/a_B^* \leq y^3/2\sqrt{\pi} \ln 2$. Considering simultaneously the equality $\lambda/a_B^* = y^3(2\sqrt{\pi} \ln 2)^{-1}$ and Eq. (D.4), we find that λ/a_B^* has a critical value, $(\lambda/a_B^*)_c \equiv \xi_c$, given by

$$\xi_c = \frac{1}{2\sqrt{\pi} \ln 2} \left(\frac{4 \ln 2}{4 \ln 2 - 1} \right)^{3/4} \approx 0.57, \quad (\text{D.5})$$

at which $\tilde{\omega}$ and γ are non-analytic functions of λ/a_B^* . Clearly, such a critical point is not present in the exact eigenstates of the Hamiltonian (5.9), and is an artifact of the variational ansatz we use. In the interval $0 \leq \lambda/a_B^* \leq (\lambda/a_B^*)_c$, we have $\gamma = 0$ and $\tilde{\omega} = \omega/y^2$, where y is the positive solution of Eq. (D.4). Although we can solve Eq. (D.4) analytically for y , it is more convenient to present here an expansion for $\tilde{\omega}$ in terms of λ/a_B^* ,

$$\frac{\tilde{\omega}}{\omega} = 1 - \frac{\sqrt{\pi}}{4} \frac{\lambda}{a_B^*} + \frac{\pi}{16} \frac{\lambda^2}{a_B^{*2}} - \frac{7\pi^{3/2}}{512} \frac{\lambda^3}{a_B^{*3}} + \dots \quad (\text{D.6})$$

Note that, since $\lambda/a_B^* \leq (\lambda/a_B^*)_c \approx 0.57$, Eq. (D.6) converges with a good accuracy; e.g., at $\lambda/a_B^* = (\lambda/a_B^*)_c$ the four terms in the series (D.6) give $\tilde{\omega}/\omega \approx 0.797$, whereas the exact solution reads $\tilde{\omega}/\omega = \sqrt{1 - 1/4 \ln 2} \approx 0.799$.

To the right of the critical point (D.5), both Eqs. (D.1) and (D.2) are valid for $m = 0$, and we can use them to study two limiting cases: (i) the neighborhood of the critical point (D.5) for $\lambda/a_B^* \geq (\lambda/a_B^*)_c$ and (ii) the limit of strong Coulomb interaction ($\lambda/a_B^* \gg 1$). Excluding λ/a_B^* from Eqs. (D.1) and (D.2), we express y as a function of x only,

$$\frac{1}{y^4} = 1 + x - \frac{1}{2[\Psi(1+x) - \Psi(1/2+x)]}. \quad (\text{D.7})$$

Next we substitute y from Eq. (D.7) into Eq. (D.2) and obtain

$$\begin{aligned} \frac{a_B^*}{\lambda} &= \frac{\Gamma(1/2+x)}{\Gamma(1+x)} [\Psi(1+x) - \Psi(1/2+x)]^{1/4} \\ &\times \{(1+x)[\Psi(1+x) - \Psi(1/2+x)] - 1/2\}^{3/4}. \end{aligned} \quad (\text{D.8})$$

Equation (D.8) gives a_B^*/λ as a function of x . The inverse function allows one to find x as a function of a_B^*/λ , and then, from Eq. (D.7), also y as a function of a_B^*/λ . Expanding Eqs. (D.8) and (D.7) for $x \ll 1$, which corresponds to the case (i), we find for $\sqrt{\gamma} = x$ and $\tilde{\omega}/\omega = 1/y^2$ in leading order,

$$\sqrt{\gamma} = C_0 \left(\frac{1}{\xi_c} - \frac{a_B^*}{\lambda} \right) + \dots, \quad (\text{D.9})$$

$$\frac{\tilde{\omega}}{\omega} = \left(\frac{\tilde{\omega}}{\omega} \right)_c + C_1 \left(\frac{1}{\xi_c} - \frac{a_B^*}{\lambda} \right) + \dots, \quad (\text{D.10})$$

where ξ_c is given in Eq. (D.5), $(\tilde{\omega}/\omega)_c = \sqrt{1 - 1/4 \ln 2}$, and the coefficients C_0 and C_1 read

$$C_0 = \frac{(2/\pi)^{1/2} (\ln 2)^{3/4} (4 \ln 2 - 1)^{1/4}}{(8 \ln 2 - 5) \ln^2 2 + \frac{2}{3} \pi^2 (\ln 2 - \frac{1}{16})} \approx 0.16, \quad (\text{D.11})$$

$$C_1 = \left(1 - \frac{\pi^2}{24 \ln^2 2} \right) \frac{C_0}{\sqrt{4 - 1/\ln 2}} \approx 0.014. \quad (\text{D.12})$$

Note that the value $\tilde{\omega}/\omega = (\tilde{\omega}/\omega)_c$ at $\lambda/a_B^* = \xi_c$ is the minimum of $\tilde{\omega}/\omega$ as a function of λ/a_B^* [see also Eq. (D.6) and the text below it].

Next we turn to the case of strong Coulomb interaction ($\lambda/a_B^* \gg 1$). Here, we have $x \gg 1$ and by expanding Eq. (D.7) in terms of $1/x$ we obtain

$$\frac{\tilde{\omega}}{\omega} \equiv \frac{1}{y^2} = \frac{\sqrt{3}}{2} - \frac{1}{16\sqrt{3}x} + \frac{11}{768\sqrt{3}x^2} + \dots \quad (\text{D.13})$$

Expanding Eq. (D.8) for large x , and inverting the obtained series by means of iteration, we find for $\gamma = x^2$,

$$\gamma = \frac{3}{4} \left(\frac{\lambda}{2a_B^*} \right)^{4/3} - \frac{7}{8\sqrt{3}} \left(\frac{\lambda}{2a_B^*} \right)^{2/3} - \frac{7}{288} + \dots \quad (\text{D.14})$$

Then, Eq. (D.13) can be rewritten as follows

$$\frac{\tilde{\omega}}{\omega} = \frac{\sqrt{3}}{2} - \frac{1}{24} \left(\frac{2a_B^*}{\lambda} \right)^{2/3} - \frac{1}{192\sqrt{3}} \left(\frac{2a_B^*}{\lambda} \right)^{4/3} + \dots \quad (\text{D.15})$$

To summarize for the case $m = 0$, the variational parameters γ and $\tilde{\omega}$ as functions of the Coulomb interaction strength λ/a_B^* are given, respectively, by $\gamma = 0$ and Eq. (D.6) in the interval $0 \leq \lambda/a_B^* \leq \xi_c$, by Eqs. (D.9) and (D.10) in the neighborhood of $\lambda/a_B^* = \xi_c$ (for $\lambda/a_B^* \geq \xi_c$), and by Eqs.(D.14) and (D.15) in the limit $\lambda/a_B^* \gg 1$.

We consider now the case $|m| \geq 1$, and without loss of generality we assume $m = |m|$. Here, we find that $\tilde{\omega}$ and γ are analytic functions of λ/a_B^* . We thus consider only the limit of weak and strong Coulomb interaction. Proceeding similarly to the previous case, we find from Eqs. (D.1) and (D.2) the following relations [cf. Eqs. (D.7) and (D.8)],

$$y^4 = \frac{2(1 + m^2/x) \Delta\Psi(x) - m^2/x^2}{2(1 + x)\Delta\Psi(x) - 1}, \quad (\text{D.16})$$

$$\begin{aligned} \frac{a_B^*}{\lambda} &= \frac{x^2\Gamma(1/2 + x)}{(x^2 - m^2)\Gamma(1 + x)} \left[\left(1 + \frac{m^2}{x} \right) \Delta\Psi(x) - \frac{m^2}{2x^2} \right]^{1/4} \\ &\times \left[(1 + x)\Delta\Psi(x) - \frac{1}{2} \right]^{3/4}, \end{aligned} \quad (\text{D.17})$$

where $\Delta\Psi(x) = \Psi(1 + x) - \Psi(1/2 + x)$ and x takes values in the interval $m \leq x < \infty$.

In the limit of weak Coulomb interaction ($\lambda/a_B^* \ll 1$), we expand the left-hand side of Eqs.(D.16) and (D.17) in terms of $x - m \approx \gamma/2m \ll 1$, and obtain in leading order

$$\frac{\gamma}{m} = \frac{\sqrt{\pi}(2m - 1)!!}{2^m(m - 1)!} \left[(1 + m)\Delta\Psi(m) - \frac{1}{2} \right] \frac{\lambda}{a_B^*} + \dots, \quad (\text{D.18})$$

$$\frac{\tilde{\omega}}{\omega} = 1 - \frac{\sqrt{\pi}(2m - 1)!!}{2^{m+1}m!} \left[\frac{1}{2} - m\Delta\Psi(m) \right] \frac{\lambda}{a_B^*} + \dots, \quad (\text{D.19})$$

where $\Delta\Psi(m) = 2 \ln 2 - \sum_{k=1}^m \frac{1}{(2k-1)k}$. In particular for the case $|m| = 1$, we obtain $\gamma = \sqrt{\pi}(2 \ln 2 - 5/4)(\lambda/a_B^*)$ and $\tilde{\omega}/\omega = 1 - \sqrt{\pi}(3/2 - 2 \ln 2)(\lambda/4a_B^*)$.

In the limit of strong Coulomb interaction ($\lambda/a_B^* \gg 1$), we expand the left-hand side of Eqs.(D.16) and (D.17) in terms of $x \gg 1$, and as a result we obtain

$$\gamma = \frac{3}{4} \left(\frac{\lambda}{2a_B^*} \right)^{4/3} - \frac{7}{8\sqrt{3}} \left(\frac{\lambda}{2a_B^*} \right)^{2/3} + \frac{72m^2 - 7}{288} + \dots, \quad (\text{D.20})$$

$$\frac{\tilde{\omega}}{\omega} = \frac{\sqrt{3}}{2} - \frac{1}{24} \left(\frac{2a_B^*}{\lambda} \right)^{2/3} + \frac{48m^2 - 1}{192\sqrt{3}} \left(\frac{2a_B^*}{\lambda} \right)^{4/3} + \dots. \quad (\text{D.21})$$

Note that in Eqs. (D.20) and (D.21) the dependence on m arises only in the last terms. Thus, for strong Coulomb interaction, the radial part of the wave function in Eq. (5.7) [see also Eq. (5.12)] is weakly depending on the quantum number m .

Appendix E

Matrix elements of V

We calculate first the matrix elements $\langle \tilde{f}_{nm}|V|\tilde{f}_{0m}\rangle$ ($n \geq 0$), with V given in Eq. (5.18) and the wave functions $\tilde{f}_{nm}(r)$ in Eq. (5.12). We divide the perturbation into three terms,

$$V_{n0} \equiv \langle \tilde{f}_{nm}|V|\tilde{f}_{0m}\rangle = V'_{n0} - V''_{n0} + V'''_{n0}, \quad (\text{E.1})$$

corresponding, respectively, to the terms proportional to $1/r$, $1/r^2$ and r^2 in Eq. (5.18). For the term $V' = \hbar^2/m^*a_B^*r$, we obtain

$$V'_{n0} = \frac{\hbar^2}{m^*a_B^*\tilde{\lambda}} \frac{(2n-1)!!2^{-n}\Gamma(t-1/2)}{\sqrt{n!\Gamma(t)\Gamma(n+t)}}. \quad (\text{E.2})$$

Here and below we use the notation $t = 1 + \sqrt{m^2 + \gamma}$. For the term $V'' = \hbar^2\gamma/m^*r^2$, we obtain

$$V''_{n0} = \frac{\hbar^2}{m^*\tilde{\lambda}^2} \frac{\gamma}{(t-1)} \sqrt{\frac{n!\Gamma(t)}{\Gamma(n+t)}}. \quad (\text{E.3})$$

Finally, for the term $V''' = \frac{1}{4}m^*(\omega^2 - \tilde{\omega}^2)r^2$, we obtain

$$V'''_{n0} = \frac{m^*\tilde{\lambda}^2}{4}(\omega^2 - \tilde{\omega}^2) \left[t\delta_{n,0} - \sqrt{t}\delta_{n,1} \right], \quad (\text{E.4})$$

where $\delta_{nn'}$ is the Kronecker δ -symbol. We note that in the case $n = 1$, we have $\langle \tilde{f}_{1m}|V|\tilde{f}_{0m}\rangle = 0$, due to Eq. (D.1).

Next, we consider the general case,

$$V_{nn'} \equiv \langle \tilde{f}_{nm}|V|\tilde{f}_{n'm}\rangle = V'_{nn'} - V''_{nn'} + V'''_{nn'}, \quad (\text{E.5})$$

with the same division of the perturbation into three as in Eq. (E.1). For the first part, we obtain

$$V'_{nn'} = \frac{\hbar^2}{m^*a_B^*\tilde{\lambda}} \sqrt{\frac{(t)_n(t)_{n'}}{n!n'}} \sum_{k=0}^n \sum_{l=0}^{n'} \frac{(t)_{k+l-\frac{1}{2}}(-n)_k(-n')_l}{(t)_k(t)_l k!!}, \quad (\text{E.6})$$

where $(x)_n = \Gamma(x+n)/\Gamma(x)$ is the Pochhammer symbol. For the second part, we obtain

$$V''_{nn'} = \frac{\hbar^2 \gamma}{m^* \tilde{\lambda}^2} \sqrt{\frac{(t)_n (t)_{n'}}{n! n'!}} \sum_{k=0}^n \sum_{l=0}^{n'} \frac{(t)_{k+l-1} (-n)_k (-n')_l}{(t)_k (t)_l k! l!}. \quad (\text{E.7})$$

We note that for $n' = n$ we have $V''_{nn} = V''_{00}$ for all values of n . Finally, for the last part, we obtain

$$V'''_{nn'} = \frac{m^* \tilde{\lambda}^2}{4} (\omega^2 - \tilde{\omega}^2) \left[(2n+t) \delta_{nn'} - \sqrt{n'(n+t)} \delta_{n,n'-1} - \sqrt{n(n'+t)} \delta_{n,n'+1} \right]. \quad (\text{E.8})$$

We note that for $n' = 0$ Eqs. (E.6), (E.7) and (E.8) coincide with Eqs. (E.2), (E.3) and (E.4), respectively.

Appendix F

Exact relations at the singlet-triplet transition

From Eqs. (5.90) and (5.91) at the singlet-triplet transition, we obtain

$$\langle \psi_S | r_{\pm} \left(1 - \frac{\lambda_0^4}{2a_B^* r^3} \right) | \psi_T \rangle = 0, \quad (\text{F.1})$$

where $|\psi_S\rangle$ and $|\psi_T\rangle$ are the exact orbital wave functions of the singlet and triplet, respectively. We assume $|\psi_S\rangle = |NMnm\rangle$ and $|\psi_T\rangle = |NMn, m-1\rangle$, with an even m . For r_- , Eq. (F.1) holds trivially, due to angular momentum conservation. For r_+ , however, the equality takes place only at the singlet-triplet degeneracy point. Integrating in Eq. (F.1) over R , φ_R and φ_r , we obtain

$$\int_0^\infty \left(r - \frac{\lambda_0^4}{2a_B^* r^2} \right) f_{nm}(r) f_{n,m-1}(r) dr = 0, \quad (\text{F.2})$$

where $f_{nm}(r)$ are the exact eigenfunctions of \mathcal{H}_m in Eq. (5.9). The condition of singlet-triplet degeneracy reads $\varepsilon_{nm} = \varepsilon_{nm-1} - \hbar\omega_c/2$, where ε_{nm} are the eigenvalues of \mathcal{H}_m .

An additional relation can be obtained if we consider the identity $\mathbf{p} = (im^*/2\hbar)[H_d, \mathbf{r}]$ for the momentum operator $\mathbf{p} = -i\hbar\partial/\partial\mathbf{r} + (e/2c)\mathbf{A}(\mathbf{r})$, with the vector potential $\mathbf{A}(\mathbf{r}) = (-r_y, r_x, 0)B_z/2$. Going to the polar coordinates, $\mathbf{r} = (r, \varphi_r)$, we use the relation

$$\frac{\partial}{\partial r_x} \pm i \frac{\partial}{\partial r_y} = e^{\pm i\varphi_r} \left(\frac{\partial}{\partial r} \pm \frac{i}{r} \frac{\partial}{\partial \varphi_r} \right) \quad (\text{F.3})$$

to evaluate the matrix elements $\langle \psi_S | \mathbf{p} | \psi_T \rangle$. Considering as before the singlet-triplet transition, we set $\langle \psi_S | \mathbf{p} | \psi_T \rangle = 0$ and obtain the relation

$$\int_0^\infty f_{nm}(r) \left(\frac{\partial}{\partial r} - \frac{m-1}{r} - \frac{eB_z^*}{4\hbar c} r \right) f_{n,m-1}(r) dr = 0, \quad (\text{F.4})$$

where B_z^* is the value of B_z at which the singlet-triplet transition occurs.

Bibliography

- [1] G.A. Prinz, Phys. Today **45**(4). 58 (1995); Science **282**, 1660 (1998).
- [2] M.N. Baibich, J.M. Broto, A. Fert, F. Nguyen Van Dau, F. Petroff, P. Eitenne, G. Creuzet, A. Friederich, and J. Chazelas, Phys. Rev. Lett. **61**, 2472 (1988).
- [3] S.A. Wolf, D.D. Awschalom, R.A. Buhrman, J.M. Daughton, S. von Molnár, M.L. Roukes, A.Y. Chtchelkanova, and D.M. Treger, Science **294**, 1488 (2001).
- [4] D.D. Awschalom, D. Loss, N. Samarth, eds., *Semiconductor Spintronics and Quantum Computing* (Springer, New York, 2002).
- [5] S. Datta and B. Das, Appl. Phys. Lett. **56**, 665 (1990).
- [6] I. Žutić, J. Fabian, and S. Das Sarma, Rev. Mod. Phys. **76**, 323 (2004).
- [7] J.M. Kikkawa, I.P. Smorchkova, N. Samarth, and D.D. Awschalom, Science **277**, 1284 (1997); J.M. Kikkawa and D.D. Awschalom, Phys. Rev. Lett. **80**, 4313 (1998); Nature **397**, 139 (1999); D.D. Awschalom and J.M. Kikkawa, Phys. Today **52**(6), 33 (1999).
- [8] R. Fiederling, M. Keim, G. Reuscher, W. Ossau, G. Schmidt, A. Waag, and L.W. Molenkamp, Nature **402**, 787 (1999).
- [9] Y. Ohno, D.K. Young, B. Beschoten, F. Matsukura, H. Ohno, and D.D. Awschalom, Nature **402**, 790 (1999).
- [10] K.E. Drexler, *Nanosystems: molecular machinery, manufacturing, and computation* (Wiley Interscience, 1992).
- [11] *Nanotechnology: Research and Perspectives*, edited by B.C. Crandall and J. Lewis (MIT Press: Cambridge, 1992).
- [12] *Prospects in Nanotechnology: Toward Molecular Manufacturing*, edited by M. Krummenacker and J. Lewis (John Wiley and Sons, Inc.: New York, 1995).
- [13] J.K. Gimzewski and Ch. Joachim, Science **283**, 1683 (1999).
- [14] H.C. Manoharan, C.P. Lutz, and D.M. Eigler, Nature **403**, 512 (2000).

- [15] H.-W. Fink and Ch. Schönenberger, *Nature* **398**, 407 (1999).
- [16] L.P. Kouwenhoven, D.G. Austing, and S. Tarucha, *Rep. Prog. Phys.* **64** 701 (2001).
- [17] M.A. Nielsen and I.L. Chuang, *Quantum Computation and Quantum Information* (Cambridge U. Press, New York, 2000).
- [18] C.H. Bennett and D.P. DiVincenzo, *Nature* **404**, 247 (2000).
- [19] D.P. DiVincenzo, G. Burkard, D. Loss, and E.V. Sukhorukov, in *Quantum Mesoscopic Phenomena and Mesoscopic Devices in Microelectronics*, eds. I.O. Kulik and R. Ellialtöglu (NATO ASI, Kluwer, Netherlands, 2000); see cond-mat/9911245.
- [20] P.W. Shor, in *Proc. 35th Symposium on the Foundations of Computer Science*, (IEEE Computer Society Press), 124 (1994).
- [21] L.K. Grover, *Phys. Rev. Lett.* **79**, 325 (1997).
- [22] A.J. Leggett, *Science* **307**, 871 (2005).
- [23] P.W. Shor, *Phys. Rev. A* **52**, R2493 (1995); A.M. Steane, *Phys. Rev. Lett.* **77**, 793 (1996); D.P. DiVincenzo and P.W. Shor, *ibid.* **77**, 3260 (1996); A.R. Calderbank and P.W. Shor, *Phys. Rev. A* **54**, 1098 (1996); A.M. Steane, *Proc. Roy. Soc. A* **452**, 2551 (1996); E. Knill and R. Laflamme, *Phys. Rev. A* **55**, 900 (1997); D. Gottesman, *ibid.* **54**, 1862 (1996); E. Dennis, *Phys. Rev. A* **63**, 052314 (2001).
- [24] J. Preskill, *Proc. R. Soc. London Ser. A* **454**, 385 (1998); J. Preskill, in *Introduction to Quantum Computation and Information*, edited by H.-K. Lo, S. Popescu, and T. Spiller (World Scientific, Singapore, 1998), pp. 213–269.
- [25] *Experimental Proposals for Quantum Computation*, edited by S. Braunstein and H.-K. Lo (Wiley, Berlin, 2000), Vol. 48, Special Focus Issue of Fortschritte der Physik.
- [26] G. Burkard, cond-mat/0409626.
- [27] D. Loss and D.P. DiVincenzo, *Phys. Rev. A* **57**, 120 (1998); cond-mat/9701055.
- [28] J.I. Cirac and P. Zoller, *Phys. Rev. Lett.* **74**, 4091 (1995).
- [29] C. Monroe, D.M. Meekhof, B.E. King, W.M. Itano, and D.J. Wineland, *Phys. Rev. Lett.* **75**, 4714 (1995).
- [30] J. Chiaverini, D. Leibfried, T. Schaetz, M.D. Barrett, R.B. Blakestad, J. Britton, W.M. Itano, J.D. Jost, E. Knill, C. Langer, R. Ozeri, and D.J. Wineland, *Nature* **432**, 602 (2004).

BIBLIOGRAPHY

- [31] T. Pellizzari, S. A. Gardiner, J. I. Cirac, and P. Zoller, *Phys. Rev. Lett.* **75**, 3788 (1995).
- [32] Q.A. Turchette, C.J. Hood, W. Lange, H. Mabuchi, and H.J. Kimble, *Phys. Rev. Lett.* **75**, 4710 (1995).
- [33] D. Cory, A. Fahmy, and T. Havel, *Proc. Nat. Acad. Sci. U.S.A.* **94**, 1634 (1997);
- [34] N.A. Gershenfeld and I.L. Chuang, *Science* **275**, 350 (1997);
- [35] I.L. Chuang, N.A. Gershenfeld, and M. Kubinec, *Phys. Rev. Lett.* **80**, 3408 (1998).
- [36] J.A. Jones, M. Mosca, and R.H. Hansen, *Nature* **393**, 344 (1998).
- [37] E. Knill, R. Laflamme, R. Martinez, and C.-H. Tseng, *Nature* **404**, 368 (2000).
- [38] L.M.K. Vandersypen, M. Steffen, G. Breyta, C.S. Yannoni, M.H. Sherwood, and I.L. Chuang, *Nature* **414**, 883 (2001).
- [39] A. Shnirman, G. Schön, and Z. Hermon, *Phys. Rev. Lett.* **79**, 2371 (1997).
- [40] D.V. Averin, *Solid State Commun.* **105**, 659 (1998).
- [41] Y. Nakamura, Yu.A. Pashkin, and J.S. Tsai, *Nature* **398**, 786 (1999).
- [42] T.P. Orlando, J.E. Mooij, L. Tian, C.H. van der Wal, L.S. Levitov, S. Lloyd, and J.J. Mazo, *Phys. Rev. B* **60**, 15398 (1999); C.H. van der Wal, A.C.J. ter Haar, F.K. Wilhelm, R.N. Schouten, C.J.P.M. Harmans, T.P. Orlando, S. Lloyd, and J.E. Mooij, *Science* **290**, 773 (2000).
- [43] I. Chiorescu, Y. Nakamura, C.J.P.M. Harmans, and J.E. Mooij, *Science* **21**, 1869 (2003); I. Chiorescu, P. Bertet, K. Semba, Y. Nakamura, C.J.P.M. Harmans, J.E. Mooij, *Nature* **431**, 159 (2004).
- [44] P. Bertet, I. Chiorescu, G. Burkard, K. Semba, C.J.P.M. Harmans, D.P. DiVincenzo, and J.E. Mooij, *cond-mat/0412485*.
- [45] D. Vion, A. Aassime, A. Cottet, P. Joyez, H. Pothier, C. Urbina, D. Esteve, and M.H. Devoret, *Science* **296**, 886 (2002);
- [46] L.B. Ioffe, V.B. Geshkenbein, M.V. Feigel'man, A.L. Fauche, and G. Blatter, *Nature* **398**, 679 (1999).
- [47] A. Barenco, D. Deutsch, A. Ekert, and R. Jozsa, *Phys. Rev. Lett.* **74**, 4083 (1995).
- [48] R. Landauer, *Science* **272**, 1914 (1996).
- [49] J.A. Brum and P. Hawrylak, *Superlattices and Microstructures* **22**, 431 (1997).

-
- [50] P. Zanardi and F. Rossi, Phys. Rev. Lett. **81** 4752 (1998).
- [51] T. Tanamoto, Phys. Rev. A **61**, 022305 (2000).
- [52] A. Imamoglu, D.D. Awschalom, G. Burkard, D.P. DiVincenzo, D. Loss, M. Sherwin, and A. Small, Phys. Rev. Lett. **83**, 4204 (1999).
- [53] C.H.W. Barnes, J.M. Shilton, and A.M. Robinson, Phys. Rev. B **62**, 8410 (2000).
- [54] D. Jaksch, H.-J. Briegel, J.I. Cirac, C.W. Gardiner, and P. Zoller, Phys. Rev. Lett. **82**, 1975 (1999).
- [55] B. Kane, Nature **393**, 133 (1998).
- [56] P.M. Platzman and M.I. Dykman, Science **284**, 1967 (1999).
- [57] V. Privman, I.D. Vagner, and G. Kventsel, Phys. Lett. A **239**, 141 (1998).
- [58] R. Vrijen, E. Yablonovitch, K. Wang, H.W. Jiang, A. Balandin, V. Roychowdhury, T. Mor, and D. DiVincenzo, Phys. Rev. A **62**, 012306 (2000).
- [59] G. Burkard, D. Loss, and D.P. DiVincenzo, Phys. Rev. B **59** 2070 (1999).
- [60] A. Barenco, C.H. Bennett, R. Cleve, D.P. DiVincenzo, N. Margolus, P. Shor, T. Sleator, J.A. Smolin, and H. Weinfurter, Phys. Rev. A **52**, 3457 (1995).
- [61] D.P. DiVincenzo and D. Loss, J. Magn. Magn. Mater. **200**, 202 (1999); cond-mat/9901137.
- [62] G. Salis, Y. Kato, K. Ensslin, D.C. Driscoll, A.C. Gossard, and D.D. Awschalom, Nature **414**, 619 (2001).
- [63] L.M.K. Vandersypen, R. Hanson, L.H. Willems van Beveren, J.M. Elzerman, J.S. Greidanus, S. De Franceschi, and L.P. Kouwenhoven, in *Quantum Computing and Quantum Bits in Mesoscopic Systems* (eds. A.J. Legget, B. Ruggiero, and P. Silvestrini) 201-209 (Kluwer Academic/Plenum, New York, 2003).
- [64] J.M. Elzerman, R. Hanson, L.H. Willems van Beveren, B. Witkamp, L.M.K. Vandersypen, and L.P. Kouwenhoven, Nature **430**, 431 (2004).
- [65] *Single Charge Tunneling*, edited by H. Grabert and M.H. Devoret (New York: Plenum, 1991).
- [66] H. Drexler, D. Leonard, W. Hansen, J.P. Kotthaus, and P.M. Petroff, Phys. Rev. Lett. **73**, 2252 (1994).
- [67] S. Tarucha, D.G. Austing, T. Honda, R.J. van der Hage, and L.P. Kouwenhoven, Phys. Rev. Lett. **77**, 3613 (1996).

BIBLIOGRAPHY

- [68] M. Ciorga, A.S. Sachrajda, P. Hawrylak, C. Gould, P. Zawadzki, S. Jullian, Y. Feng, and Z. Wasilewski, *Phys. Rev. B* **61**, R16315 (2000).
- [69] R.J. Warburton, C. Schäfflein, D. Haft, F. Bickel, A. Lorke, K. Karrai, J.M. Garcia, W. Schoenfeld, and P.M. Petroff, *Nature* **405**, 926 (2000).
- [70] J.M. Elzerman, R. Hanson, J.S. Greidanus, L.H. Willems van Beveren, S. De Franceschi, L.M.K. Vandersypen, S. Tarucha, and L.P. Kouwenhoven, *Phys. Rev. B* **67**, 161308(R) (2003).
- [71] M. Pioro-Ladriere, M. Ciorga, J. Lapointe, P. Zawadzki, M. Korkusinski, P. Hawrylak, and A. S. Sachrajda, *Phys. Rev. Lett.* **91**, 026803 (2003).
- [72] I.H. Chan, P. Fallahi, A. Vidan, R.M. Westervelt, M. Hanson, and A.C. Gossard, *Nanotechnology* **15**, 609 (2004).
- [73] J.R. Petta, A.C. Johnson, C.M. Marcus, M.P. Hanson, and A.C. Gossard, *Phys. Rev. Lett.* **93**, 186802 (2004).
- [74] M. Field, C.G. Smith, M. Pepper, D.A. Ritchie, J.E.F. Frost, G.A.C. Jones, and D.G. Hasko, *Phys. Rev. Lett.* **70**, 1311 (1993).
- [75] E. Buks, R. Schuster, M. Heiblum, D. Mahalu, and V. Umansky, *Nature* **391**, 871 (1998).
- [76] L.P. Kouwenhoven, G. Schön, L.L. Sohn, *Mesoscopic Electron Transport*, NATO ASI Series E, Vol. 345, Kluwer Academic Publishers (1997).
- [77] S. Lüscher, T. Heinzel, K. Ensslin, W. Wegscheider, and M. Bichler, *Phys. Rev. Lett.* **86**, 2118 (2001).
- [78] L.P. Kouwenhoven, T.H. Oosterkamp, M.W.S. Danoesastro, M. Eto, D.G. Austing, T. Honda, and S. Tarucha, *Science* **278**, 1788 (1997).
- [79] S. Sasaki, S. De Franceschi, J.M. Elzerman, W.G. van der Wiel, M. Eto, S. Tarucha, and L.P. Kouwenhoven, *Nature* **405**, 764 (2000).
- [80] J. Schmid, J. Weis, K. Eberl, and K. v. Klitzing, *Phys. Rev. Lett.* **84**, 5824 (2000).
- [81] W.G. van der Wiel, S. De Franceschi, J.M. Elzerman, S. Tarucha, and L.P. Kouwenhoven, J. Motohisa, F. Nakajima, and T. Fukui, *Phys. Rev. Lett.* **88**, 126803 (2002).
- [82] J. Kyriakidis, M. Pioro-Ladriere, M. Ciorga, A.S. Sachrajda, and P. Hawrylak, *Phys. Rev. B* **66**, 035320 (2002).
- [83] D.M. Zumbühl, C.M. Marcus, M.P. Hanson, and A.C. Gossard, *Phys. Rev. Lett.* **93**, 256801 (2004).

- [84] T. Fujisawa, D.G. Austing, Y. Tokura, Y. Hirayama, and S. Tarucha, *Nature* **419**, 278 (2002).
- [85] T. Fujisawa, D.G. Austing, Y. Tokura, Y. Hirayama, and S. Tarucha, *Phys. Rev. Lett.* **88**, 236802 (2002).
- [86] R. Hanson, B. Witkamp, L.M.K. Vandersypen, L.H.W. van Beveren, J.M. Elzerman, and L.P. Kouwenhoven, *Phys. Rev. Lett.* **91**, 196802 (2003).
- [87] R.M. Potok, J.A. Folk, C.M. Marcus, V. Umansky, M. Hanson, and A.C. Gosard, *Phys. Rev. Lett.* **91**, 016802 (2003).
- [88] M. Kroutvar, Y. Ducommun, D. Heiss, M. Bichler, D. Schuh, G. Abstreiter, and J.J. Finley, *Nature* **432**, 81 (2004).
- [89] A.V. Khaetskii, Yu.V. Nazarov, *Phys. Rev. B* **64**, 125316 (2001).
- [90] V.N. Golovach, A. Khaetskii, and D. Loss, *Phys. Rev. Lett.* **93**, 016601 (2004).
- [91] V.N. Golovach and D. Loss, *Phys. Rev. B* **69**, 245327 (2004).
- [92] A. Einstein, B. Podolsky, and N. Rosen, *Phys. Rev.* **47**, 777 (1935).
- [93] C.H. Bennett, S.J. Wiesner, *Phys. Rev. Lett.* **69**, 2881 (1992).
- [94] A.K. Ekert, *Phys. Rev. Lett.* **67**, 661 (1991).
- [95] C.H. Bennett, G. Brassard, C. Crépeau, R. Jozsa, A. Peres, and W.K. Wootters, *Phys. Rev. Lett.* **70**, 1895 (1993).
- [96] J.S. Bell, *Rev. Mod. Phys.* **38**, 447 (1966).
- [97] A. Aspect, J. Dalibard, and G. Roger, *Phys. Rev. Lett.* **49**, 1804 (1982).
- [98] P. Recher, E.V. Sukhorukov, and D. Loss, *Phys. Rev. B* **63**, 165314 (2001).
- [99] P. Recher and D. Loss, *Phys. Rev. B* **65**, 165327 (2002).
- [100] C. Bena, S. Vishveshwara, L. Balents, and M.P.A. Fisher, *Phys. Rev. Lett.* **89**, 037901 (2002).
- [101] P. Recher and D. Loss, *Phys. Rev. Lett.* **91**, 267003 (2003).
- [102] D.S. Saraga and D. Loss, *Phys. Rev. Lett.* **90**, 166803 (2003).
- [103] W.D. Oliver, F. Yamaguchi, and Y. Yamamoto, *Phys. Rev. Lett.* **88**, 037901 (2002).
- [104] P. Samuelsson, E.V. Sukhorukov, and M. Büttiker, *Phys. Rev. Lett.* **91**, 157002 (2003).

BIBLIOGRAPHY

- [105] C.W.J. Beenakker, C. Emary, M. Kindermann, and J.L. van Velsen, *Phys. Rev. Lett.* **91**, 147901 (2003).
- [106] X. Hu, and S. Das Sarma, *Phys. Rev. B* **69**, 115312 (2004).
- [107] P. Recher, D.S. Saraga, and D. Loss, in *Fundamental Problems of Mesoscopic Physics Interaction and Decoherence*, pp. 179-202, eds. I.V. Lerner *et al.*, NATO Science Series II, Vol. 154 (Kluwer, Dordrecht, 2004).
- [108] G. Burkard, D. Loss, and E.V. Sukhorukov, *Phys. Rev. B*, **61**, R16303 (2000).
- [109] S. Kawabata, *J. Phys. Soc. Jpn.* **70**, 1210 (2001).
- [110] J.C. Egues, G. Burkard, and D. Loss, *Phys. Rev. Lett.* **89**, 176401 (2002).
- [111] N.M. Chtchelkatchev, G. Blatter, G.B. Lesovik, and T. Martin, *Phys. Rev. B* **66**, 161320(R) (2002).
- [112] G. Burkard and D. Loss, *Phys. Rev. Lett.* **91**, 087903 (2003).
- [113] J.C. Egues, P. Recher, D.S. Saraga, V.N. Golovach, G. Burkard, E.V. Sukhorukov, and D. Loss, in *Quantum Noise in Mesoscopic Physics*, pp. 241-274 (Kluwer, The Netherlands, 2003); cond-mat/0210498.
- [114] P. Samuelsson, E.V. Sukhorukov, and M. Büttiker, *Phys. Rev. B* **70**, 115330 (2004).
- [115] V.N. Golovach and D. Loss, *Europhys. Lett.* **62**, 83 (2003).
- [116] J. Schliemann, D. Loss, and A.H. MacDonald, *Phys. Rev. B* **63**, 085311 (2001).
- [117] J. Schliemann, J.I. Cirac, M. Kus, M. Lewenstein, and D. Loss, *Phys. Rev. A* **64**, 022303 (2001).
- [118] V.N. Golovach and D. Loss, *Semicond. Sci. Technol.* **17**, 355 (2002).
- [119] H.M. Wiseman and J.A. Vaccaro, *Phys. Rev. Lett.* **91**, 097902 (2003).
- [120] D.M. Zumbühl, C.M. Marcus, M.P. Hanson, and A.C. Gossard, *Phys. Rev. Lett.* **93**, 256801 (2004).
- [121] Constantine Yannouleas, Uzi Landman, cond-mat/0501612.
- [122] L.D. Landau and E.M. Lifshitz, *Quantum Mechanics: non-relativistic theory*, (Pergamon Press Ltd. 1977).
- [123] C.P. Slichter, *Principles of Magnetic Resonance*, (Springer-Verlag, Berlin, 1980).
- [124] A.V. Khaetskii, Yu.V. Nazarov, *Phys. Rev. B* **61**, 12639 (2000).

- [125] A.V. Khaetskii, D. Loss, L. Glazman, Phys. Rev. Lett. **88** 186802 (2002); Phys. Rev. B **67** 195329 (2003).
- [126] I.A. Merkulov, Al.L. Efros, M. Rosen, Phys. Rev. B **65**, 205309 (2002).
- [127] S.I. Erlingsson and Yu.V. Nazarov, Phys. Rev. B **66**, 155327 (2002).
- [128] J. Schliemann, A.V. Khaetskii, D. Loss, Phys. Rev. B **66**, 245303 (2002).
- [129] R. de Sousa and S. Das Sarma, Phys. Rev. B **67**, 033301 (2003).
- [130] W.A. Coish and D. Loss, Phys. Rev. B **70**, 195340 (2004).
- [131] H.-A. Engel and D. Loss, Phys. Rev. Lett. **86**, 4648 (2001); Phys. Rev. B **65**, 195321 (2002).
- [132] O. Gywat, H.-A. Engel, D. Loss, R.J. Epstein, F.M. Mendoza, and D.D. Awschalom, Phys. Rev. B **69**, 205303 (2004).
- [133] J.R. Petta, A.C. Johnson, J.M. Taylor, A. Yacoby, M.D. Lukin, C.M. Marcus, M.P. Hanson, and A.C. Gossard, (unpublished).
- [134] K. Ono, D.G. Austing, Y. Tokura, and S. Tarucha, Science **297**, 1313 (2002).
- [135] D.V. Averin and Yu.V. Nazarov, in *Single Charge Tunneling*, edited by RH.Grabert and M.H. Devoret, NATO ASI Series B: Physics Vol. 294 (Plenum Press, New York, 1992).
- [136] P.W. Anderson, J. Phys. C **3**, 2436 (1970); A.C. Hewson, *The Kondo Problem to Heavy Fermions* (Cambridge University Press, 1993).
- [137] W.J. de Haas, J.H. de Boer, and G.J. van den Berg, Physica **1**, 1115 (1934).
- [138] J. Kondo, Prog. Theor. Phys. **32**, 37 (1964).
- [139] L.I. Glazman and M.E. Raikh, JETP Lett. **47**, 452 (1988).
- [140] T.K. Ng and P.A. Lee, Phys. Rev. Lett. **61** 1768 (1988).
- [141] L. Kouwenhoven and L. Glazman, Physics World **14**, 33 (2001).
- [142] D. Goldhaber-Gordon, H. Shtrikman, D. Mahalu, D. Abusch-Magder, U. Meirav, and M.A. Kastner, Nature **391**, 156 (1998).
- [143] U. Smilansky, Waves Random Media **14**, S143 (2004).
- [144] S.M. Cronenwett, T.H. Oosterkamp, and L.P. Kouwenhoven, Science **281**, 540 (1998).
- [145] J. Schmid, J. Weis, K. Eberl and K. v. Klitzing, Physica B **256-258**, 182 (1998).

BIBLIOGRAPHY

- [146] T.W. Odom, J.-L. Huang, C.L. Cheung, and C.M. Lieber, *Science* **290**, 1549 (2000).
- [147] J. Nygard, D.H. Cobden, and P.E. Lindelof, *Nature (London)* **408**, 342 (2000).
- [148] S. Tarucha, D.G. Austing, Y. Tokura, W.G. van der Wiel, and L.P. Kouwenhoven, *Phys. Rev. Lett.* **84**, 2485 (2000).
- [149] S. Sasaki, S. De Franceschi, J.M. Elzerman, W.G. van der Wiel, M. Eto, S. Tarucha, and L.P. Kouwenhoven, *Nature (London)* **405**, 764 (2000).
- [150] J. Schmid, J. Weis, K. Eberl, and K. v. Klitzing, *Phys. Rev. Lett.* **84**, 5824 (2000).
- [151] W.G. van der Wiel, S. De Franceschi, J.M. Elzerman, S. Tarucha, and L. P. Kouwenhoven, *Phys. Rev. Lett.* **88**, 126803 (2002).
- [152] D. Giuliano and A. Tagliacozzo, *Phys. Rev. Lett.* **84**, 4677 (2000); D. Giuliano, B. Jouault, A. Tagliacozzo, *Phys. Rev. B* **63**, 25318 (2001).
- [153] M. Eto and Y. Nazarov, *Phys. Rev. Lett.* **85**, 1306 (2000); *Phys. Rev. B* **64**, 085322 (2001).
- [154] M. Pustilnik and L.I. Glazman, *Phys. Rev. Lett.* **85**, 2993 (2000); *Phys. Rev. B* **64**, 045328 (2001).
- [155] M. Eto and Y. Nazarov, *Phys. Rev. B* **66**, 153319 (2002).
- [156] M. Pustilnik and L.I. Glazman, *Phys. Rev. Lett.* **87**, 216601 (2001).
- [157] W. Hofstetter and H. Schoeller, *Phys. Rev. Lett.* **88**, 016803 (2002).
- [158] T. Aono and M. Eto, *Phys. Rev. B* **63**, 125327 (2001);
- [159] A. Georges and Y. Meir, *Phys. Rev. Lett.* **82**, 3508 (1999).
- [160] W. Izumida and O. Sakai, *Phys. Rev. B* **62**, 10260 (2000).
- [161] H. Jeong, A.M. Chang, and M.R. Melloch, *Science* **293**, 2221 (2001).
- [162] F.R. Waugh, M.J. Berry, D.J. Mar, R.M. Westervelt, K.L. Campman, and A.C. Gossard, *Phys. Rev. Lett.* **75** 705 (1995).
- [163] J.R. Schrieffer and P.A. Wolff, *Phys. Rev.* **149**, 491 (1966).
- [164] I. Affleck, A.W.W. Ludwig, and B.A. Jones, *Phys. Rev. B* **52**, 9528 (1995).
- [165] P. Recher, E.V. Sukhorukov, and D. Loss, *Phys. Rev. Lett.* **85**, 1962 (2000).
- [166] A. Peres, *Quantum Theory: Concepts and Methods* (Kluwer, Dordrecht, 1993).

-
- [167] X. Hu and S. Das Sarma, Phys. Rev. A **64**, 042312 (2001).
- [168] M. Ciorga, A.S. Sachrajda, P. Hawrylak, C. Gould, P. Zawadzki, S. Jullian, Y. Feng, and Z. Wasilewski, Phys. Rev. B **61**, R16315 (2000).
- [169] D. Loss and E.V. Sukhorukov, Phys. Rev. Lett. **84**, 1035 (2000).
- [170] E.V. Sukhorukov, G. Burkard, and D. Loss, Phys. Rev. B **63**, 125315 (2001).
- [171] I.L. Aleiner, N.S. Wingreen, and Y. Meir, Phys. Rev. Lett. **79**, 3740 (1997).
- [172] Y. Levinson, Europhys. Lett. **39**, 299 (1997).
- [173] G.E. Pikus, A.N. Titkov, in *Optical Orientation*, North-Holland, Amsterdam, p.73 (1984).
- [174] B.I. Halperin, A. Stern, Y. Oreg, J.N.H.J. Cremers, J.A. Folk, and C.M. Marcus, Phys. Rev. Lett. **86**, 2106 (2001).
- [175] I.L. Aleiner and V.I. Fal'ko, Phys. Rev. Lett. **87**, 256801 (2001).
- [176] W. Zawadzki and P. Pfeffer, Semicond. Sci. Technol. **19**, R1 (2004).
- [177] V.F. Gantmakher and Y.B. Levinson, *Carrier Scattering in Metals and Semiconductors* (North-Holland, Amsterdam, 1987).
- [178] D. Loss and D.P. DiVincenzo, Phys. Rev. B **71**, 035318 (2005).
- [179] J. Schliemann, J.C. Egues, and D. Loss, Phys. Rev. Lett. **90**, 146801 (2003).
- [180] M.I. D'yakonov and V.Yu. Kachorovskii, Sov. Phys. Semicond. **20**, 110 (1986).
- [181] Y.G. Semenov and K.W. Kim, Phys. Rev. Lett. **92**, 026601 (2004).
- [182] A. Khaetskii, Physica E **10**, 27 (2001).
- [183] A.V. Khaetskii and Yu.V. Nazarov, Phys. Rev. B **61**, 12639 (2000).
- [184] J.A. Folk, S.R. Patel, K.M. Birnbaum, C.M. Marcus, C.I. Duruöz and J.S. Harris, Jr., Phys. Rev. Lett. **86**, 2102 (2001).
- [185] J.B. Miller, D.M. Zumbühl, C.M. Marcus, Y.B. Lyanda-Geller, D. Goldhaber-Gordon, K. Campman, and A.C. Gossard, Phys. Rev. Lett. **90**, 076807 (2003).
- [186] Yu.A. Bychkov, E.I. Rashba, JETP Lett. **39**, 78 (1984).
- [187] T. Fujisawa, Y. Tokura and Y. Hirayama, Phys. Rev. B **63**, R081304 (2001);
- [188] S. Dickmann and P. Hawrylak, Journal of superconductivity: Incorporating Novel Magnetism **16**, 387 (2003).

BIBLIOGRAPHY

- [189] R. Hanson, L.H. Willems van Beveren, I.T. Vink, J.M. Elzerman, W.J.M. Naber, F.H.L. Koppens, L.P. Kouwenhoven, and L.M.K. Vandersypen, *Phys. Rev. Lett.* **94**, 196802 (2005).
- [190] O. Gywat, H.-A. Engel, and D. Loss, cond-mat/0408451.
- [191] G. Mahan, *Many Particle Physics*, third edition (Plenum Press, New York, 2000).
- [192] Ya.M. Blanter and M. Büttiker, *Phys. Rep.* **336**, 1 (2000).
- [193] H.-A. Engel, V.N. Golovach, D. Loss, L.M.K. Vandersypen, J.M. Elzerman, R. Hanson, and L.P. Kouwenhoven, *Phys. Rev. Lett.* **93**, 106804 (2004).
- [194] K. Bosch, *Grosses Lehrbuch der Statistik* (R. Oldenbourg, Munich, 1996), pp. 379.
- [195] B.E. Kane, N.S. McAlpine, A.S. Dzurak, R.G. Clark, G.J. Milburn, H.B. Sun, and H. Wiseman, *Phys. Rev. B* **61**, 2961 (2000).
- [196] W. Lu, Z.Q. Ji, L. Pfeiffer, K.W. West, and A.J. Rimberg, *Nature* **423** (6938), 422 (2003).
- [197] S.A. Gurvitz, *Phys. Rev. B* **56**, 15215 (1997).
- [198] A.N. Korotkov, *Phys. Rev. B* **63**, 115403 (2001).
- [199] H.-S. Goan, G.J. Milburn, H.M. Wiseman, and H.B. Sun, *Phys. Rev. B* **63**, 125326 (2001).
- [200] K. Blum, *Density Matrix Theory and Applications* (Plenum Press, New York, 1996), Chap. 8.
- [201] T. Hayashi, T. Fujisawa, H.-D. Cheong, Y.-H. Jeong, and Y. Hirayama, *Phys. Rev. Lett.* **91**, 226804 (2003).
- [202] Y. Makhlin, G. Schön, and A. Shnirman, *Phys. Rev. Lett.* **85**, 4578 (2000).
- [203] Y. Meir and A. Golub, *Phys. Rev. Lett.* **88**, 116802 (2002).
- [204] F. Yamaguchi and K. Kawamura, *Physica B* **227**, 116 (1996).
- [205] A. Schiller and S. Hershfield, *Phys. Rev. B* **58**, 14978 (1998).

Curriculum Vitae

Vitaly N. Golovach (in passport: Vitaliy Holovach)

Date of birth: June 14, 1975

Place of birth: Voloka, Chernivtsi district, Ukraine

Citizenship: Ukraine

Marital status: married

Address: Department of Physics and Astronomy, University of Basel,
Klingelbergstrasse 82, CH-4056 Basel, Switzerland

E-mail: Vitaly.Golovach@unibas.ch

Webpage: <http://theorie5.physik.unibas.ch/golovach/>

Education

1981–1986	Primary School, Voloka, Chernivtsi district, Ukraine
1986–1990	Secondary School, Voloka, Chernivtsi district, Ukraine
1990–1992	High School, Voloka, Chernivtsi district, Ukraine
June 1992	High School Certificate with Distinction
1992–1997	State University of Chernivtsi, Ukraine
June 1997	Diploma in Physics, State University of Chernivtsi, Ukraine. Thesis: <i>Electron and hole spectra in an ellipsoidal quantum dot</i> , supervisor: Prof. Dr. N.V. Tkach
1997–1999	Department of Theoretical Bases of Microelectronics, Ioffe Physico-Technical Institute, St. Petersburg, Russia
1999-2001	School of Physics, University of Exeter, United Kingdom
2001-2005	Department of Physics and Astronomy, University of Basel, Switzerland
July 2005	Submission of PhD thesis in Theoretical Physics, entitled <i>Electron Spins in Single and Double Quantum Dots: Transport, Correlations and Decoherence</i> , supervisor Prof. Dr. D. Loss

For my education I am indebted to Prof. Dr. C. Bruder, Prof. Dr. R. Jones, Prof. Dr. A.V. Konstantinovich, Prof. Dr. D. Loss, Prof. Dr. S.V. Melnichuk, N.D. Paulenku, Prof. Dr. V.I. Perel', P.F. Pshenichka, Dr. M.E. Portnoi, Prof. Dr. J.R. Sambles, Prof. Dr. A.K. Savchenko, Prof. Dr. C. Schönenberger, Prof. Dr. G.P. Srivastava, Prof. Dr. R. A. Suris, Prof. Dr. N.V. Tkach, Dr. C.D.H. Williams, Prof. Dr. G.G. Zegrya.

Publications

H.-A. Engel, V.N. Golovach, D. Loss, L.M.K. Vandersypen, J.M. Elzerman, R. Hanson, and L.P. Kouwenhoven, *Measurement Efficiency and n -Shot Readout of Spin Qubits*, Phys. Rev. Lett. **93**, 106804 (2004).

V.N. Golovach and D. Loss, *Transport through a double quantum dot in the sequential tunneling and cotunneling regimes*, Phys. Rev. B **69**, 245327 (2004).

V.N. Golovach, A. Khaetskii, and D. Loss, *Phonon-Induced Decay of the Electron Spin in Quantum Dots*, Phys. Rev. Lett. **93**, 016601 (2004).

J.C. Egues, P. Recher, D.S. Saraga, V.N. Golovach, G. Burkard, E.V. Sukhorukov, and D. Loss, *Shot noise for entangled and spin-polarized electrons*, in NATO Science Series *Quantum Noise in Mesoscopic Physics*, Vol. **97**, pp. 241–274 (Kluwer, the Netherlands, 2003).

V.N. Golovach and D. Loss, *Kondo effect and singlet-triplet splitting in coupled quantum dots in a magnetic field*, Europhys. Lett., **62**(1), pp. 83-89 (2003).

V.N. Golovach and D. Loss, *Electron Spins in Artificial Atoms and Molecules for Quantum Computing*, Semicond. Sci. Technol., **17**(4), pp. 355–366 (2002).

V.N. Golovach and M.E. Portnoi, *Electron-phonon scattering at the intersection of two Landau levels*, cond-mat/0202179.

V.N. Golovach, G.G. Zegrya, A.M. Makhanets, I.V. Pronishin, and N.V. Tkach, *Electron and hole spectra in a superlattice of cylindrical quantum wires*, Semiconductors **33**(5), pp. 564-568 (1999).

S.D. Suchalkin, Yu.B. Vasil'ev, K. von Klitzing, V.N. Golovach, G.G. Zegrya, S.V. Ivanov, P.S. Kop'ev, and B.Ya. Mel'tser, *On the nature of the oscillations of cyclotron absorption in InAs/GaSb quantum wells*, JETP Letters **68**(10), pp. 792-798 (1998).